

THESE DE DOCTORAT

Présentée à

L'UNIVERSITE DE LILLE 1

Ecole Doctorale Régionale Sciences Pour l'Ingénieur Lille Nord-de-France



pour obtenir le grade de

DOCTEUR EN SCIENCES

Dans la spécialité

Micro et Nano Technologies, Acoustique et Télécommunications

par

Nadine AL-KHUDARY

MATERIAL THERMAL CONDUCTIVITY MEASUREMENT BY
THE 3-OMEGA METHOD
APPLICATION TO POLYMER CHARACTERIZATION USING
INKJET PRINTING TECHNOLOGY

Soutenue le 17 décembre 2014

Prof. Nathalie TRANNOY	Rapporteur	Université de Reims
Prof. Tayyeb MOHAMMED BRAHIM	Rapporteur	Université de Rennes 1
Prof. Pierre-Yves JOUBERT	Examineur	Université Paris Sud
Prof. Gilles DAMBRINE	Examineur	Université Lille 1
Prof. Tuami LASRI	Directeur de thèse	Université de Lille 1
Dr. Pierre-Yves CRESSON	Co-encadrant	Université d'Artois



This work has been carried out within Microtechnology and Instrumentation for Thermal and Electromagnetic Characterization (MITEC) group at the Institute of Electronics, Microelectronics and Nanotechnology (IEMN).

First of all, I would like to thank Mr. Lionel BUCHAILLOT and Mr. Tuami LASRI for giving me the opportunity to successfully achieve this work.

I wish to express my sincere thanks to Mrs. Nathalie TRANNOY, Professor at the University of Reims and Mr. Tayeb MOHAMMED BRAHIM, Professor at the University of Rennes for reporting my thesis.

Also, I would like to thank Mr. Pierre-Yves JOUBERT, Professor at the University of South Paris, Mr. Gilles DAMBRINE, Professor at the University of Lille 1 and Mr. Pierre-Yves CRESSON, Associate Professor at the University of ARTOIS for accepting being among my jury members.

I express my appreciation to my thesis director Mr. Tuami LASRI and to my co-supervisor Mr. Pierre-Yves CRESSON for their continuous support, patience, guidance and motivation.

I am so grateful to all the members of MITEC group, particularly Zahia BOUGRIOUA and Katir ZIOUCHE who have enthusiastically shared their knowledge and expertise and who have made me take advantage of their valuable remarks.

I express my sincere gratitude to Wei Wei and Yovan Orlic for their help and cooperation to successfully complete this work.

To my friends, thanks for listening, offering me advice, and supporting me through these entire four years. Special thanks to Abdelhatif, Abdallah, Hind, Eva, Di, Wei, Philip, Zahir, Siija and Soufiane.

I owe my deepest gratitude towards my husband for his encouragement and tolerance. Without his patience and sacrifice I couldn't have completed this work. My heart felt regard goes to my parents, my children, Nael and Samy, my brothers, Rami and Kareem, my sisters, Hiba, Sara, and Hoda, my sisters in law Souha and Aicha and my brother in law Mohammad for their love and moral support.

General introduction	3
Chapter I: The three omega method: Theoretical considerations.	
<i>Introduction</i>	9
I. Basic concepts	11
I.1. Introduction.....	11
I.2. Heat transfer.....	11
I.2.a. Heat Conduction.....	11
I.2.b. Heat Convection.....	12
I.2.c. Radiation.....	13
I.3. Parameters definition.....	14
I.3.a. Thermal conductivity.....	14
I.3.b. Thermal diffusivity.....	15
I.3.c. Thermal effusivity.....	15
I.4. Fourier's equation.....	16
I.4.a. Boundary conditions and initial conditions.....	17
I.4.b. Resolution methods.....	19
I.5. Conclusion.....	20
II. Methods used for measuring the thermal conductivity of materials	20
II.1. Introduction.....	20
II.2. Steady state methods.....	20
II.2.a. Guarded hot plate method (GHP).....	21
II.2.b. Radial heat flow method.....	22
II.3. Transient methods.....	23
II.3.a. Transient hot wire method.....	23
II.3.b. Time domain thermo-reflectance technique.....	24
II.3.c. The three omega method.....	25
II.4. Conclusion.....	26
III. Theoretical considerations of the three omega method	26
III.1. Introduction.....	26

III.2. The three omega method theoretical basis.....	27
III.3. Cahill's formula.....	30
III.3.a. Heater of finite width.....	31
III.4. Solution of the exact equation.....	32
III.4.a. Finding the approximate equation for linear regime.....	33
III.4.b. Finding the approximate equation for the planar regime.....	35
III.4.c. Linear regime boundaries.....	36
III.4.d. Estimation of the linear regime frequency interval for a sample of known thickness.....	37
III.5. Examples of temperature oscillations and third harmonic voltages for bulk materials.....	37
III.6. Conclusion.....	41
Conclusion	43
REFERENCES	45
Chapter II: The 3ω method based experimental setup: Implementation and measurement precision.	
Introduction	53
I. The 3ω method-based experimental setup	55
I.1. Introduction.....	55
I.2. Lock-in amplifier SR830.....	56
I.3. Microscope and micromanipulators.....	58
I.4. Function generator and measurement meters.....	58
I.5. Conclusion.....	59
II. Sample preparation for the 3ω method	60
II.1. Introduction.....	60
II.2. Sample design.....	60
II.3. Sample preparation by process of optical lithography.....	61
II.3.a. Cleaning substrate surface.....	61
II.3.b. Photolithography.....	61
II.3.c. Metal deposition.....	62
II.3.d. Liftoff process.....	63
II.4. Resistances of the fabricated metallic lines.....	64
II.5. Thermal coefficient measurement method.....	66

II.6. Conclusion.....	67
III. Experimental procedure of the 3ω measurement.....	67
III.1. Introduction.....	67
III.2. Wheatstone bridge method.....	68
III.2.a. Principle	68
III.2.b. Wheatstone bridge design.....	69
III.2.c. Third harmonic voltage measurement.....	71
III.3. Differential amplifier circuit.....	72
III.3.a. Principle.....	72
III.3.b. The circuit design.....	73
III.4. Conclusion.....	73
IV. Validation of the 3ω method-based experimental setup.....	74
IV.1. Introduction.....	74
IV.2. Thermal conductivity measurement of different materials.....	74
IV.3. Linear regression analysis in linear regime.....	76
IV.4. Experimental measurements.....	77
IV.5. Wheatstone bridge and differential amplifier measurements.....	77
IV.6. Conclusion.....	84
V. The 3ω experimental setup measurement precision.....	85
V.1. Introduction.....	85
V.2. Repeatability measurements.....	85
V.3. Systematic errors and measurement precision.....	87
V.3.a. The metallic line resistance R_0	88
V.3.b. The initial voltage V_0	89
V.3.c. The temperature coefficient of resistance β_h	90
V.3.d. The effect of $V_{3\omega \text{ in phase}}$ versus $\ln(2\omega)$ on the thermal conductivity value.....	93
V.3.e. The effect of V_0 , R_0 , β_h and slope measurement errors.....	95
V.4. Electronic circuits parasitic effects.....	96
V.5. Conclusion.....	100
Conclusion.....	103
REFERENCES.....	104

Chapter III: Numerical simulations using FEM: The 3ω differential technique for film-on-substrate system.

<i>Introduction</i>	111
I. Numerical simulation by Finite Element Method (FEM)	113
I.1. Introduction.....	113
I.2. FEM and COMSOL [®] Multiphysics Software.....	113
I.3. Comparison between Cahill's solution and simulation by FEM.....	116
I.3.a. Description of the studied structure.....	117
I.3.b. Boundary conditions.....	118
I.3.c. The heat source.....	119
I.3.d. Meshing of the structure.....	121
I.3.e. Determination of the temperature oscillations ΔT_{AC}	122
I.3.f. Validation of FEM modelling.....	125
I.4. Modelling improvement.....	128
I.4.a. Influence of a finite thickness substrate.....	128
I.4.b. Influence of the characteristics of the heating element.....	131
I.4.c. Real structure modelling.....	136
I.5. Conclusion.....	133
II. Application to a two layer model	134
II.1. Introduction.....	134
II.2. The 3ω differential technique.....	134
II.3. Measurement of the thermal conductivity of SiO ₂ thin film.....	136
II.4. Measurement of the thermal conductivity of thin film of impure GaAs.....	147
II.5. Numerical simulation.....	152
II.6. Conclusion.....	155
<i>Conclusion</i>	157
REFERENCES	159

Chapter IV: Inkjet printing technology for polymer testing by the 3ω method.

<i>Introduction</i>	165
I. Polymers	167

I.1. Introduction.....	167
I.2. Structure of Polymers.....	167
I.3. Classification of polymers.....	168
I.3.a. Thermoplastics.....	168
I.3.b. Elastomers.....	169
I.3.c. Thermosets.....	169
I.4. Chemical properties of polymers.....	169
I.5. Physical properties.....	170
I.5.a. Volume resistivity and electrical conductivity.....	170
I.5.b. Specific heat capacity.....	171
I.5.c. Glass transition temperature.....	172
I.5.d. Thermal conductivity.....	172
I.6. Polymers in flexible electronics.....	174
I.7. Conclusion.....	174
II. Measurement of the thermal conductivity of polymers using the 3ω method by preparing samples using photolithography.....	175
II.1. Introduction.....	175
II.2. Thermal conductivity measurement of Polyimide.....	175
II.2.a. Sample preparation using photolithography.....	176
II.2.b. Measuring the thermal conductivity at different temperatures.....	177
II.2.c. Comparison using Cahill's formula.....	182
II.3. Thermal conductivity measurement of Polydimethylsiloxane (PDMS).....	184
II.3.a. Sample preparation.....	184
II.3.b. Measuring the thermal conductivity at different temperatures.....	186
II.3.c. Comparison with Cahill's formula.....	189
II.4. Modeling improvement using FEM method.....	192
II.4.a. Applying numerical simulation to Polyimide sample.....	192
II.4.b. New FEM model designed for PDMS sample.....	194
II.5. Conclusion.....	196
III. Characterization of polymers using the 3ω method by preparing samples using inkjet printing technology.....	197

III.1. Introduction.....	197
III.2. Applying inkjet printing technology on PI and PEEK.....	198
III.2.a. Sample preparation by inkjet printing technology.....	198
III.2.b. Thermal conductivity measurement of PI.....	200
III.2.c. Thermal conductivity measurement of Polyether ether ketone (PEEK).....	202
III.3. Experimental-theoretical comparison for PI and PEEK.....	203
III.3.a. Polyimide.....	203
III.3.b. PEEK.....	205
III.4. Modeling improvement using FEM method.....	205
III.4.a. Applying numerical simulation to polyimide with printed metallic lines.....	205
III.4.b. Applying numerical simulation to PEEK with printed metallic lines.....	209
III.5. Conclusion.....	210
Conclusion	211
REFERENCES	213
General conclusion	219
APPENDIX A	A1
APPENDIX B	A2
List of personal work	

List of figures

Chapter I: The three omega method: Theoretical considerations.

Figure 1.1: Heat conducted through a material of thickness L	11
Figure 1.2: The normal heat flux at the surface of a medium.....	16
Figure 1.3: Temperature and flux continuity at the interface between two mediums.....	18
Figure 1.4: Symmetrical temperature distribution around the central plane of material.....	19
Figure 1.5: The guarded hot plate experimental setup.....	21
Figure 1.6: The radial heat flow method.....	22
Figure 1.7: Hot wire embedded in the sample at a distance r from the thermocouple.....	24
Figure 1.8: Time domain thermo-reflectance experimental setup [PER 2011].....	25
Figure 1.9: Metallic line with two contact pads deposited on surface of material of thickness t_s	27
Figure 1.10: A cross section of a semi-infinite cylindrical sample.....	30
Figure 1.11: The finite width line heater on the surface of the semi-infinite sample.....	31
Figure 1.12: The in-phase and out of phase components of the temperature oscillations versus the thermal excitation frequency 2ω	33
Figure 1.13: Temperature oscillations with respect to the natural logarithm of the thermal excitation frequency 2ω for linear regime.....	34
Figure 1.14: Comparison between the exact and approximate solutions for the linear and planar regimes.....	36
Figure 1.15: In-phase and out-of-phase component of temperature oscillations for kapton®.....	38
Figure 1.16: In-phase and out-of-phase component of temperature oscillations for silicon.....	38
Figure 1.17: The in-phase and out-of-phase third harmonic voltages for kapton®.....	41
Figure 1.18: The in-phase and out-of-phase third harmonic voltages for silicon.....	41

Chapter II: The 3ω method based experimental setup: Implementation and precision measurement.

Figure 2.1: Schematic Diagram of the 3ω experimental setup.....	55
Figure 2.2: The 3ω method experimental setup.....	55
Figure 2.3: Functional block diagram of the Lock-in amplifier.....	56
Figure 2.4: A 4 inch mask of 4-pads and 2-pads metallic lines.....	60
Figure 2.5: Photolithography procedure.....	62
Figure 2.6: Metal evaporation in vacuum chamber.....	63
Figure 2.7: Gold and chromium deposition by evaporation after photolithography process.....	63
Figure 2.8: Metallic patterns deposited on the surface of the substrate.....	64
Figure 2.9: 2-wire and 4-wire resistance connections to the micro-ohmmeter.....	64
Figure 2.10: Measurements of resistance versus temperature of a metallic line.....	67
Figure 2.11: (a) Wheatstone bridge. (b) Schematic diagram of the 3ω apparatus using the Wheatstone bridge.....	68
Figure 2.12: The Wheatstone bridge electrical circuit.....	69
Figure 2.13: Equivalent circuit of the variable resistance R_{3V}	70
Figure 2.14: The effective circuit for the measurement of the third harmonic voltage at the	

output of the Wheatstone bridge.....	71
Figure 2.15: Schematic diagram of the 3ω apparatus using the differential amplifier circuit.....	72
Figure 2.16: The equivalent circuit of the variable resistance R_v	73
Figure 2.17: The in-phase and out-of-phase third harmonic voltages measured on borosilicate substrate using both DA and WB circuits. The third harmonic voltages in blue correspond to Cahill's solution.....	79
Figure 2.18: The in-phase and out-of-phase third harmonic voltages measured on gallium arsenide substrate using both DA and WB circuits. The third harmonic voltages in blue correspond to Cahill's solution.....	80
Figure 2.19: The in-phase and out-of-phase third harmonic voltages measured on indium phosphide substrate using both DA and WB circuits. The third harmonic voltages in blue correspond to Cahill's solution.....	81
Figure 2.20: The in-phase and out-of-phase third harmonic voltages measured on high resistivity silicon substrate using both DA and WB circuits. The third harmonic voltages in blue correspond to Cahill's solution.....	82
Figure 2.21: Third harmonic voltages versus natural logarithm of 2ω for five repeated measurements on the same metallic line for borosilicate substrate when using the DA circuit (a) $p_{\text{rms}}=1.891$ W/m (b) $p_{\text{rms}}=4.537$ W/m.....	86
Figure 2.22: Average resistance versus average temperature for metallic line 3 on BrSiO_2 substrate.....	91
Figure 2.23: Slope variation corresponding to measurement error of average resistance and temperature.....	92
Figure 2.24: The variation of the slope due to the precision measurements of the lock in amplifier.....	94
Figure 2.25: Parasitic effects presents in the (a) WB and (b) DA circuits.....	98
Figure 2.26: Theoretical-experimental comparison of V_A-V_B for WB and DA circuits.....	99
Figure 2.27: A generator at frequency 3ω placed in series with the metallic line.....	99
Figure 2.28: The real (a) and imaginary (b) V_A-V_B voltages when considering and when neglecting the parasitic effects.....	100
 Chapter III: Numerical simulations using FEM: The 3ω differential technique for film-on-substrate system.	
Figure 3.1: Two-dimensional region subdivided in finite elements.....	114
Figure 3.2: Steps needed to perform modelling using FEM.....	115
Figure 3.3: (a) 3D and (b) 2D geometry of the metallic line deposited on the substrate under-test.....	119
Figure 3.4: (a) Cahill's assumptions on the structure to be simulated. (b) Symmetry condition.....	118
Figure 3.5: The use of "infinite" layers to produce a finite structure.....	119
Figure 3.6: Time evolution of current at frequency 10 Hz.....	120
Figure 3.7: Evolution of power with respect to time at frequency 10 Hz. Average power in red = P_{rms}	120
Figure 3.8: Time evolution of the heat source boundary element $Q_b(t)$ for line 2.....	121
Figure 3.9: (a) Coarse meshing and (b) fine meshing of the structure.....	121
Figure 3.10: Coarse (a) and fine meshing (b) of the heat source boundary element.....	122
Figure 3.11: Temperature evolution of the temperature oscillations ΔT_{AC} for line 2 (a). A zoom of the temperature oscillations at the beginning of the transient regime.....	123

Figure 3.12: Example of random sampling that permits the determination of A_T and ϕ_T	124
Figure 3.13: The in-phase and out-of-phase temperature oscillations plotted with respect to FEM and Cahill's solution for metallic line 2.....	125
Figure 3.14: Temperature at two instants of time at $y= 0$ mm.....	126
Figure 3.15: Thermal pattern of a half structure at ΔT_{AC} maximum (a). A zoom around the heating element (b).....	125
Figure 3.16: Thermal pattern of a half structure at ΔT_{AC} minimum (a). A zoom around the heating element (b).....	127
Figure 3.17: Structure to be simulated with isothermal conditions (a). Symmetry condition (b).....	129
Figure 3.18: Isotherm flattening due to the isothermal condition at the lower boundary of the substrate.....	129
Figure 3.19: Temperature oscillations of a structure of finite thickness simulated using FEM compared to Cahill's solution ($t_s= 700 \mu\text{m}$).....	130
Figure 3.20: Temperature oscillations obtained by FEM for 500 μm , 700 μm and 900 μm thick substrate.....	130
Figure 3.21: The in-phase temperature oscillations plotted for 500 μm , 700 μm and 900 μm thick substrate in the linear zone.....	131
Figure 3.22: The simulated structure considering the thickness of the heating element (a). Symmetry conditions (b).....	132
Figure 3.23: Meshing applied on the heating element.....	132
Figure 3.24: Temperature oscillations plotted for Cahill's solution and FEM simulations for an infinite thin metallic line ($t= 0$) and metallic line of thickness $t_{avg}= 0.4 \mu\text{m}$	133
Figure 3.25: The in-phase temperature oscillations plotted for Cahill's solution and FEM with metallic line of thicknesses $t= 0$, $t_{avg}= 0.4 \mu\text{m}$, $t_A= 0.2 \mu\text{m}$ and $t_B= 0.6 \mu\text{m}$	134
Figure 3.26: The in-phase temperature oscillations plotted in the linear regime for Cahill's solution and for FEM with three different metallic line widths.....	135
Figure 3.27: Temperature oscillations plotted for physical properties of bulk gold in blue and physical properties of bulk gold multiplied by 0.8 in red.....	135
Figure 3.28: The simulated structure with a substrate placed on a copper plate and a heat convection boundary condition on the surface (a). Symmetry condition (b).....	136
Figure 3.29: The AC temperature oscillations plotted with respect to Cahill and FEM when considering the copper plate and heat convection on the surface of substrate.....	137
Figure 3.30: A plot presenting a recapitulative of the numerical simulations performed throughout section I...137	
Figure 3.31: The experimental third harmonic voltages measured by WB and DA circuits compared to the theoretical ones obtained by FEM for models 1 and 2.....	138
Figure 3.32: The AC temperature oscillations obtained when multiplying both BrSiO_2 density and specific heat capacity by 0.8 and 1.2.....	139
Figure 3.33: A thin film of thermal conductivity k_f deposited on a substrate of thermal conductivity k_s	141
Figure 3.34: Determining the temperature rise ΔT_f through which we can calculate the thermal conductivity of thin film.....	142
Figure 3.35: SiO_2 thin film over Si doped substrate.....	143
Figure 3.36: The in-phase and out-of-phase third harmonic voltages for lines 13, 14, and 15.....	144

Figure 3.37: Frequency independent temperature oscillation ΔT_f for metallic line 13.....	145
Figure 3.38: Maximum and minimum temperature responses obtained due to the thin film deposited on substrate for metallic line 13.....	147
Figure 3.39: Thin film of impure GaAs deposited over GaAs substrate.....	148
Figure 3.40: In-phase and out of phase third harmonic voltages measured by lines 16, 17, and 18.....	149
Figure 3.41: Frequency independent temperature oscillation ΔT_f for metallic line 16.....	150
Figure 3.42: Variation of the thermal conductivity k_f of thin film with respect to thickness t_f	151
Figure 3.43: Two layer structure meshing for $\text{SiO}_2/\text{Si p}^{++}$	152
Figure 3.44: Comparison of AC temperature oscillations with respect to Cahill and FEM for metallic line 13 deposited on $\text{SiO}_2/\text{Si p}^{++}$	153
Figure 3.45: Theoretical and experimental in-phase third harmonic voltages for line 13.....	153
Figure 3.46: Comparison of AC temperature oscillations with respect to Cahill and FEM for metallic line 16 deposited on LT GaAs/GaAs.....	154
Figure 3.47: Theoretical and experimental in-phase third harmonic voltages for line 16.....	155

Chapter IV: Inkjet printing technology for polymer testing by the 3-omega method

Figure 4.1: Linear and non-linear structures of polymers.....	167
Figure 4.2: Polymers classification.....	168
Figure 4.3: The temperature dependence of heat capacity.....	171
Figure 4.4: Specific volume of various states of polymers as affected by temperature.....	172
Figure 4.5: A metallic line of 20 μm width prepared by photolithography.....	176
Figure 4.6: The in-phase and out-of-phase third harmonic voltages measured over polyimide for lines 19, 20, and 21.....	178
Figure 4.7: The in-phase third harmonic voltages measured over PI at different temperatures (metallic line 23).....	180
Figure 4.8: Thermal conductivities measured by lines 22, 23, and 24 at different temperatures.....	182
Figure 4.9: Comparison of experimental and theoretical (Cahill) third harmonic voltages at 20 $^\circ\text{C}$, 40 $^\circ\text{C}$, 90 $^\circ\text{C}$, and 135 $^\circ\text{C}$ for line 24.....	183
Figure 4.10: Main procedure steps for the fabrication of metallic line conductors embedded in the surface of PDMS.....	185
Figure 4.11: A microscopy image of a metallic line conductor embedded in PDMS surface.....	186
Figure 4.12: Third harmonic voltages measured in the linear regime for lines 25, 26, and 27.....	187
Figure 4.13: Experimental and theoretical in-phase and out-of-phase third harmonic voltages for metallic line 27.....	188
Figure 4.14: Simulated structure (not to scale). $T_0 = 20$ $^\circ\text{C}$, 40 $^\circ\text{C}$, 90 $^\circ\text{C}$, or 135 $^\circ\text{C}$	190
Figure 4.15: Comparison of experimental data and FEM solution at 20 $^\circ\text{C}$, 40 $^\circ\text{C}$, 90 $^\circ\text{C}$, and 135 $^\circ\text{C}$ for line 24.....	192
Figure 4.16: Heater embedded in PDMS.....	193
Figure 4.17: The simulated structure (not to scale).....	193
Figure 4.18: Cross-sectional view of the grid near the heater.....	194

Figure 4.19: A plot of the real and imaginary parts of temperature oscillations with respect to 2ω for line 27 at room temperature.....	195
Figure 4.20 Amplitude of the in-phase third harmonic voltages for line 27 plotted with respect to Cahill formula, models 1, 2, 3 and experimental measurements.....	196
Figure 4.21: Piezoelectric bending mode.....	198
Figure 4.22: Space between two ink droplets.....	199
Figure 4.23: Metallic lines printed by inkjet technology on PI (a) and PEEK (b).....	199
Figure 4.24: Metallic line resistance measured at different temperatures for line B.....	200
Figure 4.25: Measured in-phase third harmonic voltages for lines A, B, and C plotted over the linear regime frequency range of each line.....	201
Figure 4.26: The in-phase third harmonic voltages measured over lines D, E, and F.....	203
Figure 4.27: Theoretical and experimental in-phase and out-of-phase third harmonic voltages measured on line B over PI substrate.....	204
Figure 4.28: The in-phase third harmonic voltages plotted with respect to Cahill for $2b_1= 56 \mu\text{m}$, $2b_{\text{avg}}= 58 \mu\text{m}$ and $2b_2= 60 \mu\text{m}$	204
Figure 4.29: Theoretical and experimental in-phase and out-of-phase third harmonic voltages measured on line F over PEEK substrate.....	205
Figure 4.30: The theoretical in-phase third harmonic voltages calculated by FEM for different metallic line width $2b$ (a) different metallic line thickness t (b) and different thermal conductivities of printed ink (c).....	206
Figure 4.31: Thermal contact resistance R_f between the printed metallic line and the surface of PI.....	207
Figure 4.32: In-Phase third harmonic voltage obtained by different methods for PI substrate (Cahill's formula, FEM and experimental measurements).....	208
Figure 4.33: In-phase and out-of-phase temperature oscillations plotted over a wide frequency range.....	208
Figure 4.34: In-Phase third harmonic voltage obtained by different methods for PEEK substrate (Cahill's formula, FEM and experimental measurements).....	209

List of tables

Chapter I: The three omega method: Theoretical considerations.

Table 1.1: The lower frequency limit for a width $2b=20 \mu\text{m}$ and different specimen thickness t_s	39
Table 1.2: The upper frequency limit for a thickness $t_s=400 \mu\text{m}$ and different metallic line widths $2b$	39
Table 1.3: The lower and upper frequency limits in case of kapton®	40
Table 1.4: The lower and upper frequency limits in case of silicon.....	40

Chapter II: The 3ω method based experimental setup: Implementation and precision measurement.

Table 2.1: Average, minimum, and maximum measured resistances for several metallic lines.....	65
Table 2.2: Metal resistivity of each of the metallic lines.....	66
Table 2.3: The values of resistances and their TCR used in designing the Wheatstone bridge.....	70
Table 2.4: The values of the resistances and their TCR used in designing the differential amplifier circuit.....	73
Table 2.5: Thermal conductivities of BrSiO ₂ , GaAs, InP, and high resistivity Si given in literature.....	75
Table 2.6: Dimensions and properties of different metallic lines deposited on BrSiO ₂ , GaAs, InP, and Si.....	78
Table 2.7: The values of heat capacities, densities and thermal diffusion of BrSiO ₂ , GaAs, InP, and Si taken from literature.....	78
Table 2.8: The values of the thermal conductivities for each material measured by the wheatstone bridge and differential amplifier circuits.....	83
Table 2.9: Properties of metallic line used for repeatability measurements on borosilicate substrate.....	85
Table 2.10: The power applied and the corresponding thermal conductivity calculated for each trial when using the differential amplifier circuit.....	87
Table 2.11: The power applied and the corresponding thermal conductivity calculated for each trial when using the Wheatstone bridge circuit.....	87
Table 2.12: Minimum, maximum and average resistance values of metallic line 12 on Si substrate.....	88
Table 2.13: %errors produced due to minimum and maximum metallic line resistances.....	88
Table 2.14: AC voltage precision specifications of the multimeter.....	89
Table 2.15: R_{\min} , R_{\max} and R_{avg} at different temperatures measured for metallic line 3 on BrSiO ₂ substrate for the determination of β_h	91
Table 2.16: Variation of β_h , k_{DA} , and k_{WB} with respect to the slope.....	92
Table 2.17: The slope and thermal conductivity variations for measurements done on metallic line 3 using DA and WB circuits.....	94
Table 2.18: Percentage errors e_1 , e_2 , e_3 , e_4 and e_T for metallic lines 3, 4, 7, and 11.....	96
Table 2.19: Parasitic element corresponding to each passive element constituting the WB.....	97
Table 2.20: Parasitic element corresponding to each passive element constituting the DA.....	97

Chapter III: Numerical simulations using FEM: The 3ω differential technique for film-on-substrate system.

Table 3.1: Properties of metallic line 2 at room temperature ($T_0= 24.7 \text{ }^\circ\text{C}$) deposited on BrSiO ₂	116
Table 3.2: Properties of metallic lines deposited on boron doped Si substrate.....	143
Table 3.3: Thermal conductivity values measured using lines 13, 14, and 15.....	145

Table 3.4: ΔT_f , k_f and R_f calculated for metallic lines 13, 14, and 15.....	146
Table 3.5: Experimental, minimum and maximum valued of β_h , ΔT_f , and k_f (metallic line 13).....	147
Table 3.6: Properties of metallic lines 16, 17, and 18.....	148
Table 3.7: Thermal conductivities measured for GaAs substrate.....	150
Table 3.8: ΔT_f and k_f obtained by metallic lines 16, 17, and 18.....	150

Chapter IV: Inkjet printing technology for polymer testing by the 3 ω -method.

Table 4.1: Properties of metallic lines 19, 20, and 21.....	177
Table 4.2: Calculated thermal conductivities of Polyimide at $T_0= 25.4$ °C.....	179
Table 4.3: Properties of metallic lines 22, 23, and 24 deposited on polyimide at $T_0= 20$ °C.....	180
Table 4.4: The resistances of the metallic lines and the thermal conductivities of polyimide at different temperatures.....	181
Table 4.5: Average thermal conductivity of polyimide at different temperatures.....	182
Table 4.6: Different properties of lines 25, 26, and 27.....	186
Table 4.7: Thermal conductivity values measured at $T_0=22$ °C.....	188
Table 4.8: Thermal conductivity values at 60 °C and 100 °C.....	188
Table 4.9: Properties of metallic lines deposited by inkjet technology on polyimide substrate.....	200
Table 4.10: Temperature coefficient of resistance of lines A, B, and C measured by the hot plate method.....	201
Table 4.11: Thermal conductivities measured for polyimide through inkjet printed lines.....	201
Table 4.12: Different properties of metallic line D, E, and F printed on PEEK.....	202
Table 4.13: PEEK thermal conductivity measured by lines D, E, and F.....	203

AC: Alternating current

DA: Differential amplifier

FDM: Finite difference method

FEM: Finite element method

FVM: Finite volume method

GHP: Guarded hot plate

HMDS: Hexamethyldisilazane

HR: High resistivity

LIA: Lock-in amplifier

LPF: Low pass filter

LT: Low temperature

PDMS: Polydimethyl siloxane

PEB: Post-exposure bake

PEEK: Polyetherether ketone

PI: Polyimide

PSD: Phase sensitive detector

TCR: Temperature coefficient of resistance

THD: Total harmonic distortion

TDTR: Time domain thermo-reflectance

WB: Wheatstone bridge

General introduction

General introduction

Flexible or organic electronics consist in building electronic circuits by depositing electronic components onto flexible substrates. Among the drivers for the development of flexible electronics one can mention the possibility of high volume manufacturing, the low cost potential and the ease of device integration. Motivated by these promises, a great attention has been given to this technology in the past years. The application field of flexible electronics is extremely large and encompasses next generation of consumer electronics, healthcare, lightning, energy and so on. The high potential of flexible electronics is expected to allow large scale development in a near future. Flexible displays, cell phones, flexible and washable textiles with embedded electronics are well identified applications. Nevertheless, challenges in terms of design and fabrication, life time issues of organic materials, performance and standardized testing are still to be overcome. In this framework, polymer materials are playing a significant role thanks to their properties. Actually, their mechanical, optical and chemical properties such as high flexibility, optical clarity, high exploitation temperatures and robustness render them important materials for flexible electronics. Polymer materials are known to have high electrical resistivity and low thermal conductivity therefore they are widely used as dielectrics in the electronic industries. Their applications range from insulators and intermetallic dielectric layers to encapsulants and adhesives. Moreover, they are extensively used as resists during lithography process.

In all electronic systems thermal management is one of the main concerns. In organic electronics it is particularly true and the material used must either prevent heat transfer or be a good thermal conductor depending on the aim of the application. So, there is a need to know the material thermal conductivity. There are many methods available to measure the thermal conductivity which vary between steady state and transient. The most popular methods are the guarded hot plate method, the hot wire method, the time domain thermo-reflectance technique, and the three omega method. However, due to its simplicity and accuracy, the three omega method is the method of our choice. It requires the deposition of a metallic line conductor on the surface of the material to be tested. Initially, an alternating current at frequency ω is passed through the metallic line conductor. The metallic line acts as both a resistive heater and a thermometer. Due to Joule's effect, heat will be generated in the metallic line producing temperature oscillations at frequency 2ω . Consequently fluctuations in the resistance of the metallic line at frequency 2ω are produced. This leads to a third

harmonic voltage at frequency 3ω through which we can deduce the thermal conductivity of material under test.

The thermal conductivity of different polymers such as polyimide, polyaniline, and polymethyl methacrylate has been successfully measured by the three omega method. Nevertheless, the application of the three omega method on several kinds of polymers is difficult due to the inability to deposit metallic line conductors on polymers surface by conventional photolithography. In fact, photolithography is not the most suitable process for flexible electronics. Multiple and expensive steps are needed to deposit a metallic line conductor on surface of material. Moreover, it requires the use of different chemical products that might destroy most of polymeric substrates. Also, photolithography is considered to be time consuming and material wasting. Therefore, there is a need to find an alternative process, friendly on soft materials and capable of lowering time and cost.

In this work, we demonstrate the possibility of using the three omega method when metallic line conductors are prepared by means of an inkjet printing technology. Inkjet printing method is a non-contact and maskless approach since it has the ability to deposit the metal based ink in one single step on the surface of materials. Using this technology, cost, time and material wastage are reduced.

This dissertation is divided into four chapters.

In chapter I, we recall the different modes of heat transfer and several thermal material properties such as the thermal conductivity, thermal diffusivity and thermal effusivity. Also, we present the heat equation and the initial and boundary conditions that have to be set to solve such a differential equation. Different steady state and transient methods to measure the thermal conductivity of materials are briefly discussed. In a last section, we consider the theoretical basis and principles of the three omega method. Cahill's integral formula is presented together with an approximate solution to calculate the thermal conductivity of material.

In a second chapter, we present the three omega method-based experimental setup built in the laboratory. Each element constituting the setup is described. Before starting any three omega measurements, the sample must be prepared. To that end a metallic line conductor is deposited on the surface of substrate to be tested using photolithography. Two common mode cancellation techniques, the Wheatstone bridge and the differential amplifier circuits are implemented to extract the third harmonic voltage produced across the metallic line. The three

omega method-based experimental setup is validated by performing measurements on four materials of different thermal conductivities. An experimental-theoretical (Cahill) comparison is done. Finally, the measurement precision of the experimental setup is investigated.

Chapter III is dedicated to the simulation of the three omega method using finite element method (FEM). A metallic line-on-substrate structure holding Cahill's constraints is numerically simulated. In this treatment, different steps including boundary conditions, meshing, and heat source location are applied. Then, a theoretical study is also performed on a two layer model consisting of a film-on-substrate system. The three omega differential technique for measuring the thermal conductivity of thin films is implemented. Experimental results are then compared to both Cahill's formalism and FEM numerical simulations.

In the last chapter, the thermal conductivities of different polymer materials, polyimide (PI), polydimethyl siloxane (PDMS) and polyetherether ketone (PEEK), are measured using the three omega method. Firstly, PI sample preparation is done using conventional photolithography process. PDMS sample is prepared by applying a special procedure where the metallic line conductor is embedded onto its surface. An improved model for PDMS sample using finite element method is performed. Due to the incompatibility of photolithography with this kind of soft materials, we present an alternative to this process based on inkjet printing technology. The procedure to apply this technology is described. Several metallic lines are then printed on the surfaces of PI and PEEK polymer materials. To verify the compatibility of the three omega method with the inkjet printing technology, the thermal conductivity measurements are performed on PI and PEEK samples. FEM modelling for inkjet printed metallic lines on the surface of polymers are implemented.

Chapter I

The three omega method: Theoretical considerations

Introduction

In the recent years, there has been a growing interest for flexible materials as electronic substrates to be used in flexible electronics. One of the important parameters to be known for this kind of materials is their thermal conductivity to ascertain their usefulness for specific applications. A low thermal conductivity renders difficult the penetration of heat into the material. Conversely, a material with high thermal conductivity conducts heat more easily. Different methods, altering between steady state and transient, exist for measuring thermal conductivity. Generally, transient methods are considered to be faster than steady state ones and are more appropriate for specimens of small thickness. Among the transient methods we find the 3 omega technique which was originally developed by Cahill [CAH 1990]. This method has several advantages over other transient methods that will be explained in this chapter. Given these benefits, we have chosen the three omega method to determine the thermal conductivity of the materials of interest in this study.

In section I of the chapter, the different heat transfer modes are presented. Several physical properties of materials that will appear throughout the chapter are defined. Then, Fourier's heat conduction equation is given together with the resolution methods and boundary conditions used to solve this equation.

Section II is dedicated to the presentation of the various steady state and transient methods for measuring the thermal conductivity of materials. The advantages and drawbacks of these methods are examined.

The last section considers the theoretical basis of the three omega method. It discusses the principles of this method and shows the derivation of Cahill's integral formula of the steady state temperature oscillations. Then, we demonstrate how the thermal conductivity of the material under test is retrieved from an approximate solution of the integral formula. At the end of this section, as an example, Cahill's formula is applied to two kinds of materials, kapton which is a thermal insulator and silicon which is a good thermal conductor.

I. Basic concepts

I.1. Introduction

The transfer of heat between two physical systems occurs through three different mechanisms: conduction, convection and radiation. Each of these mechanisms takes place according to the type of systems exchanging heat. Heat is transferred by conduction according to Fourier's law of conduction. Moreover, the degree of the ability of heat to be conducted through a system is determined by its physical properties such as the thermal conductivity, thermal diffusivity and thermal effusivity. The rate of heat conducted in a system is determined by the resolution of Fourier's equation. This latter can be solved using finite element methods (FEM) or finite difference methods (FDM). The different modes of heat transfer are described thereafter.

I.2. Heat transfer

Heat transfer is the transport of thermal energy from one system to another under the influence of a temperature gradient. In general, heat transfer occurs in three different ways: by conduction when heat is exchanged between two solid systems due to the movement of their elementary particles, by convection when a fluid medium is responsible of carrying heat from one region to another, and finally by radiation when heat is transmitted in the form of electromagnetic waves.

I.2.a. Heat Conduction

Conduction is defined as the transfer of heat in a solid from a high temperature medium to a low temperature medium due to the existence of a temperature gradient in the solid body.

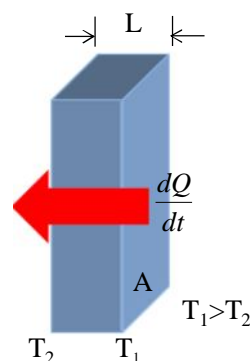


Figure 1.1: Heat conducted through a material of thickness L.

Molecules near the hot medium are heated and start to vibrate at high speed. They bounce off the neighboring molecules causing them to vibrate faster. Thus, heat is transferred from more to less energetic molecules due to the presence of an energetic gradient.

Actually, heat is transferred by both lattice vibration waves (phonons) and free electrons. Phonons transport thermal energy from high temperature to low temperature mediums. Moreover, free electrons in high temperature mediums possess kinetic energy. During their migration to colder regions collisions occur with phonons or imperfections present in the material causing some of the free electron's kinetic energy to be transferred to colder atoms as vibrational energy and consequently generating heat.

Thermal conduction is properly described by Fourier's law of conduction. It states that the amount of heat conducted per unit time in a certain direction of a homogeneous solid material is equal to the product of the conducting area perpendicular to the heat flow path, the temperature gradient along this path, and the thermal conductivity of the solid material. This is expressed as in the following equation [JIJ 2009]:

$$q_w = \frac{dQ}{dt} = -kA \frac{dT}{dx} \quad (1.1)$$

where q_w is the rate of heat transferred in W.

Q is the heat or thermal energy in J.

k is the thermal conductivity of solid material in W/m.K.

A is the surface area of material perpendicular to flow of heat in m^2 .

dT/dx is the temperature gradient through the conducting material.

The negative sign in equation 1.1 indicates the flow of heat from hot to cold regions. Fourier's heat equation is applicable when the heat flux (in W/m^2) is constant with time.

I.2.b. Heat Convection

Convection is defined as the heat transfer in fluids (liquids or a gas) by the circulation of heat currents from one region to another. This heat transfer can be due to either natural or forced convection. In natural convection, the current circulation is due to existence of a temperature gradient that affects the density of fluid. To better understand convection, let us take an example of a hot object subjected to cold air. Initially, heat is transferred at the boundary between the object and the fluid. Therefore, the temperature of the hot object will drop and the air adjacent to its surface becomes warmer. The temperature of air adjacent to the hot object is higher than the upper layers of cold air, therefore it possesses lower density.

This causes the heated air to rise where then it will be replaced by cold air. In case of forced convection, the fluid is forced across the object's surface through pumps or fans. An increase in the rate of heat exchange results when using forced convection.

Convection can be neglected in the following cases:

- When the temperature gradient between the object and the surrounding fluid is negligible.
- When the surface area of the object in contact with the fluid is very small.

Heat transfer by convection can be described by Newton's law of cooling. For a constant heat transfer coefficient, Newton's law states that the heat lost by an object due to convection is proportional to the gradient of temperature between the object and its surrounding medium [JIJ 2009].

$$q_w = hA(T - T_0) \quad (1.2)$$

where q_w is the rate of heat transfer in W.

h is the convective heat transfer coefficient in $\text{W}/\text{m}^2\cdot\text{K}$.

A is the exposed surface area in m^2 .

T is the temperature of the object at the surface.

T_0 is the temperature of surrounding fluid.

In the absence of convection, the convective heat transfer coefficient h is equal to zero.

I.2.c. Radiation

Radiation is defined as the transfer of heat by means of electromagnetic waves. Unlike conduction and convection, it does not require any movement or interaction of materials. Moreover, radiation can occur in vacuum (i.e. in the absence of a physical medium). Normally, energy is radiated by all objects possessing temperatures greater than absolute zero in different directions where then this energy travels at the speed of light to the point of absorption. An example of thermal radiation is the sun's energy travelling through the vacuum existing between the space and the earth's atmosphere [SIE 2002]. A good absorber of incident energy is defined as a body of low surface reflectivity with a high capability of absorption in order to prevent the radiations from travelling through. A perfect absorber is known as a blackbody.

The total energy radiated by a body per unit of time at a temperature T is given by Stefan-Boltzmann's law as follows [JIJ 2009]:

$$q_w = A\varepsilon\sigma T^4 \quad (1.3)$$

where q_w is the rate of heat transfer in W.

A is the surface area of the body in m^2 .

ε is the surface emissivity (unitless).

σ is the Stefan-Boltzmann constant and is equal to $5.6704 \times 10^{-8} \text{ J/s.m}^2 \cdot \text{K}^4$.

In the case of a blackbody, the emissivity $\varepsilon=1$.

I.3. Parameters definition

In this section, different thermal material properties such as thermal conductivity, thermal diffusivity, and thermal effusivity are defined.

I.3.a. Thermal conductivity

The thermal conductivity can be defined as the quantity of heat per unit of time that would flow through a one square meter of a material where a temperature gradient exists in the direction of heat flow. All in all, it is a physical property that describes the facility or difficulty of transfer of heat energy through the material by conduction. It is given as the coefficient (k) in Fourier's law of conduction (equation 1.1). Materials of high thermal conductivities are frequently used as heat sinks, while those having a low thermal conductivity are used as thermal insulators.

The thermal conductivity (k) is controlled by the combination of the contributions of phonons and free electrons. Therefore:

$$k = k_e + k_p \quad (1.4)$$

where k_e is the free electron thermal conductivity and k_p is the phonon thermal conductivity.

In metals, the number of free electrons is significant. In addition, free electrons are not as easily scattered as phonons and they possess higher velocities. Thus, their contribution to heat transport process predominates in metals. For this reason, metals are known to be extremely good conductors of heat. Introduction of impurities in metals renders the free electrons less efficient due to the existence of scattering centers and consequently causes a reduction in the thermal conductivity. On the other hand, the number of free electrons in ceramics or non-

metals is unimportant and in that case the phonons are responsible of heat conduction. Therefore, in ceramics, the phonon thermal conductivity k_p is higher than the free electron thermal conductivity k_e . In ceramics, the phonons are more scattered due to the lattice imperfections which result in a less efficient transport of thermal energy. Finally, in polymers the thermal conductivity is no more controlled by phonons and free electrons. It is the molecules chains that undergo vibrations and torsional rotations resulting in thermal energy transfer. Nevertheless, the large size of such chains leads to low mobility. So, polymers have low thermal conductivities and are often used as thermal insulators [CAM 2008, MES 2011].

The thermal conductivity values of metals, ceramics, and polymers are given as follows:

- Metals: 20 to 400 W/m.K.
- Ceramics: 2 to 50 W/m.K.
- Polymers: < 1 W/m.K.

I.3.b. Thermal diffusivity

The thermal diffusivity is the speed of propagation of energy in a material as its temperature changes. It can be calculated by dividing the material thermal conductivity by its specific heat capacity times its density.

$$\alpha = \frac{k}{\rho c_p} \quad (1.5)$$

where α is the thermal diffusivity in m^2/s .

k is the thermal conductivity in W/m.K.

ρ is the density in Kg/m^3 .

c_p is the specific heat capacity in $\text{J}/\text{Kg.K}$.

Less time is needed for the heat to penetrate and flow inside a material having a high thermal diffusivity [FRA 1993].

I.3.c. Thermal effusivity

The thermal effusivity e also known as the “thermal admittance” or “contact coefficient” is defined as the square root of the product of the thermal conductivity of material by its volumetric heat capacity” [MAR 2007].

$$e = \sqrt{k\rho c_p} = \frac{k}{\sqrt{\alpha}} \quad (1.6)$$

where e is the thermal effusivity in $\text{J/m}^2\cdot\text{K}\cdot\text{s}^{0.5}$.

k is the thermal conductivity in $\text{W/m}\cdot\text{K}$.

α is the thermal diffusivity in m^2/s .

Diffusivity is the rate at which a material can absorb heat. Through this parameter the contact temperature of two bodies at different temperatures in contact with each other can be calculated [MOA 2011].

I.4. Fourier's equation

The rate of heat q_w conducted through a medium in a certain direction is given by Fourier's law of conduction (1D) according to equation 1.1.

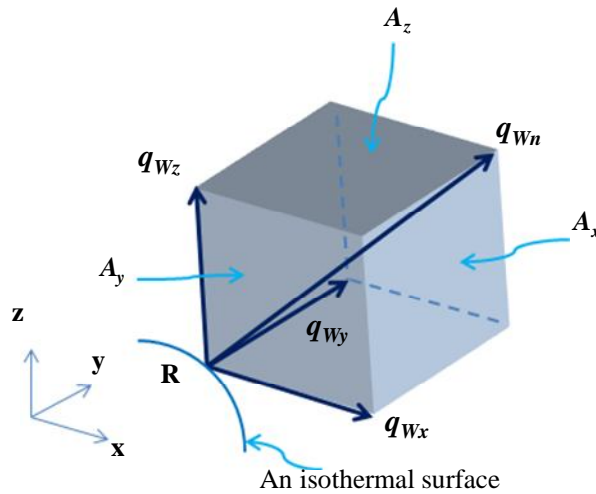


Figure 1.2: The normal heat flux at the surface of a medium.

Let us consider a point R on an isothermal surface with unit normal vector n in a medium as shown in figure 1.2. Consequently, according to Fourier's law, the rate of heat conduction at point R is [LEW 1996]:

$$q_{w_n} = -kA \frac{dT}{dn} \quad (1.7)$$

Consequently, the heat flux at point R , defined as the rate of heat transfer per unit area, is given by the following equation [LIE 2008]:

$$\frac{q_{w_n}}{A} = -k \frac{dT}{dn} \quad (1.8)$$

The heat flux q_{wn}/A is expressed in W/m^2 . It is orthogonal to the surface at point R in the decreasing temperature direction.

Fourier's law of heat conduction can be expressed in rectangular coordinates as in equation 1.9 where the temperature distribution in the medium is three dimensional.

$$\vec{q}_{wn} = q_{wx} \vec{u} + q_{wy} \vec{v} + q_{wz} \vec{w} \quad (1.9)$$

where \vec{u} , \vec{v} , and \vec{w} are the unit vectors and q_{wx} , q_{wy} , and q_{wz} are the magnitudes of the heat transfer rates in the x, y, and z directions respectively:

$$q_{wx} = -kA_x \frac{dT}{dx}, \quad q_{wy} = -kA_y \frac{dT}{dy}, \quad \text{and} \quad q_{wz} = -kA_z \frac{dT}{dz} \quad (1.10)$$

where A_x , A_y , and A_z are the surface areas perpendicular to the x, y, and z planes respectively.

From Fourier's law of heat conduction, a partial differential equation of the second order that defines the distribution of temperature with respect to time can be derived. This equation is known as the heat equation. In Cartesian coordinates, the heat equation is given by:

$$\frac{\partial^2 T}{\partial x^2} + \frac{\partial^2 T}{\partial y^2} + \frac{\partial^2 T}{\partial z^2} + \frac{e_{gen}}{k} = \frac{1}{\alpha} \frac{\partial T}{\partial t} \quad (1.11)$$

where e_{gen} is the rate of heat generation inside the medium per unit volume in W/m^3 .

In cylindrical coordinates, the heat equation is written as follows:

$$\frac{1}{r} \frac{\partial}{\partial r} \left(r \frac{\partial T}{\partial r} \right) + \frac{1}{r^2} \frac{\partial}{\partial \phi} \left(\frac{\partial T}{\partial \phi} \right) + \frac{\partial}{\partial z} \left(\frac{\partial T}{\partial z} \right) + \frac{e_{gen}}{k} = \frac{1}{\alpha} \frac{\partial T}{\partial t} \quad (1.12)$$

I.4.a. Boundary conditions and initial conditions

In order to solve the heat equation, boundary conditions which specify the value of temperature with respect to position and time on the boundaries of the medium are required. In addition, initial condition is needed at time $t=0$. For example, at $x=x_0$ the boundary conditions can be chosen to be among the following possibilities:

- The first boundary condition known as Dirichlet condition assumes a constant temperature at the surface of the medium:

$$T(x_0, t) = T_0(t) \quad (1.13)$$

- Second, the heat flux at the boundary of the medium is set to be constant. This is known as Neumann boundary condition:

$$q_w(x_0, t) = q_{w0}(t) \quad (1.14)$$

- The third is a convective boundary condition:

$$q_w(x_0, t) = hA(T(x_0, t) - T_{eq}) \quad (1.15)$$

where T_{eq} is the equivalent temperature of the surrounding medium far away from the surface as explained in section I.2.b. (equation 1.2).

- Another condition is the interface boundary condition. It requires the heat flux to be continuous at the interface from one medium to another and the temperature at the area of contact between two mediums to be equal. This is illustrated in figure 1.3.

This means that for two mediums 1 and 2 of temperatures T_1 and T_2 respectively, in contact with each other at $x=x_0$:

$$T_1(x_0, t) = T_2(x_0, t) \quad (1.16)$$

$$q_{w1}(x_0, t) = q_{w2}(x_0, t) \rightarrow -k_1 \frac{dT_1(x_0, t)}{dx} = -k_2 \frac{dT_2(x_0, t)}{dx} \quad (1.17)$$

where k_1 and k_2 are the thermal conductivities of mediums 1 and 2 respectively.

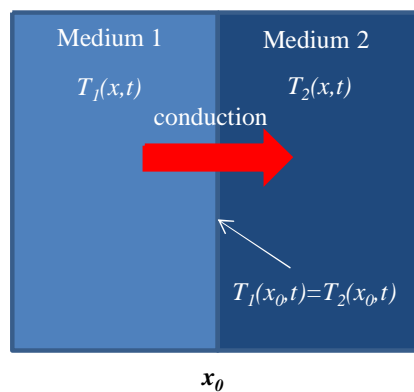


Figure 1.3: Temperature and flux continuity at the interface between two mediums.

- The last boundary condition is symmetry. This condition is applied when the thermal pattern in a medium is symmetrical around a central plane.

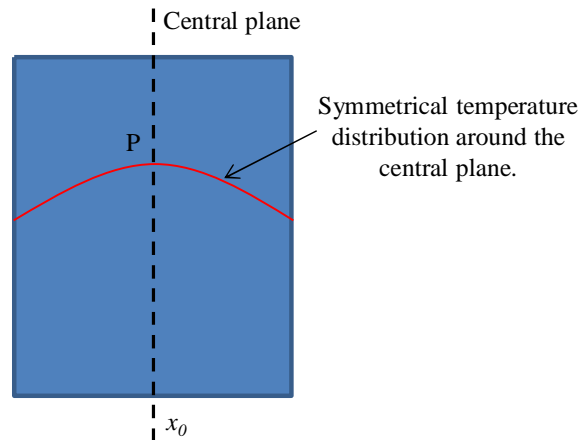


Figure 1.4: Symmetrical temperature distribution around the central plane of material.

At the point P belonging to the central plane, where $x=x_0$, the temperature can be maximum or minimum. Consequently, the slope at P is zero. Therefore,

$$\frac{dT(x_0, t)}{dx} = 0 \quad (1.18)$$

Actually, the differential equation specifies, given the initial conditions, how a system will evolve with time. Generally, the initial condition has the form $T(x, 0) = T_0(x)$ for all values of x belonging to the medium.

All in all, the heat equation can be solved uniquely when provided with the boundary and initial conditions [BRO 2002, HAN 2012].

I.4.b. Resolution methods

Several resolution methods exist for solving the partial differential heat equation among which are the finite element method (FEM) and finite difference method (FDM).

The finite element method has rapidly grown as a numerical analysis technique to solve and simulate problems in different fields of engineering concerned with partial differential equations that define different physical processes. It is based on accurately presenting a complex geometry and defining the boundary conditions, initial conditions and the physical properties of materials. It can be applied for two or three dimensional problems. FEM subdivides the original geometric structure into a large number of very small shapes (triangles in case of 2D dimensional problems and tetrahedrons in case of 3D dimensional problems) known as finite elements. This process is identified as finite element discretization. Thus, a

complex problem is divided into smaller problems that are solved separately [RAO 2005]. Before the introduction of FEM, engineers have used the FDM to solve the differential equations. The difference between the two methods is that the FDM requires small cubes when subdividing a structure. Moreover, FDM can only handle rectangular shape structures whereas, FEM has the ability to handle complicated geometries.

I.5. Conclusion

In this section we have summarized some basic concepts starting with the different modes of heat transfer, then defining some of the physical parameters of a material and ending with the resolution of Fourier's heat conduction equation. Among these parameters is the thermal conductivity that describes the ability of heat to be transferred through a material. Different methods to measure the thermal conductivity are available, in this work we are interested in the three omega method for which only the heat transfer through conduction is taken into account. As initial approximation, the other two modes, convection and radiation, are considered to be negligible. The material structure can be numerically simulated using finite element methods thanks to software like Comsol multiphysics and Matlab. Initial and boundary conditions are applied in order to solve the equation of heat conduction.

Before presenting the three omega method, we briefly describe several methods used to measure materials thermal conductivity.

II. Methods used for measuring the thermal conductivity of materials

II.1. Introduction

Methods for determining the thermal conductivity of materials can be divided into two categories: steady state and transient methods. Actually, transient methods have some advantages over the steady state methods. They are faster and considered to be simpler in design. In this section different steady state and transient methods for measuring the thermal conductivity are presented.

II.2. Steady state methods

Steady state methods are based on the steady state heat flow equation (Fourier's law of heat conduction equation 1.1) [SAL 2001]. In such measurements, heat is passed through the material of surface area A normal to the heat flow direction as shown in figure 1.1. Then, temperature is measured at different points using thermocouples. Knowing the distance between thermocouples, the thermal conductivity can be determined. For steady state

methods, the measurements are taken after reaching thermal equilibrium, so a long time is needed. Also, they are used to measure thermal conductivities of low to average values of large size specimens [JAN 2010, SAL 2001]. The most common steady state techniques are the guarded hot plate and radial heat flow methods.

II.2.a. Guarded hot plate method (GHP)

The guarded hot plate method (GHP) method is designed to measure thermal conductivities of slab or plate sample forms [DET 1989].

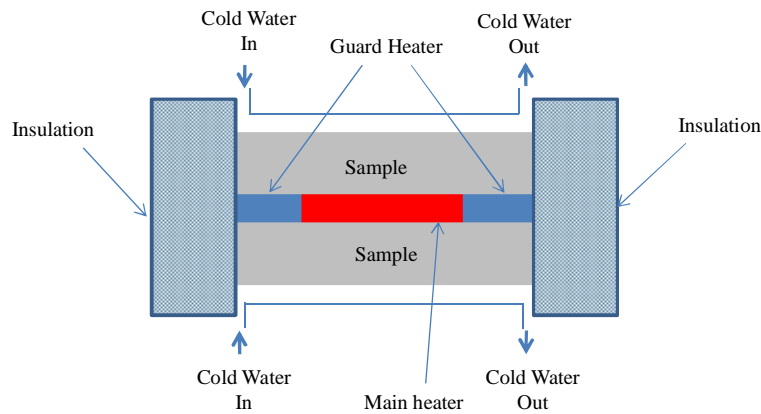


Figure 1.5: The guarded hot plate experimental setup.

Two identical samples, made of the same material and having the same dimensions, are placed between the main heater and a cooling plate as presented in figure 1.5.

In the case of heat conduction, heat flows from a medium of high temperature to a medium of lower one; so heat flows from the main heater through the sample to the cooling plate. In order to ensure a unidirectional uniform heat transfer in a direction perpendicular to the sample's surface area, two guard heaters are placed at the lateral edges of the main heater [SOM 1951]. This minimizes heat losses from the lateral edges of the main heater. Also, insulation is set at the samples lateral edges, which almost plays the same role as the guard heaters. A certain number of thermocouples are placed on the sample sides, the main heater side and the cooling plate side. When temperature distribution through the sample keeps the same with time, this means that steady state is established. At this moment, the temperature gradient can be estimated. Subsequently, the thermal conductivity is determined according to equation 1.1.

II.2.b. Radial heat flow method

Unlike the GHP method, the radial heat flow method considers heat transfer in radial direction. In such a method, measurements are done over hollow cylindrical shaped samples. A heated wire or cylinder is embedded in the center of the sample. Thermocouples are placed at two different distances from the central heater at the mid-section of the sample. An electric current is applied to the central heater where heat is generated radially outwards. This produces a temperature difference at the thermocouples placed throughout the sample. When thermal equilibrium is reached, the thermocouples' temperatures are recorded and the thermal conductivity of the sample can be determined according to equation 1.19.

Normally, temperature measurements are done at the mid-section of the sample where a uniform heat flux is radially generated. Heat losses in the upwards and downwards directions might occur causing a change in the temperatures of the thermocouples. Therefore, to provide accuracy, it is better for the length of the sample to be large compared to its radius. In this way a uniform radial heat flow at the mid-section of the sample is ensured [FLY 1963, IYE 2009].

$$q_w = -kA \frac{dT}{dx} = -k(2\pi rL) \frac{dT}{dr} \quad (1.19)$$

where L is the length of the hollow cylindrical shaped sample and $A=2\pi rL$ is the surface area of the cylinder.

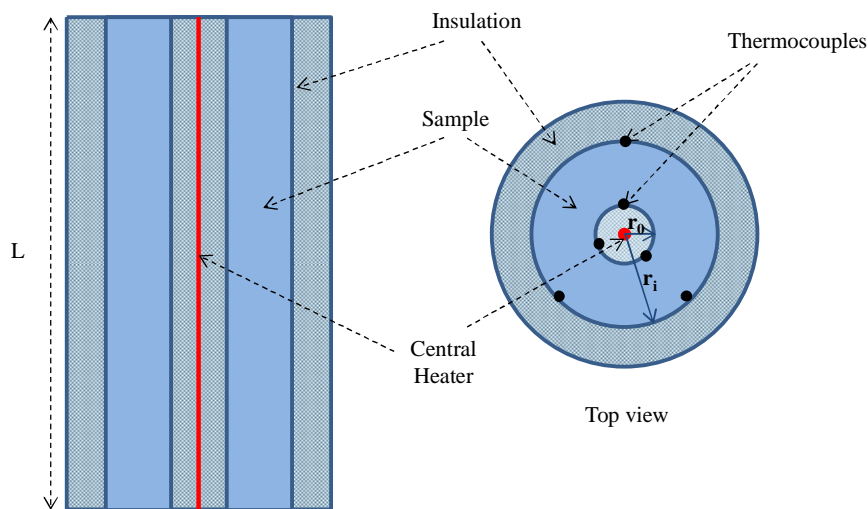


Figure 1.6: The radial heat flow method

$$k = \frac{q_w \ln(r_o/r_i)}{2\pi L(T_i - T_o)} \quad (1.20)$$

T_i and T_o are the temperatures measured at different radii r_i and r_o as shown in figure 1.6.

The radial heat flow method is one of the simplest methods to measure thermal conductivities. However, it is limited to samples with cylindrical shapes only. As large size samples are required, it is costly and might produce longer time to reach thermal equilibrium.

II.3. Transient methods

As presented above, the steady state techniques require samples of large size and specific form. Transient methods were then introduced to allow smaller sample sizes to be tested. Also, such methods are known to be rapid and able to directly measure different materials thermal properties like thermal diffusivity and heat capacity. In addition, they are considered to be simple methods through their concept and design [TYE 2005]. Transient methods became more popular than steady state ones since the equilibration times are reduced to few minutes or seconds [MAT 2000]. Several transient methods are briefly discussed below.

II.3.a. Transient hot wire method

Basically, the transient hot wire method is a transient radial flow technique used to measure the thermal conductivity of different materials and especially refractories such as insulating bricks and powders or fibrous materials [DOS 2003, SAI 2009, MER 2012]. It consists of a linear heat source (metallic hot wire) embedded in the material under test. When passing an electrical current through the wire, the wire temperature begins to increase rapidly with respect to time and heat will be transferred to the surrounding material. Then a moment is reached where the rate of temperature rise in the wire becomes constant. Heat is entirely stored in the material and then some heat losses occur at the outer boundary of the material causing a cease in temperature rise. The thermal conductivity can be deduced by plotting temperature versus time (from the linear portion of this curve). The equation of temperature rise is derived from the non-stationary heat diffusion Fourier equation in cylindrical coordinates (equation 1.12) where the metallic hot wire is considered to be infinitely long, surrounded by an isotropic medium of a constant initial temperature [CAR 1959]. Heating the metallic wire with a constant heat flux q_w per unit length of the metallic wire and neglecting

heat losses by convection and radiation, the temperature rise at a radial distance r is given by [VOZ 1996]:

$$\Delta T(r, t) = \frac{q_w}{4\pi k} \ln\left(\frac{4t\alpha}{r^2 C}\right) \quad (1.21)$$

where $C = \exp(\gamma)$, $\gamma = 0.5772$ is Euler's constant, k is the thermal conductivity of the material and α is the thermal diffusivity of material.

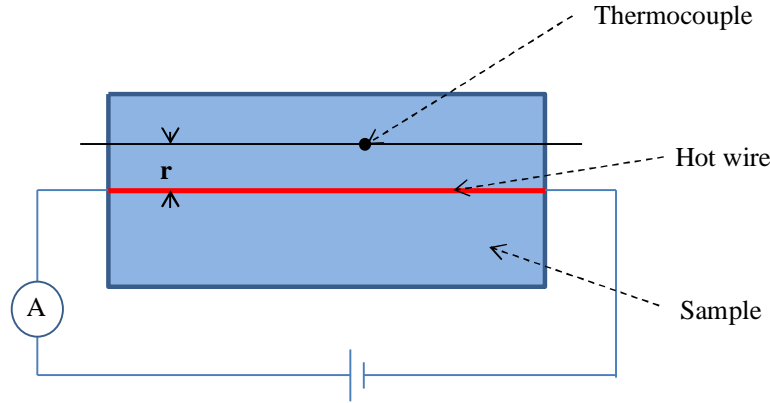


Figure 1.7: Hot wire embedded in the sample at a distance r from the thermocouple.

According to equation 1.21, plotting the temperature $T(t)$ with respect to the natural logarithm of measurement time $\ln(t)$ results in a slope $s = q_w / 4\pi k$. Consequently, the thermal conductivity can be calculated as follows:

$$k = \frac{q_w}{4\pi s} \quad (1.22)$$

The sample preparation for measuring the thermal conductivity of solids using the transient hot wire method is considered to be somehow difficult. It consists of two cuboids or half cylinders of the same material where the heat source is sandwiched between them. The size of the samples is considered to be large [SAI 2009]. For example, in the case of soil and granular materials, the measurement is done by filling long cylindrical tubes or cells [MER 2012] [ALV 2012] where the hot wire is implanted inside.

II.3.b. Time domain thermo-reflectance technique

Another transient method used to measure the thermal conductivity of materials is the time domain thermo-reflectance (TDTR). A schematic of TDTR experimental setup is shown in figure 1.8.

Basically in this technique the sample is heated through a probe (pump beam) that generates ultra-short laser pulses [KOM 2004]. Another time delayed probe beam is used to monitor the changes in the surface reflectivity of the heated sample. Actually, the surface of the sample is covered with a thin layer of metal which permits the incident energy to transmit through the sample as heat flux. For most metals, the changes in surface temperature can be deduced from the change in its surface reflectivity [SMI 2000]. The change in the reflectivity of the probe beam is recorded by a photodiode and a lock-in-amplifier. The thermo physical properties of the sample such as the thermal conductivity can then be deduced from the temporal temperature data related to the detected reflectivity [HOP 2010].

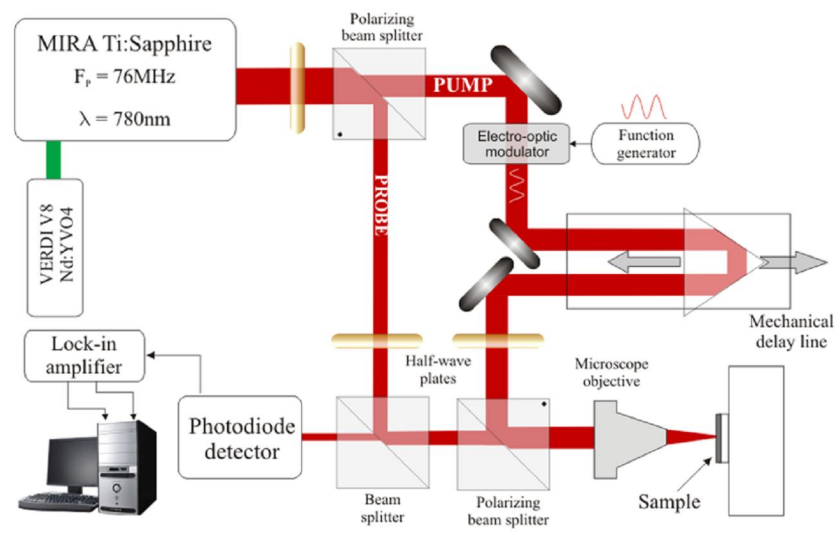


Figure 1.8: Time domain thermo-reflectance experimental setup [PER 2011]

The TDTR method offers picosecond time resolution which can produce nanometric thermal penetration depths. Consequently, thin film samples measurements can be directly performed using such technique [CAH 2003]. Nevertheless, the laser probes and the optical equipment used to build the TDTR experimental setup are expensive rendering TDTR a relatively costly technique.

II.3.c. The three omega method

The three omega method was originally developed by Cahill [CAH 1990]. At first, this method was applied on different amorphous solids (glass) of low thermal conductivity [CAH 1987]. Then it was used to measure the thermal conductivity of thin films of hundred nano meters to several micrometers thickness with low thermal conductivities, deposited on substrates possessing a high thermal conductivity compared to those of the thin films [CAH

1994]. Recently, Shen et al, have succeeded in measuring thermal conductivity of amorphous multilayer films using the three omega method [SHE 2013].

The three omega method is an AC technique and it is somehow similar to the hot wire method. Both techniques use a metallic element that heats the material to be tested and serves as a sensor too. However, in the case of three omega technique this metallic element of micro-meter thickness is deposited on the surface of the material. Measurements using the transient hot wire method are done in the time domain, while those using the three omega method are performed in the frequency domain by introducing a lock-in-amplifier during manipulation [CAH 1987].

II.4. Conclusion

Different steady state and transient methods used for the measurement of the thermal conductivity of materials have been described. The guarded hot plate and the radial heat flow methods are steady state methods which require long measuring time and large sample size. In case of transient methods, the time needed for measurements is reduced to few minutes. Despite this advantage, the transient hot wire method has some drawbacks. The sample preparation in case of solids is considered to be difficult. Also, the fragility of the long thin wire is another problem when the method is applied on solids and fluids [WAK 2000]. The time domain thermo-reflectance and the three omega methods are both transient methods that can measure the thermal conductivities of thin films in the order of several nanometers to several micrometers. However, for the thermo-reflectance method, the equipment used to build up the experimental setup is expensive rendering this method a relatively costly one. It is for this reason that our choice fell on the three omega method for measuring the thermal conductivity of materials. One can mention that there exist other techniques capable of mapping thermal conductivity images on the surface of materials [GUO 2006, GRO 2007].

III. Theoretical considerations of the three omega method

III.1. Introduction

As it has been said before in the case of three omega technique, a metallic element of micro-meter thickness is deposited on the surface of the material to be tested. The metallic line has two contact pads whose dimensions are: a width $2b$ and a length l (figure 1.9).

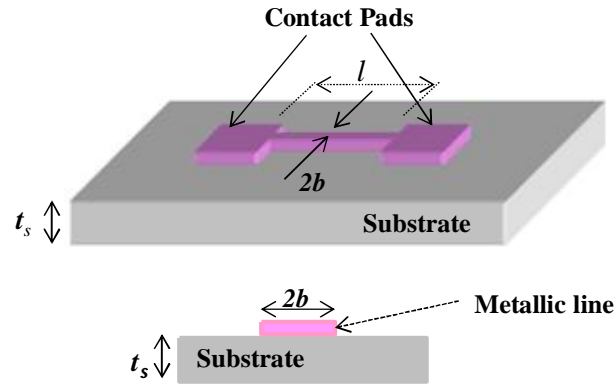


Figure 1.9: Metallic line with two contact pads deposited on surface of material of thickness t_s .

When passing an AC current at an angular frequency ω through it, heat will be generated due to Joule's effect producing temperature oscillations at an angular frequency of 2ω . Consequently fluctuations in the resistance of the metallic line are produced. This leads to a third harmonic voltage $V_{3\omega}$ through which we can deduce the temperature oscillation amplitude. A plot of temperature oscillation amplitude versus excitation frequency is analyzed to calculate the thermal conductivity of the material.

III.2. The three omega method theoretical basis

The resistance of the metallic line on the surface of the material under test is given by equation 1.23:

$$R = \rho \frac{l}{A} \quad (1.23)$$

where R is the resistance in ohms, l is the length of the metallic line in meters, A is the cross-sectional area in m^2 , and ρ is the static resistivity in $\Omega.m$ supposed to be constant along the length l .

For the three omega measurements, the metallic lines are made of a pure metal whose resistance varies with temperature changes as shown in equation 1.24:

$$R = R_0(1 + \beta_h \Delta T) \quad (1.24)$$

where R_0 is the resistance (in Ω) of the metallic line at room temperature (T_0) and β_h is the temperature coefficient of resistance of the metallic line in K^{-1} . Normally, the metal of our heating element has a high temperature coefficient of resistance.

According to Joule's first law, the passage of a current through a conductor will result in dissipation of heat which is proportional to the square of this current multiplied by the

conductor's resistance. Consequently, at temperature T_0 the power dissipated by the metallic line is given by:

$$P(t) = R_0 I^2(t) \quad (1.25)$$

If we consider an AC current $I(t)$ of angular frequency ω passing through the metallic line,

$$I(t) = I_0 \cos(\omega t) \quad (1.26)$$

then,
$$P(t) = R_0 I_0^2 \cos^2(\omega t) = \frac{1}{2} R_0 I_0^2 + \frac{1}{2} R_0 I_0^2 \cos(2\omega t) = P_{DC} + P_{AC} \quad (1.27)$$

We can notice that the dissipated power consists of a time independent component P_{DC} and an oscillating component P_{AC} . Actually, P_{DC} can be denoted by the rms (root mean square) power dissipated by the metallic line:

$$P_{rms} = R_0 I_{rms}^2 = \frac{1}{2} R_0 I_0^2 = P_{DC} \quad (1.28)$$

As the metallic line is heated the temperature oscillations produced at frequency 2ω are given in equation 1.29:

$$\Delta T = \Delta T_{DC} + \Delta T_{AC} = \Delta T_{DC} + |\Delta T_{AC}| \cos(2\omega t + \phi) \quad (1.29)$$

where ΔT is the rise in global temperature with respect to the initial temperature T_0 , ΔT_{DC} is the steady state temperature increase due to time independent component of power P_{DC} , ΔT_{AC} is the steady state temperature oscillations due to the oscillating component of power $P_{AC}(t)$, and ϕ is the phase angle between the oscillating power P_{AC} of frequency 2ω and the temperature oscillations.

Substituting equation (1.29) in equation (1.24), the resistance of the metallic line due to temperature increase is:

$$R(t) = R_0 (1 + \beta_h \Delta T_{DC} + \beta_h |\Delta T_{AC}| \cos(2\omega t + \phi)) \quad (1.30)$$

The voltage drop across the metal line is obtained by multiplying the metal line current by its resistance i.e. multiplying equations (1.26) and (1.30):

$$V(t) = R(t) * I(t) = R_0 I_0 \left[(1 + \beta_h \Delta T_{DC}) \cos(\omega t) + \frac{1}{2} \beta_h |\Delta T_{AC}| \cos(\omega t + \phi) + \frac{1}{2} \beta_h |\Delta T_{AC}| \cos(3\omega t + \phi) \right] \quad (1.31)$$

Examining equation 1.31, it represents the sum of three terms. Generally, the value of the temperature coefficient of resistance β_h is very small. Therefore, the first term is considered to be much larger than the other two terms. ΔT_{AC} does not appear in the first term rendering it

useless in determining the AC temperature oscillations. Next, the first two terms possess the same angular frequency ω . As the amplitude of the second term is considered to be very small compared to that of the first term it is difficult to extract ΔT_{AC} and ϕ from the second term. Consequently, only the third harmonic component can lead us to the values of ΔT_{AC} and ϕ as demonstrated in equation (1.32).

$$V_{3\omega} = \frac{1}{2} V_0 \beta_h |\Delta T_{AC}| \cos(3\omega + \phi) \quad (1.32)$$

$$|V_{3\omega}| = \frac{1}{2} V_0 \beta_h |\Delta T_{AC}| \quad \text{and} \quad \text{Arg}(V_{3\omega}) = \phi \quad (1.33)$$

where $V_0 = R_0 I_0$ is the peak amplitude metallic line voltage at angular frequency ω measured at room temperature.

Each of the third harmonic voltage $V_{3\omega}$ and the temperature oscillation ΔT_{AC} is composed of an in-phase (real) component and an out of phase (imaginary) one.

$$V_{3\omega} = V_{3\omega \text{ in-phase}} + i V_{3\omega \text{ out-phase}} \quad (1.34)$$

$$\text{So,} \quad \Delta T_{AC} = \Delta T_{AC \text{ in-phase}} + i \Delta T_{AC \text{ out-phase}} \quad (1.35)$$

where $\Delta T_{AC \text{ in-phase}} = |\Delta T_{AC}| \cos(\phi)$

$$\Delta T_{AC \text{ out-phase}} = |\Delta T_{AC}| \sin(\phi)$$

Experimentally, the first term in equation 1.31 will be cancelled by common mode cancellation techniques as will be explained later. The very small third harmonic voltage will then be detected by a special instrument called the lock-in-amplifier.

Cahill has found a solution for the temperature oscillations by considering a radial flow of heat from a line source of heat on the surface of a half volume semi-infinite cylinder [CAH 1990]. He initiated his work by the use of the heat conduction equation in cylindrical coordinates given by Carslaw and Jaeger [CAR 1959]. In the following section, we present the complete solution starting from the heat conduction equation till finding the temperature oscillation exact equation through which the thermal conductivity of the specimen can be determined. The heat source is first considered as a narrow line heater inside an infinite cylinder. The infinite cylinder is cut longitudinally to half to produce a heat source on the surface of a semi-infinite specimen. The solution is further developed for a finite heat source of width $2b$.

III.3. Cahill's formula

Starting with Carslaw and Jaeger equation of heat conduction of an infinite heat source inside an infinite cylinder and considering the constraints given by Cahill, we can derive Cahill's formula for AC temperature oscillations. This cylinder is then cut longitudinally into half to study the effect of a linear source of heat at the surface of a semi-infinite material (figure 1.10). This produces temperature oscillations having the form of zero order modified Bessel function of the second kind as shown in equation 1.35. This equation is derived in appendix A.

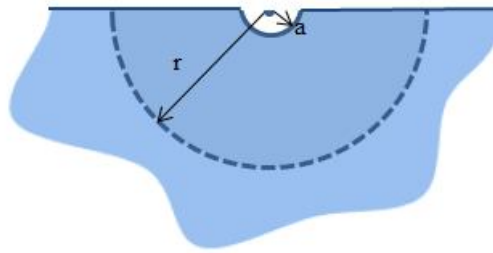


Figure 1.10: A cross section of a semi-infinite cylindrical sample.

$$\begin{aligned}\Delta T_{ACin-phase}(r) &= \frac{P_{rms}}{\pi k} \Re(K_0(qr)) \\ \Delta T_{ACout-phase}(r) &= \frac{P_{rms}}{\pi k} \Im(K_0(qr))\end{aligned}\quad (1.36)$$

where q is the wave number (equation A11).

P_{rms} is the root mean square power applied in W/m.

k is the thermal conductivity of the material in W/m.K.

K_0 is a zero order modified Bessel function of the second kind.

\Re and \Im are the real and imaginary parts of K_0 respectively.

The thermal penetration depth is a measure of how deep the thermal waves penetrate inside the specimen. It is defined as [CAH 1990]:

$$\lambda = \frac{1}{|q|} = \sqrt{\frac{\alpha}{2\omega}}\quad (1.37)$$

The thermal penetration depth is expressed in meters.

III.3.a. Heater of finite width

Equation 1.36 is derived for a one dimensional line heater on the surface of the specimen. For a heater with a finite width $2b$, we have to consider an infinite number of one-dimensional lines over the width of the heater.

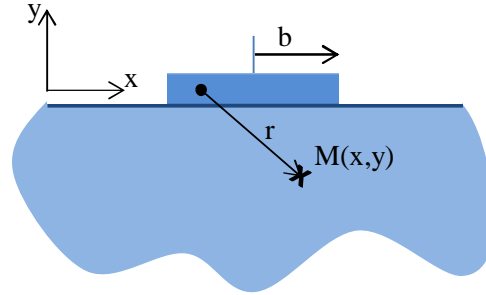


Figure 1.11: The finite width line heater on the surface of the semi-infinite sample.

Mathematically this is done by taking a Fourier transform of equation 1.36 with respect to x -coordinate. Only the oscillations at the surface are important, so $y = 0$. Consequently,

$$r = \sqrt{x^2 + y^2} = x \quad (1.38)$$

$$\Delta T_{AC}(\eta) = \int_{-\infty}^{\infty} \Delta T_{AC}(x) \exp(-i\eta x) dx \quad (1.39)$$

$$\Delta T_{AC}(x) = \frac{1}{2\pi} \int_{-\infty}^{\infty} \Delta T_{AC}(\eta) \exp(i\eta x) d\eta \quad (1.40)$$

In equations 1.39 and 1.40, η is defined as the wave number. Bessel function of an odd integer order is considered an odd function while a Bessel function of an even integer order is an even function. Thus, equations 1.39 and 1.40 are reduced to the cosine Fourier transform since the temperature field is an even function:

$$\Delta T_{AC}(\eta) = 2 \int_0^{\infty} \Delta T_{AC}(x) \cos(\eta x) dx \quad (1.41)$$

$$\Delta T_{AC}(x) = \frac{1}{\pi} \int_0^{\infty} \Delta T_{AC}(\eta) \cos(\eta x) d\eta \quad (1.42)$$

Then the temperature oscillations in Fourier space η will be [ERD 1954]:

$$\Delta T_{AC}(\eta) = \frac{p_{rms}}{2k} \left(\frac{1}{\sqrt{\eta^2 + q^2}} \right) \quad (1.43)$$

The heat is assumed to enter the specimen uniformly across the finite line width $2b$. This behavior can be expressed as a rectangular function with values 1 for $x < b$ and 0 elsewhere.

Then the Fourier transform of the heat source of finite width $2b$ is given by:

$$\int_0^b \text{rect}(x) \cos(\eta x) dx = \frac{\sin(\eta b)}{\eta b} \quad (1.44)$$

In order to include the finite width of the heater, equation 1.44 is multiplied by equation 1.43 giving:

$$\Delta T_{AC}(\eta) = 2 * \frac{P_{rms}}{2k} \left(\frac{1}{\sqrt{\eta^2 + q^2}} \right) \int_0^b \text{rect}(x) \cos(\eta x) dx = \frac{P_{rms}}{k} \frac{\sin(\eta b)}{\eta b \sqrt{\eta^2 + q^2}} \quad (1.45)$$

Performing the inverse Fourier transform of equation 1.43 by applying equation 1.42 we can find the steady state temperature difference in real space:

$$\Delta T_{AC}(x) = \frac{1}{\pi} \int_0^{\infty} \Delta T_{AC}(\eta) \cos(\eta x) d\eta = \frac{P_{rms}}{\pi k} \int_0^{\infty} \frac{\sin(\eta b)}{\eta b \sqrt{\eta^2 + q^2}} \cos(\eta x) d\eta \quad (1.46)$$

Equation 1.46 is then integrated over the line width $2b$ and averaged by dividing by $2b$:

$$\Delta T_{AC} = \frac{1}{2b} \int_{-b}^b \Delta T_{AC}(x) dx = \frac{P_{rms}}{\pi k} \int_{-b}^b \int_0^{\infty} \frac{\sin(\eta b)}{\eta b \sqrt{\eta^2 + q^2}} \cos(\eta x) d\eta dx \quad (1.47)$$

Finally, by solving equation 1.47 we can obtain the magnitude of the temperature oscillations of a finite width line on the surface of the specimen [CAH 1990].

$$\Delta T_{AC}(2\omega) = \frac{P_{rms}}{\pi k} \int_0^{\infty} \frac{\sin^2(\eta b)}{(\eta b)^2 \sqrt{\eta^2 + q^2}} d\eta \quad (1.48)$$

III.4. Solution of the exact equation

The integral in equation 1.48 is solved using an adaptive Simpson quadrature algorithm in MATLAB. The integration was carried out for η varying between 10^{-10} and 10^{10} . The integral was solved assuming the rms power $P_{rms} = 1 \text{ W/m}$, the metallic line half width $b = 10 \mu\text{m}$, the specimen's thermal conductivity $k = 1 \text{ W/m.K}$, and the thermal diffusivity $\alpha = 1 \text{ mm}^2/\text{s}$. These parameter values are in the same order as those measured when performing manipulations.

Figure 1.12 exhibits a linear regime at low frequencies and a planar regime at high frequencies. Between these two extremes there is a transition regime.

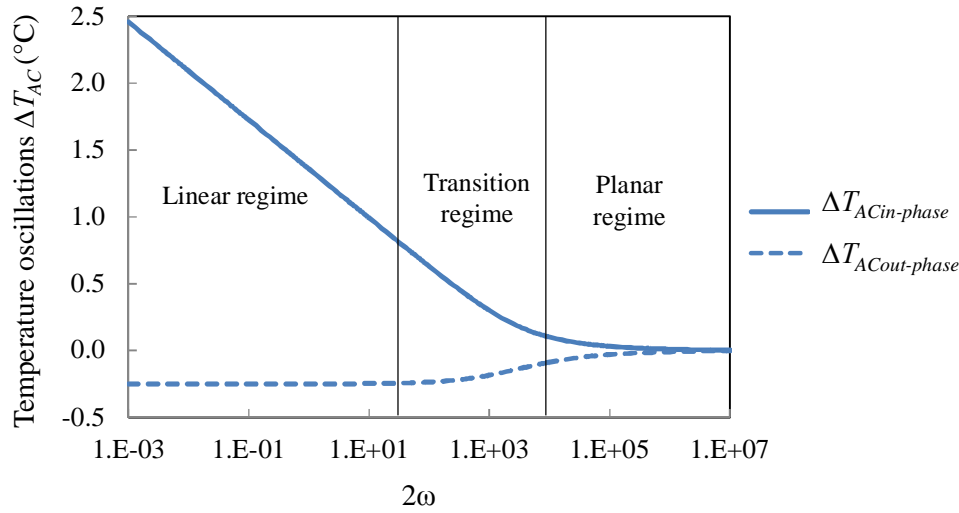


Figure 1.12: The in-phase and out of phase components of the temperature oscillations versus the thermal excitation frequency 2ω .

III.4.a. Finding the approximate equation for linear regime

As presented in figure 1.12, the linear regime is that part where the in-phase temperature oscillations decay linearly with respect to the thermal excitation frequency 2ω and where the out of phase temperature oscillations component is negative and constant. This regime is defined for low frequencies when the thermal penetration depth is high compared to the half width of the metallic line, $\lambda \gg b$.

For very small values of b ,

$$\lim_{b \rightarrow 0} \frac{\sin(b\eta)}{(b\eta)} = 1 \quad (1.49)$$

So, equation 1.48 is dominated by wavenumber η varying between $1/\lambda$ and $1/b$. Substituting equation 1.49 in equation 1.48 and integrating with an upper bound equals to $1/b$, we obtain:

$$\Delta T_{AC}(2\omega) = \frac{P_{rms}}{\pi k} \int_0^{1/b} \frac{1}{\sqrt{\eta^2 + q^2}} d\eta \approx \frac{P_{rms}}{\pi k} (\ln(qb) - \varepsilon) \quad (1.50)$$

where ε is a fitting constant equal to 0.923 [LEE 1997, MOO 1996].

Substituting $q = \sqrt{\frac{i2\omega}{\alpha}}$ in the equation 1.50 gives a relation between the temperature oscillation magnitude and the excitation frequency 2ω :

$$\Delta T_{AC} = -\frac{P_{rms}}{2\pi k} \left(\ln\left(\frac{b^2}{\alpha}\right) + \ln(2\omega) - 2\varepsilon \right) - i \frac{P_{rms}}{4k} \quad (1.51)$$

Equation 1.51 is plotted for $p_{rms}= 1\text{W/m}$, metallic line half width $b=10\ \mu\text{m}$, thermal conductivity $k=1\ \text{W/m.K}$, and thermal diffusivity $\alpha=1\ \text{mm}^2/\text{s}$ (Figure 1.13).

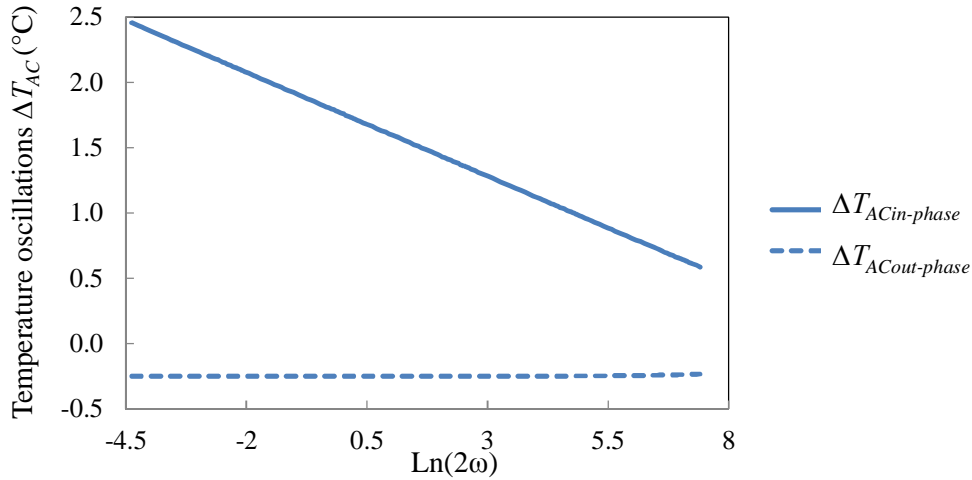


Figure 1.13: Temperature oscillations with respect to the natural logarithm of the thermal excitation frequency 2ω for linear regime.

This figure (obtained from equation 1.51) proves that for the linear regime, the in-phase component decays logarithmically with respect to 2ω . However, over the same frequency range, the out-of-phase temperature oscillations keep the same magnitude.

Substituting equation 1.51 in equation 1.32 yields the third harmonic voltage $V_{3\omega}$:

$$V_{3\omega} = -\frac{V_0^3 \beta_h}{4\pi l k R_0} \left(\ln(2\omega) + \ln\left(\frac{b^2}{\alpha}\right) - 2\varepsilon \right) - i \frac{V_0^3 \beta_h}{8 l k R_0} \quad (1.52)$$

Finding the slope (Figure 1.13) of the linear relation between the in-phase harmonic voltage and the natural logarithm of the thermal excitation frequency 2ω , we can calculate the thermal conductivity as follows:

$$k = \frac{V_0^3 \beta_h}{4\pi l R_0} * \frac{1}{slope} \quad (1.53)$$

The thermal conductivity can also be calculated using the out of phase component of the third harmonic voltage. Nevertheless, Cahill has found that computing the value of k using the slope of the in-phase component is more reliable [CAH 1990].

III.4.b. Finding the approximate equation for the planar regime

For in-phase and out-of-phase temperature oscillations equal in magnitude but opposite in signs, we can define a planar regime at higher frequencies where the thermal penetration depth is considered to be lower than the metallic line half width ($\lambda \ll b$). So we can write [MOO 1996]:

$$\lim_{b \rightarrow \infty} \frac{1}{\pi b} \left[\frac{\sin(b\eta)}{\sin(\eta)} \right]^2 = \delta(\eta) \quad (1.54)$$

Substituting equation 1.54 in equation 1.47 we obtain:

$$\Delta T_{AC}(2\omega) = \frac{P_{rms}}{bk} \int_0^{\infty} \frac{\sin^2(\eta) \delta(\eta)}{\eta^2 \sqrt{\eta^2 + q^2}} d\eta = \frac{P_{rms}}{2bkq} \quad (1.55)$$

Given that $\sqrt{i} = \frac{1+i}{\sqrt{2}}$, equation 1.55 can be written as:

$$\Delta T_{AC}(2\omega) = \frac{P_{rms}}{2bk \sqrt{\frac{2\omega}{\alpha}}} \exp(-i \frac{\pi}{4}) \quad (1.56)$$

We can notice a $-\pi/4$ phase shift which indicates a phase delay between the temperature oscillations and power P_{AC} . Also, equation 1.56 shows that the real and imaginary parts of temperature oscillations have the same magnitude while their signs are opposite.

Substituting equation 1.56 in equation 1.32 yields:

$$V_{3\omega} = \frac{V_0^3 \beta_h}{4\sqrt{2} I R_0 b k \sqrt{\frac{2\omega}{\alpha}}} (1-i) \quad (1.57)$$

The approximate solutions are compared with the exact solution by plotting equations 1.48, 1.51 and 1.56 (Figure 1.14). The rms power, the metal line half width, the thermal conductivity and the thermal diffusivity are the same as in figure 1.13.

The solid lines are the exact solutions while the dotted lines are the approximate solutions for the planar regime and the dashed lines are the approximate solutions for the linear regime. The blue lines represent the in-phase temperature oscillations while the red lines represent the out-of-phase ones.

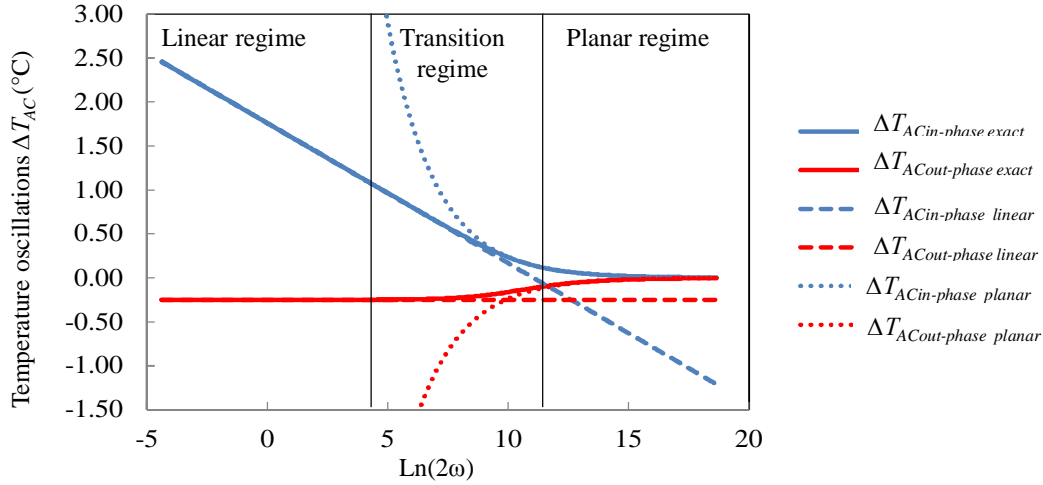


Figure 1.14: Comparison between the exact and approximate solutions for the linear and planar regimes.

In order to calculate the thermal conductivity, measurements must be done at frequencies belonging to the linear zone. In the next section, we determine the conditions that must be applied to define the linear regime boundaries.

III.4.c. Linear regime boundaries

Cahill's integral formula of temperature oscillations considers a sample of semi-infinite thickness as explained in section III.3. However, in reality, the sample has a finite thickness. Therefore, the boundaries of the linear regime must be determined according to the thickness of the sample and the width of the metallic line. In order to accurately define the boundary conditions for linear regime, an error analysis was made. It was found that for $\lambda > 5b$ the in-phase temperature oscillation rms error is less than 0.25 %.

Merging the condition in the above paragraph with equation 1.37, the boundaries of the linear regime become:

$$\frac{t_s}{5} > \lambda > 5b \quad (1.58)$$

$$\rightarrow t_s > 25b \quad (1.59)$$

Finally, equation 1.59 provides the maximum metallic line width possible for a given specimen thickness to perform measurements by means of the three omega method.

III.4.d. Estimation of the linear regime frequency interval for a sample of known thickness

The linear regime can be defined as the part where the in-phase temperature oscillations decay logarithmically with respect to the thermal excitation frequency 2ω and where the out-of-phase temperature oscillations are constant. Its upper and lower frequency limits can be calculated by substituting equation 1.36 in equation 1.58. Thus, these frequency limits of the linear regime are given:

$$\frac{25\alpha}{4\pi t_s^2} < f_{linear} < \frac{\alpha}{100\pi b^2} \quad (1.60)$$

Practically, equation 1.60 is applied to determine the range of frequencies where the measurements will be achieved. However, this equation requires the knowledge of the thermal diffusivity of material and consequently the knowledge of the thermal conductivity. Therefore, initially the values of the thermal conductivity, specific heat capacity and density of the material to be tested are taken from literature and substituted in equation 1.60 in order to have a first estimation of the linear frequency zone.

III.5. Examples of temperature oscillations and third harmonic voltages for bulk materials

After the theoretical developments presented before, in this section simulations based on the three omega method are proposed for two different kind of materials, kapton® and silicon.

Kapton® is a polyimide film created by DuPont company. It is widely used in flexible printed circuits. Moreover, due to its low thermal conductivity it is mostly used as an insulator. Jacquot et al. have found out a thermal conductivity of 0.32 W/m.K for kapton® [JAC 2002]. The density and the specific heat capacity of kapton® are equal to 1420 Kg/m³ and 1090 J.Kg⁻¹.K⁻¹ respectively. Substituting all these parameters in equation 1.48 and solving it using MATLAB, we can find the temperature oscillations for kapton® versus the natural logarithm of the thermal excitation frequency as shown in figure 1.15. The rms power and the metallic line width are assumed to be 1 W/m and 20 µm respectively. Actually, the highest widths possible for 1000 µm and 400 µm thick substrates are 32 µm and 80 µm respectively.

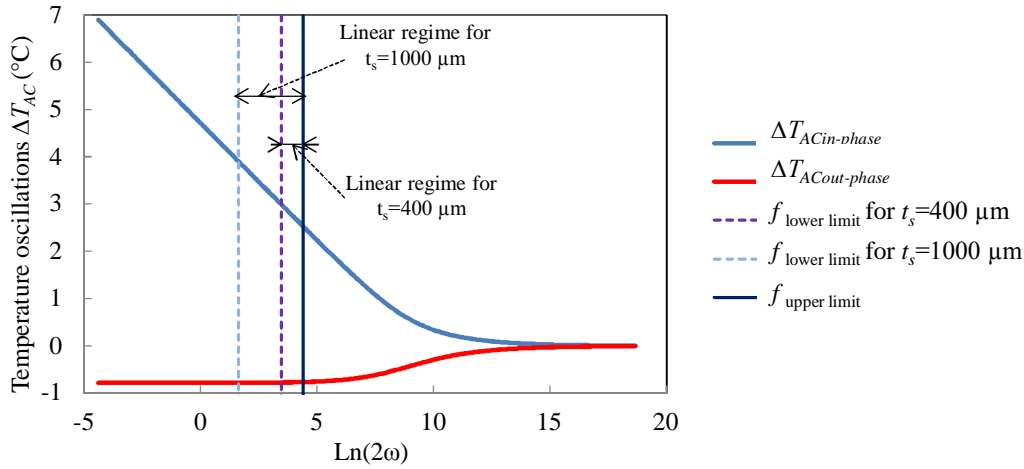


Figure 1.15: In-phase and out-of-phase component of temperature oscillations for kapton®.

On the other hand, silicon is a semiconductor, mostly used in integrated circuits and microchips. It has a density, specific heat capacity, and thermal conductivity of 2330 Kg/m³, 711 J.Kg⁻¹.K⁻¹ and 148 W.m⁻¹.K⁻¹ respectively. Figure 1.16 is plotted for rms power p_{rms}=1 W/m and the metal line width 2b= 20 μm.

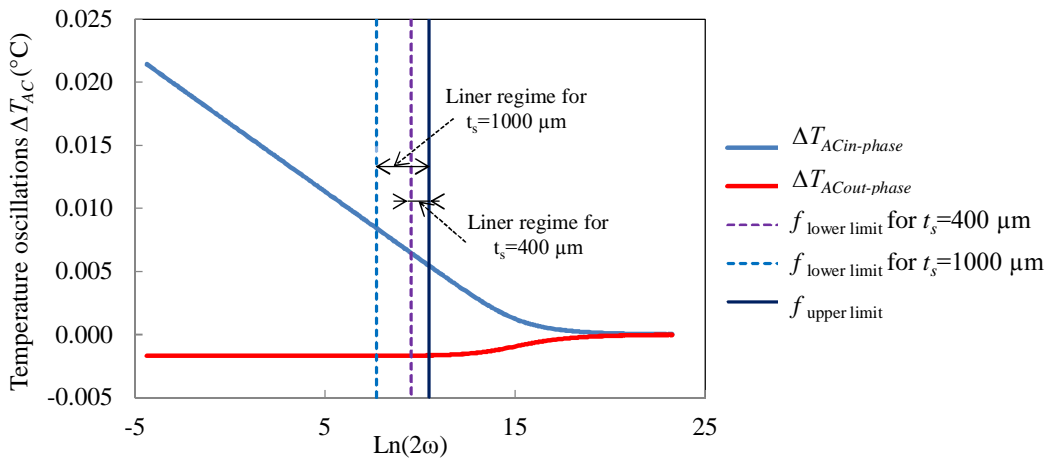


Figure 1.16: In-phase and out-of-phase component of temperature oscillations for silicon.

Comparing figures 1.15 and 1.16, the temperature oscillations for kapton® is higher than that for silicon. This is due to the fact that the thermal conductivity of silicon is higher than the one of kapton®, i.e. silicon is a much better thermal conductor.

The upper and lower frequency limits of the linear regime for both silicon and kapton® are determined according to equation 1.60. The thermal diffusivities of kapton® and silicon are found to be 2.067E-7 m²/s and 8.934E-5 m²/s respectively. For 2b= 20 μm the upper limit frequency for kapton® and silicon are given in table 1.2.

The lower frequency limit changes with the thickness of specimen. The larger is the thickness of the specimen the wider is the linear frequency zone. For a 20 μm width metallic line the minimum specimen thickness according to equation 1.59 is 250 μm . This thickness results in a very narrow linear regime. Consequently larger thicknesses are considered in table 1.1.

Table 1.1: The lower frequency limit for a width $2b=20 \mu\text{m}$ and different specimen thickness t_s .

t_s (μm)	400	600	800	1000
$f_{\text{kapton lower limit}}$ (Hz)	2.6	1.1	0.6	0.4
$f_{\text{silicon lower limit}}$ (Hz)	1110.8	493.7	277.7	177.7

Fixing the specimen's thickness to 400 μm , the maximum metallic line width allowed is 32 μm . Table 1.2 shows the variation of the upper frequency limits for kapton® and silicon for different metallic line widths. The lower is the metallic line width, the higher is the upper frequency limit. A 32 μm width metallic line cannot be considered since a linear regime of the same upper and lower frequency limits will be produced.

Table 1.2: The upper frequency limit for a thickness $t_s=400 \mu\text{m}$ and different metallic line widths $2b$.

$2b$ (μm)	5	10	15	20
$f_{\text{kapton upper limit}}$ (Hz)	105.3	26.3	11.7	6.6
$f_{\text{silicon upper limit}}$ (Hz)	45 499	11 374	5 055	2 843

Tables 1.3 and 1.4 summarize the values of the lower and upper frequency limits for figures 1.15 and 1.16 where the width of metallic line is fixed to 20 μm and two thicknesses of the sample are considered.

Table 1.3: The lower and upper frequency limits in case of kapton® (figure 1.15)

$t_s(\mu m)$	400	1000
$f_{kapton-lower\ limit} (Hz)$	2.6	0.4
$f_{kapton-upper\ limit} (Hz)$	6.6	6.6

Table 1.4: The lower and upper frequency limits in case of silicon (figure 1.16).

$t_s(\mu m)$	400	1000
$f_{silicon-lower\ limit} (Hz)$	1110.8	177.7
$f_{silicon-upper\ limit} (Hz)$	2843.7	2843.7

In order to determine the thermal conductivity of a material, a wide linear regime would be better. The higher the number of third harmonic voltages measured, the more accurate we can calculate the slope of the linear zone. Consequently, from the theoretical study done considering kapton® and silicon we can conclude that the higher is the thickness of the sample and the lower is the width of the metallic line the wider is the linear regime. Nevertheless, sometimes it is not possible to fabricate metallic lines of very small width (example $2b= 0.5 \mu m, 1 \mu m$). Also, samples of large thickness (example $t_s=1000 \mu m$) might not be commercially available. Moreover, in case of measuring the thermal conductivity of very thin films, another technique called the differential three omega method is applied as will be explained in chapter three.

The third harmonic voltages for kapton® and silicon can be calculated according to equation 1.32. Figures 1.17 and 1.18 show the in phase and out of phase third harmonic voltages plotted with respect to the natural logarithm of 2ω . For example, the thickness of the samples is taken to be $t_s= 1000 \mu m$. The metallic lines on both silicon and kapton® are assumed to have a width of $20 \mu m$, a length of 3 mm and a thickness of 400 nm . The temperature coefficient of resistance and the resistivity of the golden lines are fixed to $0.0034 /^\circ C$ and $2.44E-8 \Omega m$ respectively. The applied rms power is $1 W/m$.

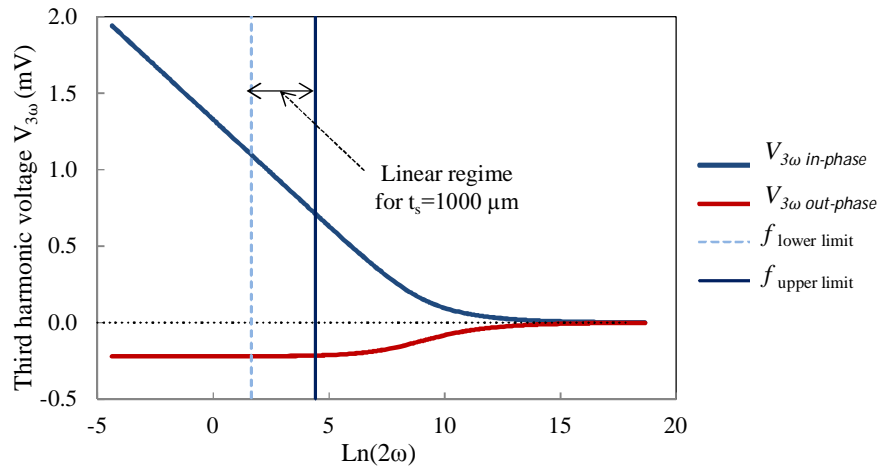


Figure 1.17: The in-phase and out-of-phase third harmonic voltages for kapton®.

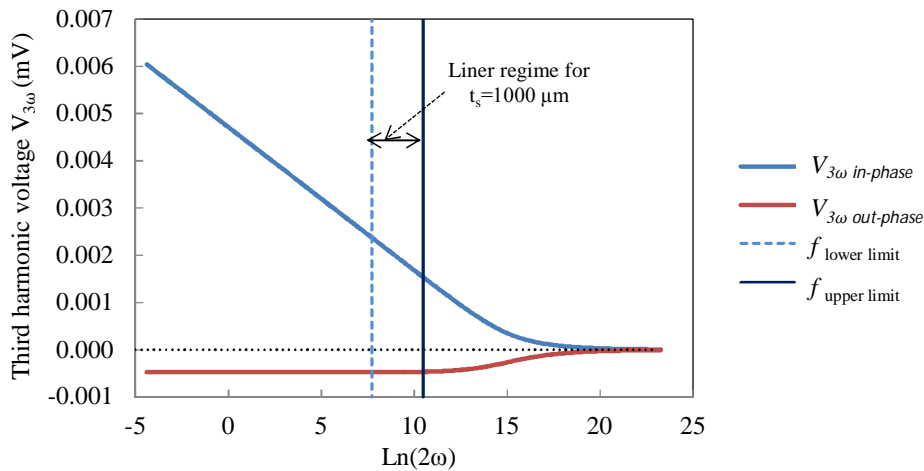


Figure 1.18: The in-phase and out-of-phase third harmonic voltages for silicon.

Since kapton is an insulator and silicon is a good thermal conductor, the resulted third harmonic voltages for kapton are higher than those of silicon. We can notice that the third harmonic voltages in the case of silicon are in the micro volts range. If vibrations exist in the 3ω -based experimental setup due to the surrounding environment, we might face some difficulties in measuring such small range voltages using the lock-in amplifier.

III.6. Conclusion

In section III, we have theoretically shown how the thermal conductivity of a material can be determined when using the three omega method. The steady state temperature oscillations were first determined by considering a one dimensional line heater inside an infinite cylinder. This infinite cylinder is then cut into half to produce a line heater on the surface of a semi-infinite cylinder. Afterwards, the single one dimensional line heater is replaced by an infinite

number of one dimensional line heaters where the temperature oscillations are averaged over a $2b$ width line. This leads to Cahill's formula of steady state temperature oscillations over a finite width line deposited on the surface of the material under test. An approximate equation for a linear regime is derived. Through this equation we can directly obtain the thermal conductivity from the slope of the in-phase temperature oscillations. The frequency limits of the linear regime are determined for thermal penetration depth greater than the heater's half width and much lower than the sample's thickness. The three omega method has several advantages over other conventional techniques used to measure the thermal conductivity. In particular, it can directly determine the thermal conductivity of materials with a high accuracy [WOJ 2009]. Moreover, errors from the blackbody radiations can be eliminated thanks to the small surface area of the metallic line heater [CAH 1990]. Finally, the three omega method is a transient technique. Thus the long equilibration time that lasts for hours in case of steady state techniques is reduced to a few minutes.

Simulations using MATLAB are performed for kapton® and silicon. The AC temperature oscillations are plotted with respect to $\ln(2\omega)$ for a large range of frequencies for both materials. The temperature oscillations of kapton are higher than those of silicon since the former is an insulator while the latter is a semiconductor. The linear regime frequency limits have been calculated for kapton® and silicon by assuming different metallic line widths and substrate thicknesses. We have concluded that the higher is the thickness of the substrate and the lower is the width of the metallic line the wider is the linear regime.

Conclusion

In this chapter we have presented several steady state and transient methods used to measure the thermal conductivity of materials. Transient measurements can be performed on commercially available samples and are considered to be faster than steady state ones. Among the transient techniques is the three omega method that makes use of a metallic line to produce heat on surface of specimen and consequently measure its thermal conductivity. The metallic line is heated through an alternating current at angular frequency ω . This yields metallic line resistance fluctuation at angular frequency 2ω and consequently a third harmonic voltage at angular frequency 3ω across the metallic line. We have derived the temperature oscillations integral formula found by Cahill. We have started by assuming, as Cahill, a line heater embedded in an infinite cylinder and then developing the solution for a finite width heater on the surface of a semi-infinite specimen. The linear regime upper and lower frequency limits were determined. It is in this region that the third harmonic voltage measurements must be done in order to deduce the thermal conductivity of the specimen under test. Initially, a three omega experimental setup must be constructed to measure accurately the third harmonic voltage across the heater. Therefore, any spurious signals at angular frequency 3ω that might appear due to any apparatus in the three omega experimental setup must be eliminated. Samples for the three omega measurements are prepared so that the metallic line heater is in intimate contact with the material's surface. So, the thermal resistance between the metallic line and the surface of material is considered to be negligible. After this theoretical chapter presenting the implementation of the mathematical tools for the three omega method, in following chapter, the metallic line heater fabrication process will be presented. In addition, the three omega method experimental setup will be described together with the common mode cancellation techniques used to get rid of spurious signals at angular frequency 3ω .

REFERENCES

- [ALV 2012] S. ALVARADO, E. MARIN, A. G. JUAREZ, A. CALDERON, and R. IVANOV
“A hot wire method based on thermal conductivity measurement apparatus for teaching purposes,”
European Journal Of Physics, Vol. 33, pp 897-906, 2012.
- [BRO 2002] P. BROADBRIDGE and G. R. FUFORD
“Industrial Mathematics, Case studies in the diffusion of heat and matter,”
Published by the press syndicate of the university of Cambridge, 2002.
- [CAH 1987] D. G. CAHILL and R. O. POHL
“Thermal conductivity of amorphous solids above the plateau,”
Physical Review B, Vol. 35, pp 4065-4073, 1987.
- [CAH 1990] D. G. CAHILL
“Thermal conductivity measurement from 30 to 750 K: the 3ω method,”
Review of Scientific Instruments, Vol. 61, pp 802-808, 1990.
- [CAH 1994] D. G. CAHILL, M. KATIYAR, and J. R. ABELSON
“Thermal conductivity of a-Si:H thin films,”
Physical Review B, Vol. 50, pp 6077-6081, 1994.
- [CAH 2003] D. G. CAHILL, W. K. FORD, K. E. GOODSON, G. D. MAHAN, A. MAJUMDAR, H. J. MARIS, R. MERLIN, and S. PHILLPOT
“Nanoscale thermal transport,”
Journal of Applied Physics, Vol. 93, pp793-818, 2003.
- [CAM 2008] F.C. CAMPBELL
“Elements of metallurgy and engineering alloys,”
ASM international, Copyright 2008.
- [CAR 1959] H.S. CARSLAW and J.C. JAEGER
“Conduction of heat in solids,”
Second edition, Oxford: Clarendon Press, 1959.
- [DET 1989] E. S. DETTMER, B. M. ROMENESKO, H. K. CHARLES, B. G. CARKHUFF, and D. J. MERRILL
“Steady state thermal conductivity measurements of AlN and SiC substrate materials,”
IEEE Transactions on Components, Hybrids, and Manufacturing Technology, Vol.12, pp 543-547, 1989.
- [DOS 2003] W.N. DOS SANTOS, and R. GREGORIO
“Numerical and experimental determination of the minimum and maximum measuring times for the hot wire parallel technique,”
Cerâmica, Vol 49, pp 29-35, 2003.

- [ERD 1954] A. ERDELYI
 “Tables of integral transforms,”
 New York, McGraw Hill, 1954.
- [FLY 1963] D. R. FLYN
 “A radial-flow apparatus for determining the thermal conductivity of loose-fill insulations to high temperatures,”
 Journal Of Research of the National Bureau of Standards-C. Engineering and Instrumentation, Vol. 67C, pp 129-137, 1963.
- [FRA 1993] R. FRANK, V. DRACH, and J. FRICKE
 “Determination of thermal conductivity and specific heat by a combined 3ω decay technique,”
 The Review of Scientific Instruments, Vol. 64, pp 760-765, 1993.
- [GRO 2007] P. GROSSEL, O. RAPHAEL, F. DEPASSE, T. DUVAUT, and N. TRANNOY
 “Multifrequential AC modeling of the SThM probe behavior, ”
 International journal of thermal sciences, Vol. 46, pp 980-988, 2007.
- [GUO 2006] F.A. GUO, N. TRANNOY, and J. LU
 “Characterization of the thermal properties by scanning thermal microscopy in ultrafine-grained iron surface layer produced by ultrasonic shot peening,”
 Materials chemistry and physics, Vol. 96, pp 59-65, 2006.
- [HAN 2012] D. W. HAHN and M. N. OZISIK
 “Heat conduction,”
 John Wiley & Sons, 3rd Edition, Copyright 2012.
- [HOP 2010] P. E. HOPKINS, C. M. REINKE, M. F. SU, R. H. OLSSON III, E. A. SHANER, Z. C. LESEMAN, J. R. SERRANO, L. M. PHINNEY, and I. EL-KADY
 “Reduction in the thermal conductivity of single crystalline silicon by phononic crystal patterning,”
 Nano Letters, Digital Object Identifier DOI: 10.1021/nl102918q, 2010.
- [IYE 2009] A.S. IYENGAR and A.R. ABRAMSON
 “Comparative radial heat flow method for thermal conductivity measurement of liquids,”
 Journal of Heat Transfer, Vol. 131, pp 064502, 2009.
- [JAC 2002] A. JACQUOT, B. LENOIR, A. DAUSCHER, M. STOLZER, and J. MEUSEL
 “Numerical simulation of the 3ω method for measuring the thermal conductivity,”
 Journal of Applied Physics, Vol. 91, pp 4733-4738, 2002.

- [JIJ 2009] L. M. JIJ
“Heat Conduction,”
Springer-Verlag Berlin Heidelberg, 2009.
- [JAN 2010] Y. JANNOT, V. FELIX, and A. DEGIOVANNI
“A centered hot plate method for measurement of thermal properties of thin insulating materials,”
Measurement Science and Technology, Vol. 21, pp 035106, 2010.
- [KOM 2004] P. L. KOMAROV, and P. E. RAAD
“Performance analysis of the transient thermo-reflectance method for measuring the thermal conductivity of single layer materials,”
International Journal of Heat and Mass Transfer, Vol. 47, pp 3233-3244, 2004.
- [LEE 1997] S. M. LEE and D. CAHILL
“Heat transport in thin dielectric films,”
Journal of Applied Physics, Vol. 81, pp 2590-2595, 1997.
- [LEW 1996] R.W. LEWIS, K. MORGAN, H.R. THOMAS, and K.N. SEETHARAMU
“The finite element method in heat transfer analysis,”
John Wiley & Sons Ltd, 1996.
- [LIE 2008] J. H. LIENHARD IV and J. H. LIENHARD V
“A heat transfer text book”,
Published by Phlogiston Press, Cambridge USA, 3rd edition 2008.
- [MAR 2007] E. MARIN
“The role of thermal properties is periodic time-varying phenomena,”
European Journal of Physics, Vol. 28 pp 429-445, 2007.
- [MAT 2000] N. MATHIS
“Transient thermal conductivity measurements: comparison of destructive and nondestructive techniques,”
High Temperatures-High Pressures, Vol. 32 pp 321-327, 2000.
- [MER 2012] B. MERCKX, P. DUDOIGNON, J. P. GARNIER, and D. MARCHAND
“Simplified transient hot wire method for effective thermal conductivity measurement of geo materials; microstructure and saturation effect,”
Advances in Civil Engineering, Article ID 62539, 10 pages,
doi: 10.1155/2012/625395, 2012.
- [MES 2011] R.W. MESSLER, JR.
“The essence of materials for engineers,”
Jones & Bartlett Learning, LLC, Copyright 2011.
- [MOA 2011] E. M. MOARES
“Time varying heat conduction in solids, Heat conduction-Basic research,”
Prof. Vyacheslav Vikhrenko (Ed.), ISBN:978-953-307-404-7, InTech,

2011.

- [MOO 1996] I.K. MOON, Y. H. JEONG, and S. I. KWUN
 “The three omega technique for measuring dynamic specific heat and thermal conductivity of a liquid or solid,”
 Review of Scientific Instruments, Vol. 67, pp 29-35, 1996.
- [PER 2011] G. PERNOT, H. MICHEL, B. VERMEERSCH, P. BURKE, H. LU, J. M. RAMPNOUX, S. DILHAIRE, Y. EZZAHRI, A. GOSSARD, and A. SHAKOURI
 “Frequency-dependent thermal conductivity in time domain thermo-reflectance analysis of thin films,”
 Material Research Society Symposium Proceedings, Vol. 1347
 Materials Research Society, Digital Object Identifier DOI: 10.1557/opl.2011.1277, © 2011.
- [RAO 2005] S.S. RAO
 “The finite element method in engineering,”
 Elsevier Inc., 2005.
- [SAI 2009] Y. SAITO, K. KANEMATSU, and T. MATSUI
 “Measurement of thermal conductivity of magnesia brick with straight brick specimens by hot wire method,”
 Materials Transactions, Vol. 50, pp 2623-2630, 2009.
- [SAL 2001] D. SALMON
 “Thermal conductivity of insulations using guarded hot plates, including recent developments and sources of reference material,”
 Measurement Science and Technology, Vol. 12, pp R89-R98, 2001.
- [SHE 2013] B. SHEN, Z. ZENG, C. LIN, and Z. HU
 “Thermal conductivity measurement of amorphous Si/SiGe multilayer films by the 3 omega method,”
 International Journal of Thermal Sciences, Vol. 66, pp 19-23, 2013.
- [SIE 2002] R. SIEGEL and J. HOWELL
 “Thermal Radiation Heat Transfer,”
 Published by Taylor & Francis, 4th edition, 2002.
- [SMI 2000] A. N. SMITH, J. L. HOSTETLER, and P. M. NORRIS
 “Thermal boundary resistance measurements using a transient thermoreflectance technique,”
 Microscale Thermophysical Engineering, Vol. 4, pp 51-60, 2000.
- [SOM 1951] E. D. SOMERS and J. A. CYPHERS
 “Analysis of errors in measuring thermal conductivity of insulating materials,”
 The Review of Scientific Instruments, Vol. 22, pp 583-586, 1951.

- [TYE 2005] R. P. TYE, L. KUBICAR, and N. LOCKMULLER
“The development of a standard for contact transient methods of measurement of thermophysical properties,”
International Journal of Thermophysics, Vol. 26, pp 1917-1938, 2005.
- [WAK 2000] W. A. WAKEHAM and M. J. ASAEL
“Thermal conductivity measurement,”
Copyright 2000 CRC Press LLC. <<http://www.engnetbase.com>>.
- [WOJ 2009] K.T. WOJCIECHOWSKI, R. ZAYBALA, and R. MANIA
“Application of DLC layers in 3-omega thermal conductivity method,”
Journal of Achievements in Materials and Manufacturing Engineering,
Vol. 37, pp 512-517, 2009.
- [VOZ 1996] L. VOZAR
“A Computer-Controlled apparatus for thermal conductivity measurement by the transient hot wire method,”
Journal of Thermal Analysis, Vol. 46, pp 495-505, 1996.

Chapter II

The 3ω method-based experimental setup: Implementation and measurement precision

Introduction

After the first chapter mainly devoted to the description of the basics of heat transfer and the different methods available for measuring the thermal conductivity of materials, this chapter is entirely dedicated to the three omega method and its implementation in our laboratory. Briefly speaking, the method consists in using a function generator to produce an AC signal at a frequency ω which passes through a metallic line deposited on the surface of the material under test. In order to measure the third harmonic voltage generated by the metallic line, it is placed in one of the arms of a Wheatstone bridge circuit or in series with a potentiometer in a differential amplifier circuit. Both circuits are used as common mode cancellation techniques to suppress the undesired harmonics of the function generator. All the instrumentation used in the three omega experimental setup is described in section I.

As mentioned in chapter I, the metallic line must be made of a material possessing a high temperature coefficient of resistance in order to produce measurable third harmonic voltages. Section II explains all the steps needed to deposit the metallic line on the surface of the substrate. Moreover, the 2-wire and 4-wire methods to measure the resistance of the metallic line are presented. The hot plate method for measuring the temperature coefficient of resistance is also described in this part of the chapter.

In section III, we present the principles and the designs of each of the Wheatstone bridge and the differential amplifier circuits.

In section IV, the three omega method-based experimental setup is validated through investigations on several types of materials. Finally, we terminate this chapter by an error analysis to estimate the precision of the experimental setup and to evaluate the error produced on the measured thermal conductivity.

I. The 3ω method-based experimental setup

I.1. Introduction

To build up the three omega method setup, initially, a low distortion function generator is used to supply the metallic line deposited on the surface of the sample with an AC current. As explained in chapter I, joule's heating results in a third harmonic signal at the level of the metallic line. In order to detect this signal, the metallic line is put in a Wheatstone bridge or a differential amplifier circuit. Then the output of such circuits is measured by means of a lock-in amplifier (Figure 2.1). The objective is to measure the in-phase and out-of-phase third harmonic voltages through which the thermal conductivity can be deduced. Therefore, any other third harmonics that might be produced by any measuring instrument or resistive component must be eliminated. Figure 2.2 shows the three omega experimental setup built in the laboratory.

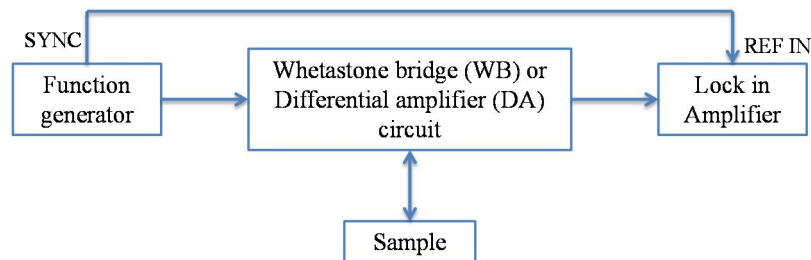


Figure 2.1: Schematic Diagram of the 3ω experimental setup.

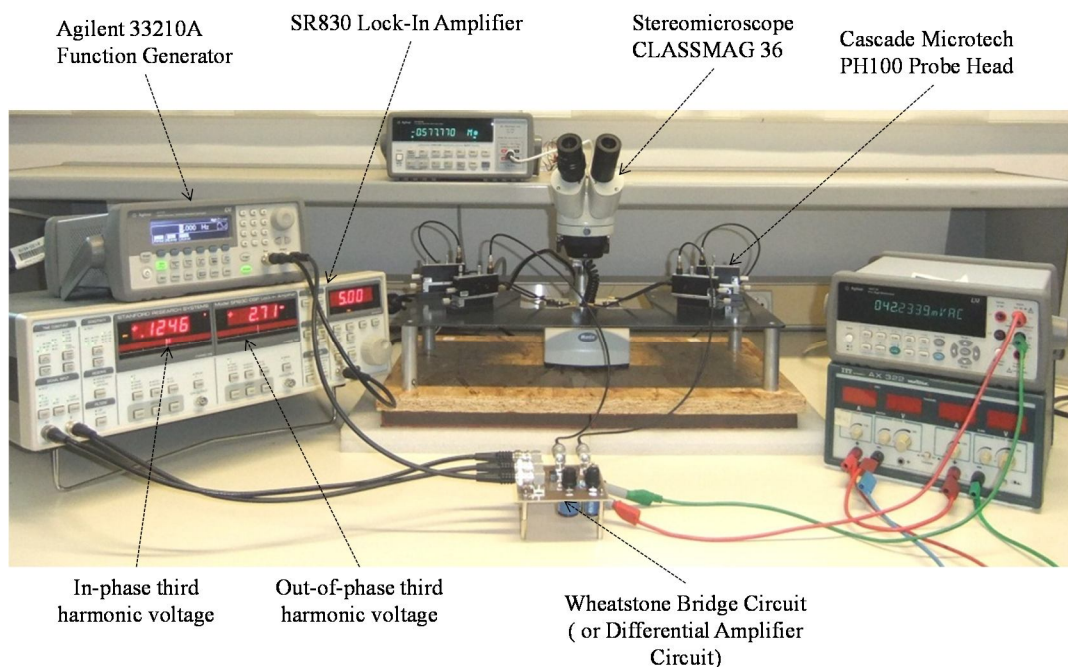


Figure 2.2: The 3ω method experimental setup.

In the following sections, the function of each instrument used in the three omega measurements is described.

I.2. Lock-in amplifier SR830

In order to measure the third harmonic voltage a Stanford Research SR830 Lock-in amplifier (LIA) is used. This instrument is a narrow band detector that can accurately determine the real and imaginary parts of a very small voltage signal at a certain frequency even if it is flooded by a noise signal. To achieve this, a phase sensitive detection technique is introduced. The phase sensitive detector multiplies the input signal by a reference one. Then, the LIA will respond only to the part of the input signal that occurs at the reference frequency. In figure 2.3 is shown the functional block diagram of the lock-in amplifier with two phase sensitive detectors. For the three omega measurements, two input signals are differentiated by the LIA by switching it to the A-B mode. The reference signal is a synchronous one provided by an Agilent 33210A function generator used to supply the metallic line with an AC current. A phase locked loop (PLL) then locks the internal oscillator to the reference frequency ω_r , producing a reference signal at frequency ω_r with a phase shift of θ_r :

$$V_{reference} = V_r \sin(\omega_r t + \theta_r) \quad (2.1)$$

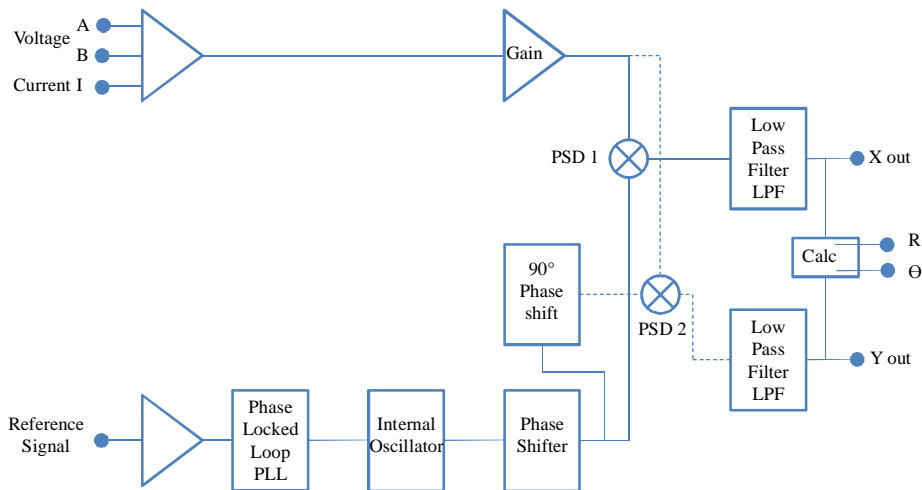


Figure 2.3: Functional block diagram of the lock-in amplifier.

The input signal is given by equation 2.2. The output of the phase shift detector PSD1 results in the multiplication of equation 2.1 with 2.2 as shown in equation 2.3.

$$V_{input} = V_i \sin(\omega_i t + \theta_i) \quad (2.2)$$

$$V_{PSD1} = V_i V_r \sin(\omega_i t + \theta_i) \sin(\omega_r t + \theta_r)$$

$$V_{PSD1} = \frac{1}{2} V_i V_r \cos((\omega_i - \omega_r)t + \theta_i - \theta_r) - \frac{1}{2} V_i V_r \cos((\omega_i + \omega_r)t + \theta_i + \theta_r) \quad (2.3)$$

When $\omega_r = \omega_i$ equation 2.3 becomes:

$$V_{PSD1} = \frac{1}{2} V_i V_r \cos(\theta_i - \theta_r) - \frac{1}{2} V_i V_r \cos(2\omega_r t + \theta_i + \theta_r) \quad (2.4)$$

Following the phase sensitive detector PSD1 by a low pass filter (LPF) and dividing out half the reference voltage amplitude, what remains from equation 2.4 is the DC signal:

$$X = V_i \cos(\theta) \quad (2.5)$$

where $\theta = \theta_i - \theta_r$ (for simplification θ_r is set to 0).

We can notice that equation 2.5 represents the real or in-phase component of the input signal. In order to determine the out-of-phase component, a second phase sensitive detector (PSD2) is used where the input signal is multiplied by the reference signal phase shifted by 90° . Therefore the output of PSD2 followed by a LPF is:

$$Y = V_i \sin(\theta) \quad (2.6)$$

The magnitude R and the phase θ of the measured signal are calculated as follows:

$$R = \sqrt{X^2 + Y^2} \quad (2.7)$$

$$\theta = \tan^{-1}\left(\frac{Y}{X}\right) \quad (2.8)$$

As explained above, the low pass filter removes the AC signal at $2\omega_r$. The bandwidth of the low pass filter is determined by setting the value of the time constant t_c . It is defined by:

$$t_c = \frac{1}{2\pi f_c} \quad (2.9)$$

where f_c is the cutoff frequency and defined as the point where the power of signal is 3 dB below its maximum value. The low pass filter attenuates signals with frequencies higher than the cut off frequency. By increasing the time constant, the cutoff frequency becomes lower and the AC signal at $2\omega_r$ will be better attenuated. Therefore, the time constant is chosen in a way where the cutoff frequency is equal to or less than the reference frequency. For SR830 lock-in amplifier the time constant can be set between $10 \mu\text{s}$ and 30ks which is equivalent to cutoff frequencies between 5.3E-6 Hz and 15915.5 Hz . Another parameter which describes

the performance of the low pass filter is the roll-off-rate. It defines the rate of loss or attenuation of the power of the filtered signal above the cutoff frequency. The roll-off-rate changes with different filter order. The SR830 Lock-in amplifier can achieve up to 4 stages of filtering (fourth order low pass filter) where the roll-off-rate reaches 24 dB/octave [SR 830].

I.3. Microscope and Micromanipulators

As presented in Figure 2.2, a probe station to hold four micromanipulators, a stereomicroscope, and the sample holder, was built of a metallic plate with four aluminum legs fixed on a wooden block. Two boards of foam were placed under the wooden block to help in absorbing vibrations. The metallic plate was cut by laser in a way that it surrounds the base of the stereomicroscope. DPP105-AI-S CascadeMicrotech micromanipulators are used which provide good accuracy and excellent repeatability. It offers a linear travel in X and Y positions over 7 mm and 8 mm respectively and a Z vertical displacement over 25 mm. It has a resolution down to 20 μm rendering it convenient for probing pads down to 100 μm x 100 μm . The micromanipulator tips are held at the end of the micromanipulator's arm (probe holder) through clamping. They are made of tungsten and have a radius of 7 μm at the extremity.

The sample under test is mounted on the plate of a CLASSMAG 36 stereomicroscope. It offers a 10 times or 20 times magnification, consequently precise manipulation of the tips on the surface of the sample is provided.

I.4. Function generator and measurement meters

The experimental setup for the three omega method measurement is supplied by an Agilent 33210A Function/Arbitrary Waveform Generator. It provides sine waveforms of 7 mVrms till 7.07 Vrms amplitude with a frequency range from 1 mHz to 10 MHz. One of the important concerns is the third harmonic noise produced by the function generator. Such harmonic might add to the third harmonic voltage generated by the metallic line on the surface of the sample and would cause errors when calculating the thermal conductivity.

The total harmonic distortion (THD) is a parameter that specifies the quantity of harmonic noise of an electronic instrument. It is defined as the ratio of the sum of all harmonic components of the voltage produced to the fundamental component of the voltage. It is given by the following equation [SHM 2005]:

$$THD = \frac{\sqrt{\sum_{n=2}^{\infty} V_{n\omega}^2}}{V_{\omega}} \quad (2.10)$$

where V_ω is the amplitude of the fundamental voltage and $V_{n\omega}$ ($n>1$) is the amplitude of the voltages produced at higher harmonic frequencies.

The total harmonic distortion of the function generator is equal to 0.04% [HP 2008].

$$V_\omega = 2500 \sum_{n=2}^{\infty} V_{n\omega} \quad (2.11)$$

We can notice that the harmonic noise is 2500 smaller than the fundamental voltage. For a fundamental voltage $V_\omega = 1$ Vrms and for $n=3$, the third harmonic voltage $V_{3\omega}$ produced by the function generator is equivalent to 0.4 mVrms. This harmonic is in the same order of magnitude as the third harmonic voltage produced by the metallic line. Thus it has to be removed. This can be done by common mode cancellation techniques like the Wheatstone bridge or the differential amplifier circuit as explained in section III.

The multimeter used to measure the initial voltage V_0 across the metallic line is an Agilent 34411A digital multimeter. Moreover, an Agilent 34420A micro-ohm meter is used to measure the resistance of the metallic lines. The characteristics of both the ohm-meter and the multimeter will be discussed in a later section together with the precision measurements.

I.5. Conclusion

We have introduced in this section different instruments needed to perform the three omega measurements. As we have explained, the function generator produces harmonics that results in errors when measuring the third harmonic voltages. This problem can be solved by techniques that are introduced in a later section.

After constructing the three omega method experimental setup, thermal characterization of materials can be achieved. This requires the deposition of a metallic line or heater on the surface of the material to be tested by a special process called photolithography. The steps of this process are explained in the following section.

The cost of the three omega method experimental setup built in the laboratory is around 20K euros. The quality of such a setup is considered to be good with respect to its price. Also, the materials to be tested can either be commercially found or fabricated and the thermal conductivity values measured by using this set-up, as will be shown in a later section are quite acceptable.

II. Sample preparation for the 3ω method

II.1. Introduction

Metallic line resistances of high temperature coefficient of resistance are needed for the three omega measurements in order to generate third harmonic voltages and consequently determine the thermal conductivity. These lines are prepared by optical lithography or photolithography process. This process requires the design of an optical mask and then the application of different steps on the surface of the material to be characterized which lead to the desired metallic line.

II.2. Sample design

Metallic lines of width $2b$ and length l are required to be deposited on the sample under test to perform the three omega measurements. As discussed in the first chapter, the width $2b$ and the length l are chosen according to the thickness of the sample. The metallic lines are designed to have two or four contact pads. These pads serve in passing the current through the metallic line and at the same time measuring the voltage across it. Simple software called CleWin [CLE 2002] is used to create a photolithographic mask layout consisting of different metallic line patterns. A 4 inch mask with the metallic line patterns designed by CleWin is represented in figure 2.4.

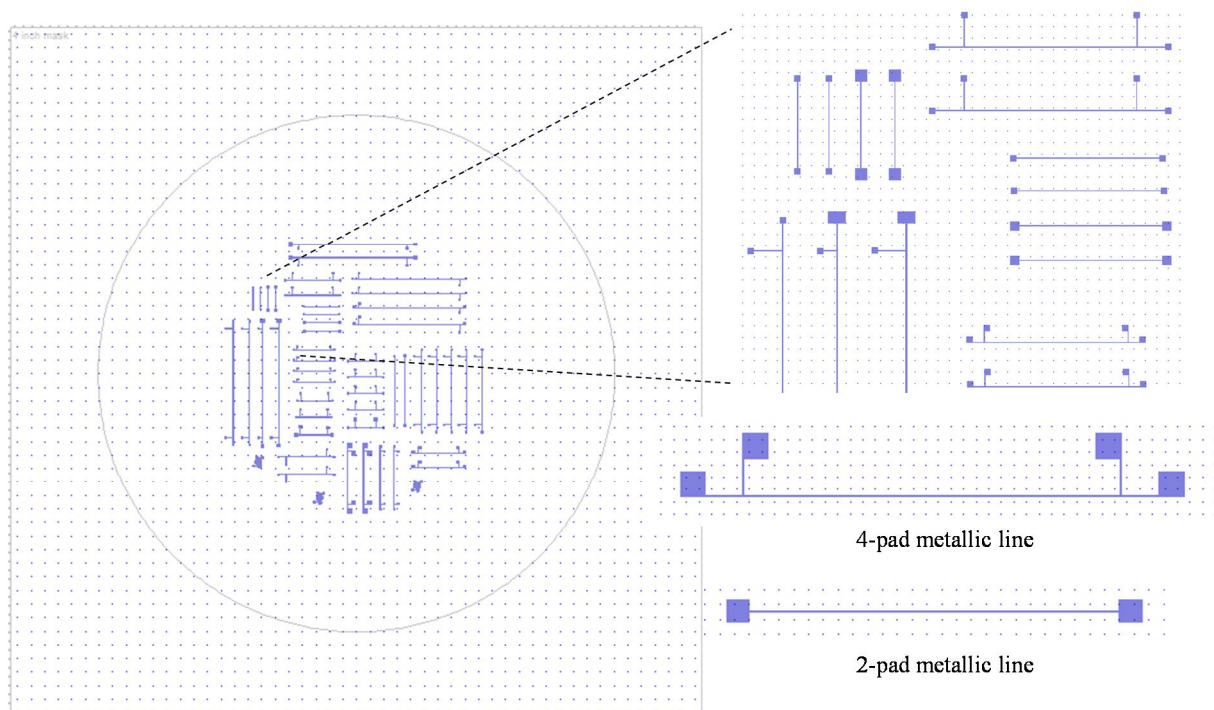


Figure 2.4: A 4 inch mask of 4-pads and 2-pads metallic lines.

The circle in figure 2.4 represents the surface of the substrate or sample which is in most cases 3 inch in diameter. Patterns are always kept away from the edge of the substrate to insure complete metallic lines and to easily manipulate the substrate by tweezers.

The metallic lines must be made of a metal possessing a high temperature coefficient of resistance (TCR) to produce a measurable change in its resistance as a function of temperature. Gold is the metal of choice. For small temperature variations, remarkable changes in the resistivity of gold can be produced since it has a high TCR of $0.0034\text{ }^{\circ}\text{C}^{-1}$ [BOY 2010]. In addition, gold maintains without oxidation in air and is not too expensive compared to other metals like platinum for example. However, gold is a metal that does not adhere well to the surface of substrates. To improve adhesion, a small layer of chromium is deposited in between. It has a very small thickness compared to that of the golden layer so that its effect can be neglected during measurements. The next section describes the different steps followed for the deposition of the gold metallic lines on the surface of solid substrates.

II.3. Sample preparation by process of optical lithography

II.3.a Cleaning substrate surface

Prior to any deposition technique, the substrate surface must be well cleaned from any organic or inorganic contaminations. This must be done to insure good adhesion between the metal and the substrate and to minimize thermal interface resistance. Initially, the substrate is immersed in acetone and cleaned with ultrasonic agitation for 5 minutes. It is known that acetone leaves its residues behind. In order to remove such residues, the substrate is treated ultrasonically in propanol-2 for 5 minutes then rinsed thoroughly by distilled water. Finally, the substrate is blown dry by compressed nitrogen.

II.3.b Photolithography

Photolithography is a process that uses a photomask to transfer a desired pattern to a light sensitive material called photoresist just placed on the surface of substrate. This process starts with a prebake or soft bake where the substrate is heated on a hot plate at $110\text{ }^{\circ}\text{C}$ for 5 minutes to insure the absence of any water molecule on the surface. Following this step is the development of a photoresist layer on the substrate's surface. First, an HMDS (Hexamethyldisilazane) solution is applied on the substrate and spin coated for 20 seconds at 2000 rpm. The substrate is then covered by a liquid photoresist (AZnLOF 2020 from AZ

Electronic Materials) by spin coating at 2500 rpm for 20 seconds. This produces a $1\ \mu\text{m}$ uniform thick layer of photoresist. The initial application of HMDS is to promote the adhesion of the photoresist to the substrate. After photoresist coating, the solid substrate is prebaked at $110\ ^\circ\text{C}$ for 1 minute to remove excess photoresist solvent. A negative optical mask is placed over the photoresist where it is exposed to ultraviolet light ($\lambda=365\ \text{nm}$, intensity= $11\ \text{mW}/\text{cm}^2$) for 3.5 seconds. Before development, the substrate is reheated at $110\ ^\circ\text{C}$ for another 1 minute. This step is usually called post-exposure bake (PEB). Holding the substrate vertically in AZ 326 MIF developer (AZ Electronic Materials) for around 1 minute and 15 seconds, the negative photoresist that was not exposed to ultraviolet light is dissolved therefore leaving behind the desired pattern. Afterwards, the substrate is directly placed in diluted water for 20 seconds and dried with compressed nitrogen gas. Figure 2.5 demonstrates the steps followed during the photolithography process.

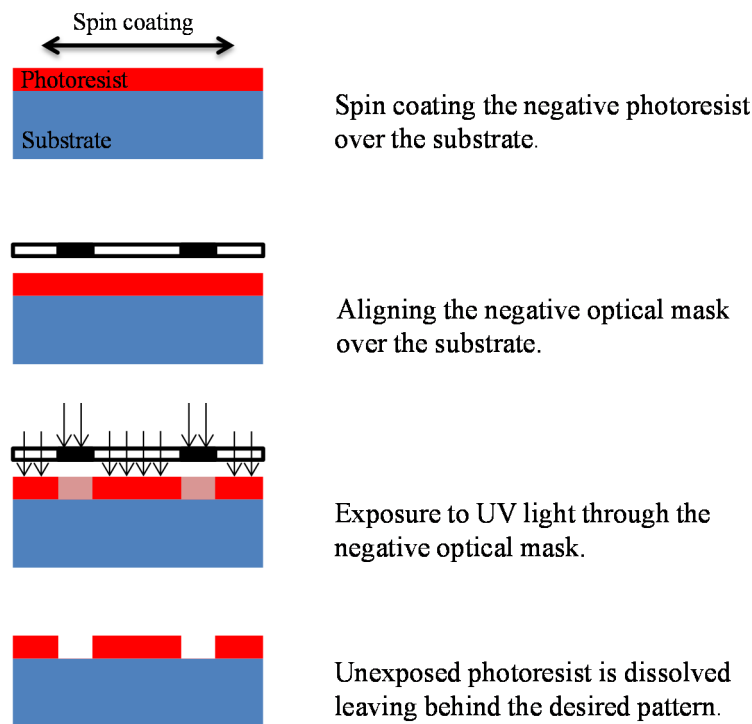


Figure 2.5: Photolithography procedure.

II.3.c. Metal deposition

One of the techniques used to deposit the material on the surface of specimen is evaporation. Such a technique takes place inside a vacuum chamber. Initially, the metal is heated by means of a resistive wire till it evaporates. Afterwards, the vapor particles travel freely through the chamber and condense on the surface of the substrate as illustrated in Figure 2.6.

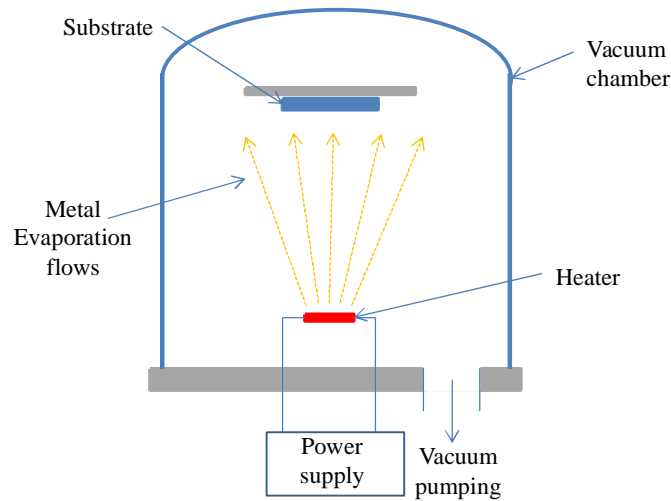


Figure 2.6: Metal evaporation in vacuum chamber.

Evaporation process is performed in a vacuum chamber to make sure that no other particles will add to the metal vapor.

In Figure 2.7 we can notice that thin metallic films are produced covering the photoresist and the areas where the photoresist has been dissolved. The evaporation process is initiated with chromium and continues with gold. The thickness of the deposited layer depends on the value of power applied to heat the metal and on the deposition rate.

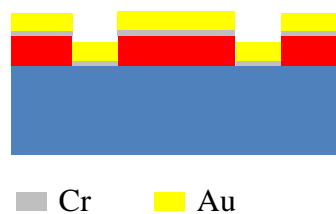


Figure 2.7: Gold and chromium deposition by evaporation after photolithography process.

II.3.d. Liftoff process

Following the metal deposition is the liftoff process. The substrate is fixed in a special holder and placed in a beaker containing SVC-14 remover with its metallized face downwards. The beaker is heated at $75\text{ }^{\circ}\text{C}$ and a thermocouple is immersed inside the solvent to control temperature. Agitation can be introduced during liftoff; in that case a magnetic agitator is placed inside the beaker to rotate at 250 rpm. The photoresist will be dissolved in SVC-14 solution taking away the metallic layer that has been created above it. What will remain is the metallic film in good adhesion with the substrate (Figure 2.8). At the end of the

liftoff process, the substrate is rinsed with acetone and isopropanol and finally blown dry with compressed nitrogen.



Figure 2.8: Metallic patterns deposited on the surface of the substrate.

II.4. Resistances of the fabricated metallic lines

The value of the resistance of the metallic line at room temperature is an important factor in calculating the thermal conductivity of the substrate. This resistance can be simply measured by a 2-wire method. However, such a method causes measurement errors. We can remove these errors by using a 4-wire method that employs four connections to the resistance instead of two as shown in Figure 2.9. The Agilent 34420A micro-ohm meter is used to perform such measurements.

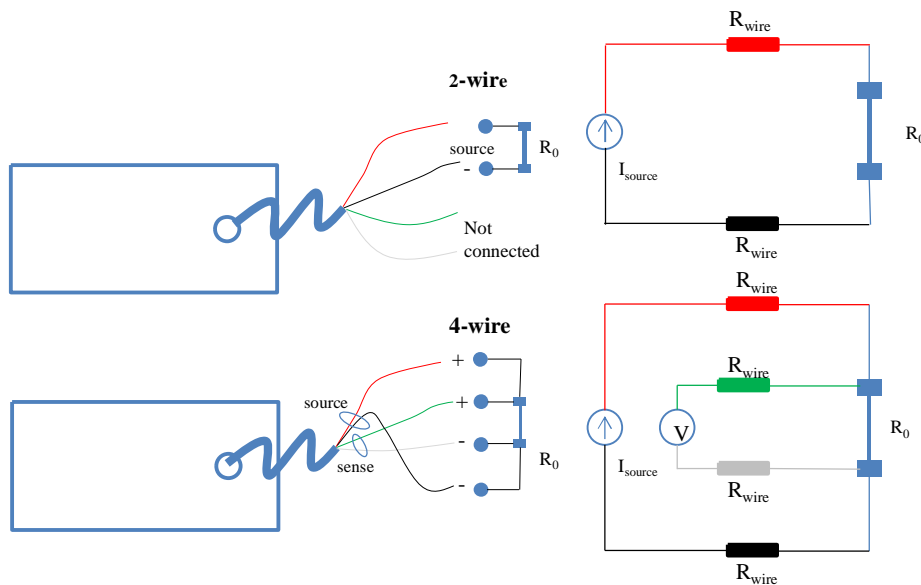


Figure 2.9: 2-wire and 4-wire resistance connections to the micro-ohm meter.

The error problem aroused in the 2-wire method is due to the series resistance of each of the wire connections. Only two wire connections are used through which the multimeter sends a source current and across which the voltage in the loop is measured. So, the wire resistance voltage drop adds to that across R_0 and error is produced. While applying the 4-wire method, two connections are used to pass the source current through resistance R_0 and another two to

measure the voltage across. The voltage input of a multimeter has very high input impedance. Therefore the injected current through the wire connections (green and grey) is very small and the voltage across them can be neglected. On the other hand, the wire resistances (red and black) have no effect on the source current supplied by the multimeter. Consequently, the resistance R_0 can be calculated by applying Ohm's law:

$$R_0 = \frac{V}{I_{source}}$$

where I_{source} is the current supplied by the multimeter and V is the voltage measured across the resistance R_0 .

The ohm-meter is connected to the metallic line through four micromanipulators. When reading the resistance value, we can notice some small fluctuations varying between a minimum and a maximum value. This might be explained by the existence of some small vibrations due to the fact that measurements are done on an ordinary table and not on an anti-vibratory one. Therefore, statistics are enabled to record the minimum, maximum and average value of the metallic line resistance. Table 2.1 shows the width $2b$, length l and the measured resistances at room temperature of three metallic lines deposited on the surface of borosilicate substrate. Also, the percentage variations of the minimum and maximum resistances with respect to the average, $\% var_{min}$ and $\% var_{max}$ respectively, are calculated.

Table 2.1: Average, minimum, and maximum measured resistances for several metallic lines.

Metallic line	$2b$ (μm)	l (mm)	$R_{0\text{ avg}}$ (Ω)	$R_{0\text{ min}}$ (Ω)	$\% var_{min}$	$R_{0\text{ max}}$ (Ω)	$\%var_{max}$
1	10	5	32.2984	32.29714	-0.0039%	32.29947	0.0033%
2	30	18	40.6959	40.6857	-0.0250%	40.7055	0.0236%
3	10	7.2	45.5721	45.5652	-0.0151%	45.5767	0.0101%

When substituting the values given in table 2.1 in equation 2.12, the resistivity of gold can be calculated for a 450 nm metal thickness.

$$\rho = R_0 \frac{A}{l} \quad (2.12)$$

where ρ is the resistivity of metal in $\Omega\cdot\text{m}$.

l is the length of the metallic line in m.

A is the cross sectional area of the metallic line in m^2 .

Table 2.2: Metal resistivity of each of the metallic lines.

Metallic line	Resistivity ρ ($\Omega.m$)
1	2.91E-8
2	3.05E-8
3	2.85E-8

We can notice that the calculated resistivities in table 2.2 are close to the values given in literature [WIS 2007].

II.5. Thermal coefficient measurement method

The temperature coefficient of resistance (TCR) is defined as the change in the value of resistance when the temperature is changed by one degree kelvin. It is given by:

$$\beta_h = \frac{1}{R_0} \frac{\Delta R}{\Delta T} \quad (2.13)$$

where β_h is the temperature coefficient of resistance in $^{\circ}C^{-1}$, R_0 is the metallic line resistance at room temperature in ohm and ΔR is the change in resistance at a temperature T .

The more accurate we measure the temperature coefficient of resistance the more precise we can determine the thermal conductivity. One of the techniques to measure β_h is the hot plate method. Placing the substrate on a hot plate and increasing the temperature between one reading and another, the resistance of the metallic line is measured for every temperature by means of the Agilent 34420A micro-ohm meter. The temperature measurements are accomplished by the use of several thermocouples connected by thermal paste just near the metal line. The temperature and resistance values are noted after around 15 minutes when both appear to be stable (i.e. the temperature when each of the thermocouple readings does not vary by more or less than 0.5 $^{\circ}C$). Consequently, plotting the variation of resistance versus average temperature, the coefficient of resistance can be calculated.

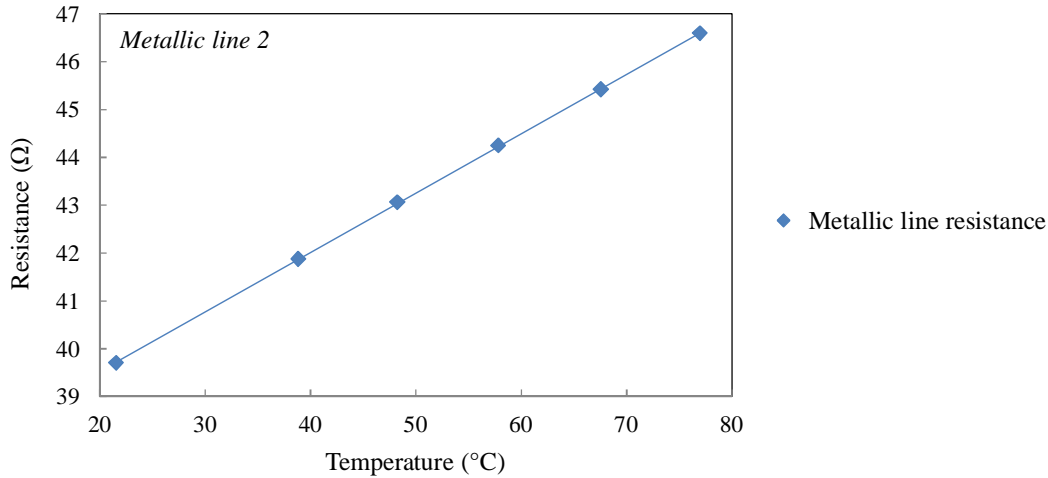


Figure 2.10: Measurements of resistance versus temperature of a metallic line.

Figure 2.10 represents the linear increase of the resistance of a gold metallic line with respect to temperature of metallic line 2 (table 2.1). The temperature coefficient of resistance for this metallic line is calculated to be $\beta_h=0.00313 / ^\circ\text{C}$. We can find that this value agrees well with the temperature coefficient of resistance of gold ($\beta_h=0.0034 / ^\circ\text{C}$) found in literature.

II.6. Conclusion

Metallic lines of different length and width and around 450 nm thick were prepared by photolithography. Two of the characteristics of these metallic lines are important to determine for the thermal conductivity calculations: the resistance and the temperature coefficient of resistance. First, the metallic line resistance is measured by the aide of a micro-ohm meter by applying the 4-wire method. Then, the temperature coefficient of resistance is determined using the hot plate method. We still need to measure the third harmonic voltages across the metallic line over the linear regime frequency range. These voltages are extracted through common mode cancellation techniques: the Wheatstone bridge or the differential amplifier circuit.

III. Experimental procedure of the 3ω measurement

III.1. Introduction

As mentioned in section I, the function generator used in our experimental setup has a total harmonic distortion of 0.04 %, therefore generating voltages at different harmonics. This causes the addition of a voltage at frequency 3ω to the three omega measurements. In order to prevent this, two circuits are designed which serve in cancelling the third harmonic voltage

due to the generator and therefore measuring separately the metallic line third harmonic voltage. The following sections describe the design and the function of the Wheatstone bridge and the differential amplifier circuits.

III.2. Wheatstone bridge method

III.2.a. Principle

The Wheatstone bridge (Figure 2.11.a) is an electrical circuit with two known resistances R_1 and R_2 , one variable resistance R_{3v} and an unknown one R_x .

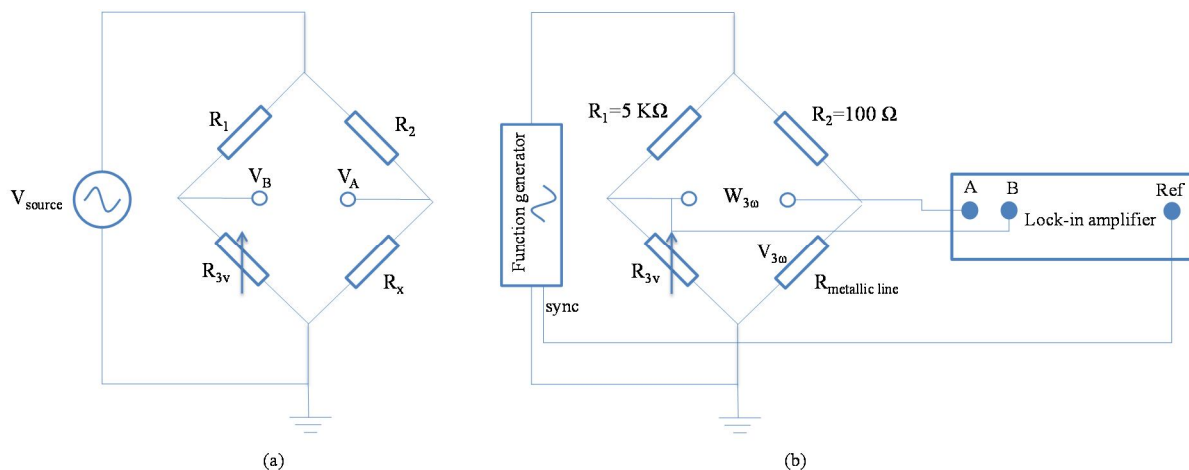


Figure 2.11: (a) Wheatstone bridge. (b) Schematic diagram of the three omega apparatus using the Wheatstone bridge.

Wheatstone bridge is commonly used to measure resistances of unknown values. This is achieved by balancing the bridge where the variable resistance is tuned till reading a zero voltage $V_A - V_B$ (Figure 2.11). Consequently, the ratios R_{3v}/R_1 and R_x/R_2 are equal.

The aim of using the Wheatstone bridge in the three omega experimental setup is to suppress the harmonics produced by the function generator in order to be capable of measuring only the induced third harmonic voltage in the metallic line. The metallic line resistance is placed in one of the arms of the Wheatstone bridge as shown in Figure 2.11.b. It is the only element that generates third harmonic voltage during operation. Therefore, R_1 , R_2 and R_{3v} are chosen to have a very small temperature coefficient of resistance compared to that of the metallic line resistance. Generally, the metallic lines are made of gold. A first measurement of the TCR of the gold metallic lines resulted in a value of $\beta_h = 0.00313\ /^\circ\text{C}$ (section II.5).

III.2.b. Wheatstone bridge design

To produce a measurable third harmonic voltage it is preferable to direct most of the current supplied by the function generator in the arm where the metallic line resistance is installed. In this case we have chosen R_2 to be 50 times smaller than R_1 ($R_1=5\text{ K}\Omega$ and $R_2=100\ \Omega$) therefore directing 98% of the current through the metallic line resistance.

In figure 2.12 is given the circuit of the designed Wheatstone bridge.

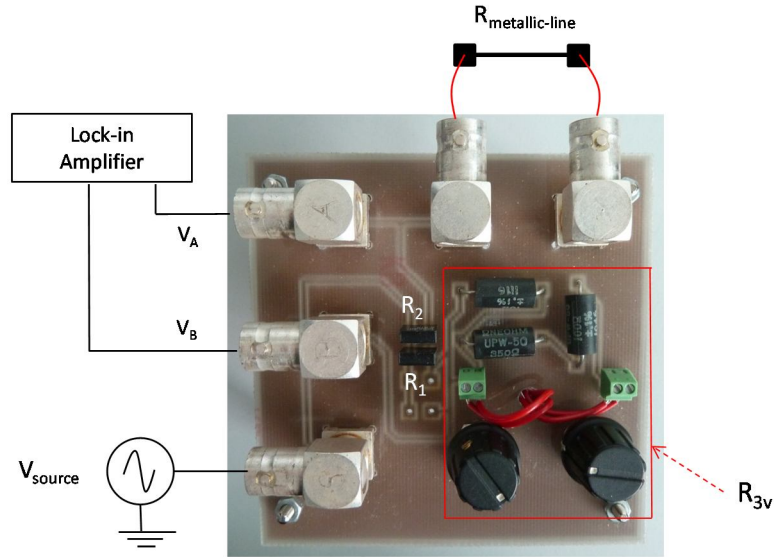


Figure 2.12: The Wheatstone bridge electrical circuit.

The metallic line resistances are deposited on the material under test by photolithography as explained in section II. The values of the resistances were found to vary between $9\ \Omega$ and $48\ \Omega$.

$$9\ \Omega < R_{\text{metallic-line}} < 48\ \Omega$$

One of our concerns is to have a variable resistance R_{3v} with a good resolution in order to accurately balance the Wheatstone bridge.

$$R_{3v} = \frac{R_x R_1}{R_2} \quad (2.14)$$

$$\rightarrow 500\ \Omega < R_{3v} < 2400\ \Omega$$

Previous works [BIR 1987] have used decade resistors of wide ranges up to $10\text{ K}\Omega$ and a resolution of $0.01\ \Omega$. However such a device is costly. Consequently, a variable resistance

with fine and basic adjustments was built using resistances and potentiometers of low TCR as shown in the following figure:

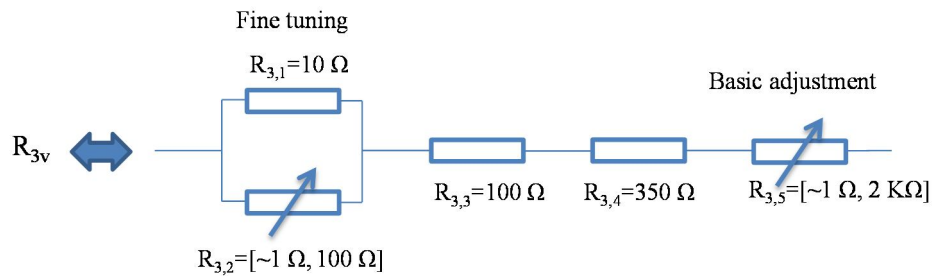


Figure 2.13: Equivalent circuit of the variable resistance R_{3v} .

As calculated above, the variable resistance R_{3v} varies between 500 Ω and 2400 Ω . Initially, $R_{3,1} = 10 \Omega$ is set in parallel to a potentiometer $R_{3,2}$ of minimum and maximum resistance of approximately 1 Ω and 100 Ω respectively. This forms the fine tuning that varies between $\sim 0.9 \Omega$ and $\sim 9 \Omega$. $R_{3,3}$ and $R_{3,4}$ are chosen to be equal to 100 Ω and 350 Ω respectively and are placed in series to the fine tuning. The basic adjustment is a potentiometer $R_{3,5}$ of $\sim 1 \Omega$ minimum resistance and 2 K Ω maximum resistance. As a result, the equivalent minimum and maximum resistances of the above circuit are around 450 Ω and 2460 Ω respectively. Consequently, we have achieved the variable resistance needed to balance the Wheatstone bridge. The following table summarizes the values of the Wheatstone bridge resistances and potentiometers together with their TCR in parts per million per degrees Celsius (ppm/ $^{\circ}\text{C}$).

Table 2.3: The values of resistances and their TCR used in designing the Wheatstone bridge.

Resistor or potentiometer	Resistance (Ω)	TCR (ppm/ $^{\circ}\text{C}$)
R_1	5 K	± 0.2
R_2	100	± 0.2
$R_{3,1}$	10	± 3
$R_{3,3}$	100	± 0.2
$R_{3,4}$	350	± 3
$R_{3,2}$ (10 turn potentiometer)	100	± 20
$R_{3,5}$ (10 turn potentiometer)	2 K	± 20

The TCR values for the resistances and potentiometers are the minimum available at different distributors. We can observe that all of these values are less than one percent of that of the metallic line ($\beta_h = 0.00313 / ^\circ\text{C}$).

III.2.c. Third harmonic voltage measurement

Balancing the Wheatstone bridge, the third harmonic voltage $W_{3\omega}$ at the output can be measured through the differential input (A-B) of the lock-in amplifier. The induced third harmonic voltage in the metallic line is then calculated by considering the Wheatstone bridge as a voltage divider with the input source V_{source} replaced by the 50Ω resistance of the function generator (Figure 2.14).

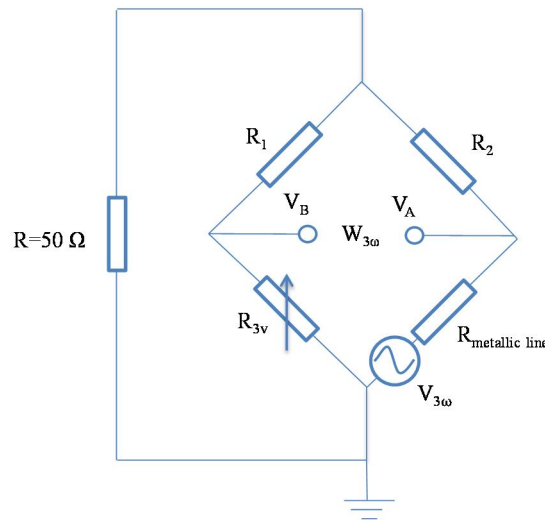


Figure 2.14: The effective circuit for the measurement of the third harmonic voltage at the output of the Wheatstone bridge.

To determine the voltage $V_A - V_B$ we first calculate the voltages at points A and B respectively.

$$\begin{aligned} V_A &= V_{3\omega} \left(\frac{R_2 + 50}{R_2 + 50 + R_{\text{metallic-line}}} \right) \\ V_B &= 0 \end{aligned} \quad (2.15)$$

$$\rightarrow W_{3\omega} = V_A - V_B = V_{3\omega} \left(\frac{R_2 + 50}{R_2 + 50 + R_{\text{metallic-line}}} \right) \quad (2.16)$$

$$V_{3\omega} = W_{3\omega} \left(\frac{R_2 + 50 + R_{\text{metallic-line}}}{R_2 + 50} \right) \quad (2.17)$$

Therefore, the third harmonic voltage $W_{3\omega}$, measured by the lock-in amplifier at the output of the Wheatstone bridge, is multiplied by the factor $(R_2 + 50 + R_{\text{metallic-line}})/(R_2 + 50)$ as shown in

equation 2.17 to obtain the third harmonic voltage $V_{3\omega}$ which serves in calculating the thermal conductivity of material.

III.3. Differential amplifier circuit

III.3.a. Principle

The differential amplifier circuit consists of a variable resistance in series with the metallic line resistance as presented in Figure 2.15.

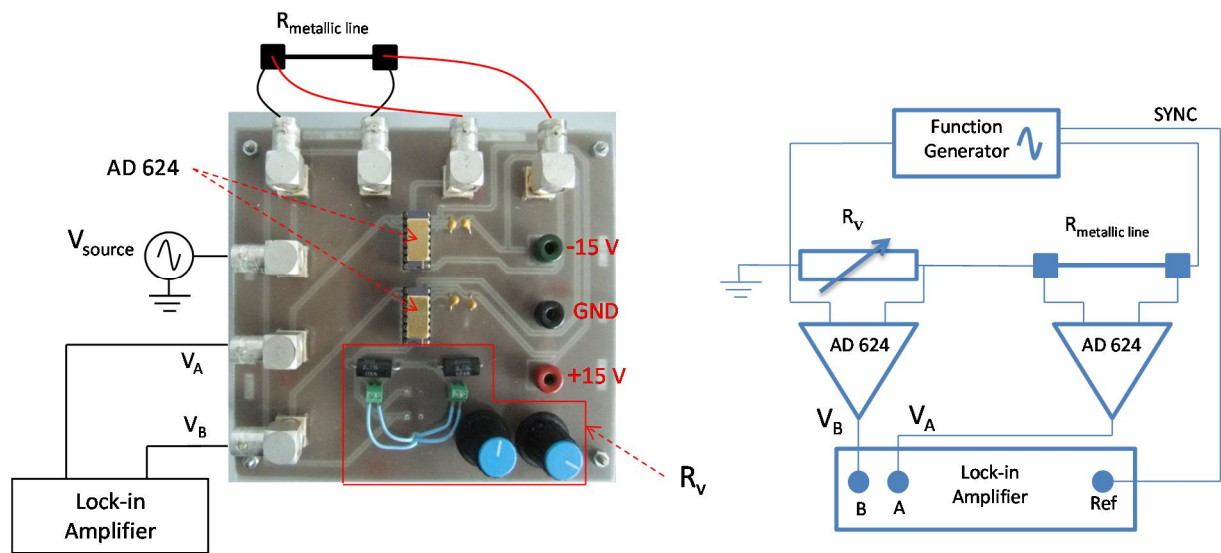


Figure 2.15: Schematic diagram of the three omega apparatus using the differential amplifier circuit.

Two AD 624 differential amplifiers of gain=1 are used to isolate the voltages across R_v and $R_{\text{metallic line}}$. These differential amplifiers are of high precision and low noise of $0.2 \mu\text{Vp-p}$ between 0.1 Hz and 10 Hz. The outputs of the differential amplifiers are connected to the inputs A and B of the lock-in amplifier and differentiated through (A-B) mode. The variable resistance R_v is tuned till acquiring a zero voltage at frequency ω at the output of the lock-in amplifier. At this moment the variable resistance R_v is equal to the resistance of the metallic line $R_{\text{metallic-line}}$. The harmonics produced by the function generator and that exist in both R_v and $R_{\text{metallic line}}$ are differentiated and will no more appear in the final measurements. Switching the lock-in amplifier harmonic detect number to 3, the third harmonic voltage $V_{3\omega}$ only generated by the metallic line can be measured. The thermal conductivity of the sample under test can then be calculated.

III.3.b. The circuit design

As for the Wheatstone bridge, the components of the differential amplifier circuit are chosen to have a small TCR. Also, the variable resistance is designed to have a resistance range similar to that of the metallic line. Figure 2.16 shows the equivalent arrangement of R_v .

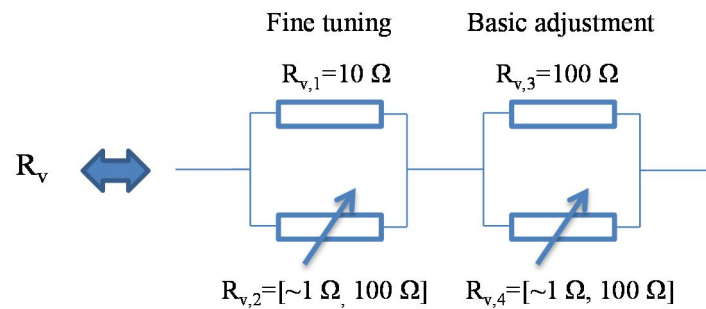


Figure 2.16: The equivalent circuit of the variable resistance R_v .

We can see that R_v can be varied between a minimum of $\sim 2 \Omega$ and a maximum of $\sim 60 \Omega$. The following table shows a list of the resistances and potentiometers used to build the circuit and their TCR values.

Table 2.4: The values of the resistances and their TCR used in designing the differential amplifier circuit.

Resistor or potentiometer	Resistance (Ω)	TCR (ppm/ $^{\circ}$ C)
$R_{v,1}$	10	± 3
$R_{v,2}$ and $R_{v,4}$ (10 turn potentiometers)	100	± 20
$R_{v,3}$	100	± 0.2

III.4. Conclusion

After designing the Wheatstone bridge and the differential amplifier circuits, we are able to measure separately the third harmonic voltage induced by the metallic line and consequently measuring the thermal conductivity of different materials. To make sure that our experimental setup is working correctly, measurements are done on several samples of different thermal conductivities and then compared to literature values.

IV. Validation of the 3ω method-based experimental setup

IV.1. Introduction

Different samples are prepared with metallic line resistances deposited on their surface. To validate the three omega-based experimental setup, measurements are performed on these samples of different thermal conductivity. Measurements are done using both the Wheatstone bridge and the differential amplifier circuits. Results are then compared to Cahill's solution.

IV.2. Thermal conductivity measurement of different materials

The three omega measurements are applied on Borosilicate (BrSiO_2), Gallium Arsenide (GaAs), Indium Phosphide (InP) and high resistivity Silicon (Si (HR)) substrates.

Borosilicate is a kind of glass normally made of silica and boron oxide. It has an excellent thermal resistance and mostly used in electroluminescent displays, thin film devices, solar cells, and electronic substrates. The three omega method has been performed on a $50\ \mu\text{m}$ thick borosilicate glass by Hartung *et al.* [HAR 2012] and the thermal conductivity found was around $1.14\ \text{W/m.K}$ at room temperature.

Gallium arsenide is a semiconductor belonging to III-V group. This material is mostly used in the design of optoelectronic and microelectronic devices. One of its constraints is its inability to resist excessive temperature which influences the device performance and reliability [LUO 2013]. Multiple literature citations for thermal conductivity of Gallium arsenide at room temperature exist. A thermal conductivity of $46\ \text{W/m.K}$ was reported by Sze *et al.* [SZE 1985], while Blakemore [BLA 1987] has given a higher value of $55\ \text{W/m.K}$. Iny *et al.* [INY 2003] have mentioned a reasonable average value of $50\ \text{W/m.K}$. Different essays were done to enhance the thermal conductivity of GaAs through Ga isotopes enrichment. Iny *et al.* [INY 2003] have measured the thermal conductivity at $300\ \text{K}$ of natural GaAs and enriched GaAs to be $47\ \text{W/m.K}$ and $49.3\ \text{W/m.K}$ respectively. These measurements were done by the standard steady state longitudinal method. However, the thermal conductivities of natural and isotope-enriched GaAs calculated by the first-principles lattice dynamics were found to be higher by 7% to 10% and 14% to 20% respectively over the temperature range of $95\ \text{K}$ to $400\ \text{K}$ [LUO 2013].

Indium phosphide is another semiconductor possessing a thermal conductivity higher than that of GaAs. This renders InP more favorable than GaAs in solar cell and continuous wave applications, light emitting diodes, and electronic devices [SRI 2008]. Moreover, InP has appeared as an important material in the growth of lattice-matched epitaxial layers of

GaInPAs [BAC 1981]. Adachi has reported an InP thermal conductivity value of 68 W/m.K at room temperature [ADA 2009]. Kud et al. have determined a thermal conductivity of 68 W/m.K at 300 K [KUD 1963]. Moreover, the 3 omega method was applied to measure the thermal conductivity of InGaAs/InP superlattice. Through these measurements they were able to deduce the thermal conductivity of InP substrate. It was found to be around 68 W/m.K [HUX 1999]. Another work showed the interest in characterizing porous InP due to its importance in optoelectronics [SRI 2008]. It was observed that the thermal conductivity decreases with increasing porosity.

Another semiconductor widely spread in microelectronics is silicon (Si). Actually, its high thermal conductivity renders it an important material in microelectronic systems [HOP 2011]. In 1964, Glassbrenner et al. have measured the thermal conductivity of silicon single crystal from 300 °K till the melting point using a longitudinal heat flow apparatus. It was found to be around 150 W/m.K at 300 °K [GLA 1964]. Also, silicon has been used as a heat sink substrate in organic light emitting diodes (OLEDs) due to its good thermal conductivity compared to other materials [CHU 2009]. Moreover, Jacquot et al. have performed experimental measurements using the three omega method to measure the thermal conductivity of a SiO₂ film placed on a silicon substrate. For such measurements, the thermal conductivity of silicon was considered to be 148 W/m.K [JAC 2002].

Table 2.5: Thermal conductivities of BrSiO₂, GaAs, InP, and high resistivity Si given in literature.

Material	Reference	Thermal conductivity k (W/m.K)
BrSiO₂	[HAR 2012]	1.14
GaAs	[SZE 1985]	46
	[BLA 1987]	55
	[INY 2003]	47
InP	[ADA 2009]	68
	[KUD 1963]	68
	[HUX 1999]	68
Si (HR)	[GLA 1964]	150
	[JAC 2002]	148

The thickness t_s of BrSiO₂, GaAs, InP and Si (HR) substrates used in the three omega method measurements are 700 μm , 350 μm , 355 μm , and 500 μm respectively (table 2.6).

IV.3. Linear regression analysis in linear regime

In order to calculate the thermal conductivity, the in-phase and out-of-phase third harmonic voltages are measured for the linear region frequency range. A linear fit is then plotted for the in-phase third harmonic voltage experimental data. The thermal conductivity is deduced through the slope of this linear fit.

As explained in chapter 1, the in-phase third harmonic voltage measured in the linear regime by means of the differential amplifier or Wheatstone bridge circuit is linearly proportional to the natural logarithm of the thermal excitation frequency 2ω over the linear regime frequency range as follows:

$$V_{3\omega-in-phase} = -\frac{V_0^3 \beta_h}{4\pi l k R_0} * \ln(2\omega) - \frac{V_0^3 \beta_h}{4\pi l k R_0} \left(\ln\left(\frac{b^2}{\alpha}\right) - 2\varepsilon \right) \quad (2.18)$$

The above equation has the form of a straight line in a plot $y=f(\ln(2\omega))$:

$$y = A + Bx \quad (2.19)$$

$$\begin{aligned} & y = V_{3\omega-in-phase} \text{ and } x = \ln(2\omega) \\ \text{where: } & A = -\frac{V_0^3 \beta_h}{4\pi l k R_0} \left(\ln\left(\frac{b^2}{\alpha}\right) - 2\varepsilon \right) \\ & B = -\frac{V_0^3 \beta_h}{4\pi l k R_0} \end{aligned}$$

As presented in chapter 1, the thermal conductivity k is calculated as follows:

$$k = -\frac{V_0^3 \beta_h}{4\pi l R_0} * \frac{1}{B} \quad (2.20)$$

where V_0 is the initial voltage measured across the metallic line in V.

β_h is the temperature coefficient of resistance in $^\circ\text{C}^{-1}$.

l is the length of the metallic line in m.

R_0 is the resistance of the metallic line in Ω at initial temperature T_0 .

IV.4. Experimental measurements

The substrate under test is mounted on a copper plate placed under the microscope's binoculars. The metallic line is connected to the Wheatstone bridge or to the differential amplifier circuits by the use of four micromanipulators. The linear regime for the metallic line is initially calculated by applying equation 1.60 where the value of the thermal conductivity is taken from literature. The function generator is turned on with appropriate voltage amplitude at a frequency corresponding to the higher frequency in the linear regime. Several minutes are needed till the substrate reaches thermal equilibrium. Then, the Wheatstone bridge or the differential amplifier circuit is balanced by tuning the variable resistor such that the differential lock-in amplifier's output at fundamental frequency ω is zero. The lock-in amplifier is then switched to harmonic 3 and the in-phase and out-of-phase voltages at frequency 3ω are recorded. These steps are repeated for a large number of frequencies included in the linear regime. Normally, we start at the highest frequency since the time constant is smaller and manipulations can be done faster. Afterwards, we start decreasing the frequency till the lowest value in the linear regime. At the beginning of every manipulation, the metallic line resistance R_0 is measured by the 4 wire method at room temperature.

After the three omega measurements, the substrate under test is taken off the copper plate and placed on a hot plate for the temperature coefficient of resistance measurements.

In the following section, we present the third harmonic voltage measurements performed using the Wheatstone bridge and differential amplifier circuits for each of borosilicate, gallium arsenide, indium phosphide, and silicon substrates.

IV.5. Wheatstone bridge and differential amplifier measurements

Measurements are done on several metallic lines of different dimensions by the use of both the Wheatstone bridge (WB) and differential amplifier (DA) circuits among which are those listed in table 2.6. We present the average resistance measured at room temperature, the initial voltage, the measured temperature coefficient of resistance and the applied power on each of the metallic lines. Initially, measurements are performed by the use of DA circuit. Afterwards, the micromanipulator cables are slowly disconnected from the DA circuit and connected to the WB circuit without displacing the micromanipulator tips on the pads of the metallic line under test. The same power per unit length is applied on the metallic line to compare the three omega measurements carried out by each of the circuits.

Table 2.6: Dimensions and properties of different metallic lines deposited on BrSiO₂, GaAs, InP, and Si.

Material	Line	$2b$ (μm)	l (mm)	R_0 (Ω)	V_0 (V)	β ($^{\circ}\text{C}$)	p_{rms} (W/m)
BrSiO ₂ $t_s = 700 \mu\text{m}$	1	10	5	32.2984	0.5528	0.003068	1.8920
	2	30	18	40.6959	0.4268	0.0031303	0.2487
	3	10	7.2	45.5721	0.4661	0.003178	0.6622
GaAs $t_s = 350 \mu\text{m}$	4	20	5	19.3343	0.4374	0.003072	1.9792
	5	20	3	11.9441	0.1475	0.003058	0.6070
	6	10	5	39.5784	0.4175	0.003044	0.8810
InP $t_s = 355 \mu\text{m}$	7	10	5	27.6405	1.0689	0.003301	8.2667
	8	20	5	15.5386	0.6059	0.003282	4.7245
	9	20	5	15.1167	0.5945	0.003386	4.6761
Si $t_s = 500 \mu\text{m}$	10	20	5	17.32056	0.8080	0.003131	7.5377
	11	10	5	31.9190	1.3693	0.003165	11.7484
	12	30	9.2	21.2112	1.3350	0.003126	9.1332

Figures 2.17, 2.18, 2.19, and 2.20 represent the in-phase and out-of-phase third harmonic voltages measured in the linear regime versus the natural logarithm of the thermal excitation frequency 2ω for BrSiO₂, GaAs, InP, and Si respectively. The squares and circles in red represent the measurements done by the DA circuit while the triangles and crosses in black correspond to those performed by the WB. Moreover, theoretical values are shown in blue for every metallic line by applying Cahill's solution (equation 1.48). The values of the heat capacity and density used for each material are listed in table 2.7. Cahill's solution is plotted for a thermal conductivity equivalent to the average value taken over the calculated thermal conductivities using each of the WB and DA circuits (table 2.8).

Table 2.7: The values of heat capacities, densities and thermal diffusion of BrSiO₂, GaAs, InP, and Si taken from literature.

Material	Heat capacity (J/Kg.K)	Density (Kg/m ³)	Thermal diffusion α (m ² /s)
Borosilicate	750	2230	6.82E-7
Gallium Arsenide	327	5320	3.16E-5
Indium Phosphide	310	4810	4.56E-5
Silicon	710	2329	9.07E-5

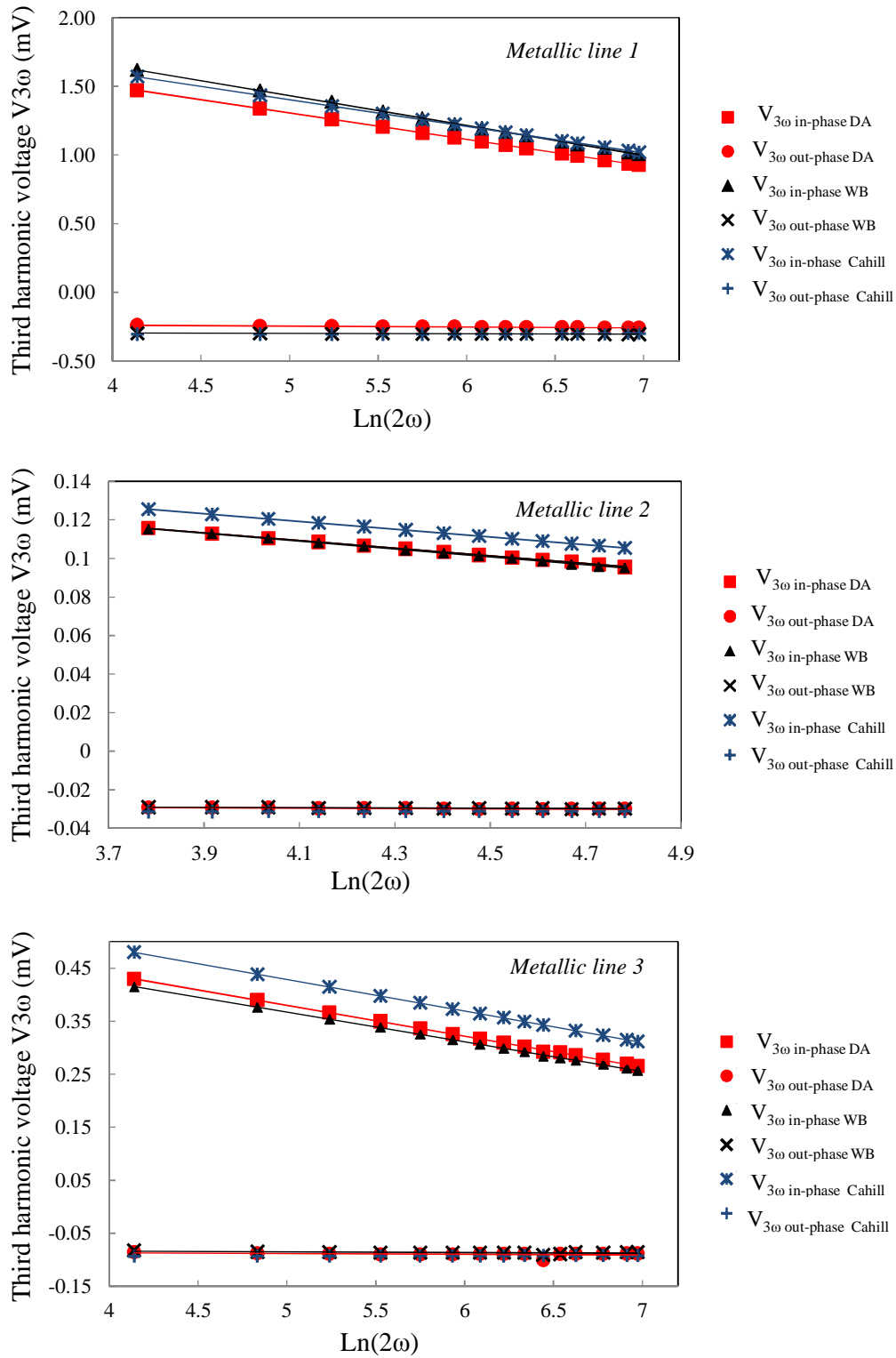


Figure 2.17: The in-phase and out-of-phase third harmonic voltages measured on borosilicate substrate using both DA and WB circuits. The third harmonic voltages in blue correspond to Cahill's solution.

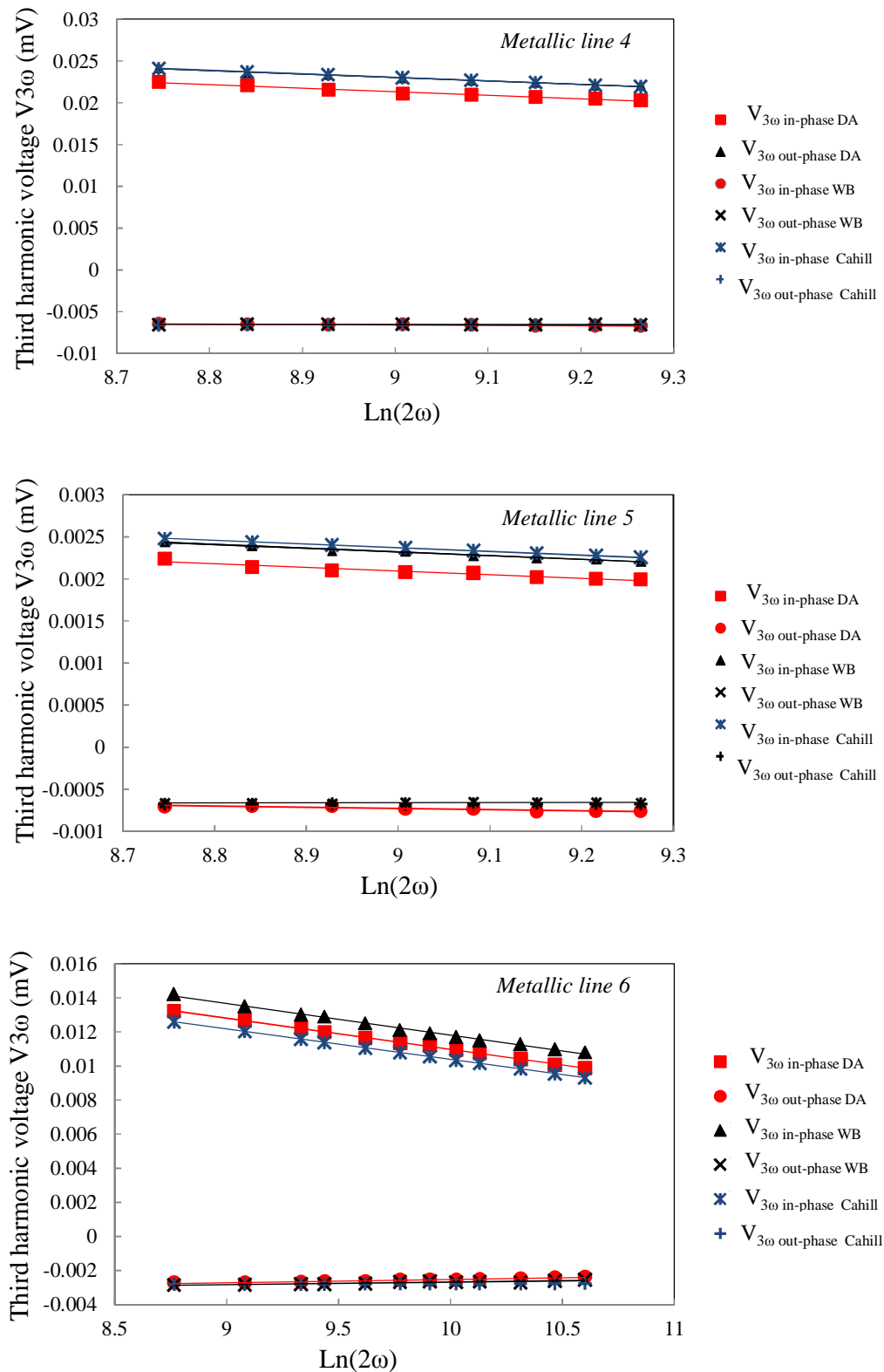


Figure 2.18: The in-phase and out-of-phase third harmonic voltages measured on gallium arsenide substrate using both DA and WB circuits. The third harmonic voltages in blue correspond to Cahill's solution.

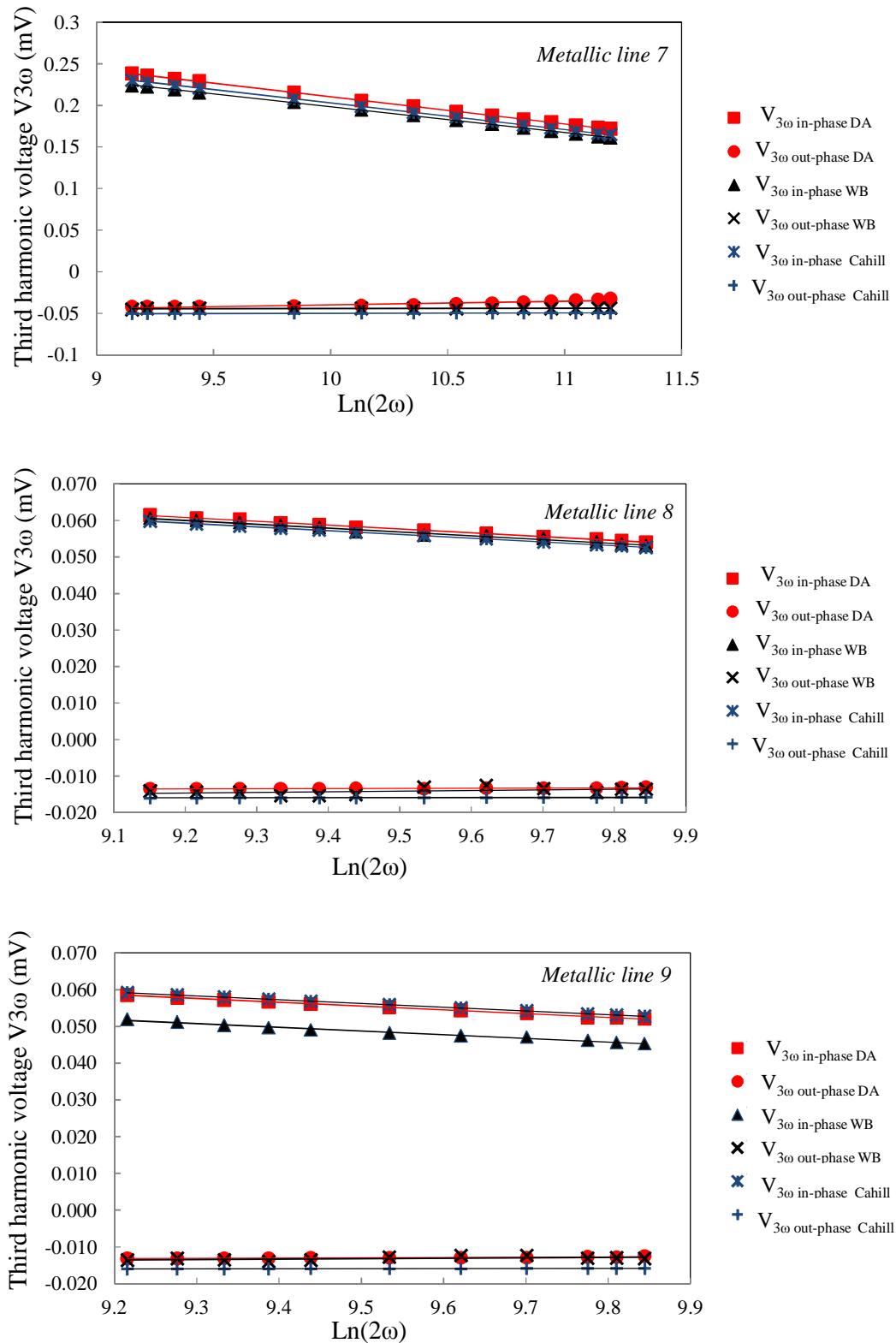


Figure 2.19: The in-phase and out-of-phase third harmonic voltages measured on indium phosphide substrate using both DA and WB circuits. The third harmonic voltages in blue correspond to Cahill's solution.

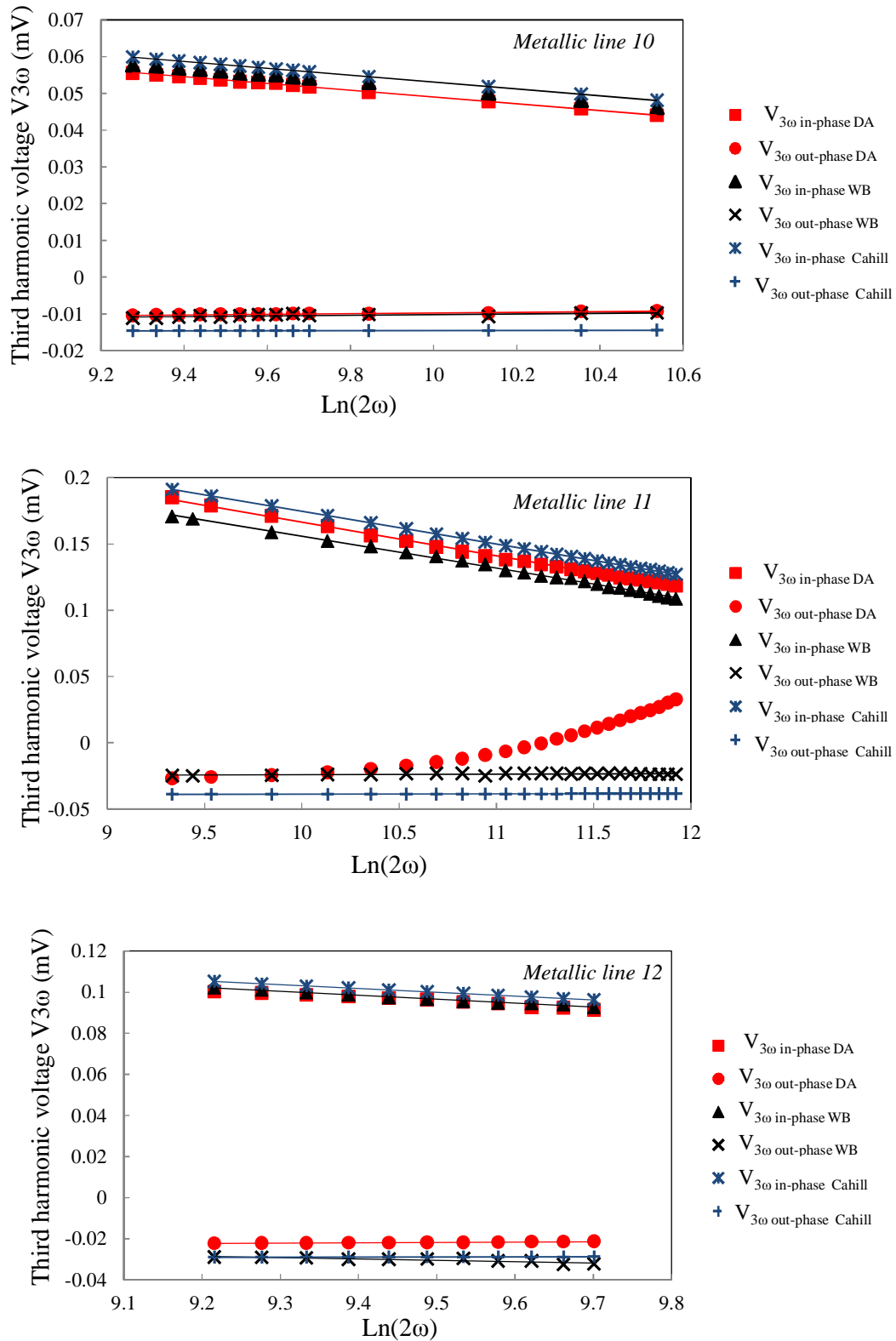


Figure 2.20: The in-phase and out-of-phase third harmonic voltages measured on high resistivity silicon substrate using both DA and WB circuits. The third harmonic voltages in blue correspond to Cahill's solution.

For each of the four materials studied we can observe that the values of the third harmonic voltages measured by both the Wheatstone bridge and the differential amplifier circuits are close. Also, the slopes of the linear relationship between the real third harmonic voltages and $\ln(2\omega)$ for both circuits are practically the same. Furthermore, a good agreement between our measurements and the data obtained from Cahill's solution is observed for all the materials tested. We can also notice that the experimental measurements for in-phase voltages (in red and black) are always lower than the theoretical measurements (in blue) except for metallic line 3 on borosilicate, metallic line 6 on gallium arsenide and metallic lines 7 and 8 on indium phosphide. Moreover, we can observe an increase of the out-of-phase third harmonic voltages in the linear frequency zone for metallic line 11. This increase can be explained by the existence of parasitic effect in the DA circuit. Such an effect appears as we go higher in frequency. In table 2.8, we can find the thermal conductivities k_{WB} and k_{DA} determined using the Wheatstone bridge and the differential amplifier circuits respectively. Also, the average thermal conductivity k_{avg} for the whole measurements done on different metallic lines for every material investigated is calculated.

Table 2.8: The values of the thermal conductivities for each material measured by the wheatstone bridge and differential amplifier circuits.

Material	Line	k_{WB} (W/m.K) and % difference with respect to k_{avg}		k_{DA} (W/m.K) and % difference with respect to k_{avg}		k_{avg} (W/m.K)
BrSiO2	1	1.1725	-10.51%	1.3294	1.47%	1.31
	2	1.292	-1.4%	1.331	1.56%	
	3	1.394	6.37%	1.343	2.51%	
GaAs	4	52.614	5.69%	50.266	0.97%	49.78
	5	49.269	-1.03%	49.699	-0.17%	
	6	48.041	-3.5%	48.81	-1.95%	
InP	7	74.848	3.35%	70.782	-2.26%	72.42
	8	71.2656	-1.6%	70.488	-2.67%	
	9	75.191	3.82%	71.958	-0.64%	
Si	10	162.963	-0.11%	166.475	2.04%	163.1
	11	169.33	3.79%	159.289	-2.37%	
	12	158.432	-2.89%	162.402	-0.46%	

The percentage difference in the values of k_{WB} and k_{DA} corresponding to each metallic line are calculated with respect to the average thermal conductivity k_{avg} . First, we can notice that the values k_{AD} for every material are more reproducible. Moreover, the percentage differences calculated for k_{AD} are lower than those of k_{WB} .

In appendix B, a linear regression analysis is done for the third harmonic voltage measurements performed on $BrSiO_2$, GaAs, InP, and Si (HR). We can observe in tables B.1, B.2, B.3, and B.4 that the coefficient of determination R^2 for every measurement is approximately equal to 1 which shows that $V_{3\omega \text{ in-phase}}$ is strongly linear with respect to $Ln(2\omega)$. In addition, examining the slopes \hat{B} estimated for the measurements performed using the Wheatstone bridge and the differential amplifier circuits for every metallic line, we can find that they are close in value.

IV.6. Conclusion

In order to validate the constructed three omega method-based experimental setup, measurements were performed using both the Wheatstone bridge and the differential amplifier circuits on four different samples of different thermal conductivities. We have found out that the measured in-phase third harmonic voltages using both circuits are in good agreement with Cahill's theoretical data. In addition, the calculated average thermal conductivity for each sample agrees well with the value found in literature. To determine the slope, a linear regression analysis was done. The coefficient of determination was found to be approximately equal to 1 thus indicating a good linear relation between the in-phase third harmonic voltages and the natural logarithm of the thermal excitation frequency. The percentage differences of the thermal conductivities k_{WB} and k_{DA} with respect to the average value k_{avg} were calculated for each metallic line. It was found that these percentages in k_{DA} are lower than those in k_{WB} . Also, we have noticed that the values k_{DA} for each material are more repetitive. For these reasons, we can conclude that it is more reliable to use the differential amplifier circuit in the experimental setup. Therefore, in chapters 3 and 4 only the measurements done using the DA circuit will be presented.

V. The 3ω experimental setup measurement precision

V.1. Introduction

An error analysis over the three omega method experimental setup is proposed thereafter. Initially, repeatability measurements are performed and the repeatability standard deviation is calculated. Afterwards, the precision of measurement of each of the instruments used in the experimental setup is determined together with its effect on the value of the thermal conductivity. Finally, it was found that parasitic capacitance exists in the Wheatstone bridge and the differential amplifier electronic circuits.

V.2. Repeatability measurements

Repeatability is defined by the degree to which an experimental measurement can be accurately repeated by the same observer using the same procedure at the same location and within a short period of time. Normally it is represented by the repeatability standard deviation S_r [SUR 2010]:

$$S_r = \sqrt{\frac{\sum (x_i - \bar{x})^2}{n-1}} \quad (2.21)$$

where \bar{x} is the mean value of x_i and n is the number of data measured.

Repeatability measurements were done for the three omega method-based experimental setup. For example, thermal conductivity measurements were repeated for several times on metallic line 1 of 10 μm width and 5 mm length for borosilicate substrate. Table 2.9 shows the properties of the metallic line.

Table 2.9: Properties of metallic line used for repeatability measurements on borosilicate substrate.

<i>Metallic line</i>	<i>2b (μm)</i>	<i>l (mm)</i>	<i>R₀ (Ω)</i>	<i>β_h ($^{\circ}\text{C}^{-1}$)</i>
1	10	5	32.2984	0.003068

The micromanipulator tips were placed in the correct position at the beginning of the experiment and were never repositioned between one measurement and another therefore keeping the same value of the metallic line resistance for all trials. Such measurements were performed in around two hours at a room temperature of 25 $^{\circ}\text{C}$. The manipulations were

repeated by applying two different values of power p_{rms} on the metallic line. Figure 2.21 shows six repeated measurements over the metallic line on borosilicate substrate. For Figure 2.21.a the average applied power is 1.891 W/m.K for trials 1, 2 and 3 and for Figure 2.21.b the average power per unit length is 4.537 W/m for each of the trials 4, 5, and 6. For both cases, we can notice similar slopes for the linear relation between the third harmonic voltages versus the natural logarithm of the thermal excitation frequency.

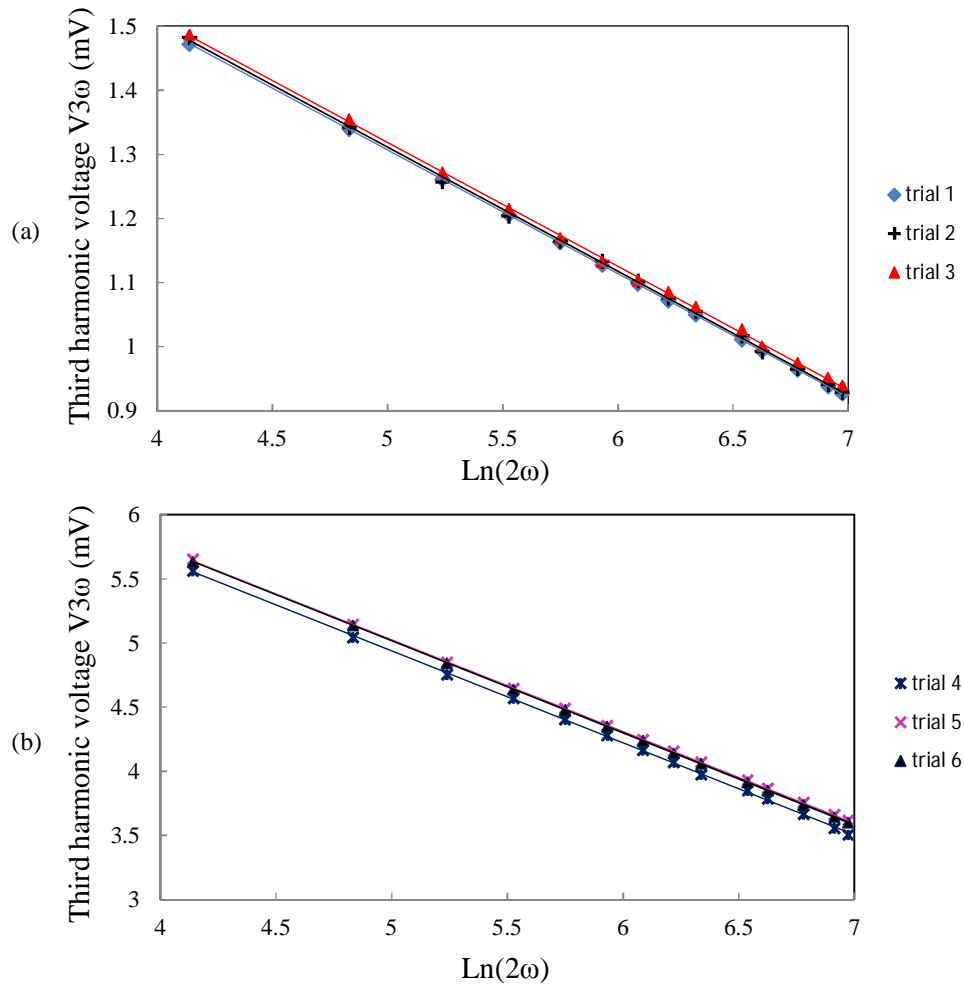


Figure 2.21: Third harmonic voltages versus natural logarithm of 2ω for six repeated measurements on the same metallic line for borosilicate substrate when using the DA circuit (a) $p_{rms}=1.891$ W/m (b) $p_{rms}=4.537$ W/m.

In tables 2.10 and 2.11 we can see the values of the thermal conductivities obtained together with the power applied in each trial when measurements are done using the differential amplifier circuit and the Wheatstone bridge respectively. Trial 0 corresponds to the initial measurements done on BrSiO₂ substrate over metallic line 1 (see tables 2.6 and 2.8).

Table 2.10: The power applied and the corresponding thermal conductivity calculated for each trial when using the differential amplifier circuit.

Trial	0	1	2	3	4	5	6
p_{rms} (W/m)	1.8920	1.8887	1.8935	1.8901	4.5370	4.5370	4.5375
k (W/m.K)	1.3294	1.3231	1.3226	1.3204	1.3241	1.3254	1.3231

Table 2.11: The power applied and the corresponding thermal conductivity calculated for each trial when using the Wheatstone bridge circuit.

Trial	0	1	2	3	4	5	6
p_{rms} (W/m)	1.8920	1.8798	1.8832	1.8874	4.5410	4.5407	4.5409
k (W/m.K)	1.1725	1.1851	1.1875	1.1941	1.2011	1.2008	1.2008

We can notice that the thermal conductivities are very close in value for both rms applied average powers. The repeatability standard deviation was calculated according to equation 2.21. It was found that the measured thermal conductivities for borosilicate deviate by $S_r = 0.00167$ W/m.K and by $S_r = 0.0072$ W/m.K around the mean value when using the DA circuit and the WB circuit respectively. These repeatability measurements showed average thermal conductivities $k_{DA} = 1.3231 \pm 0.127$ % W/m.K and $k_{WB} = 1.1937 \pm 0.6$ % W/m.K for borosilicate substrate in case of metallic line 1. Repeatability measurements were also performed on gallium arsenide, indium phosphide and silicon substrates. These measurements showed thermal conductivity errors which are always less than 1% with respect to the average value. Also, as for $BrSiO_2$, the repeatability measurements showed less error when using the DA circuit than when using the WB circuit.

V.3. Systematic errors and measurement precision

In this section we discuss the systematic errors that occur during the measurements and affect the thermal conductivity value. The measurement precision of the initial voltage V_0 , the metallic line resistance R_0 , and the temperature coefficient of resistance β_h are also determined.

V.3.a. The metallic line resistance R_0

As mentioned in section II.4, the metallic line resistance is measured by the 4-wire method using an Agilent 34420A micro-ohm meter. Moreover, the minimum R_{\min} , maximum R_{\max} , and average resistance R_0 values were measured due to the existence of fluctuations aroused because of the contact between the micromanipulator tips and the metallic pads.

Let us consider metallic line 12 (table 2.6) which is deposited on Si substrate. The ohm-meter was left connected for around one hour to the metallic line where at the same time statistics option was enabled. In the table below we can see the values of the minimum, maximum and average resistances of this metallic line.

Table 2.12: Minimum, maximum and average resistance values of metallic line 12 on Si substrate.

Metallic line	$2b$ (μm)	l (mm)	R_{\min} (Ω)	R_0 (Ω)	R_{\max} (Ω)
12	30	9.2	21.1927	21.2112	21.2227

The ohm-meter has precision specifications of \pm (0.0015% of reading +0.0002% of range) for a resistance in the range of 100 Ω [HP 2003]. Thus, the total resistance error calculated when measuring the metallic line average resistance using the ohm meter is $R_e = \pm 0.5181$ m Ω . This results in an error E_I of $\pm 0.0024\%$ on the values of the thermal conductivities measured by both the Wheatstone bridge and the differential amplifier circuits. Consequently, one can consider the error introduced due to ohm meter precision measurements to be negligible.

Now, let us study the error produced due to the minimum and maximum values of the metallic line resistance. Table 2.13 shows the values of the errors, % e_I , that affect the thermal conductivity considering the ohm meter's error R_e on one hand and neglecting it on the other hand. Although the resulting errors are higher than E_I , they are still low in value and their impact on the thermal conductivity can be dismissed.

Table 2.13: %errors produced due to minimum and maximum metallic line resistances.

	$R_{\min} - R_e$	R_{\min}	R_{\max}	$R_{\max} + R_e$
Resistance (Ω)	21.1921	21.1927	21.2227	21.2232
% e_I	0.0898%	0.0873%	-0.0541%	-0.0565%

The same study was done on all the metallic lines used in our measurements and the percentage error was always found to be insignificant.

V.3.b. The initial voltage V_0

The initial voltage V_0 across the metallic line has to be measured just at the beginning of the experiment before the metallic line starts to heat up. Crocodile clip connectors are attached to the micromanipulator tips to achieve the parallel connection between the multimeter and the metallic line resistance. The multimeter used is an Agilent 34411A 6 ½ digit. It is important to know the measurement precision of the multimeter since V_0 is cubed when calculating the thermal conductivity of materials. In addition, this precision changes as frequency changes. Table 2.14 shows the multimeter's precision specifications with respect to frequency [HP 2013].

Table 2.14: AC voltage precision specifications of the multimeter.

Frequency	$\pm(\% \text{ of reading} + \% \text{ of range})$
3 Hz – 5 Hz	0.5% of reading + 0.02% of range
5 Hz – 10 Hz	0.10% of reading + 0.02% of range
10 Hz – 20 KHz	0.02% of reading + 0.02% of range

For GaAs, measurements are done for frequencies higher than 10 Hz. Just at the beginning of manipulations, the initial voltage V_0 measured by the multimeter across metallic line 4 is equal to 0.4374 V. Therefore, the calculated voltage error V_e is:

$$V_e = \pm(0.4374 \text{ V} * 0.02\%) + (1 \text{ V} * 0.02\%) = \pm 0.287 \text{ mV}$$

This leads to an error $e_2 = \pm 0.197\%$ on the thermal conductivity value.

For borosilicate substrate, sometimes measurements are done for frequencies lower than 5 Hz. For example, for metallic line 2, we initiated our third harmonic voltage measurements at a frequency equals to 3.5 Hz. The calculated error produced on the thermal conductivity value is found to be $e_2 = \pm 1.65\%$.

The same calculations were performed on all the metallic lines over BrSiO_2 , GaAs, InP and Si. For the four materials, the highest thermal conductivity percentage error aroused due to the multimeter precision measurement was found to be $\pm 1.65\%$.

V.3.c. The temperature coefficient of resistance β_h

The temperature coefficient of resistance has been measured using the hot plate method. Temperature of the metallic line resistance was monitored by attaching the thermocouples over the substrate's surface near the metallic line by the use of thermal paste. The thermocouples were held in their position by the aide of adhesive tape. This method produces several systematic errors in addition to uncertainties in the value of β_h .

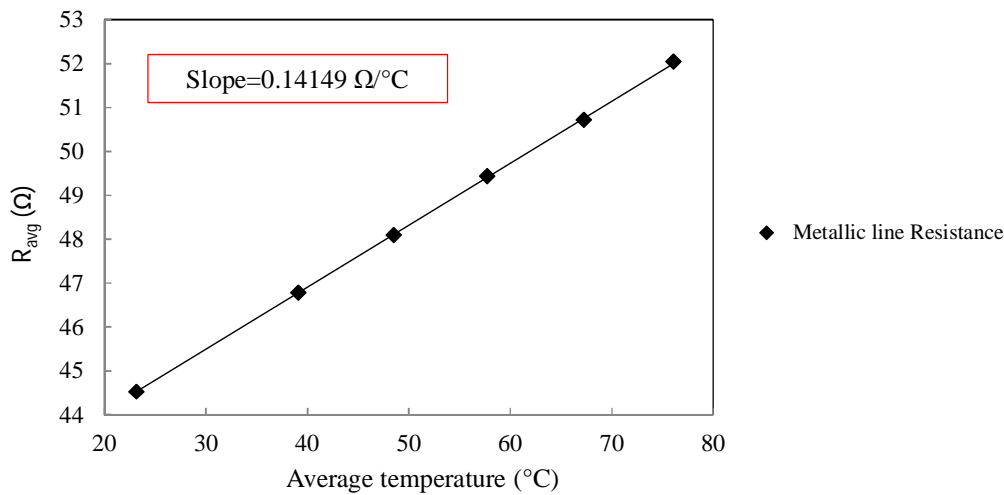
One of the systematic errors is due to the fact that the metallic line is heated through the substrate underneath. If this substrate is of a low thermal conductivity, it will need a long time to reach thermal equilibrium. Moreover, the temperature of the hot plate is adjusted manually. Varying the hot plate temperature might cause the micromanipulators tips to move a little from their original place on the metallic line pads and consequently resulting in a change in the value of the metallic line resistance.

The uncertainty in the value of β_h is due to the small variations around an average value in the metallic line resistance and its temperature. The thermometer used to measure the temperature of the metallic line is a DIGI-SENSE 12 channel thermocouple scanning thermometer with an accuracy measurement of $E = \pm 0.5\text{ }^\circ\text{C} \pm 0.1\%$ of reading at temperatures above $-150\text{ }^\circ\text{C}$ [DIGI DOC]. The thermometer's channels are enabled in order to read the different temperatures of the thermocouples taped on the surface of the substrate. Table 2.15 shows the average, minimum, and maximum resistances of metallic line 3 (see table 2.6) at different average temperatures (average temperature of the thermocouples) together with the minimum T_{\min} and maximum T_{\max} temperatures measured between these thermocouples. $(T_{\min}-E)$ and $(T_{\max}+E)$ are calculated in order to be able to plot the minimum and the maximum slopes as will be shown.

Table 2.15: R_{\min} , R_{\max} and R_{avg} at different temperatures measured for metallic line 3 on BrSiO_2 substrate for the determination of β_h .

T_{\min} ($^{\circ}\text{C}$)	T_{avg} ($^{\circ}\text{C}$)	T_{\max} ($^{\circ}\text{C}$)	R_{\min} (Ω)	R_{avg} (Ω)	R_{\max} (Ω)	$T_{\min}-E$ ($^{\circ}\text{C}$)	$T_{\max}+E$ ($^{\circ}\text{C}$)
23	23.13	23.2	44.5107	44.5219	44.5324	22.47	23.72
38.5	39.1	39.5	46.7645	46.7763	46.7873	37.96	40.04
48.1	48.5	49	48.0777	48.0897	48.1011	47.55	49.54
57.1	57.73	57.9	49.4087	49.4211	49.4328	56.54	58.45
67	67.23	67.5	50.7058	50.7185	50.7305	66.43	68.06
75.8	76.1	76.3	52.0240	52.0371	52.0494	75.22	76.87

In the above table, the ohm meter's measurement precision error is neglected. Figure 2.22 presents the linear increase of the average resistance of metallic line 3 with respect to the average temperature. The slope is then calculated in order to determine the temperature coefficient of resistance β_h .

**Figure 2.22:** Average resistance versus average temperature for metallic line 3 on BrSiO_2 substrate.

Dividing the slope by the average resistance of metallic line 3 over BrSiO_2 substrate at room temperature gives a temperature coefficient of resistance $\beta_h=0.003178 /^{\circ}\text{C}$. The vertical and horizontal error bars corresponding to the resistance and temperature measurement errors are plotted in figure 2.23. Accordingly, we can obtain the uncertainty in the slope and consequently in the value of β_h .

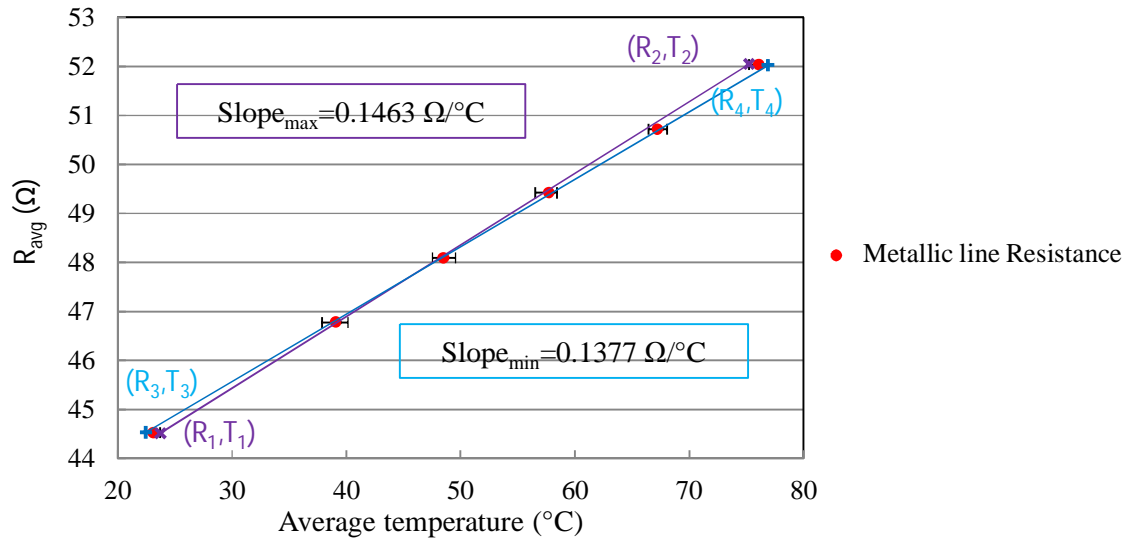


Figure 2.23: Slope variation corresponding to measurement error of average resistance and temperature.

The maximum slope is plotted in violet for $R_1 = R_{\min}$ at $T_1 = (T_{\max} + E) = 23.72$ °C and $R_2 = R_{\max}$ at $T_2 = (T_{\min} - E) = 75.22$ °C. While the minimum slope is traced in blue for $R_3 = R_{\max}$ at $T_3 = (T_{\min} - E) = 22.47$ °C and $R_4 = R_{\min}$ at $T_4 = (T_{\max} + E) = 76.87$ °C. In table 2.16 we can observe the change in the value of the temperature coefficient of resistance as the value of the slope varies. This change corresponds to an error e_3 of -2.65 % to +3.48 % on the average thermal conductivity k_{avg} of the material.

Table 2.16: Variation of β_h , k_{DA} , and k_{WB} with respect to the slope.

	Minimum	average	maximum
Slope ($\Omega/^\circ\text{C}$)	0.1377	0.1415	0.1463
β ($^\circ\text{C}$)	0.003094	0.003178	0.003288
k_{DA} (W/m.K)	1.307	1.343	1.390
k_{WB} (W/m.K)	1.357	1.394	1.442
% e_3 w.r.t. k_{avg}	-2.65 %	—	+3.48 %

In some cases, while measuring the resistance during the TCR measurements, some vibrations might occur causing the resistance value to jump and then retain its original value. This jump is memorized as a maximum according to the ohm meter's statistics. This results in a higher slope variation and consequently adds higher error to the thermal conductivity value which might reach 10%. Such a problem can be solved by collecting the ohm meter's

measurement data and omitting the undesired value. The data can be saved by connecting the ohm meter to a personal computer possessing a special kind of programs such as LabVIEW.

This error analysis was performed on all the metallic lines over BrSiO_2 , GaAs, InP, and Si substrates. The maximum for e_3 is found to be $\pm 6\%$.

In conclusion, the above mentioned systematic errors can be reduced by heating the metallic line in a precise temperature controlled oven instead of using a hot plate. The benefits of using such oven are:

- 1) the metallic line is heated by surrounding air rather than through underneath the substrate,
- 2) no thermocouples are needed to be connected to the metallic line,
- 3) no vibrations are generated when varying the oven's temperature.

V.3.d. The effect of $V_{3\omega \text{ in phase}}$ versus $\text{Ln}(2\omega)$ on the thermal conductivity value

The SR830 lock-in amplifier used in measuring the third harmonic voltages across the metallic line has a measurements precision of $\pm 1\%$ of reading. This precision is given after calibration done by Stanford Research laboratories on the lock-in amplifier. Therefore, an error analysis was done to check the influence of this measurement precision on the slope of the linear relation between the in-phase third harmonic voltage and the natural logarithm of 2ω .

Let us recall the equation used in calculating the material thermal conductivity (equation 2.20):

$$k = -\frac{V_0^3 \beta_h}{4\pi l R_0} * \frac{1}{B}$$

The vertical error bars corresponding to the in-phase third harmonic voltage ($V_{3\omega \text{ in-phase DA}}$ and $V_{3\omega \text{ in-phase WB}}$) measurement precision are plotted for metallic line 3 on BrSiO_2 substrate as shown in Figure 2.24. Consequently, the minimum and maximum slopes are determined for each of the measurements done by the differential amplifier circuit and the Wheatstone bridge. According to equation 2.20, a minimum thermal conductivity is calculated for a maximum slope and vice versa. Table 2.17 summarizes the values of the slopes, the resulting thermal conductivities and the errors e_4 with respect to the average thermal conductivity produced due to the slope variation.

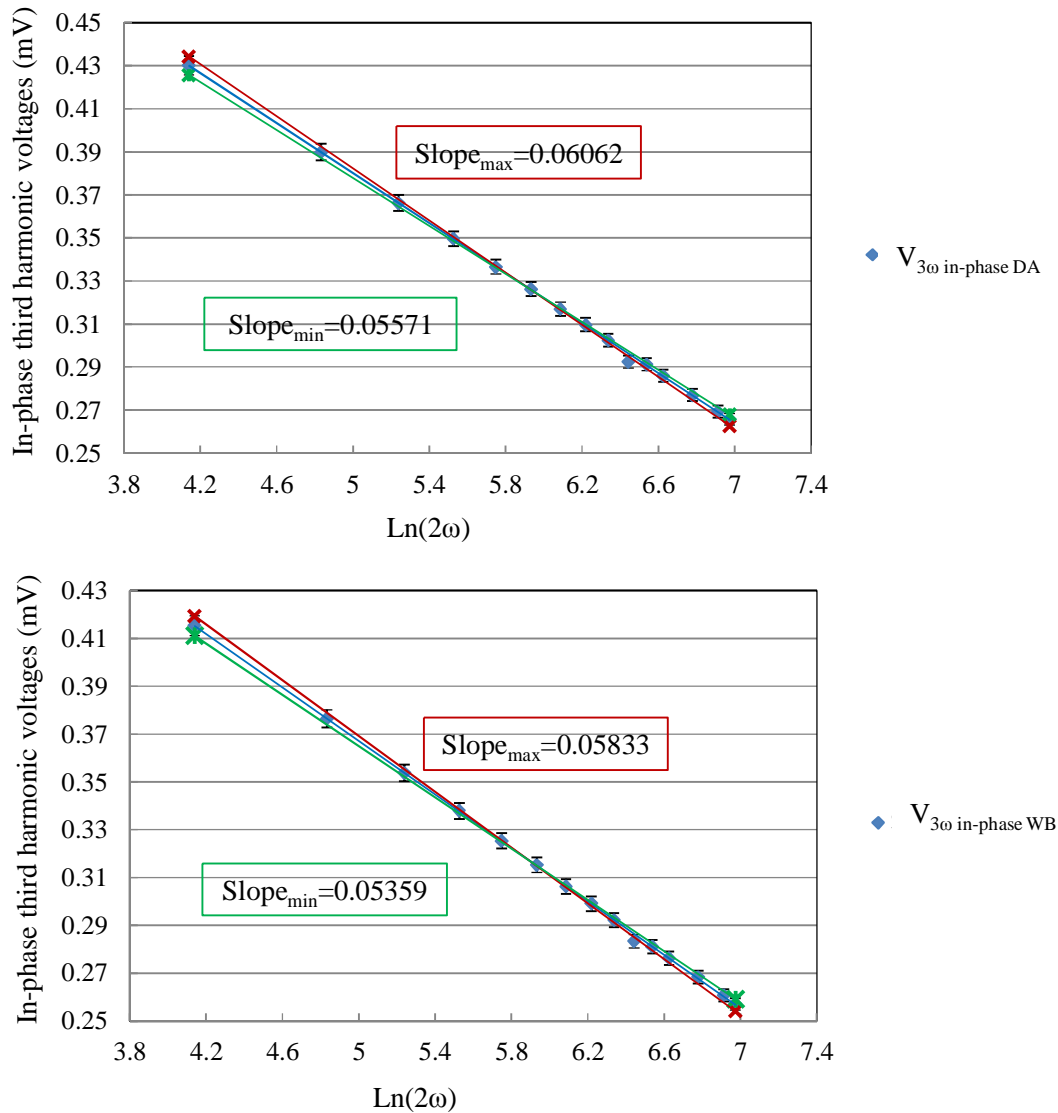


Figure 2.24: The variation of the slope due to the precision measurements of the lock-in amplifier.

Table 2.17: The slope and thermal conductivity variations for measurements done on metallic line 3 using DA and WB circuits.

		Minimum	average	maximum
DA circuit	Slope	0.05571	0.05817	0.06062
	k_{DA} (W/m.K)	1.289	1.343	1.402
	% e_4	-4.05 %	—	+4.41 %
WB circuit	Slope	0.05359	0.05596	0.05833
	k_{WB} (W/m.K)	1.337	1.394	1.455
	% e_4	-4.06 %	—	+4.43 %

We can notice in table 2.17 that the percentage error e_4 is the same for both the DA and WB circuits. The highest percentage error e_4 produced when applying this error analysis on all the measurements done over BrSiO₂, GaAs, InP, and Si is $\pm 6.5\%$.

V.3.e. The effect of V_0 , R_0 , β_h and slope measurement errors

After studying the effect of each of R_0 (error e_1), V_0 (error e_2), β_h (error e_3), and slope (error e_4) measurement errors separately, we evaluate the contribution of these errors altogether on the value of the thermal conductivity of materials.

The maximum error over the thermal conductivity is calculated by taking the maximum error over the factors present in the numerator (V_0 and β_h) of equation 2.20 and the minimum error over those found in the denominator (R_0 and $slope$) of the same equation. This is demonstrated in equation 2.22:

$$k_{\max} = -\frac{(V_0 + V_e)^3 \beta_{h\max}}{4\pi l R_{\min}} * \frac{1}{slope_{\min}} \quad (2.22)$$

where V_e is the voltage error produced when measuring V_0 due to the multimeter precision measurement, $\beta_{h\max}$ is the maximum temperature coefficient of resistance of metallic line (section V.3.c.), R_{\min} is the minimum metallic line resistance detected by the micro-ohm meter (section V.3.a.), and $slope_{\min}$ is the minimum slope obtained for a $\pm 1\%$ measurement precision of the in-phase third harmonic voltages measured by the lock-in amplifier.

Inversely, the minimum value of the thermal conductivity is calculated as follows:

$$k_{\min} = -\frac{(V_0 - V_e)^3 \beta_{h\min}}{4\pi l R_{\max}} * \frac{1}{slope_{\max}} \quad (2.23)$$

The following table represents a summary of the percentage errors e_1 , e_2 , e_3 , and e_4 produced due to R_0 , V_0 , β_h , and slope measurement errors respectively. Also we can find e_T which is the error due to the total contribution of e_1 , e_2 , e_3 , and e_4 on the value of the thermal conductivity of materials. We present the error results corresponding to metallic lines 3, 4, 7, and 11 on BrSiO₂, GaAs, InP, and Si (HR) respectively. These metallic lines have the lowest percentage errors calculated over each material.

Table 2.18: Percentage errors e_1 , e_2 , e_3 , e_4 and e_T for metallic lines 3, 4, 7, and 11.

Metallic line	% e_1	% e_2	% e_3	% e_4	% e_T
3 BrSiO₂	± 0.00194 %	± 1.60 %	-2.65 % +3.48 %	-4.06 % +4.43 %	-8.12 % +9.83 %
4 GaAs	± 0.00253 %	± 0.197 %	-3.24 % +3.58 %	-5.66 % +5.21 %	-9.85 % +10.53 %
7 InP	-0.023 % +0.025 %	± 0.62 %	-3.50 % +4.67 %	-5.76 % +5.50 %	-9.6 % +10.2 %
11 Si (HR)	± 0.00213 %	± 0.5 %	-5.64 % +5.93 %	-4.37 % +4.79 %	-10.22 % +10.57 %

As mentioned before, the percentage error e_1 is minimal and can be ignored. The error e_2 aroused due to the multimeter's measurements is considered to be small where it affects slightly the thermal conductivity value. We can notice that accordingly, the error is mostly due to measurement of the temperature coefficient of resistance β_h and the lock-in amplifier's precision measurement. The total error e_T on the values of the thermal conductivities determined using both the differential amplifier and the Wheatstone bridge circuits is calculated to be around ± 10 %.

V.4. Electronic circuits parasitic effects

As discussed before, the common mode cancellation techniques (WB and DA) are used to eliminate the third harmonic voltage produced by the function generator. This is done by balancing the Wheatstone bridge or the differential amplifier circuit. Normally, at the output, a zero voltage at angular excitation frequency ω must be acquired. Nevertheless, while balancing the experimental setup (WB or DA), an out-of-phase voltage is detected. In fact, only the real part of the voltage V_ω at angular frequency ω is attenuated. Consequently, we can conclude that reactive parasitic elements, inductive or capacitive, exist in the electronic circuit.

Actually, we cannot perform a complete study over the experimental circuit, since it is difficult to quantify the influence of the ground plane or every line belonging to the electronic

circuit on the experimental measurements. However, the presence of the reactive parasitic elements corresponding to every passive component in the electronic circuit can be investigated. Therefore, we were able to measure the value of these parasitic elements on each component by the aide of two impedance analyzers (FLUKE PM6306 and AGILENT 4294A). The results given by both instruments are the same, particularly when the capacitive elements measured are superior to 10 pF. The measuring instruments have a common disadvantage. The FLUKE PM6306 and AGILENT 4294A cannot measure impedances for frequencies lower than 50 Hz and 40 Hz respectively. So, impedance measurements cannot be done for materials possessing high thermal conductivities whose linear zone limits are at around ten Hz.

This study is presented on line 4 belonging to GaAs substrate (table 2.6). We can find in table 2.19 and 2.20 the values of the parasitic elements measured at 700 Hz. This frequency corresponds approximately to the central frequency of the linear zone of metallic line 4. However, we have to keep in mind that the values of the parasitic elements change with frequency. The impedance measurements are done for potentiometers $R_{3,v}$ (WB) and R_v (DA) as a whole. They are not performed on every passive element constituting these variable resistances.

Table 2.19: Parasitic element corresponding to each passive element constituting the WB.

Resistor or potentiometer	Parasitic element
R_2	Capacitor in parallel < 1pF
R_1	Capacitor in parallel ~ 20 pF
$R_{3,v}$	Capacitor in parallel ~ 150 pF

Table 2.20: Parasitic element corresponding to each passive element constituting the DA.

Resistor or potentiometer	Parasitic element
R_v	Capacitor in parallel ~ 120 pF

Impedance measurements are done for many metallic lines of different lengths and widths deposited on the material under-test. The real part of the impedance changes according to the resistance measured, while its imaginary part is found to be quasi constant and corresponds to

an average inductance in series equals to $4 \mu\text{H}$. The impedance measurements for the metallic line consider the micromanipulator needles and their coaxial cables.

After characterizing the passive elements, we simulate the behavior of the WB and DA circuits using the electro-kinetic equations operating in a permanent sinusoidal regime (figure 2.25(a) and 2.25(b)). Also, these equations are inserted in MATLAB in order to calculate $V_A - V_B$. The voltage at the generator is fixed to 2 V_{rms} . The capacitive effect over R_2 is neglected and the differential amplifiers AD624 are assumed to be ideal. As we have done experimentally, the real part of the complex impedance measured across the potentiometers $R_{3,v}$ and R_3 is adjusted in a way that the real part of the voltage $V_A - V_B$ is equal to zero.

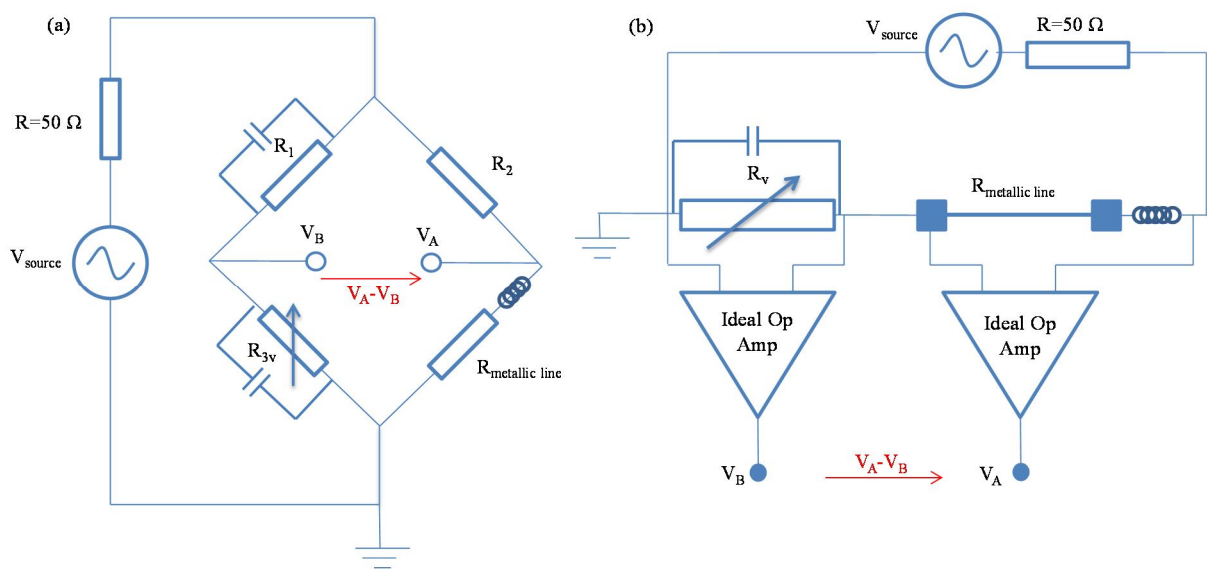


Figure 2.25: Parasitic effects presents in the (a) WB and (b) DA circuits.

Figure 2.26 represents a theoretical-experimental comparison for the WB and DA circuits. We can notice in both cases an increase in the imaginary part of $V_A - V_B$ similar to the rise in experimental measurements with respect to frequency. However, the experimental measurements are always superior to theoretical ones. The study done here is a first approach where only certain reactive elements are taken into account. As shown in figure 2.26, the values of $V_A - V_B$ obtained are less than 1 mV which indicates that the generator's voltage at frequency ω set at 2 V_{rms} is attenuated by a factor superior to 2000. Also, if any third harmonic voltage is produced by the generator, it will be highly attenuated and consequently negligible when measuring $V_A - V_B$.

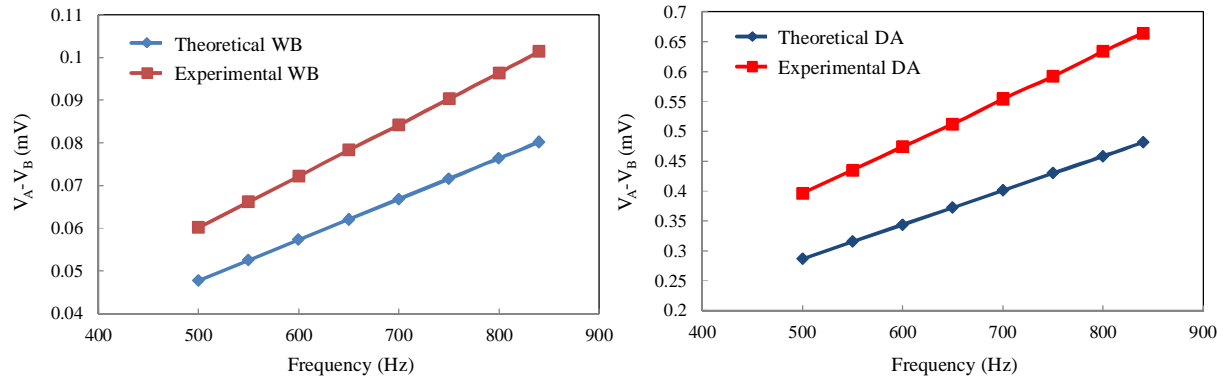


Figure 2.26: Theoretical-experimental comparison of out of phase V_A-V_B for WB and DA circuits.

In the following, the influence of the parasitic elements on the third harmonic voltage is studied. For the WB and DA circuits, a generator operating at frequency 3ω possessing an electromotive force given by Cahill's equation (equations 1.51 and 1.52) when translated into voltage is placed in series with the metallic line. The simulated electric circuits are shown in figure 2.27(a) and 2.27(b).

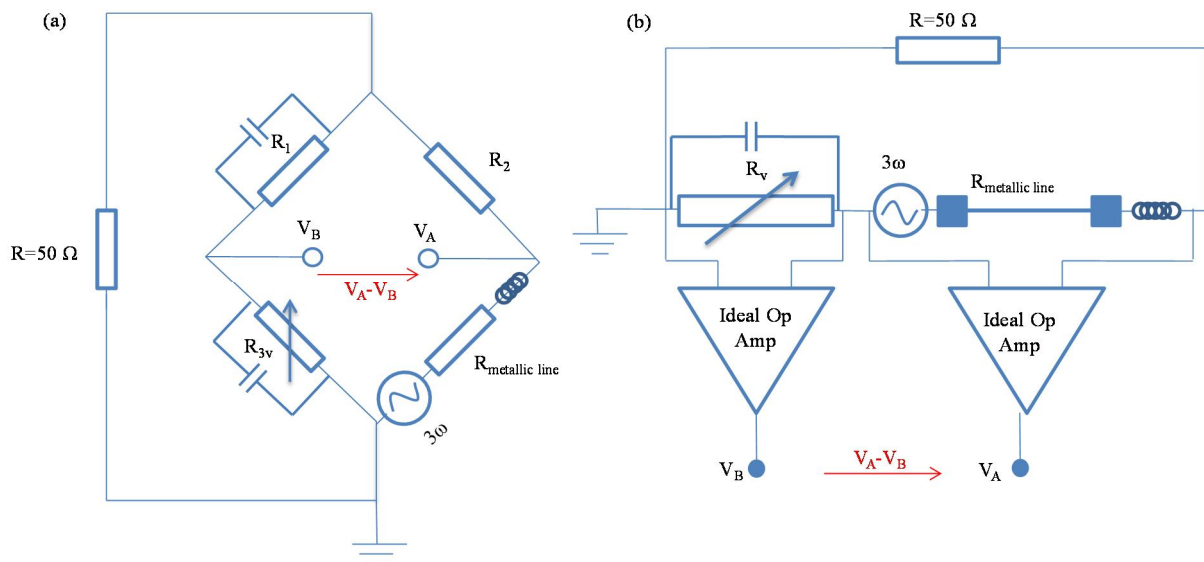


Figure 2.27: A generator at frequency 3ω placed in series with the metallic line for the (a) WB and (b) DA circuits.

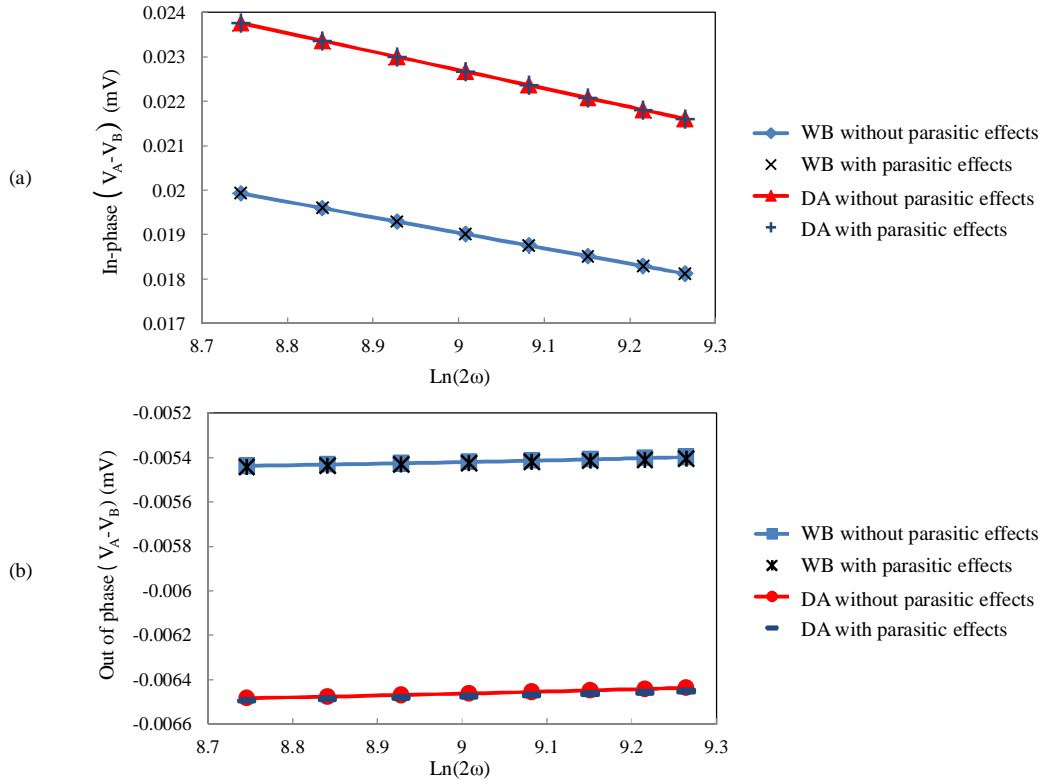


Figure 2.28: The in-phase (a) and out of phase (b) $V_A - V_B$ voltages when considering and when neglecting the parasitic effects.

Figure 2.28(a) and 2.28(b) represent respectively the theoretical in-phase and out of phase values of the voltage $V_A - V_B$ (in the linear regime) for the WB and DA circuits where the components are purely resistive on one hand and where the parasitic effects are taken into account on the other hand. We can clearly notice that the parasitic elements have no influence on the voltage $V_A - V_B$ when the measurements are done for frequencies between 500 Hz and 1000 Hz which correspond to $\text{Ln}(2\omega)$ equal to 8.745 and 9.438 respectively.

V.5. Conclusion

The instrumentation measurement precision and its influence on the thermal conductivity value have been studied. The error e_1 due to measuring the metallic line resistance R_0 was found to be negligible. Also, the error e_2 produced due to the measurement of the initial voltage V_0 has a slight influence on the thermal conductivity value. It is the measurement errors e_3 and e_4 , aroused when determining the temperature coefficient of resistance β_h and the slope of linearity respectively that have stronger effects on the value of the thermal conductivity. Finally an error analysis combining all ohm-meter, multimeter, hot plate method and lock-in amplifier measurement errors has been performed. This error e_T was calculated to be around $\pm 10\%$. The presence of parasitic reactive elements in the WB and DA circuits has

caused the appearance of an out-of-phase voltage at frequency ω . We were not able to cancel such voltage. However, we were able to perform a study through which we have shown that the reactive elements have practically no effect on the measured voltage V_A-V_B .

Conclusion

The three omega method-based experimental setup was built up. It consists of a function generator that feeds the metallic line with an alternating current and a lock-in amplifier to measure the in-phase and out-of-phase third harmonic voltages produced by the metallic line. The lock-in amplifier was connected to the output of a Wheatstone bridge or a differential amplifier circuit used to isolate the third harmonic voltage across the metallic line and to suppress any other third harmonic signal that might add to the measurements. The metallic line was chosen to be made of gold since this metal has a high TCR. It was deposited on the surface of the material under test through photolithography process. The Wheatstone bridge and the differential amplifier circuit were designed such that all their components possess a very small TCR compared to the one of the metallic line. It is important to precisely measure the resistance of the metallic line at room temperature, its temperature coefficient of resistance, and the initial voltage across the metallic line before it starts to heat up.

The three omega method-based experimental setup was validated. Measurements were performed on four kinds of materials, borosilicate, gallium arsenide, indium phosphide, and silicon. The average thermal conductivities measured for these materials agreed well with the values found in literature. The thermal conductivities measured when using the differential amplifier circuit were found to be repetitive and with lower error with respect to the average thermal conductivity when compared to the Wheatstone bridge. An error analysis for the three omega method-based experimental setup was done. The errors due to ohm-meter and the multimeter measurements were found to be negligible. It was found that the measurement of the temperature coefficient of resistance of the metallic line using the hot plate method produces an average error of -3 % to +4 % on the value of the thermal conductivity. Also, measuring the third harmonic voltage by the aide of the SR830 lock-in amplifier, produces an error of -5.7 % to +6.5 %. Taking into account the effect of all the errors produced by the instruments used in the 3 omega method-based experimental setup results in a total error e_T of around ± 10 %.

Using the differential amplifier circuit in the experimental setup has shown better results than when using the Wheatstone bridge. Therefore, in the coming chapters we will only present the third harmonic voltage measurements done by means of the differential amplifier circuit.

REFERENCES

- [ADA 2009] S. ADACHI
“Properties of semiconductor alloys: Group-IV, III-V, and II-VI,”
John Wiley & Sons 2009, pp 52.
- [BAC 1981] K. J. BACHMANN
“Properties, preparation and device application of indium phosphide,”
Annual Review of Material Science, Vol. 11, pp 441-484, 1981.
- [BIR 1987] N. O. BIRGE and S.R. NAGEL
“Wide-frequency specific heat spectrometer,”
Review of Scientific Instruments, Vol. 58, pp 1464-1470, 1987.
- [BLA 1987] J.S. BLAKEMORE
“Key papers in physics Gallium Arsenide,”
Oregon Graduate Center, American Institute of Physics, pp 55, 1987.
- [BOY 2010] W. BOYES
“Instrumentation reference book,”
Fourth Edition, Copyright 2010, Elsevier Inc.
- [CHU 2009] S. CHUNG, J. LEE, J. JEONG, J. KIM, and Y. HONG
“Substrate thermal conductivity effect on heat dissipation and lifetime
improvement of organic light-emitting diodes,”
Applied Physics Letters, Vol. 94, pp 253302, 2009.
- [CLE 2002] [http://sindhu.ece.iisc.ernet.in/nanofab/twikii/pub/Main/OpticalAndE-
beamLithography/clewin_manual.pdf](http://sindhu.ece.iisc.ernet.in/nanofab/twikii/pub/Main/OpticalAndE-beamLithography/clewin_manual.pdf)
- [DIGI DOC] [http://www.coleparmer.com/Product/Digi_Sense_12_Channel_Scanning_
Benchtop_Thermometer_115_VAC/EW-92000-00](http://www.coleparmer.com/Product/Digi_Sense_12_Channel_Scanning_Benchtop_Thermometer_115_VAC/EW-92000-00)
- [GLA 1964] C.J. GLASSBRENNER and G. SLACK
“Thermal conductivity of silicon and germanium from 3 °K to the melting
point,”
Physical Review, Vol. 134, pp A1058-A1060, 1964.
- [HAR 2012] D. HARTUNG, F. GATHER, and P.J. KLAR
“Comparison of different methods for measuring thermal conductivities,”
9th European Conference on Thermoelectrics AIP Conf. Proc., Vol. 1449,
pp 381-384, 2012.
- [HOP 2011] P.E. HOPKINS, C. M. REINKE, M. F. SU, R. H. OLSSON III, E. A.
SHANER, Z. C. LESEMAN, J. R. SERRANO, L. M. PHINNEY, and I.
EL-KADY
“Reduction in the thermal conductivity of single crystalline silicon by
phononic crystal patterning,”

Nano Letter, Vol. 11, pp 107-112, 2011.

- [HP 2008] Agilent 33210A 10 MHz Function/ Arbitrary Waveform Generator.
Publication number 33210-90010 (order as 33210-90000 manual set),
Edition 1, August 2008.
- [HP 2003] Agilent 34420A Nano Volt/ Micro Ohm Meter.
Manual Part Number 34420-90010 (order as 34420-90000 manual set),
Edition 2, March 2003.
- [HP 2013] Agilent 34410A and 34411A 6 ½ digit multimeters.
© Agilent Technologies , Inc. 2013
Published in USA, 2013, 5989-3738EN.
- [HUX 1999] S. HUXTABLE, A. SHAKOURI, P. ABRAHAM, Y. J. CHIU, X. FAN, J.
E. BOWERS, and A. MAJUMDAR
“Thermal conductivity of Indium phosphide based superlattices,”
18th International Conference on Thermoelectrics, pp 594-597, 1999.
- [INY 2003] A. V. INYUSHKIN, A. N. TALDENKOV, A. Y. YAKUBOVSKY, A.V.
MARKOV, L. MORENO-GARSIA, and B.N. SHARONOV
“Thermal conductivity of isotopically enriched ⁷¹GaAs crystal,”
Semiconductor Science and Technology, Vol. 18, pp 685-688, 2003.
- [JAC 2002] A. JACQUOT, B. LENOIR, A. DAUSCHER, M. STOLZER, and J.
MEUSEL
“Numerical simulation of the three omega method for measuring the
thermal conductivity,”
Journal of Applied Physics, Vol. 91, pp 4733-4738, 2002.
- [KUD 1963] I. KUDMAN and E.F. STEIGMEIER
“Thermal conductivity and seebeck coefficient of InP,”
Physical Review, Vol. 133, pp A1665-A1667, 1963.
- [LUO 2013] T. LUO, J. GRAG, J. SHIOMI, K. ESFERJANI, and G. CHEN
“Gallium Arsenide thermal conductivity And optical phonon relaxation
times from first-principle calculations,”
European Letters, Vol. 101, pp 16001, 2013.
- [SHM 2005] D. SHMILOVITZ
“On the definition of total harmonic distortion and its effects on
measurement interpretations,”
IEEE Transactions on Power Delivery, Vol. 20, pp 526-528, 2005.
- [SR 830] SR830 DSP Lock-In-Amplifier, Operating manual and programming
reference, Stanford Research Systems.
- [SRI 2008] R. SRINIVASAN and K. RAMACHANDRAN
“Thermal diffusion in nanostructured porous InP,”
Bulletin of Material Science, Vol. 31, pp 863-868, 2008.

- [SUR 2010] L.M. SURBONE, M.T. TIMPLEDON, and S.F. MARSEKEN
“Reproducibility: Scientific method, experiment, research, standard deviation, repeatability, protoscience, accuracy, and precision,”
Editor Betascript Publishing 2010.
ISBN: 6130350422, 9786130350420.
- [SZE 1985] S.M. SZE
“Semi-conductor devices physics and technology,”
2nd edition John Wiley & sons, Inc. Appendix G, pp 538, 1985.
- [WIS 2007] P. WISSMANN
“Electrical resistivity of thin metal films,”
Springer-Verlag Berlin Heidelberg 2007.

Chapter III

Numerical simulations using FEM: The 3ω differential technique for film on substrate system

Introduction

In the previous chapter, the thermal conductivities of different solid materials have been measured by the three omega method and compared to Cahill's analytical solution. Cahill's solution stands over several assumptions such as a substrate of semi-infinite thickness, a metallic line of infinite length and negligible thickness. In reality, the samples prepared for the three omega measurements are of finite thickness and the metallic lines deposited on their surfaces are very thin and of finite length. Consequently, we have thought of a second theoretical study capable of examining the sample with its real dimensions.

In the past, the three omega method has been theoretically investigated using numerical simulation based on finite volume method (FVM) [JAC 2002]. In this study Jacquot et al. have developed their own home-made software. In this chapter, we develop another numerical simulation based on finite element method (FEM) in order to calculate the temperature oscillations at the level of the metallic line. Both FVM and FEM can adapt to all geometrical structures. The choice of a FEM technique has been mainly motivated by the availability of efficient and user friendly software. The FEM theoretical simulation results are then compared to the experimental data and Cahill's analytical solution.

In a second step, numerical simulations using FEM are applied to a two layer model consisting in a thin film is deposited on the substrate surface. In this chapter an alternative method to study the transfer of heat in a metallic line on substrate structure is developed. The three omega method has been used extensively to measure the thermal properties of thin film materials. It is worth to notice that Cahill et al. have also expanded the three omega method to obtain the thermal conductivity of a thin film on substrate [CAH 1994]. Initially, they have measured experimentally the temperature response produced because of the film-on-substrate system. Then, the temperature oscillations due to the substrate alone are calculated using Cahill's formula. The difference of the temperature responses between the two cases is then attributed to the presence of the thin film.

In a first part of the chapter, numerical simulations using finite element method are implemented to study the influence of Cahill's assumptions on the evolution of temperature of a heater deposited on the surface of a material. A structure consisting of a semi-infinite substrate with an infinitely thin metallic line deposited on its surface is initially designed. Then, the numerical simulations are turned on to determine the evolution of temperature with respect to time at the metallic line level. Afterwards, the FEM results are compared to those

obtained by Cahill's formalism and then the influence of the finite thickness substrate, the thin metallic line, and the heat convection at the surface are studied.

In section II, the three omega differential technique for measuring the thermal conductivities of thin films is briefly described. Two thin film-on-substrate systems are studied using this technique. The first is a dielectric thin SiO_2 film deposited over a boron doped Silicon substrate. The second film is an epitaxial grown layer on gallium arsenide substrate. Numerical simulations are performed for both samples. Then, the measurement data are compared to the results obtained by means of Cahill's formalism and by FEM treatment. Finally, conclusions are drawn for these comparisons.

I. Numerical simulation by Finite Element Method (FEM)

I.1. Introduction

In chapter 1, we have used analytical equations to determine the evolution of the temperature oscillations amplitude over the metallic line with respect to frequency. Nevertheless, these equations stand over a number of assumptions. First, Cahill considers a substrate of a semi-infinite thickness when solving Carslaw and Jaeger's equation of heat conduction. Then, the metallic line is assumed to be infinitely thin. Finally, heat convection at the surface of the substrate is neglected. In order to study the effect of these assumptions, we have developed a numerical simulation based on a finite element method in time domain using COMSOL[®] Multiphysics software which permits the determination of the evolution of temperature rise on every point in space. The finite element method is briefly recalled and the steps needed to apply this method are described. Then numerical simulations are performed for a structure similar to Cahill's model and the results are compared to the analytical solution. The impact of different parameters related to the metallic line and the substrate are then studied. The influence of heat convection on the surface of the sample is also investigated.

I.2. FEM and COMSOL[®] Multiphysics Software

Originally the finite element method has been developed to study a given structure from a mechanical point of view, but since it has been extended to different physical domains such as heat transfer analysis in many materials [CUI 2011, DHA 2005]. In the case of a thermal study, we need to determine the distribution of temperature in space, $T(x, y, z)$ inside a volume Ω having a closed boundary Γ . The objective is to find an approximate solution to a given problem defined by its boundary and initial conditions. When solving thermal problems using the finite element method, boundary conditions (mentioned in chapter 1, section I.4) can be defined at the boundary Γ (figure 3.1) [LEW 1996].

When performing simulations using the finite element method, the continuous space to be studied must be replaced by a discrete structure. Therefore, meshing is applied and so the domain is divided into simple geometric elements such as triangles. The finite elements produced have a common vertex, a common side or a common surface with the neighboring element. The vertices formed are called nodes. The solution of a given problem is calculated at these nodes. Theoretically, the dimensions of the finite elements must tend to zero, however this is not possible. A finite number of elements must be tested in order to estimate the error

due to the applied meshing and consequently the precision of the results. Figure 3.1 shows a two dimensional region subdivided into finite elements.

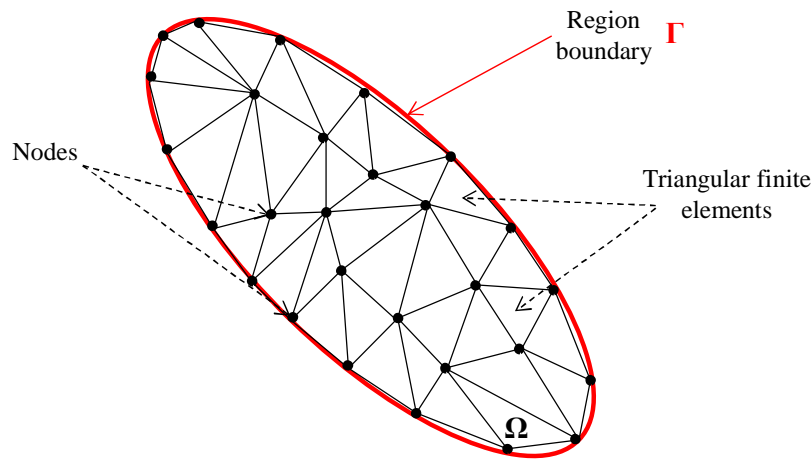


Figure 3.1: Two-dimensional region subdivided in finite elements.

For two dimensional structures, meshing is simply applied and the 2D problem is easily solved. However, tetrahedral meshing for three dimensional objects results in structures which are complex to solve even by using efficient software. This becomes even more complicated when the elements to be simulated possess high lengths but very low thicknesses. If the size of the meshing elements is successfully adapted to the smallest dimension of a given object, then meshing is well applied, however the total number of the tetrahedrons constituting the object is too high. Consequently, it is not possible to easily numerically simulate such a problem. The same difficulty exists when we need to simulate the three omega method for a three dimensional structure. The heating element is considered to be long (several millimeters) and has a thickness lower than one micrometer. All in all, the 3D finite element method simulations can become costly in terms of both computational time and memory requirements.

Modeling using FEM consists of several steps as presented in figure 3.2. Initially, the exact geometry of the structure to be studied is created. Then, meshing is applied on the structure (triangular for 2D structures). Afterwards, physical conditions such as boundary and initial conditions are required. The material and its physical properties (density, heat capacity, thermal conductivity...) are also specified. Numerical simulations can then be initiated and the computational time depends on the size of the structure and meshing. Finally, distribution of temperature (in case of thermal problem) in the structure is obtained.

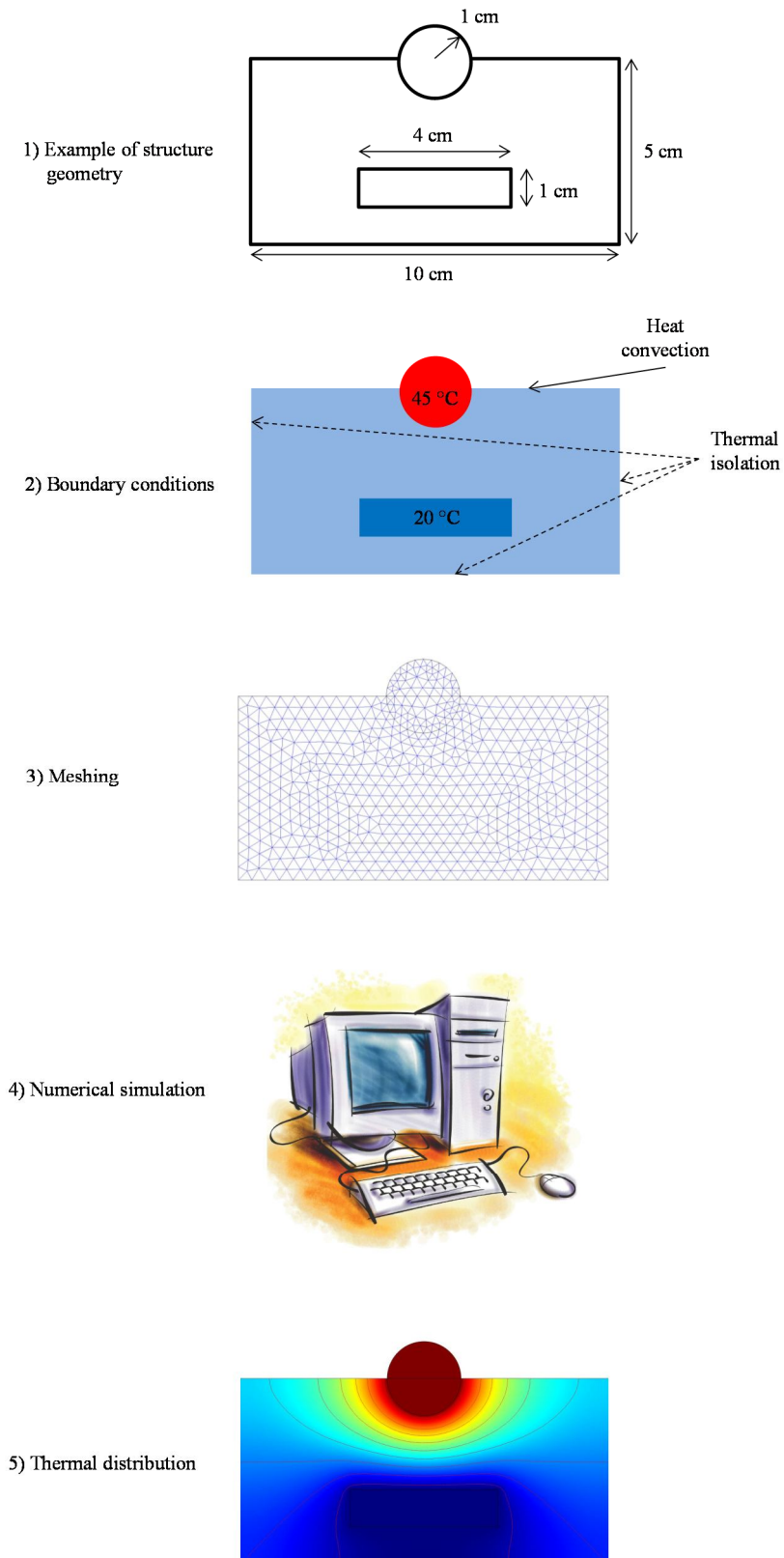


Figure 3.2: Steps needed to perform modelling using FEM.

Nowadays, different software have been developed and used in a large number of scientific research domains. The FEM-based software used in this work is COMSOL[®] Multiphysics. Many problems of different physical fields are solved using this software by applying the equations corresponding to the desired domain. Examples of such physical domains are heat transfer, expansion of fluids, electromagnetism, acoustics, mechanics of structures... This multiphysical capacity permits the user to mix different physical domains (such as electromagnetism and heat transfer) to solve a particular problem. COMSOL[®] has been created by M. Svante Littmarck and M. Farhad [COM 2009] in Sweden in 1986 and now distributed all around the world. COMSOL[®] facilitates the simulations by FEM since all the steps needed for the structure's modelling are accessible with a friendly graphical interface: geometry design, definition of physical domain, initial and boundary conditions, material choice, meshing, calculation and post treatment of results [CUI 2011]. The studied structure can be one dimensional, two dimensional, or three dimensional. Simulation in stationary or transient regimes can be carried out.

I.3. Comparison between Cahill's solution and simulation by FEM

In this study, a structure using FEM is simulated by applying the same approximations used to obtain Cahill's formula: infinitely thin metallic line, semi-infinite substrate, and thermal isolation on the surface of structure.

In order to validate experimentally the numerical simulations, we have chosen a reference metallic line that will be used all over sections I.3 and I.4 of this chapter. Therefore, it will be easier for the reader to follow the influence of various parameters. We have chosen metallic line 2 deposited on borosilicate substrate. We recall the properties of this metallic line in table 3.1. The thickness of the metallic line and the substrate are $0.4 \mu\text{m}$ and $700 \mu\text{m}$ respectively. The average thermal conductivity of BrSiO_2 measured using metallic line 2 is 1.31 W/m.K .

Table 3.1: Properties of metallic line 2 at room temperature ($T_0 = 24.7 \text{ }^\circ\text{C}$) deposited on BrSiO_2 .

Line	$2b$ (μm)	l (mm)	R_0 (Ω)	V_0 (V)	β ($^\circ\text{C}$)	p_{rms} (W/m)
2	30	18	40.6959	0.4268	0.0031303	0.2487

Metallic line 2 has been selected among other metallic lines since the amplitude of the in-phase third harmonic voltages obtained using the Wheatstone bridge corresponds well to the results found when using the differential amplifier circuit (figure 2.17). Moreover, the

measured values of the third harmonics (\sim one hundred microvolts) represent approximately the average value of the measurements done for the 4 materials (BrSiO₂, GaAs, InP, Si HR). The results of modelling using metallic line 2 are presented in the following section. It can be also noted that the numerical simulations have been tested on other metallic lines deposited over different materials.

I.3.a. Description of the studied structure

Numerical simulations of the 3ω method based on the FEM give the possibility to take into account the exact geometry of the heater (metallic line), the materials underneath the heater and the physical properties of these different materials. Normally the problem should be solved using a 3D geometry as shown in figure 3.3(a). We can notice a copper plate placed under the substrate under-test. During manipulations, this plate has been used as a heat sink. Its role is to keep its surrounding temperature equal to ambient one. In the case of a very long metal strip ($l \gg 2b$), the 3D problem can be reduced to a 2D problem considering only a plane perpendicular to the metallic line (Figure 3.3(b)).

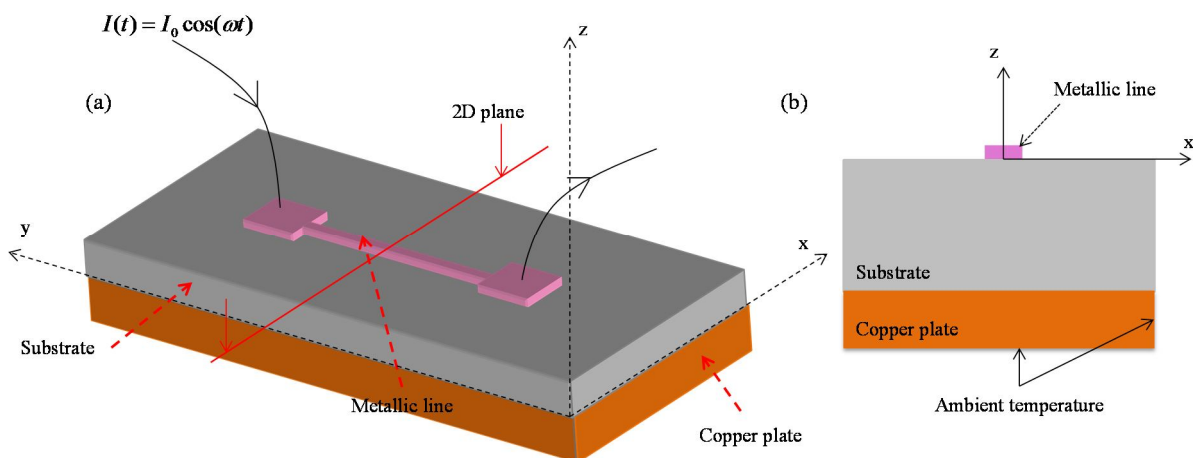


Figure 3.3: (a) 3D and (b) 2D geometry of the metallic line deposited on the substrate under-test.

Figure 3.4 presents the simplified structure proposed in figure 3.3(b) that is similar to Cahill's model. The metallic line no more exists and it is replaced by a boundary element which behaves like a heat source. Also, the convection existing at the upper surface of the structure is replaced by thermal isolation where no heat flux crosses the boundary (equation 1.14). However, a problem lies in the fact that a semi-infinite substrate must be simulated, whereas simulations by finite element method can only be done for a closed structure.

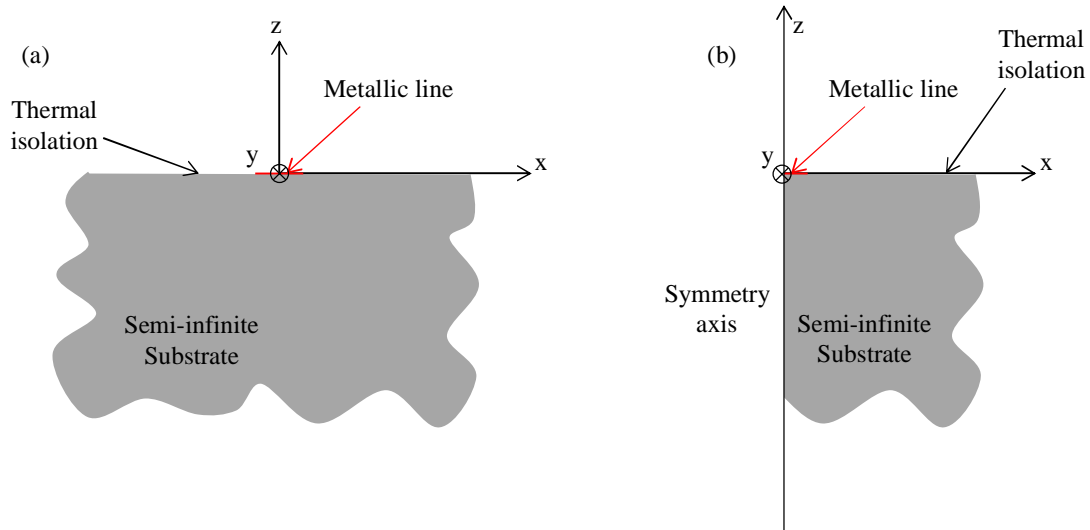


Figure 3.4: (a) Cahill's assumptions on the structure to be simulated. (b) Symmetry condition.

Before going forward in simulations, we can notice symmetry along the normal line to the metallic strip. Consequently only half of the structure is considered as shown in figure 3.4(b). Thermal isolation boundary conditions exist at the axis of symmetry. Therefore, no temperature gradient exists at the symmetry axis. Using the symmetry conditions reduces the memory size and the calculation time needed.

I.3.b. Boundary conditions

Most of the times, the structures simulated using finite element method have no boundaries. In this case it is said to be an open structure. Simulating an infinite structure is possible if it can be transformed to a finite one. A first solution is to increase the size of the finite structure as much as possible in order to cancel the influence of the boundary conditions set at its extremities. This approach creates useless meshing elements that might render the simulations impractical in terms of computational time and memory size. Another solution consists of using regions or layers called “infinities”. These layers are made of elements that make the simulations in an infinite space possible without increasing the number of meshing elements. Moreover, the “infinite” layer possesses a thickness that is lower than that of the substrate. An “infinite” layer surrounds the open structure transforming it into a closed structure compatible with the finite element method. COMSOL[®] Multiphysics software permits the use of “infinite” layers when simulating the heat equation [COM 2012].

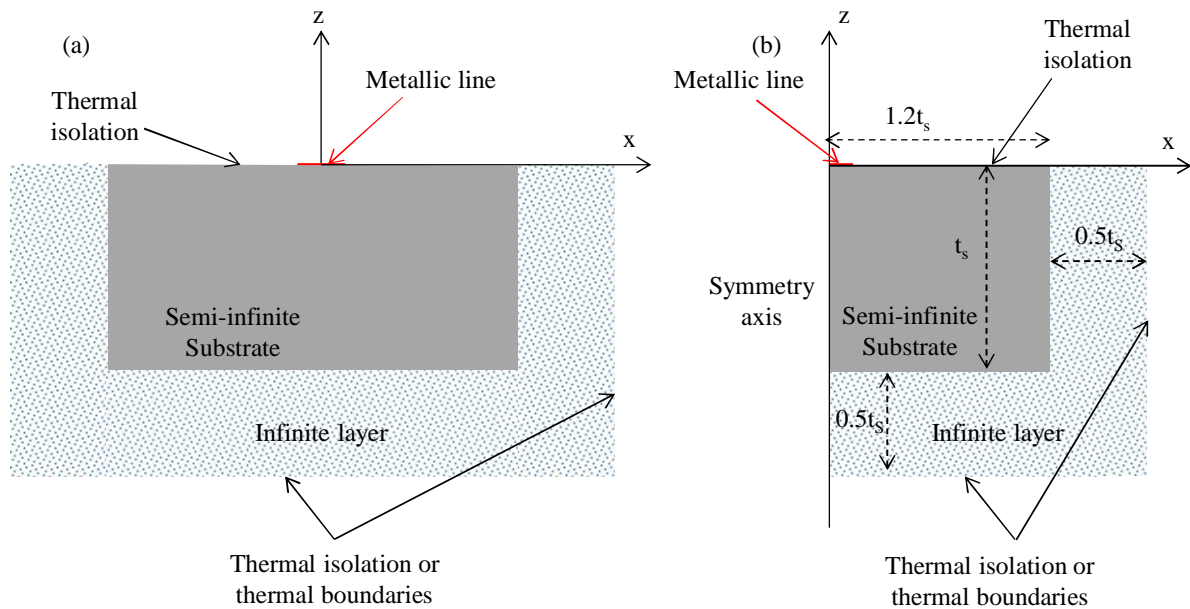


Figure 3.5: The use of “infinite” layers to produce a finite structure.

We can find in figure 3.5 the “infinite” layers added in the simulated structure. The “infinite” layers can be terminated by temperature conditions or thermal isolation. In fact, the extremities of the “infinite” layers are not of importance since they are supposed to be at infinity. They have no influence on the simulation results. The “infinite” layers are placed at a distance on the vertical axis equal to the thickness of the tested substrate ($t_s = 700 \mu\text{m}$ for BrSiO_2 substrate) and at a distance on the horizontal axis equal to $1.2t_s$ (half width of substrate superior to t_s) from the center of the heat source. Numerical simulation study has been done to study the effect of the thickness of the “infinite” layer on the FEM results when it is varied between $0.1t_s$ and $2t_s$. It was found that thicknesses superior to $0.3t_s$ do not affect the simulation results. Consequently, the “infinite” layer thickness is fixed to $0.5t_s$ (thickness of the “infinite” layer greater than $0.3t_s$ by taking into account the appropriate memory size) for the structure shown in figure 3.5.

At the surface and at the symmetry axis of the structure, thermal isolation boundary conditions are set. At last, a heat source must be set before turning on simulations.

I.3.c. The heat source

One of the important issues when starting thermal simulation problems is to add a heat source in order to produce temperature rise inside the structure. In the previous model (figure 3.5(a) or 3.5(b)) we have considered a metallic line of a negligible thickness. Consequently the heat source is located on a boundary element which represents the metallic line conductor. This boundary element behaving as a heat source corresponds to a thermal heat flux (in

W/m^2) entering the domain. To determine the value of the heat source, we start with an initial voltage V_0 across the metallic line and its measured resistance R_0 at temperature T_0 (see table 3.1). The evolution of current passing through the metallic line with respect to time is then deduced. Figure 3.6 represents the current $i(t)$ over three periods of time at frequency $F= 10$ Hz for metallic line 2 over BrSiO_2 substrate. This frequency is included in the linear regime frequency zone of the metallic line 2 ($F_{\text{lower}} \approx 3.2$ Hz and $F_{\text{upper}} \approx 11.1$ Hz).

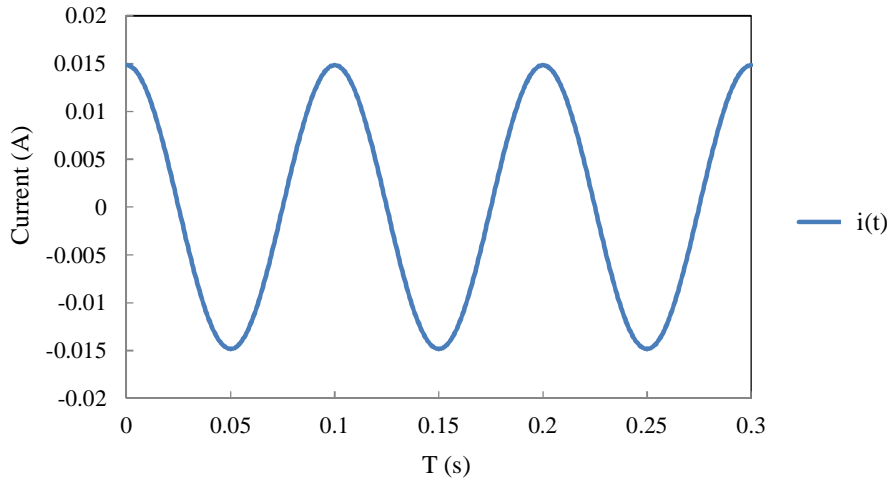


Figure 3.6: Time evolution of current at frequency 10 Hz.

According to equation 1.27, the evolution of power $p(t)$ with respect to time can be deduced (figure 3.7). The line in red corresponds to the average value $p(t)$ and is equal to P_{rms} (see chapter I). We can observe that the frequency of $p(t)$ is twice that of $i(t)$.

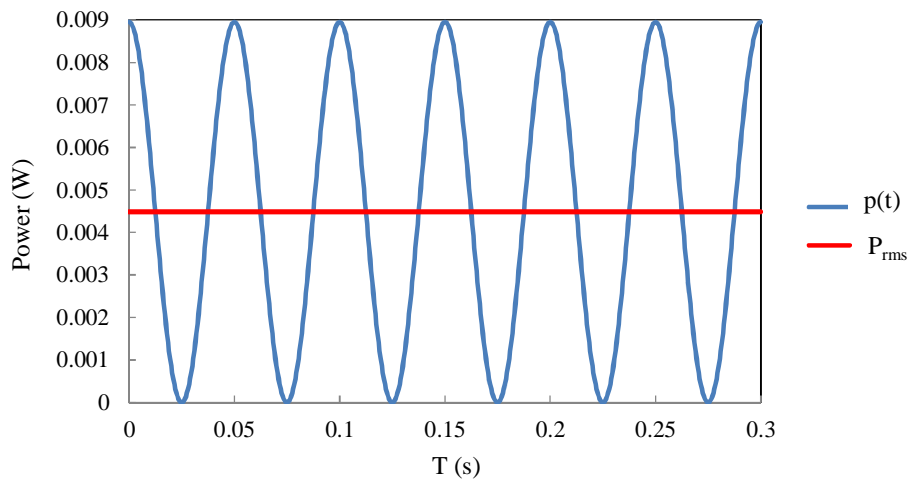


Figure 3.7: Evolution of power with respect to time at frequency 10 Hz. Average power in red = P_{rms} .

The heat source boundary element is represented by $Q_b(t)$ (in W/m^2). $Q_b(t)$ can be calculated according to the following equation:

$$Q_b(t) = \frac{p(t)}{l * 2b} \quad (3.1)$$

The time evolution of $Q_b(t)$ for metallic line 2 over BrSiO_2 substrate is shown in figure 3.8.

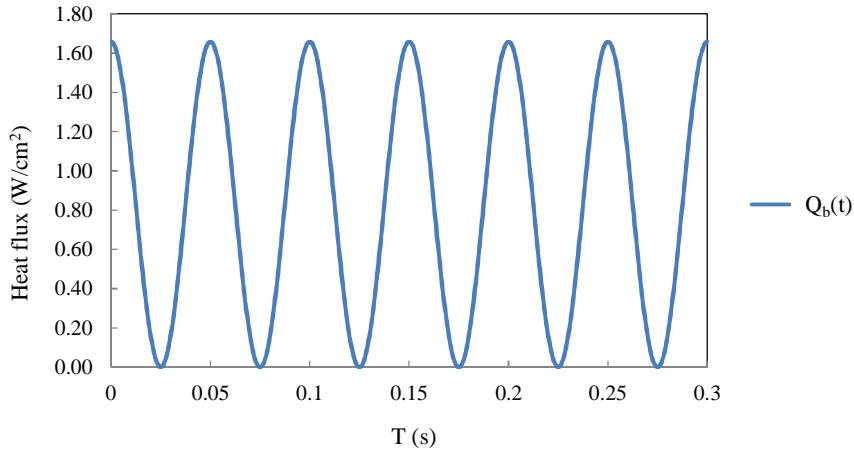


Figure 3.8: Time evolution of the heat source boundary element $Q_b(t)$ for line 2.

Similarly, we can notice that $Q_b(t)$ has a frequency two times that of the alternating current $i(t)$.

Before presenting the simulations performed to solve the problem and to determine the characteristics of temperature oscillations, the meshing applied on the structure is briefly discussed in the following section.

I.3.d. Meshing of the structure

As it has been mentioned before, the finite element method requires the creation of mesh for the studied structure.

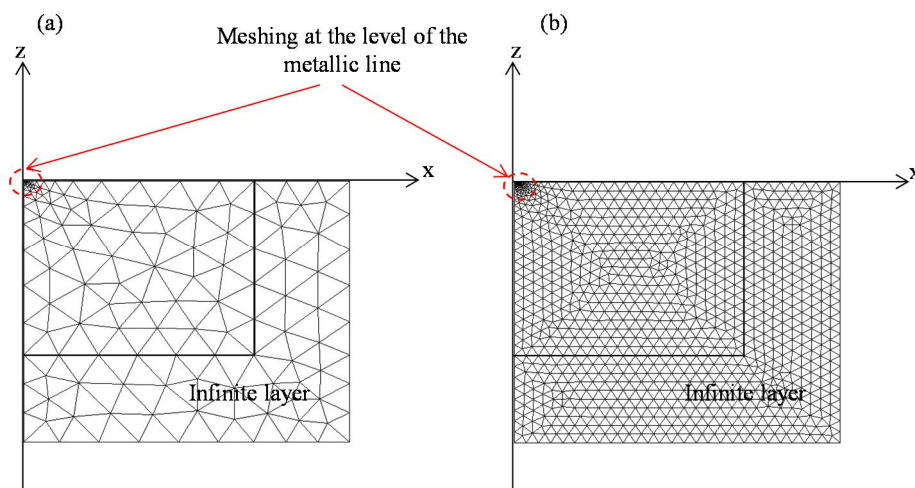


Figure 3.9: (a) Coarse meshing and (b) fine meshing of the structure.

It is possible to use coarse meshing (figure 3.9(a)) but it is better to apply fine meshing to produce a more reliable heat transfer modeling (figure 3.9(b)).

The most important part in the studied structure is the boundary element which supplies the system with heat. Therefore, meshing of good quality must be applied on this segment. In the case of coarse meshing, the boundary element of width $b=15\ \mu\text{m}$ for line 2, is divided only into three elements (figure 3.10(a)). Such division produces unsatisfactory modelling of the physical phenomenon. On the other hand, in the case of fine meshing, the boundary element is divided for example into 10 elements (figure 3.10(b)) which is obviously better. Fine meshing is always more preferable than coarse meshing, but a compromise must be found between the precision of results, the computational time, and the memory size.

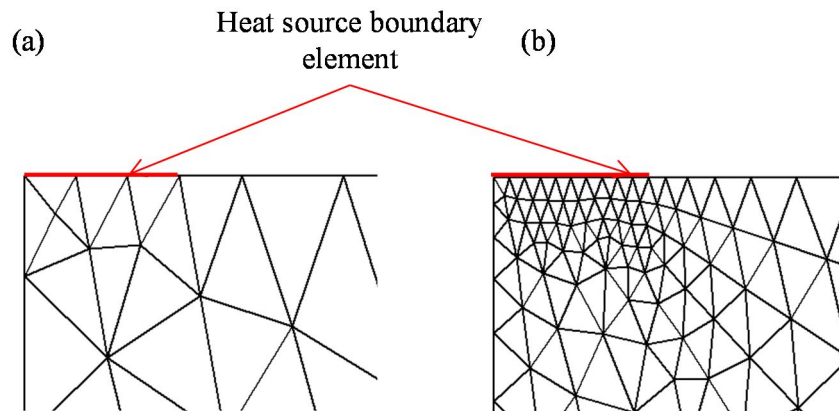


Figure 3.10: Coarse (a) and fine meshing (b) of the heat source boundary element.

I.3.e. Determination of the temperature oscillations ΔT_{AC}

The numerical simulations must be performed with respect to time since the heat source is sinusoidal at frequency 2ω knowing that ω is the generator's frequency. The amplitude of the temperature oscillations ΔT_{AC} at frequency 2ω must be determined together with its phase shift with respect to the heat source $Q_b(t)$. At $t=0$, the heat source is applied. A certain period of time or a certain number of periods of the excitation signal passes before reaching a sinusoidal permanent regime. When performing manipulations, such a period of time is estimated to be around ten seconds which is acceptable. However, in the case of theoretical simulations, this period corresponds to a computational time which is long and useless for the determination of the temperature oscillations of the metallic line. In fact, when performing simulations, two steps are followed. The first step consists of a stationary study where the derivatives with respect to time are equal to zero. Therefore, the metallic line is fed by continuous power P_{DC} equals to P_{rms} . In this case, the initial temperature of the structure is set

to ambient temperature. The final thermal pattern obtained serves as the initial conditions of the second step which consists of a time dependent study. Consequently, the time dependent study initiates at a temperature T_0 equals to the temperature obtained at the end of the stationary study (figure 3.11(a)). In this way time needed to perform theoretical simulations in the transient regime is reduced. Moreover, the transient regime that appears during the time dependent simulations is very short. We present in figure 3.11(a) the time evolution of the temperature oscillations ΔT_{AC} obtained theoretically in case of line 2 for 10 signal periods supplied by the generator ($f=10$ Hz).

The temperature oscillation ΔT_{AC} is calculated by taking the average value of the heating boundary element temperature at each time step (ΔT) calculation. The time step calculated and set for this simulation and all other simulations presented in this thesis, is equal to $T/200$ where T is the period of the generator. Therefore, 100 calculation points permit to construct one period of temperature oscillations (frequency 2ω).

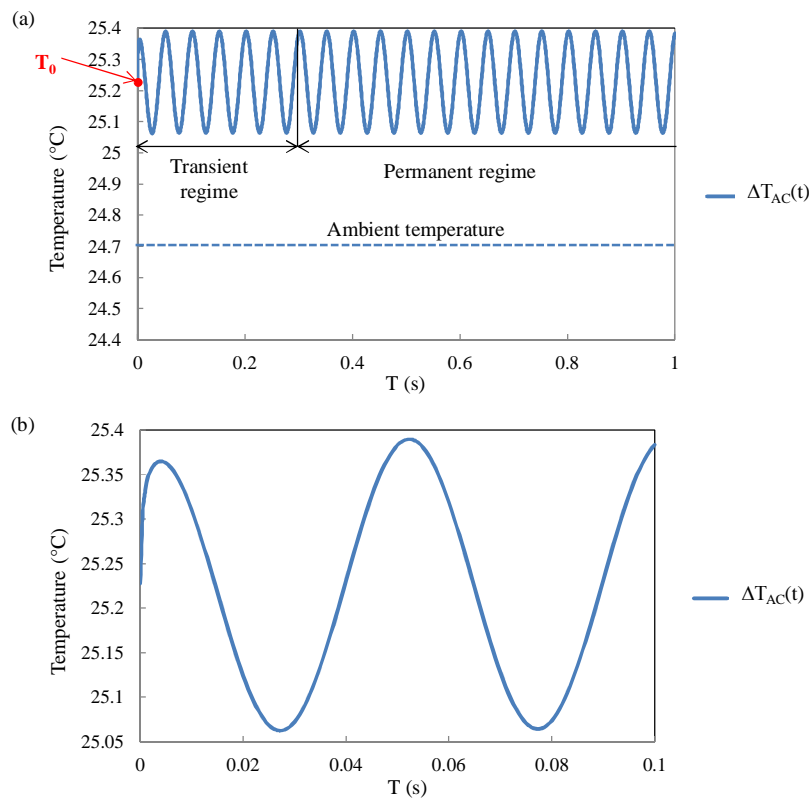


Figure 3.11: (a) Temperature evolution of the temperature oscillations ΔT_{AC} for line 2. (b) A zoom of the temperature oscillations at the beginning of the transient regime.

Figure 3.11(b) shows a zoom over temperature oscillations in the transient regime which appears at the beginning of the calculation. This transient regime is short. We have estimated that the permanent regime where the temperature oscillation variation is stable, is reached

after three periods T supplied by the generator. Therefore in this case it begins at 0.3 s. Then for times superior to $3T$, we can determine the temperature oscillation amplitude and phase with respect to the power oscillation at 2ω where the reference phase is that of the heat source $Q_b(t)$.

Having designed the structure, set the boundary and initial conditions, located a heat source, applied meshing, started the calculations and obtained the expected results, we still need to determine the amplitude and phase of the temperature oscillations at the level of the heating element. This is the last step to be considered in this simulation.

To determine the parameters A_T and ϕ_T of equation 3.2, the results in figure 3.11(a) corresponding to the permanent sinusoidal regime, are considered. The temperature oscillations $\Delta T_{AC}(t)$ represent the evolution of temperature oscillations for metallic line with respect to time at frequency 2ω .

$$\Delta T_{AC}(t) = A_T \cos(2\omega t + \phi_T) \quad (3.2)$$

The two parameters A_T and ϕ_T are adjusted in a way that equation 3.2 corresponds to the maximum possible number of points of temperature oscillations found by FEM simulations. For this purpose, we use an optimization algorithm available in the Optimization toolbox of MATLAB called “lsqcurvefit” which stands for least square curve fit [MATLAB].

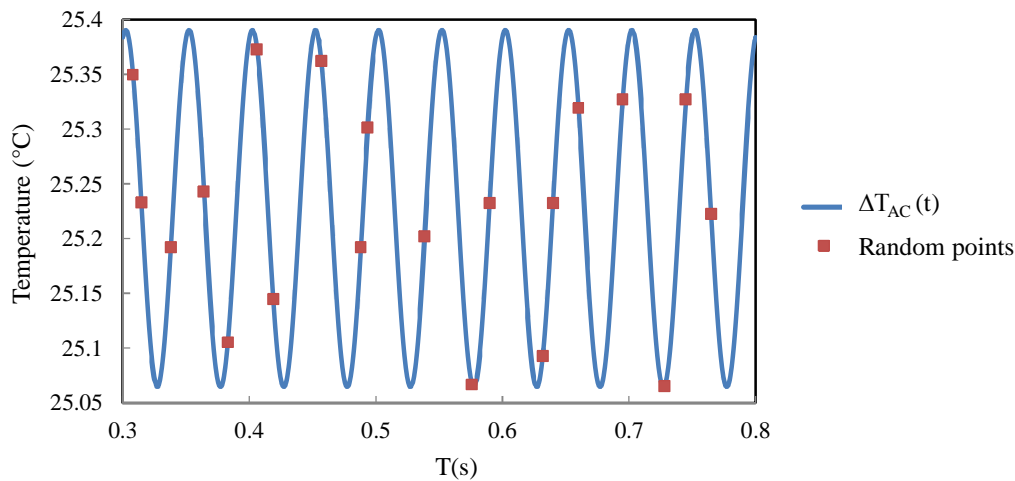


Figure 3.12: Example of random sampling that permits the determination of A_T and ϕ_T .

To calculate A_T and ϕ_T , the following procedure is applied. Initially, at the end of the transient regime at $3T$, all the points needed to perform calculations are saved for a $5T$ period of time. Therefore, for a time step $T/200$, 1000 points are obtained. Afterwards, a random sampling of hundreds of points is performed in order to determine A_T and ϕ_T using the

optimization procedure. Around 40 random draws of this set of points are done. For every random draw A_T and ϕ_T are determined and finally their average values over all the draws are calculated.

In figure 3.12, we present the temperature oscillations ΔT_{AC} and an example of random sampling of 20 points. This graph is obtained for metallic line 2 at frequency $F=10$ Hz. Thanks to the FEM simulations, A_T and ϕ_T are found to be equal to 0.163 °C and -0.283 rad respectively.

I.3.f. Validation of FEM modelling

In order to compare our numerical model to the analytical solution proposed by Cahill [CAH 1990], we study the results obtained for the temperature oscillations calculated at the level of the heating element over a large range of frequencies starting from 0.01 Hz to 1 MHz.

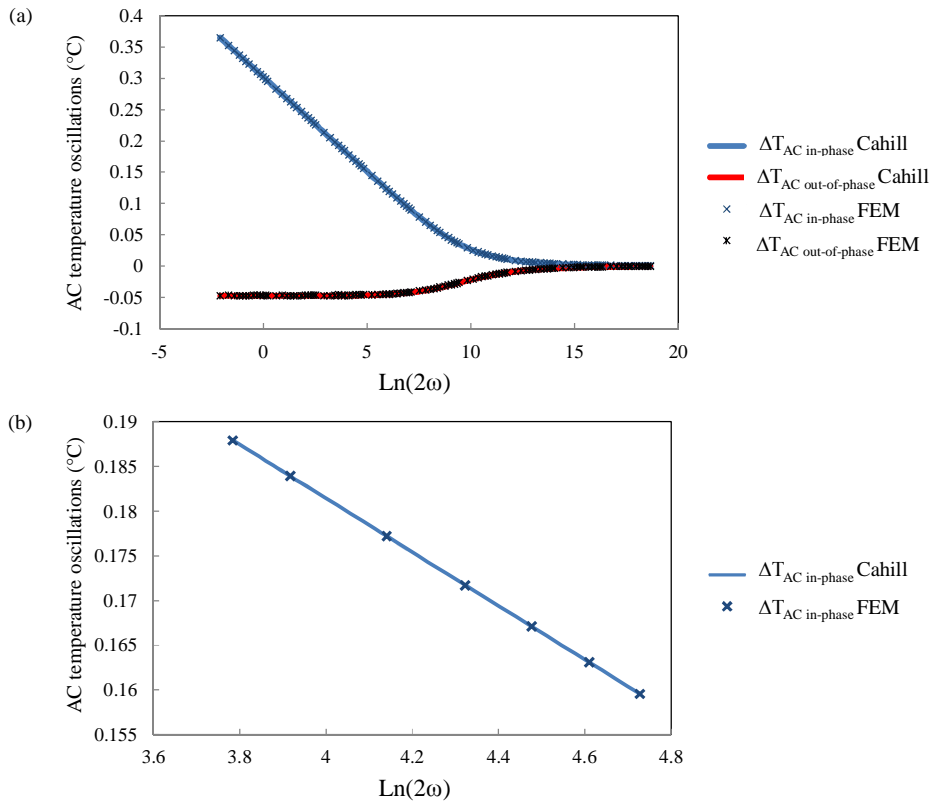


Figure 3.13: The in-phase and out-of-phase temperature oscillations plotted with respect to FEM and Cahill's solution for metallic line 2.

We can notice in figure 3.13 that the same results are obtained by Cahill's formula and the numerical modelling by FEM. This result was predictable since the structure simulated by FEM is similar to that considered in Cahill's formalism. For both theoretical studies, the same approximations are applied. In figure 3.13(b), a zoom is made on the important part of the

graph through which we can deduce the thermal conductivity of materials by the three omega method. This part of the curve corresponds to the evolution of the in-phase temperature oscillations in the linear regime. We can always notice no difference between the two results.

At this stage of the study, it is necessary to verify if the hypothesis of the uniformity of the distribution of temperature over the boundary element (infinitely thin metallic line) is correct. Till now, we always consider an average temperature on the half width of the heating element which is equal to the average temperature on the whole heating element. In figure 3.14, the evolution of temperature along the upper edge of the structure including the heating element ($y=0$ mm) is plotted at two different instants of time for metallic line 2 at $F=10$ Hz.

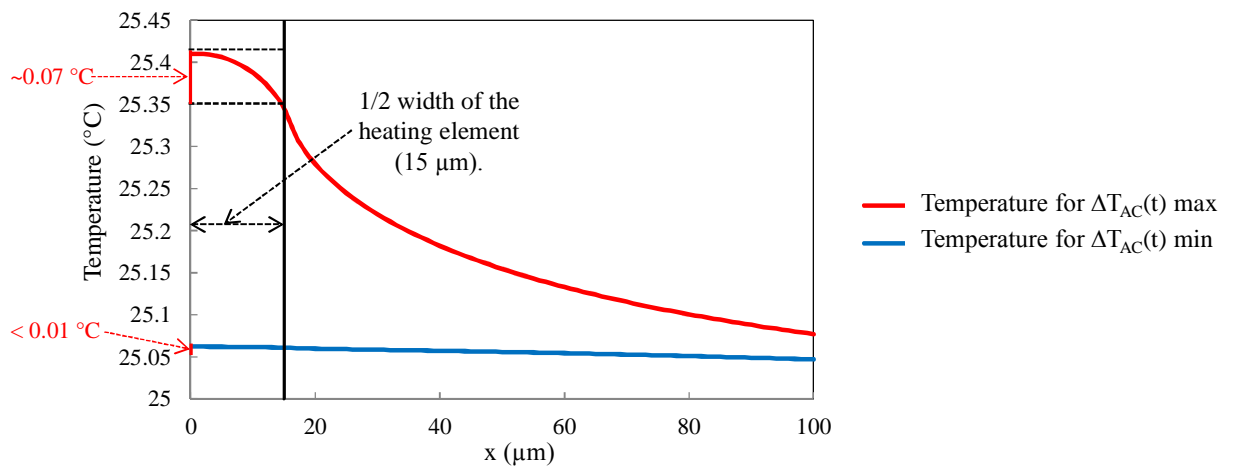


Figure 3.14: Temperature at two instants of time at $y=0$ mm.

The plot in red corresponds to the temperature when $\Delta T_{AC}(t)$ is maximum while the one in blue is plotted for $\Delta T_{AC}(t)$ minimum (see figure 3.11(a)). When $\Delta T_{AC}(t)$ is maximum, the variation in temperature at a distance equal to the half width of the heating element ($b=15 \mu m$) from the axis of symmetry is around $0.07 \text{ } ^\circ\text{C}$. However, when $\Delta T_{AC}(t)$ is minimum, the temperature variation is inferior to $0.01 \text{ } ^\circ\text{C}$. The average values of temperature are calculated for both instants of time (minimum and maximum $\Delta T_{AC}(t)$) and are found to be equal to $25.39 \text{ } ^\circ\text{C}$ and $25.06 \text{ } ^\circ\text{C}$ respectively.

As a result, the temperature all along the width of the heating element is found to be uniform. Consequently our results are identical to Cahill's solution which also consists in calculating the average temperature over the metallic line in order to determine $\Delta T_{AC}(t)$. As the frequency decreases, the temperature of the heating element becomes less uniform whereas it is more uniform as the frequency increases.

We present in the following figures the thermal patterns of a half structure obtained at the instants when $\Delta T_{AC}(t)$ is maximum (figure 3.15) and minimum (figure 3.16).

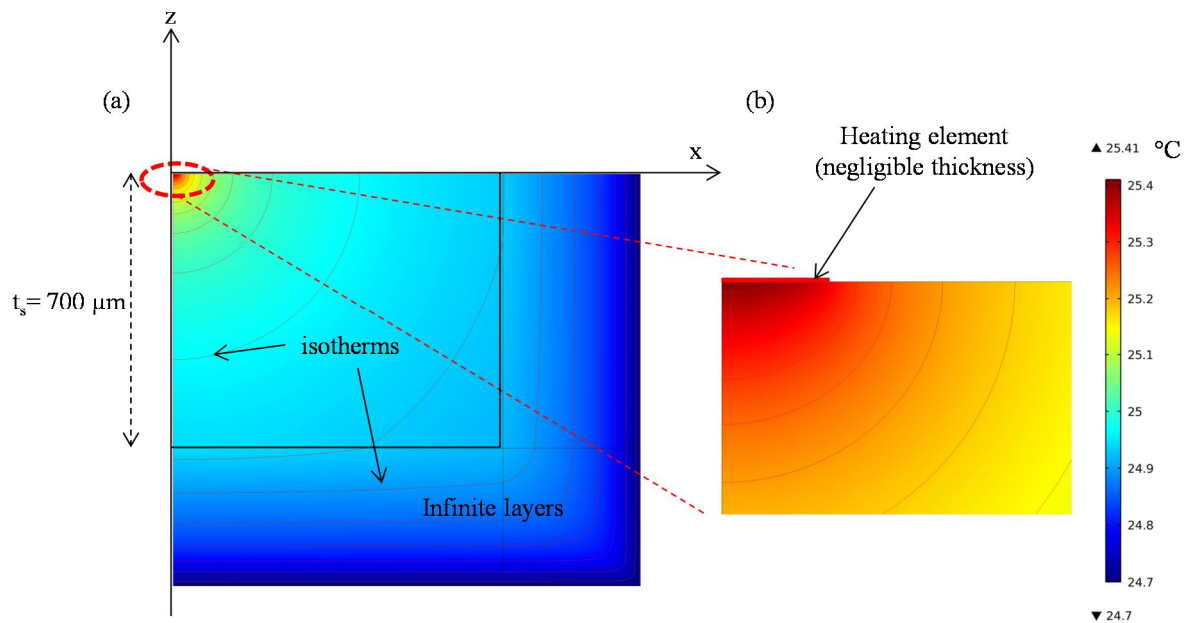


Figure 3.15: (a) Thermal pattern of a half structure at ΔT_{AC} maximum. (b) A zoom around the heating element.

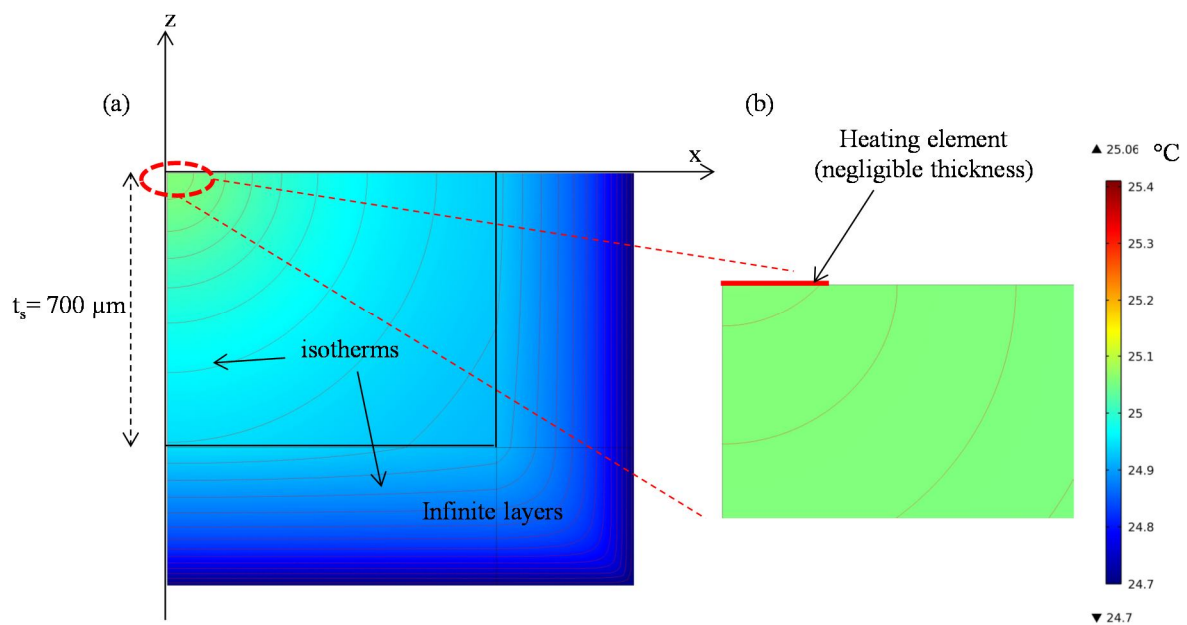


Figure 3.16: (a) Thermal pattern of a half structure at ΔT_{AC} minimum. (b) A zoom around the heating element.

We can notice a very low rise in temperature, inferior to 1°C , with respect to the initial temperature ($T_0 = 24.7^{\circ}\text{C}$) as previously noted in figure 3.11(a). Moreover, we can observe a

very small “hot” zone of low thickness situated under the heating element. Also, the isotherms shown in the substrate are perfectly circular proving the effectiveness of the “infinite” layers applied during the simulations. However at the level of the “infinite” layers these isotherms become parallel, indicating the presence of planar thermal waves in this zone.

I.4. Modelling improvement

In this section the influence on the AC temperature oscillations of different parameters related to the structure are studied. First, the effect of a finite thickness substrate is examined. Simulations are performed for a metallic line of different widths deposited on material and the results are compared to Cahill’s solution. Similarly, the variation of the metallic line thickness is investigated. Finally, the real structure is simulated considering heat convection at the surface of substrate placed on a thick copper plate.

I.4.a. Influence of a finite thickness substrate

In the analytical solution proposed by Cahill, the approximation which seems to be questionable is the fact that the metallic line must be deposited on a semi-infinite substrate. Therefore, the influence of a substrate of finite thickness on the amplitude of temperature oscillations is initially studied for that purpose. The “infinite” layers discussed in the previous studied structure are removed. Consequently, a boundary condition must be set at the structure’s limits (figure 3.17). An isothermal condition considering a constant room temperature is selected. This condition is considered to be the most appropriate since the substrate is placed over a thick copper plate where the temperature is said to be quasi constant throughout the measurements. The influence on the heat transfer inside the structure initially appears at the substrate boundary situated just under the heating element. At the upper side of the substrate, thermal isolation boundary condition is set. Also, the thickness of the metallic line is considered to be infinitely thin.

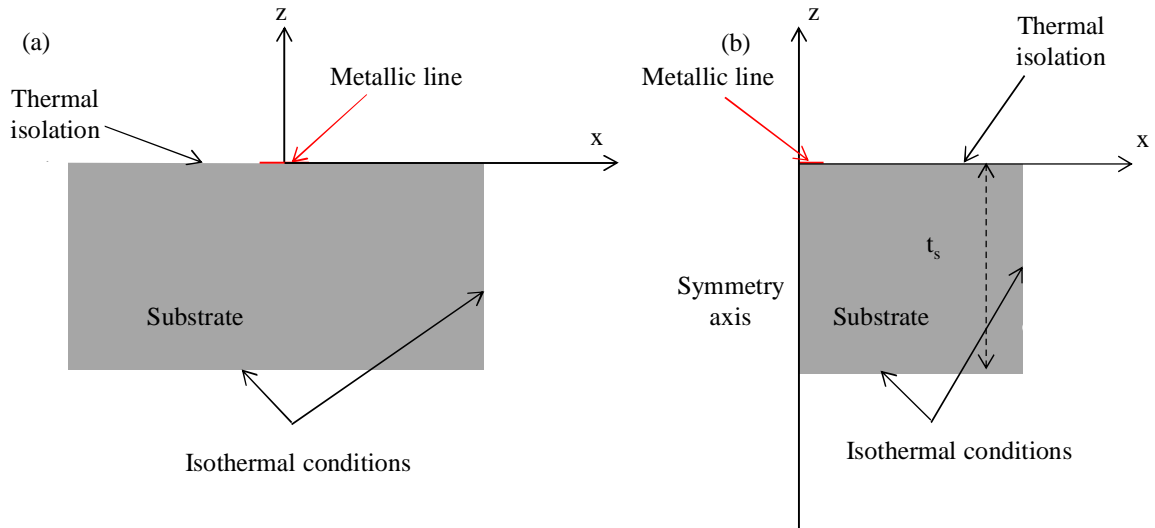


Figure 3.17: (a) Structure to be simulated with isothermal conditions. (b) Symmetry condition.

Figure 3.18 represents the thermal pattern obtained for these simulation conditions for metallic line 2 at frequency $F=10$ Hz. We recall that the thickness of the substrate is equal to $700\ \mu\text{m}$. We can notice the influence of the isothermal condition at the lower boundary of the substrate. Moreover, we can observe the flattening of the isotherms as we approach to this boundary.

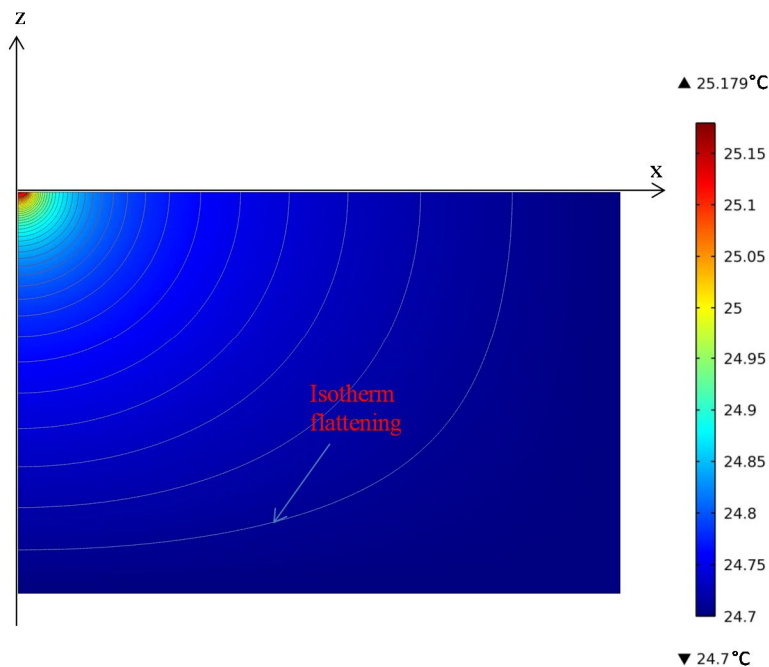


Figure 3.18: Isotherm flattening due to the isothermal condition at the lower boundary of the substrate.

By applying the methods presented in section 1.3. of this chapter, we can calculate the temperature oscillations at the level of the metallic line for a large range of frequencies

starting at 0.01 Hz up to 1 MHz. The results are compared to those calculated by Cahill's solution (figure 3.19).

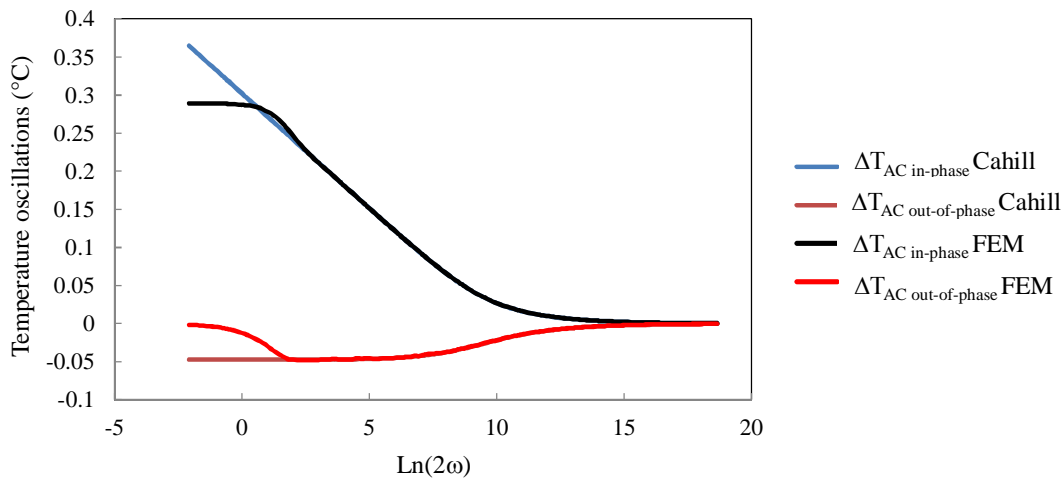


Figure 3.19: Temperature oscillations of a structure of finite thickness simulated using FEM compared to Cahill's solution ($t_s = 700 \mu\text{m}$).

The influence of the finite thickness of the substrate on the in-phase and out-of-phase temperature oscillations at low frequencies is clearly noticed. At these frequencies, the in-phase temperature oscillation obtained by FEM are constant while the out-of-phase one tends to zero and consequently, the phase shift no more exists between the temperature oscillations and the heat source. When getting higher in frequency, we can observe that the temperature oscillations calculated by Cahill's analytical formula and the finite element method are equal.

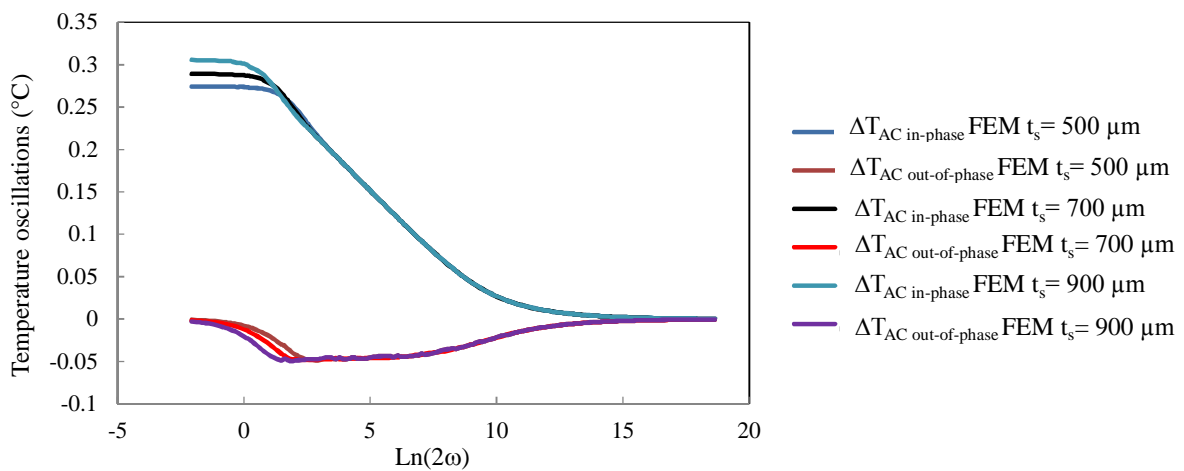


Figure 3.20: Temperature oscillations obtained by FEM for 500 μm , 700 μm and 900 μm thick substrate.

In order to better understand this phenomenon at low frequencies, we present in figure 3.20 a comparison between the temperature oscillations previously obtained for a 700 μm thick BrSiO_2 substrate and those calculated for two other substrate thicknesses, 500 μm and 900

μm . Metallic line 2 is used in this study. The parameters used to obtain each plot are all identical except for the thickness of the substrate.

We can observe that the larger is the thickness of the substrate the closer are the temperature oscillations obtained by FEM to those calculated by Cahill's analytical formalism. This phenomenon at low frequencies explains the existence of a lower frequency limit (see chapter 1) for the linear regime through which we can deduce the thermal conductivity of substrate. The frequency limits of the linear zone have been defined in chapter I. The lower frequency limit is inversely proportional to the thickness t_s of the substrate. The lower is the substrate thickness the higher is this frequency limit resulting in a smaller range of frequencies in the linear zone.

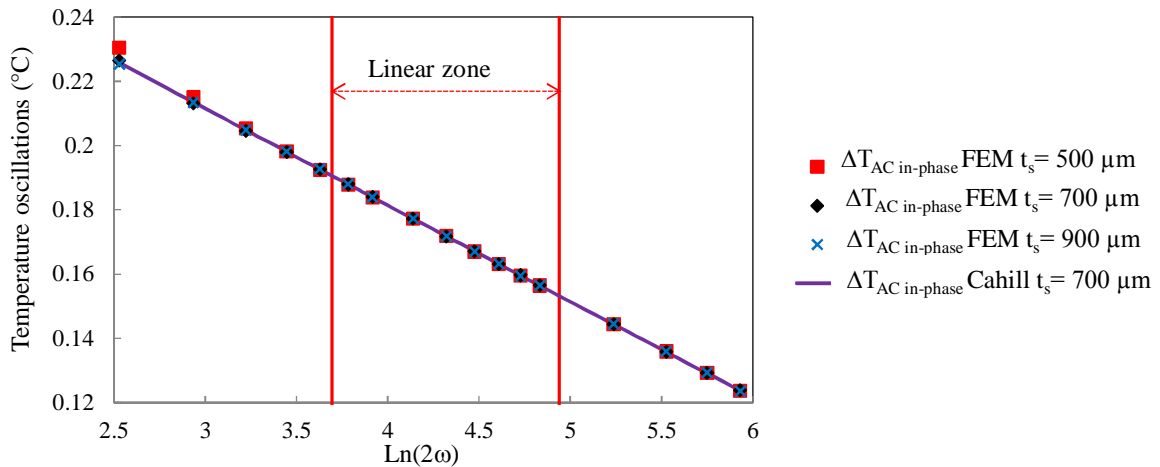


Figure 3.21: The in-phase temperature oscillations plotted for 500 μm , 700 μm and 900 μm thick substrate in the linear zone.

In figure 3.21, we focus on the in-phase temperature oscillations in the linear zone of metallic line 2. The linear zone upper and lower frequency limits (see chapter I) are indicated in the figure for a substrate of 700 μm thick. The in-phase temperature oscillations for the three different thicknesses mentioned previously are plotted together with Cahill's solution for a substrate thickness of 700 μm . We can notice that all the plots are superimposed which means that the substrate thickness has no influence on the results in the linear zone. Moreover, it is possible to perform measurements for frequencies slightly outside the linear zone which is defined by Cahill without affecting the value of the thermal conductivity of the substrate.

I.4.b. Influence of the characteristics of the heating element

A second study consists of determining the influence of the heating element on the AC temperature oscillations. This heating element has a width equals to $2b$, a very small thickness

($t_{\text{avg}} \sim 0.4 \mu\text{m}$), and is made of gold which, like the substrate under test, has a certain thermal conductivity.

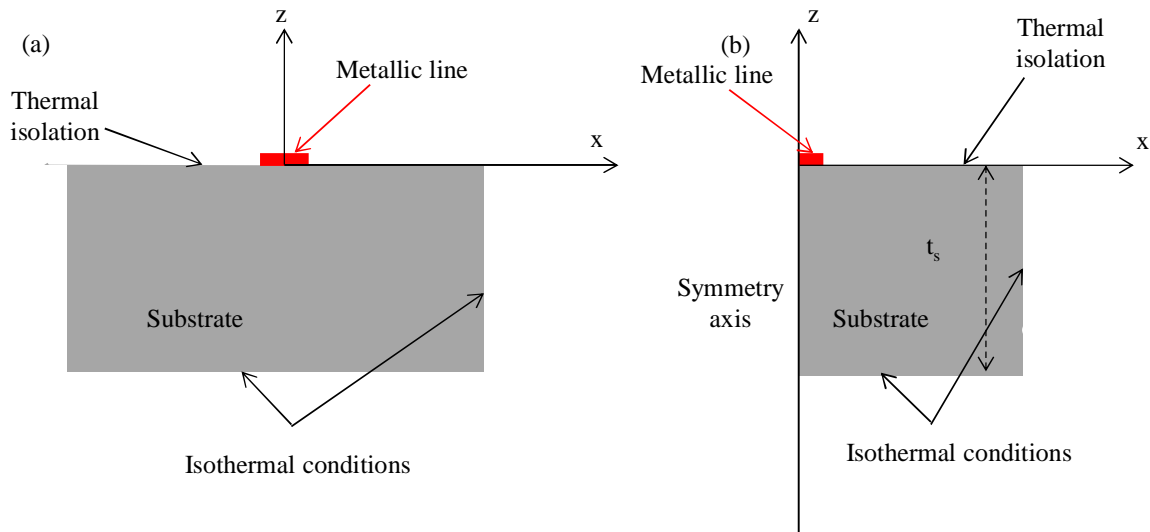


Figure 3.22: (a) The simulated structure considering the thickness of the heating element. (b) Symmetry conditions.

The structure simulated here is identical to the one presented in figure 3.17. The only difference is the addition of the heating element of a non-negligible thickness to the structure (figure 3.22(a)). As usual, in order to reduce computational time, only half of the structure is simulated (figure 3.22(b)). Also, as done for the whole structure, this element possessing a small size must be correctly meshed. Consequently, this element is decomposed into two layers of triangles (figure 3.23).

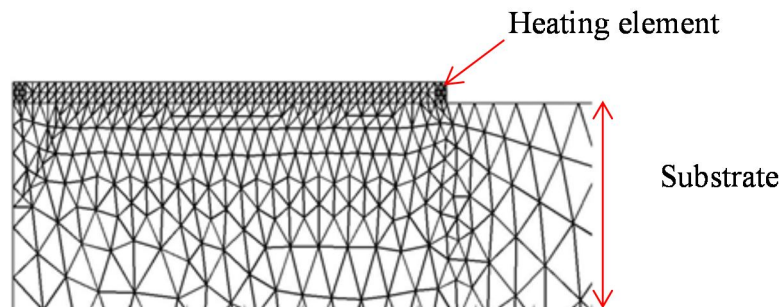


Figure 3.23: Meshing applied on the heating element.

There are two differences between the simulations performed in this study and the ones presented in section I.3, the calculation method of $\Delta T_{\text{AC}}(t)$ and the application of the heat source. Actually, $\Delta T_{\text{AC}}(t)$ is calculated by taking at every time step the average value of temperature over the lateral surface of the heating element. Moreover, the heating source can no more be considered as a thermal flux. In this study it is set as a volume heat source that

exists inside the heating element. Thereby, equation 3.1 is modified in order to express $Q(t)$ in W/m^3 .

$$Q(t) = \frac{p(t)}{l * 2b * t_{avg}} \quad (3.3)$$

Figure 3.24 presents the evolution of the temperature oscillations with respect to $\ln(2\omega)$ for three different cases. The first corresponds to the results obtained by Cahill's analytical equation. The second case considers an infinitely thin metallic line placed on the surface of a $700 \mu m$ thick substrate. The final case consists of a metallic line of thickness t_{avg} equals to $0.4 \mu m$ on a $700 \mu m$ thick substrate. The first two cases have already been presented in figure 3.19. The study done for the third case permits the evaluation of the influence of the thickness of the heating element. We can notice no influence on the out-of-phase temperature oscillations. However, we observe that the in-phase temperature oscillations plotted for the third case are a little bit lower than those obtained for the other two plots.

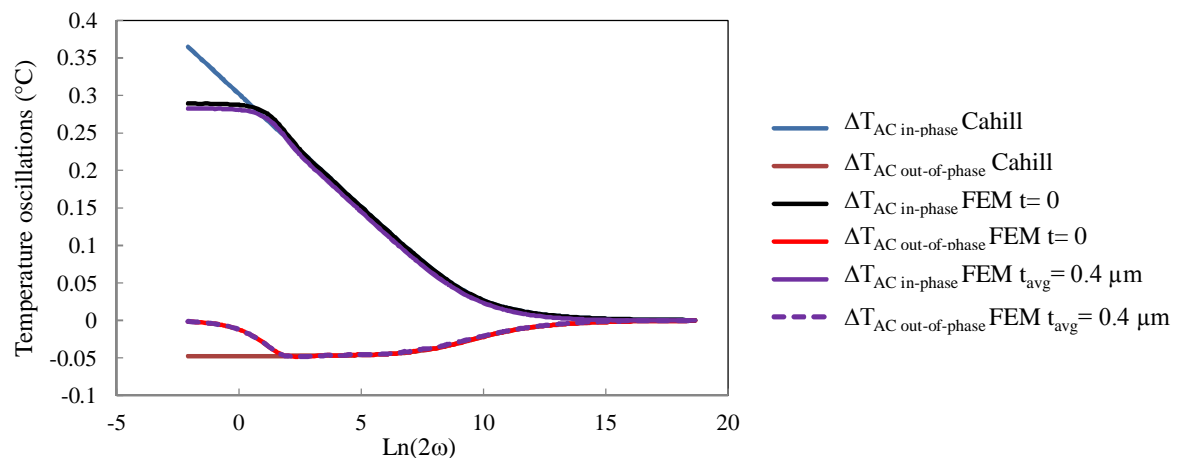


Figure 3.24: Temperature oscillations plotted for Cahill's solution and FEM simulations for an infinitely thin metallic line ($t=0$) and metallic line of thickness $t_{avg}=0.4 \mu m$.

The metallic line thickness $t_{avg}=0.4 \mu m$ considered in the preceding simulation is the same thickness obtained when depositing gold by evaporation on the surface of material under test. Measurements using a profilometer on several metallic lines have showed a certain disparity over the thickness values of deposited gold. Moreover, the thickness of gold might not be uniform all over the length of the tested metallic line. So, in order to investigate the influence of this parameter, two studies considering two different thicknesses $t_A=0.2 \mu m$ and $t_B=0.6 \mu m$ are performed. In the case of 2D modelling, the thickness stays constant throughout the length of the metallic line. The non-uniformity of the metallization thickness over the length of the metallic line can only be studied by applying 3D modelling. The results obtained for

each of the three thicknesses t_{avg} , t_A , and t_B are compared by considering the same applied power on the metallic line ($p_{\text{rms}} = 0.2487 \text{ W/m}$) and the same substrate thickness ($t_s = 700 \text{ }\mu\text{m}$). Figure 3.25 represents the in-phase temperature oscillations in the linear zone between 3.2 Hz and 11 Hz, obtained when considering three metallic line thicknesses, Cahill's solution and FEM for an infinitely thin metallic line. We observe similar results for Cahill's solution and FEM modeling (FEM $t = 0$). As the thickness of the heating element becomes superior to zero, we can notice that the in-phase temperature oscillations are slightly lower than those obtained by Cahill's formalism and FEM for an infinitely thin metallic line (FEM $t = 0$). However, the exact value of the metallization thickness of this heating element is of little importance.

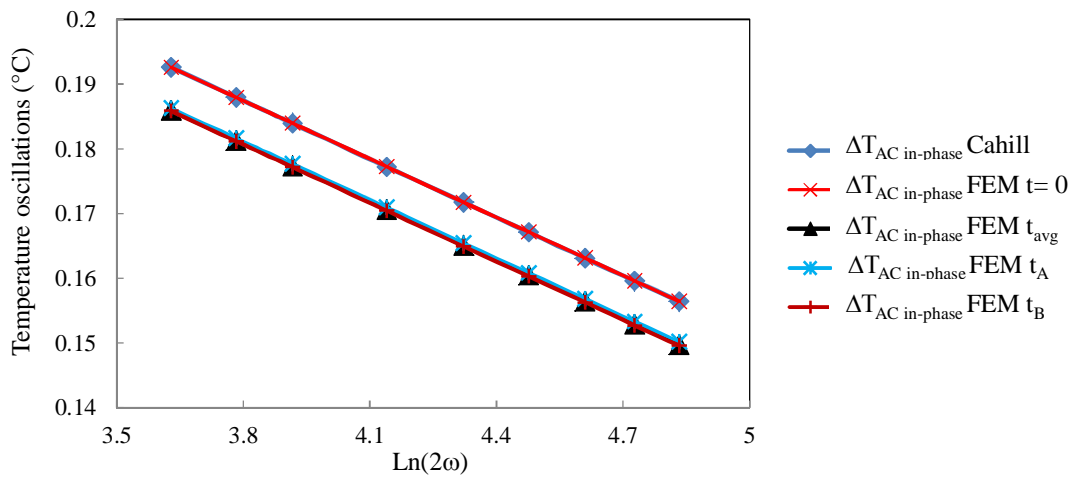


Figure 3.25: The in-phase temperature oscillations plotted for Cahill's solution and FEM with metallic line of thicknesses $t = 0$, $t_{\text{avg}} = 0.4 \text{ }\mu\text{m}$, $t_A = 0.2 \text{ }\mu\text{m}$ and $t_B = 0.6 \text{ }\mu\text{m}$.

On the other hand, the width of the metallic line fabricated by photolithography process is not strictly uniform. Therefore, we have estimated a precision of $\pm 1 \text{ }\mu\text{m}$ for the width of the deposited metallic lines. A metallic line on substrate having the same characteristics as that of metallic line 2 is numerically simulated where the width is varied from $2b_1 = 29 \text{ }\mu\text{m}$ to $2b_{\text{avg}} = 30 \text{ }\mu\text{m}$ and to $2b_2 = 31 \text{ }\mu\text{m}$. Figure 3.26 indicates that the in-phase temperature oscillations plotted in the linear regime increase as the width of the metallic line decreases and vice versa. It is important to note that the three linear plots are parallel. Consequently, the slope between the temperature oscillations and the natural logarithm of 2ω keeps its value when varying the metallic line width. Therefore, a slight inaccuracy in the width of the metallic line has no effect when determining the value of the thermal conductivity of material.

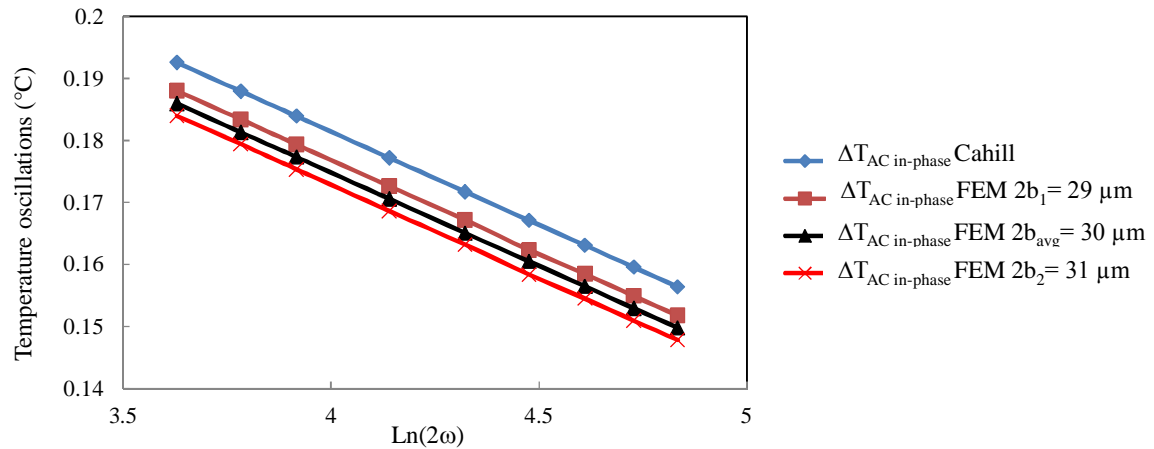


Figure 3.26: The in-phase temperature oscillations plotted in the linear regime for Cahill's solution and for FEM with three different metallic line widths.

Moreover, the heating element fabricated by photolithography is made up of gold. The thermal conductivity of gold considered throughout the study is equal to $k=317 \text{ W/m.K}$. Also, its specific heat capacity and density are set to $c_p=129 \text{ J/Kg.K}$ and $\rho=19300 \text{ Kg/m}^3$ respectively. These values correspond to bulk gold material and may not necessarily be the same for the deposited thin gold metallic line. Consequently, we have carried out two distinct studies. The first consists of a gold metallic line on substrate possessing the same physical property values (k , c_p , and ρ) mentioned just above. For the second study, we suppose that these physical property values are lower than those given for a bulk material. Therefore, we have thought of multiplying them, for example, by a factor of 0.8. Consequently the following values: $k=253.6 \text{ W/m.K}$, $c_p=103.2 \text{ J/Kg.K}$, and $\rho=15440 \text{ Kg/m}^3$ are obtained.

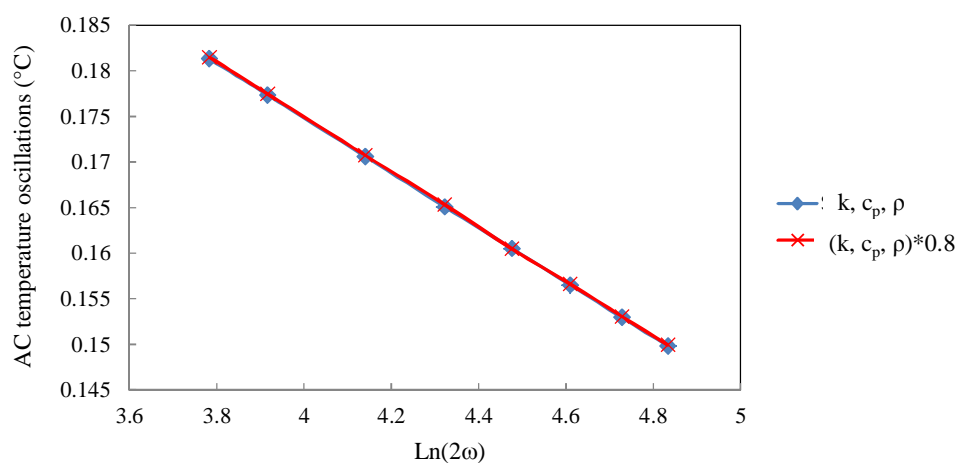


Figure 3.27: Temperature oscillations plotted for physical properties of bulk gold in blue and physical properties of bulk gold multiplied by 0.8 in red.

Figure 3.27 shows the temperature oscillations obtained by FEM for the two studies. Metallic line 2 is always considered to be the reference line of width $2b_{\text{avg}} = 30 \mu\text{m}$, thickness $t_{\text{avg}} = 0.4 \mu\text{m}$ deposited on a substrate of thickness $t_s = 700 \mu\text{m}$. We can observe that the in-phase temperature oscillations plotted for the given physical properties of bulk gold agree with those calculated for the same physical properties multiplied by a factor of 0.8. Consequently, variation in the values of the thermal conductivity, heat capacity and density of the metal deposited on the material under test has insignificant effect on the calculation of the thermal conductivity of the material under test.

I.4.c. Real structure modelling

After studying the effects of the metallic line width and thickness variation on the AC temperature oscillations and the thermal conductivity of material, a real structure model is simulated in this section. To that end heat convection at the surface of substrate and a copper plate underneath the sample similar to the one used during the experimental measurements are considered (figure 3.28(a)).

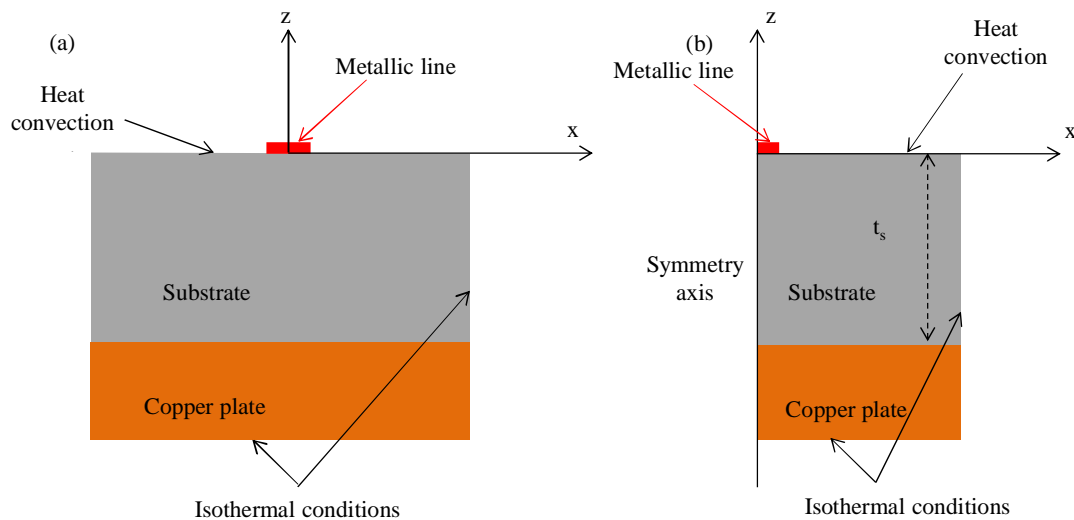


Figure 3.28: (a) The simulated structure with a substrate placed on a copper plate and a heat convection boundary condition on the surface. (b) Symmetry condition.

As in the previous numerical simulations presented during this chapter, symmetry conditions are applied to the structure as shown in figure 3.28(b). The copper plate has a thickness of 3 mm. Its thermal conductivity, specific heat capacity and density are equal to 390 W/m.K , 390 J/Kg.K , and 8960 Kg/m^3 respectively. On lateral faces and bottom of our structure, the temperature is fixed to ambient temperature. Heat is conducted inside the material; however it is convective on the upper surface of the substrate. Therefore, heat

exchange with the surrounding is presented by a coefficient of thermal convection ($H=3 \text{ W.m}^2.\text{°C}^{-1}$). It corresponds to a natural convection over a horizontal surface for a low temperature difference between the heated medium and ambient temperature.

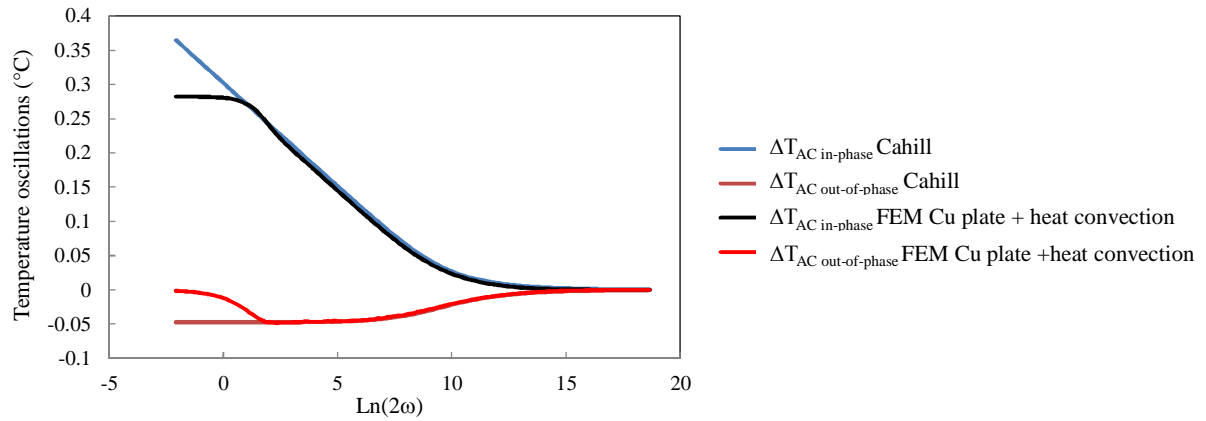


Figure 3.29: The AC temperature oscillations plotted with respect to Cahill and FEM when considering the copper plate and heat convection on the surface of substrate.

In figure 3.29, we present the AC temperature oscillations obtained by the numerical simulations performed for the real structure (Cu plate and heat convection on the surface) and by Cahill's analytical solution for a large range of frequencies. The in-phase and out-of-phase temperature oscillations for both cases are in good agreement.

We present in figure 3.30 a recapitulative of the studies performed throughout this section by plotting the in-phase temperature oscillations obtained for four FEM modellings together with Cahill's analytical solution.

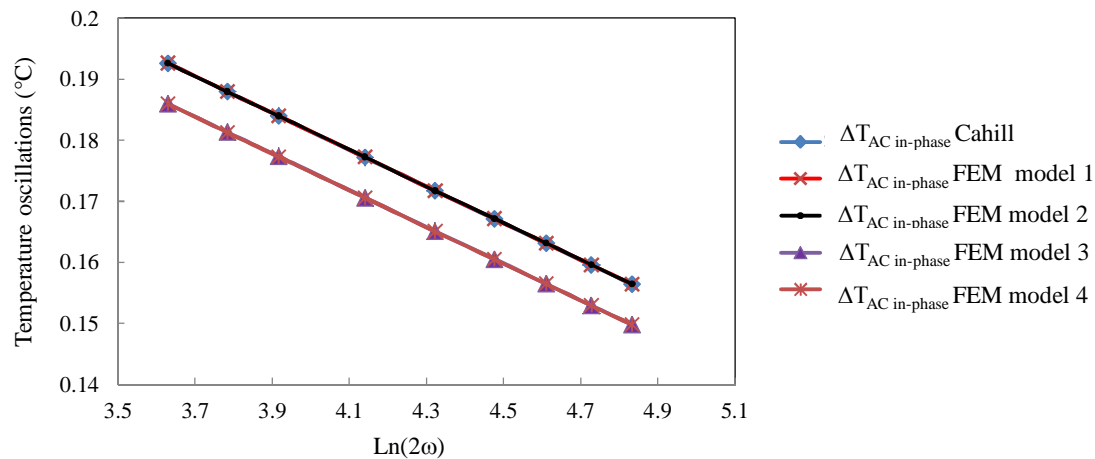


Figure 3.30: A recapitulative plot of the numerical simulations performed throughout section I.

The first model considers the constraints imposed by Cahill's formalism while the second is done for an infinitely thin metallic line but a finite substrate of $700 \mu\text{m}$ thickness. Model three takes into account the thicknesses of both the metallic line and substrate of $0.4 \mu\text{m}$ and

700 μm respectively. Finally model four represents the real structure where natural heat convection is present at the surface and the sample is placed on a 3 mm copper plate.

We can notice a good agreement between Cahill's formalism and the FEM results for models 1 and 2. As we start taking the thickness of the metallic line into consideration, the AC temperature oscillations decrease slightly as shown for models 3 and 4. The results plotted for models 3 and 4 are superimposed demonstrating that the heat convection at the surface of the substrate has no effect on the obtained AC temperature oscillations.

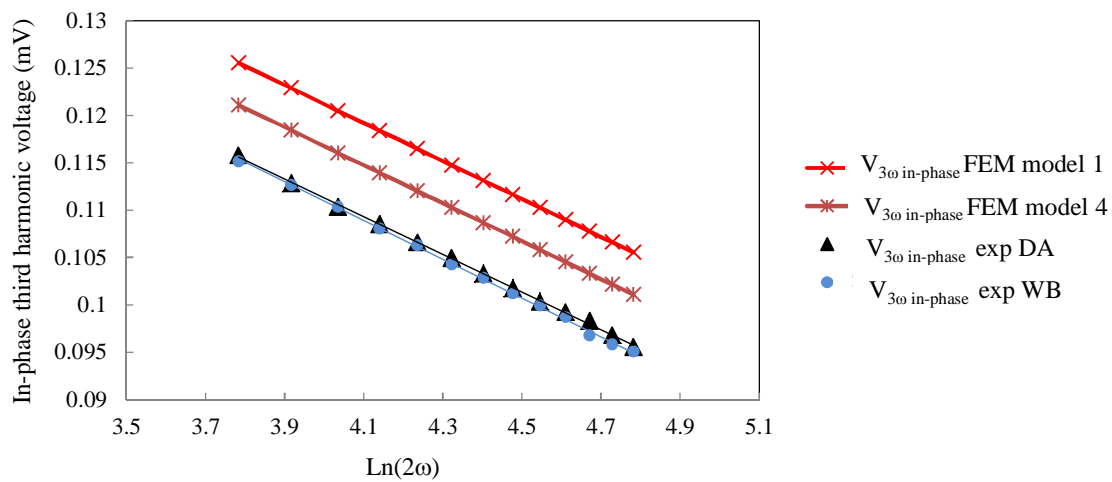


Figure 3.31: The experimental third harmonic voltages measured by WB and DA circuits compared to the theoretical ones obtained by FEM for models 1 and 2.

The in-phase third harmonic voltages measured by the Wheatstone bridge (WB) and differential amplifier (DA) circuits are compared to those obtained by FEM for models 1 and 4 (figure 3.31). The experimental measurements are closer to the results found by FEM for model 4 than those obtained by FEM for model 1. We can conclude that FEM allows to better reflect reality. Whereas, a major advantage of Chill's solution is that it is analytic. There is no need for important IT resources to simulate such solution.

At the end of the experimental measurements, the linearity slope of the in-phase temperature oscillations plotted with respect to $\text{Ln}(2\omega)$ is determined and we are able to calculate the thermal conductivity of material. In a last study we suppose that we are not sure of the values of the specific heat capacity c_p and density ρ of material used in the beginning of manipulations. We assume an error of $\pm 20\%$ on these values. Consequently, the simulations are turned on once for specific heat capacity and density multiplied by a factor of 0.8 and another by a factor of 1.2.

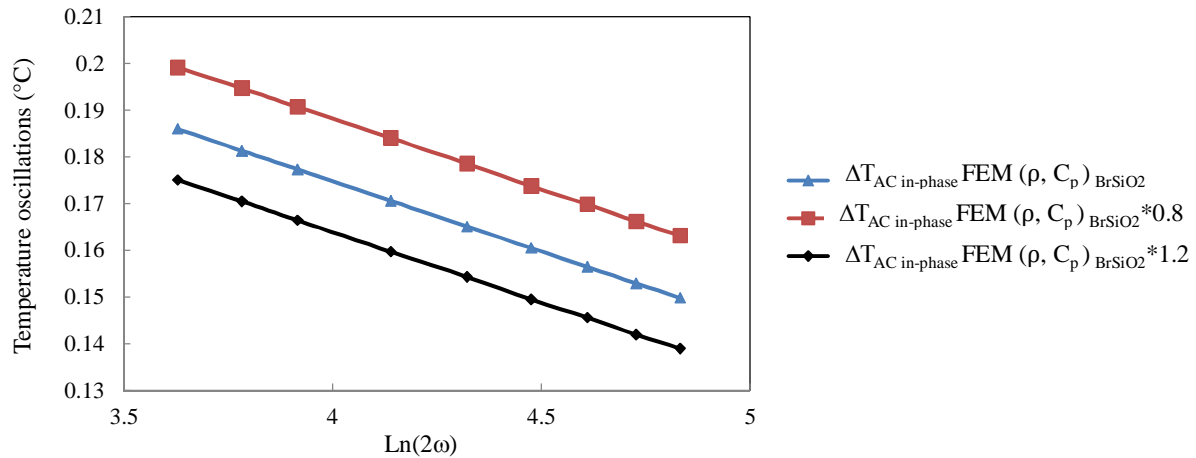


Figure 3.32: The AC temperature oscillations obtained when multiplying both BrSiO_2 density and specific heat capacity by 0.8 and 1.2.

We can notice in figure 3.32 an increase in the in-phase temperature oscillations for a density and specific heat capacity lower than the original values used at the beginning of the experimental measurements and vice versa. Moreover, we observe similar slopes for the three linear graphs plotted in the linear regime. Consequently, one can conclude that the inaccuracy in the values of the density and specific heat capacity of material under test do not affect the calculated thermal conductivity.

I.5. Conclusion

Numerical simulations using finite element method were briefly described. The different steps applied on a given structure to perform modelling by FEM were also defined. Numerical simulations were performed to study the assumptions of Cahill's solution on a metallic line-on-substrate system. This study was done for metallic line 2 deposited on borosilicate substrate. Initially, "infinite" layers are added to the simulated structure to represent a semi-infinite substrate. Then, a boundary element is placed on the surface of the substrate which behaves as a heat source. Meshing is applied to the structure and afterwards the simulations are turned on to calculate the AC temperature oscillations. Actually, two studies, stationary and time dependent, were performed to reduce the computational time when calculating ΔT_{AC} . The stationary study final results are considered to be the initial conditions for the time dependent investigation. The results obtained for the simulated structure holding Cahill's constraints agreed very well with those given by Cahill's analytical solution. The effects of a finite substrate and of the characteristics of the heating were examined with respect to Cahill's solution. The influence of a finite substrate appears at low frequencies. At these frequencies, we observe that the in-phase temperature oscillation stays constant and the out-of-phase one

tends to zero. The non-zero metallic line thickness showed a decrease in the temperature oscillations. However, the variation of the thickness of the substrate has no effect on the slope in the linear zone. The inaccuracy in the value of the physical properties of both the heating element and the material under test was found to be of insignificant effect. The real structure considering the heat convection on the surface of the substrate is finally simulated. The substrate is placed on a copper plate similar to the one used during the experimental measurements. We found out that the addition of heat convection condition at the surface of material does not affect the results.

II. Application to a two layer model

II.1. Introduction

Free standing thin films are extensively used in many applications such as microelectronic [HOR 2010], micromechanical systems (MEMS) [MAI 2009] and thermoelectric [FAN 2006]. One of the crucial parameters linked to the electronic device performance is the thermal conductivity. Actually, the thermal conductivity of thin films is smaller than that of bulk substrates of the same material. This is due to a variety of reasons including size effects and structure imperfections [CAH 2003]. Many methods have been used to measure the thermal conductivity of thin films among which the three omega differential technique has been widely used. The first extension of the three omega method was proposed in 1994 by Cahill. He has measured the thermal conductivity of thin films deposited on the surface of a substrate. Specifically he was able to determine the thermal conductivity of sputtered a-Si:H thin films of thicknesses between $0.2 \mu\text{m}$ and $1.5 \mu\text{m}$ on MgO substrate using the 3ω differential technique [CAH 1994]. In this section, the thermal conductivity of a 180 nm thick SiO_2 thin film placed on a boron doped silicon substrate is determined. Also, the thermal conductivity of a 250 nm epitaxial grown layer on GaAs substrate is measured using the 3ω differential technique. Finally, the experimental results are compared to theoretical data obtained by FEM method.

II.2. The 3ω differential technique

Let us consider a thin film of thickness t_f and thermal conductivity k_f deposited on the surface of a substrate of thickness t_s and thermal conductivity k_s (figure 3.33).

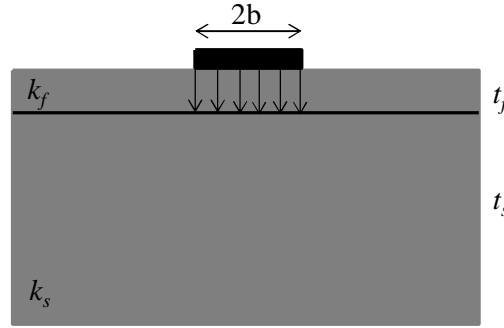


Figure 3.33: A thin film of thermal conductivity k_f deposited on a substrate of thermal conductivity k_s .

When the film thickness t_f is far smaller than the width of the heater $2b$ ($t_f \ll 2b$), a one dimensional heat flow will occur perpendicular to the film/heater interface.

Moreover, if the thin film thermal conductivity k_f is smaller than the substrate's thermal conductivity k_s ($k_f \ll k_s$), the thin film can be considered as an added thermal resistance.

Consequently, a frequency independent temperature rise ΔT_f due to the thin film adds to the in-phase temperature oscillations across the metallic line. This temperature rise can be expressed as the heat flux amplitude multiplied by the resistance of the thin film [BOR 2001, TON 2006].

$$\Delta T_f = \frac{p_{rms}}{2b} * R_f = \frac{p_{rms}}{2b} \frac{t_f}{k_f} \quad (3.4)$$

where p_{rms} is the rms power per unit length in W/m.

$2b$ is the width of the metallic line in meters.

R_f is the thermal resistance of the thin film in $m^2 \cdot K/W$.

t_f is the thickness of the thin film in meters.

k_f is the thermal conductivity of the thin film in W/m.K.

The temperature ΔT_{AC} at the level of the metallic line is expressed as:

$$\Delta T_{AC} = \Delta T_s + \Delta T_f \quad (3.5)$$

where ΔT_s is the temperature rise due to substrate.

ΔT_f is the temperature rise due to thin film.

The temperature rise ΔT_f due to thin film is a real value consequently increasing the in-phase part of the temperature oscillations ΔT_s . The result is the complex (in-phase and out-of-phase) temperature oscillation ΔT_{AC} .

Initially, the third harmonic voltages are measured for a film-on-substrate structure. The in-phase third harmonic voltage decreases linearly with respect to $\ln(2\omega)$ and the out-of-phase voltage is constant all over the linear zone. The slope of $V_{3\omega \text{ in-phase}}$ versus $\ln(2\omega)$ yields the thermal conductivity k_s of the substrate. The temperature response ΔT_{AC} of a film-on-substrate system is deduced from the measured in-phase third harmonic voltages (equation 1.33). These temperature oscillations ΔT_{AC} are then plotted with respect to $\ln(2\omega)$. Then, the temperature rise due to the substrate is either measured (if the substrate alone is available) or calculated by using Cahill's formula considering the value of the substrate thermal conductivity k_s calculated previously. The difference between the two responses leads to the temperature rise due to the presence of the thin film and the thermal conductivity k_f can be determined (figure 3.34).

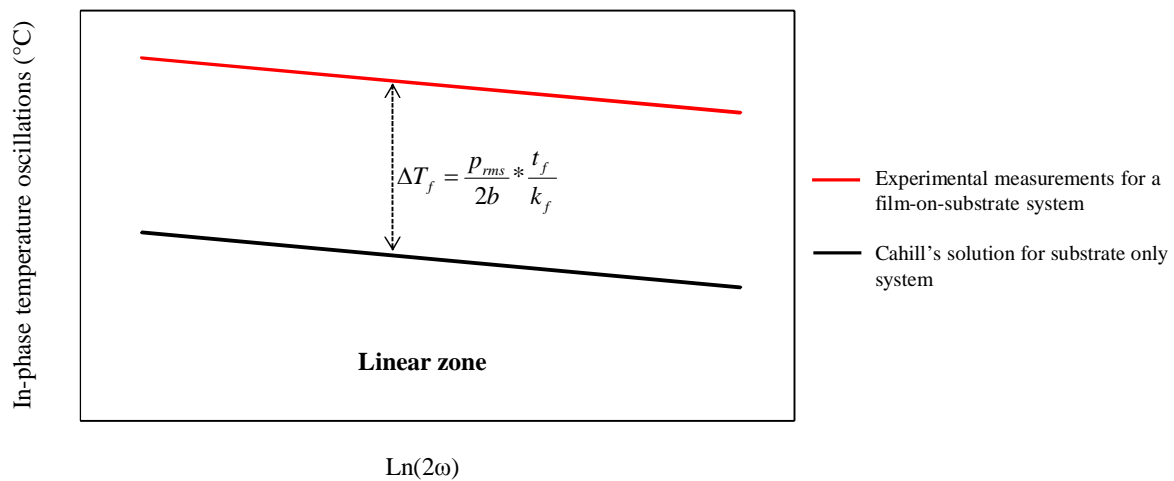


Figure 3.34: Determining the temperature rise ΔT_f through which we can calculate the thermal conductivity of thin film.

II.3. Measurement of the thermal conductivity of a SiO_2 thin film

In chapter 2, the thermal conductivity of high resistivity silicon has been measured using the three omega method. It was found to be 163 W/m.K. The sample used here is boron doped silicon substrate of thickness $t_s = 380 \mu\text{m}$. Its electrical resistivity is given by $\rho = 0.0014 \Omega \cdot \text{cm}$. An SiO_2 dielectric layer of unknown thermal conductivity k_f is deposited over this Si doped substrate. The SiO_2 layer is of a thickness $t_f = 180 \text{ nm}$.

The three omega method cannot be performed directly on an electrically conductor material. This causes a leak in the current applied on the metallic line inside the conducting material leading to false measurements. In our case, since the Si boron doped substrate is of

low electrical resistivity, a SiO_2 dielectric layer is deposited on its surface to prevent current leakage through the sample.

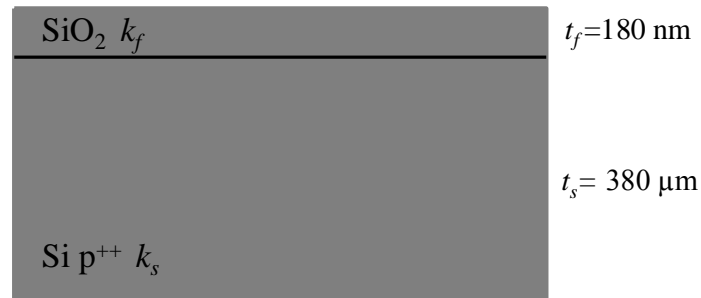


Figure 3.35: SiO_2 thin film over Si doped substrate.

Figure 3.35 shows a SiO_2 film deposited over p-type Si substrate. The resistivity $\rho = 0.0014 \Omega \cdot \text{cm}$ of p-type Si corresponds to impurity concentration $p \sim 10^{20} \text{ atom/cm}^3$. Different works have been done to measure the thermal conductivity at 300 K of impure silicon with different doping levels. For example, Slack has used a steady state longitudinal heat flow method to determine the thermal conductivity of boron doped silicon. He found thermal conductivities of 50 W/m.K and 40 W/m.K for impurity concentration of $3 \times 10^{20} \text{ atom/cm}^3$ and $5 \times 10^{20} \text{ atom/cm}^3$ respectively [SLA 1964]. Moreover, Asheghi et al. have theoretically interpreted the thermal conductivity value of boron doped silicon with different concentrations [ASH 2002]. For $p = 10^{19} \text{ atom/cm}^3$ and $p = 10^{20} \text{ atom/cm}^3$, the thermal conductivity was calculated to be around 100 W/m.K and 80 W/m.K respectively.

In this study, different metallic lines are deposited on the surface of the sample using photolithography. The three omega method was applied on different metallic lines among which are those presented in table 3.2.

Table 3.2: Properties of metallic lines deposited on boron doped Si substrate.

Metallic line	$2b$ (μm)	l (mm)	R_0 (Ω)	p_{rms} (W/m)	β ($^\circ\text{C}^{-1}$)	T_0 ($^\circ\text{C}$)
13	10	5	30.05	24.14	0.00348	24.7
14	20	8	23.74	7.37	0.00362	19.2
15	20	3	9.59	31.97	0.00347	24.7

The in-phase and out of phase third harmonic voltages are measured for metallic lines 13, 14, and 15 over the linear zone as presented in figure 3.36.

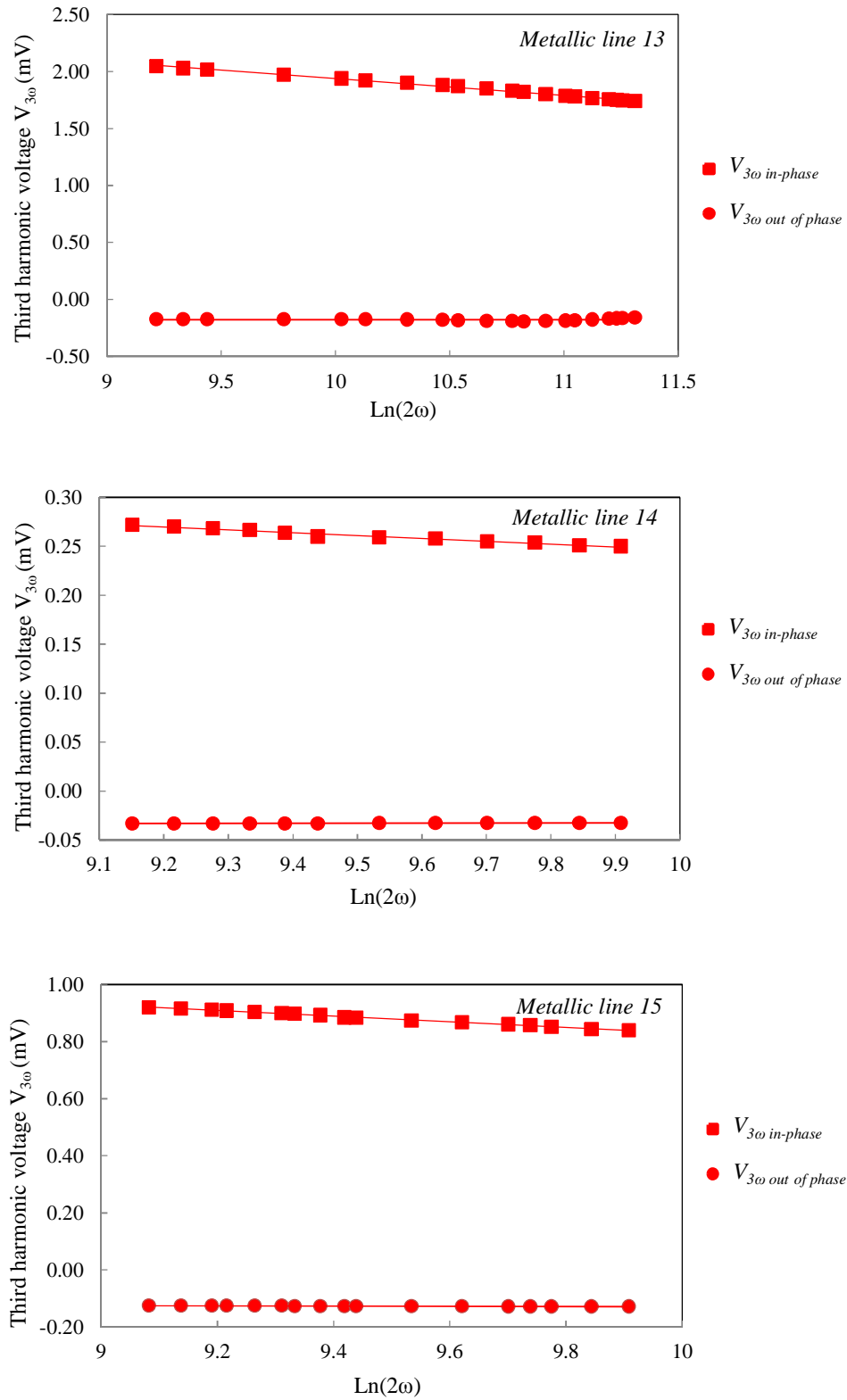


Figure 3.36: The in-phase and out-of-phase third harmonic voltages for lines 13, 14, and 15.

Table 3.3 presents the thermal conductivity values obtained for metallic lines 13, 14, and 15.

Table 3.3: Thermal conductivity values measured using lines 13, 14, and 15.

Metallic line	13	14	15
Thermal conductivity k_s (W/m.K)	86.11	86.55	84.76

For carrier concentrations p of around 10^{20} atom/cm³, the average thermal conductivity of the boron doped silicon substrate measured using the three omega method was found to be $k_{s \text{ avg}} = 85.81$ W/m.K. We can notice that this value is in good agreement with Asheghi et al. interpretations for a carrier concentration of $p = 10^{20}$ atom/cm³ [ASH 2002].

In order to calculate the thermal conductivity of SiO₂ film, the temperature oscillations ΔT_s over the boron doped Si substrate are calculated according to Cahill using MATLAB for each of the metallic lines. Figure 3.37 presents Cahill's theoretical data plotted in black for metallic line 13. The experimental temperature oscillations are presented in red ($\Delta T_{AC} = \Delta T_f + \Delta T_s$). They are deduced from the measured third harmonic voltages using equation 3.6.

$$|\Delta T_{AC}| = \frac{2V_{3\omega}}{V_0\beta_h} \quad (3.6)$$

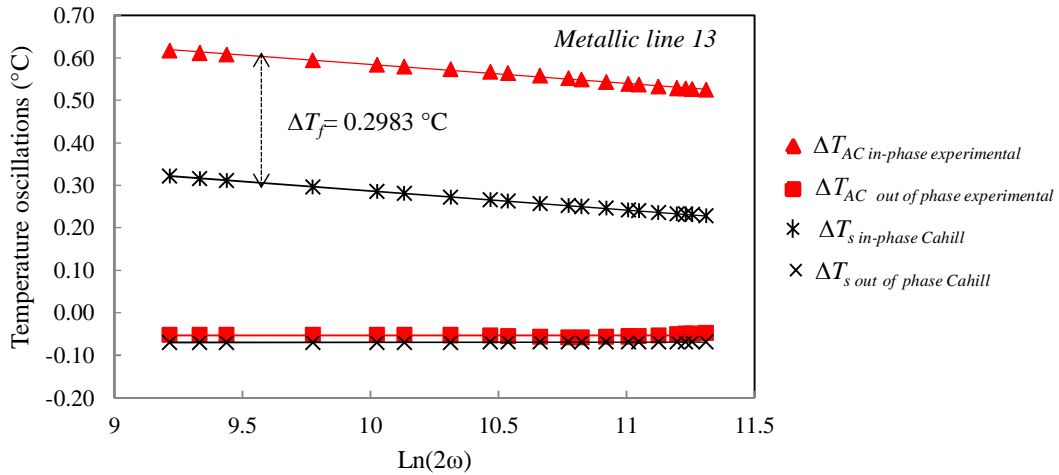


Figure 3.37: Frequency independent temperature oscillation ΔT_f for metallic line 13.

We can notice that the presence of a SiO₂ film over Si substrate produces a frequency-independent increase ΔT_f on the in-phase temperature oscillations $\Delta T_{s \text{ in-phase}}$. No change in the out-of-phase measurements is observed. Consequently, ΔT_f can be calculated as follows:

$$\Delta T_f = \Delta T_{AC \text{ in-phase}} - \Delta T_{s \text{ in-phase}} \quad (3.7)$$

The thermal conductivity of SiO_2 can then be deduced from equation 3.4. Table 3.4 represents ΔT_f obtained for metallic lines 13, 14, and 15 and the corresponding thermal conductivities. Also, the thermal resistance of the thin film is calculated.

Table 3.4: ΔT_f , k_f and R_f calculated for metallic lines 13, 14, and 15.

Metallic line	ΔT_f (°C)	k_f (W/m.K)	R_f (m ² .K/W)
13	0.2983	1.42	1.236E-7
14	0.0461	1.4	1.251E-7
15	0.2087	1.34	1.305E-7

The average thermal conductivity of SiO_2 , $k_{f \text{ avg}} = 1.38$ W/m.K, measured using Cahill's differential method agrees well with the values found in literature [LEE 1996].

After performing the three omega differential technique measurements for $\text{SiO}_2/\text{Si p}^{++}$ sample, the percentage error on the value of the thermal conductivity produced due to instrumentation measurement precision is calculated. As presented in equation 3.6, the AC temperature oscillations depend on three parameters, the third harmonic voltage $V_{3\omega}$, the initial voltage V_0 measured across the metallic line, and the temperature coefficient of resistance β_h . As explained in chapter II, the error when measuring V_0 is small and can be neglected. Only the uncertainties in the value of β_h (maximum error of $\sim \pm 6\%$) and the lock-in amplifier measurement precision of $\pm 1\%$ are taken into account (see chapter II sections V.3.c. and V.3.d.). The maximum in-phase AC temperature oscillations are calculated as follows:

$$\Delta T_{AC \text{ in-phase max}} = \frac{2V_{3\omega \text{ in-phase max}}}{V_0 \beta_{h \text{ min}}}$$

Similarly, the minimum AC temperature oscillations are obtained for minimum in-phase third harmonic voltages and maximum measured temperature coefficient of resistance β_h . Figure 3.38 shows the minimum and maximum temperature responses found due to the presence of the thin film.

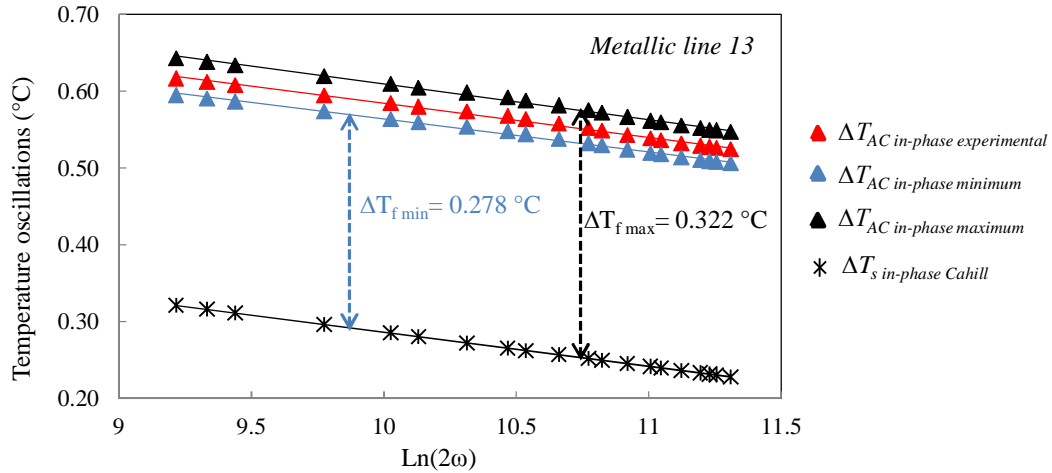


Figure 3.38: Maximum and minimum temperature responses obtained due to the thin film deposited on substrate for metallic line 13.

The following table presents the experimental, minimum and maximum values for β_h and ΔT_f and the corresponding thin film thermal conductivities k_f when the measurements are done on metallic line 13.

Table 3.5: Experimental, minimum and maximum valued of β_h , ΔT_f , and k_f (metallic line 13).

	minimum	experimental	maximum
β_h ($^\circ\text{C}$)	0.00337	0.00348	0.00357
ΔT_f ($^\circ\text{C}$)	0.2780	0.2983	0.3220
k_f (W/m.K)	1.31	1.42	1.52

The error on the measured thermal conductivity value of SiO_2 thin film is found to be around $\pm 7.3 \%$.

II.4. Measurement of the thermal conductivity of a low temperature epitaxial grown GaAs layer on GaAs substrate

In the previous section, the thermal conductivity of a SiO_2 thin film placed on boron doped Si substrate was successfully measured using the three omega method. Another thin film-on-substrate system is considered in this section where the ratio of the thermal conductivity of substrate to thin film is lower than in the case of $\text{SiO}_2/\text{Si } p^{++}$. The goal is to study the three omega differential technique for different substrate to film thermal conductivity ratios (k_s/k_f) and to examine the effect of this ratio on the AC temperature oscillations.

The sample here consists of a 250 nm epitaxial grown layer on a 470 μm GaAs substrate (Figure 3.39). Such process has been performed at low temperature (LT) and has consequently produced defects at the level of the LT GaAs grown layer. In addition, this layer possesses a high electrical resistivity of 10^{17} $\Omega\cdot\text{cm}$. The thermal conductivities of GaAs found in literature have been given in chapter II. These values vary between 46 W/m.K and 55 W/m.K at 300 K. Moreover, the thermal conductivity of a GaAs substrate has been measured in chapter II using the three omega method and was found to be 49.78 W/m.K. Jackson et al. have measured the thermal conductivity of 1 μm thick LT GaAs layer at room temperature using a self-heated photolithographic patterned aluminum wire on the surface of the sample [JAC 1999]. A value equals to 46 % of the thermal conductivity of GaAs substrate was obtained. Also, the thermal conductivities of polycrystalline grown GaAs thin films on polycrystalline chemical vapor deposition (CVD) diamond by low temperature molecular beam epitaxy have been determined using the pump probe time domain thermoreflectance method [CLA 2011]. The thermal conductivities were found to be 14.5 W/m.K, 10.4 W/m.K and 8.1 W/m.K for 1 μm , 500 nm and 100 nm thick GaAs films respectively.

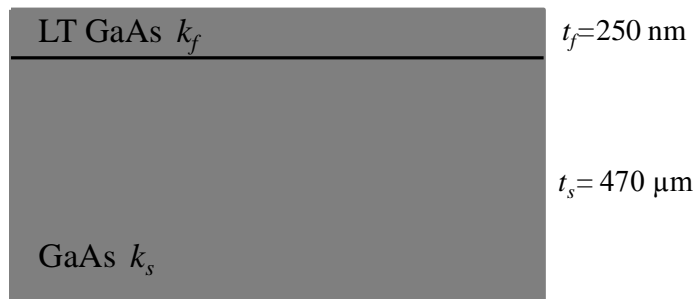


Figure 3.39: Thin film of impure GaAs deposited over GaAs substrate.

The three omega measurements are performed to retrieve the thermal conductivities of LT GaAs layer and GaAs substrate. In table 3.6 are given the properties of metallic lines 16, 17, and 18 deposited on the surface of the sample.

Table 3.6: Properties of metallic lines 16, 17, and 18.

Metallic line	$2b$ (μm)	l (mm)	R_0 (Ω)	p_{rms} (W/m)	β ($^{\circ}\text{C}^{-1}$)
16	10	6	39.88	18.99	0.00335
17	15	6.5	29.09	17.72	0.00339
18	10	5	9.59	33.43	0.00334

The in-phase and out-of-phase third harmonic voltages are measured over the linear regime frequency range as presented in figure 3.40. The thermal conductivities extracted for GaAs substrate are listed in table 3.7.

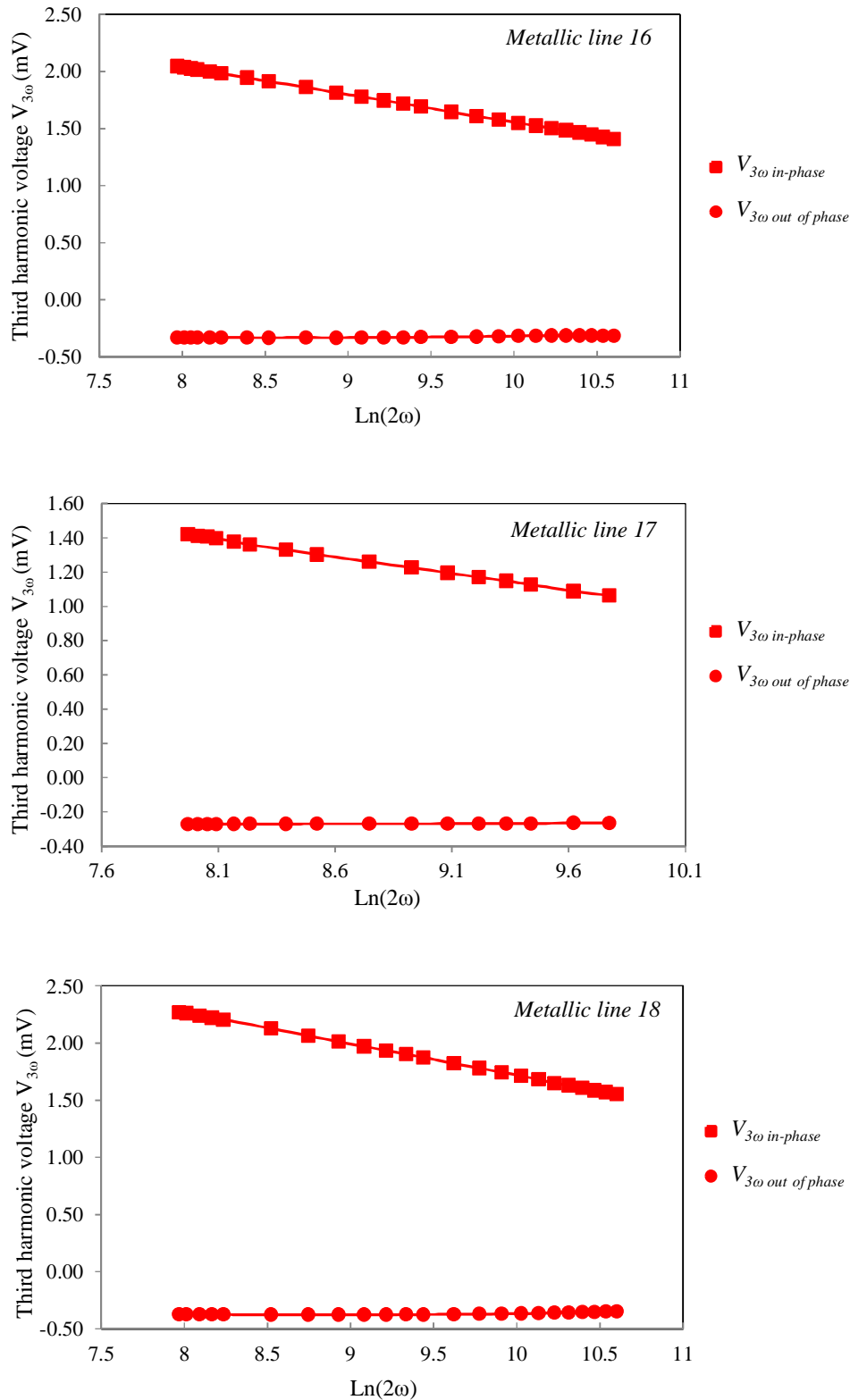


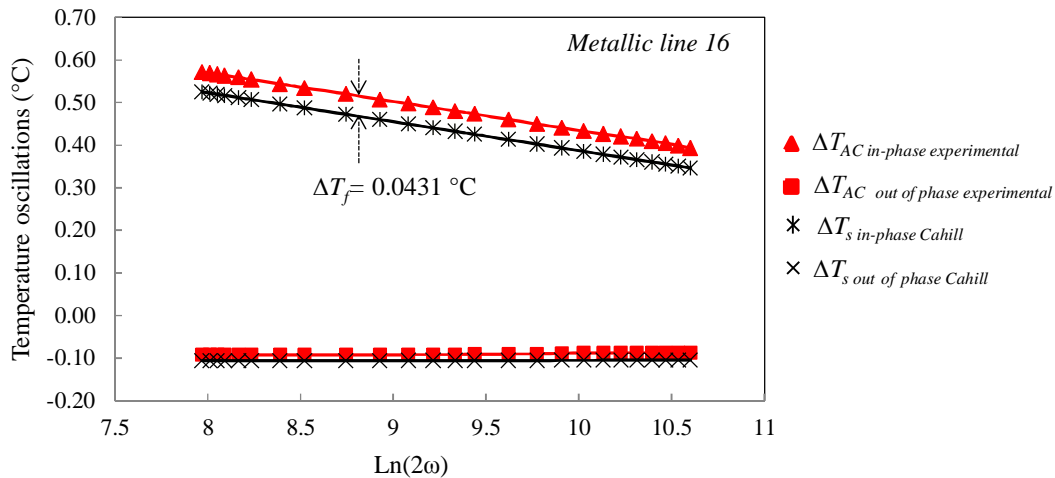
Figure 3.40: In-phase and out of phase third harmonic voltages measured by lines 16, 17, and 18.

Table 3.7: Thermal conductivities measured for GaAs substrate.

Metallic line	16	17	18
Thermal conductivity k_s (W/m.K)	44.86	44.07	44.25

The average thermal conductivity of gallium arsenide obtained is $k_{s \text{ avg}} = 44.39$ W/m.K. This value corresponds well to the thermal conductivities measured by Sze et al. [SZE 1985] and Iny at al. [INY 2003] of 46 W/m.K and 47 W/m.K respectively.

Then, the thermal conductivity k_f of LT GaAs layer is calculated by the three omega differential technique. Cahill's AC temperature oscillations ΔT_s for GaAs substrate of $k_{s \text{ avg}} = 44.39$ W/m.K are plotted in figure 3.41 for metallic line 16.

**Figure 3.41: Frequency independent temperature oscillation ΔT_f for metallic line 16.**

ΔT_f is calculated according to equation 3.7 for each metallic line and the thermal conductivity k_f (table 3.8) of LT GaAs thin layer is determined using equation 3.4. The resulting thermal resistance value is also given in the following table.

Table 3.8: ΔT_f and k_f obtained by metallic lines 16, 17, and 18.

Metallic line	ΔT_f (°C)	k_f (W/m.K)	R_f (m ² .K/W)
16	0.0431	11.02	2.269E-8
17	0.0239	12.35	2.024E-8
18	0.0505	11.48	2.177E-8

Consequently, the average thermal conductivity of the 250 nm layer of LT GaAs measured using the three omega differential technique is found to be $k_{f\text{ avg}}= 11.62$ W/m.K. The thermal conductivity of LT GaAs film is expected to be smaller than that of GaAs substrate due to the presence of defects which increase the phonon scattering inside the thin layer. The thermal conductivity of around 21 W/m.K was obtained by Jackson et al. for a 1 μm thick LT GaAs film [JAC 1999]. However, in our case we have found a smaller thermal conductivity value of $k_{f\text{ avg}}= 11.62$ W/m.K for LT GaAs layer due to its lower thickness which is equal to 250 nm. Actually, as the film thickness becomes smaller, the size effects increase producing a rise in the phonon scattering event and consequently reducing the value of the thermal conductivity [CAH 2003].

Comparing the epitaxy process performed at IEMN with the work done on epitaxial grown polycrystalline GaAs on polycrystalline CVD diamond at low temperature, we can find that the experimental conditions set for each process are not the same. Moreover, the method used to measure the thermal conductivity of polycrystalline GaAs films is pump probe time domain thermoreflectance method. Thermal conductivities of 10.4 W/m.K and 8.1 W/m.K were found for 500 nm and 100 nm thick films respectively [CLA 2011] which are not far from the value measured by the three omega method of 11.62 W/m.K for a 250 nm thick film.

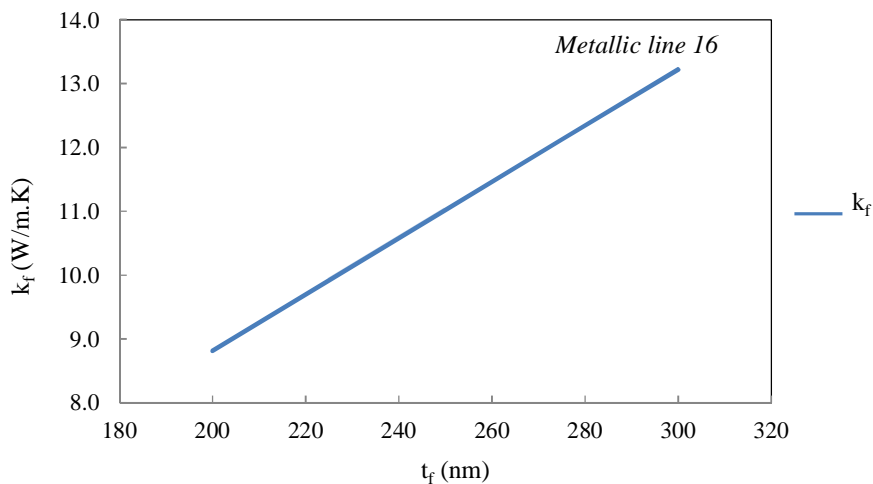


Figure 3.42: Variation of the thermal conductivity k_f of thin film with respect to thickness t_f .

The calculation for the thermal conductivity k_f of LT GaAs layer has been done for a thickness $t_f= 250$ nm. However, we are not sure of the exact thickness of the layer grown on GaAs substrate. Therefore, a study is performed by varying the thickness t_f between 200 nm and 300 nm to observe the change in the value of the thermal conductivity k_f . The temperature

rise ΔT_f due to the thin film is kept constant. We can notice in figure 3.42 that k_f increases linearly with respect to the thickness t_f according to the following equation:

$$k_f = \frac{P_{rms}}{2b * \Delta T_f} * t_f \quad (3.8)$$

The thermal conductivity k_f varies by $\pm 20\%$ for a thickness $t_f = 250 \text{ nm} \pm 20\%$. This variation is considered to be large. In conclusion, it is of great importance to measure precisely the thickness of a uniformly deposited thin film on a substrate in order to obtain an accurate thin film thermal conductivity value when applying the three omega differential technique.

Now that the thermal conductivities of the thin films SiO_2 and LT GaAs have been measured, a theoretical study based on FEM is done. This permits the comparison between experimental measurements and theoretical data obtained. Cahill's solution is also considered during this study.

II.5. Numerical simulation

Numerical simulation using finite element method is done for a thin film-on-substrate model as in the case of $\text{SiO}_2/\text{Si p}^{++}$ and LT GaAs/GaAs in the previous sections. The same steps needed to perform modelling using FEM are followed for both samples. In figure 3.43, meshing is applied on the two layer structure for $\text{SiO}_2/\text{Si p}^{++}$. We recall the thermal conductivities of the SiO_2 thin film and Si p^{++} substrate which are equal to $k_f = 1.38 \text{ W/m.K}$ $k_s = 85.81 \text{ W/m.K}$ respectively. This simulation study is done for metallic line 13.

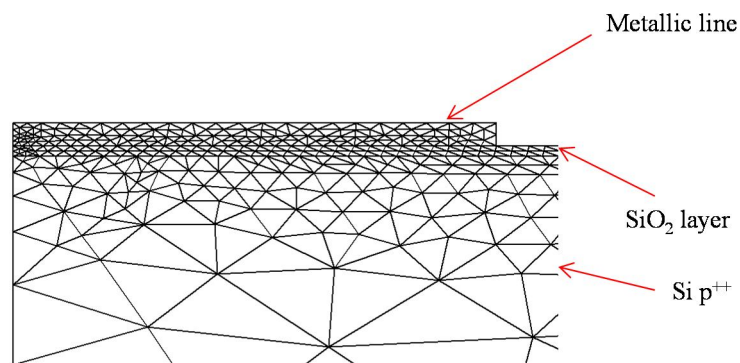


Figure 3.43: Two layer structure meshing for $\text{SiO}_2/\text{Si p}^{++}$.

Fine meshing is applied on the metallic line and the thin layer of SiO_2 . As mentioned before this produces a more reliable heat transfer modeling. FEM is done for two models, thin film on semi-infinite substrate (FEM semi-inf sub) and thin film on a substrate placed on a

copper plate (FEM sub + Cu plate). For the second model, the heat convection on the surface of substrate is taken into consideration. These two models are compared to Cahill's solution when considering the thin film-on-substrate on one hand (Cahill + ΔT_f) and a substrate-only system on the other hand. This comparison is presented in figure 3.44.

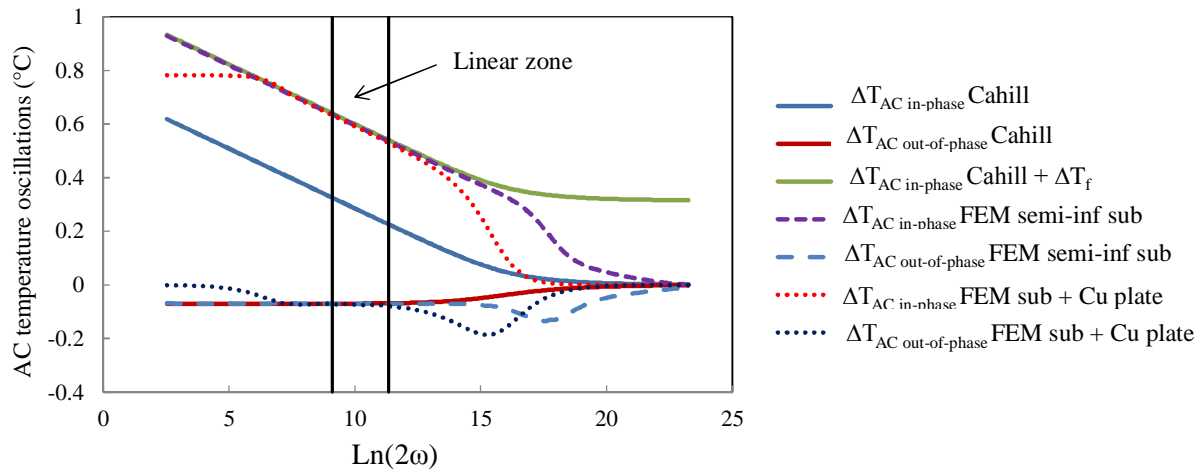


Figure 3.44: Comparison of AC temperature oscillations with respect to Cahill and FEM for metallic line 13 deposited on $\text{SiO}_2/\text{Si p}^{++}$.

The AC temperature oscillations plotted for Cahill's solution for a thin film-on-substrate system is at an offset ΔT_f from those plotted for a substrate-only system all over the frequency range. In the linear zone we can notice a good agreement between the in-phase and out-of-phase temperature oscillations plotted for Cahill + ΔT_f , FEM semi-inf sub, and FEM sub + Cu plate. For frequencies higher than the linear zone upper frequency limit the three plots no more correspond.

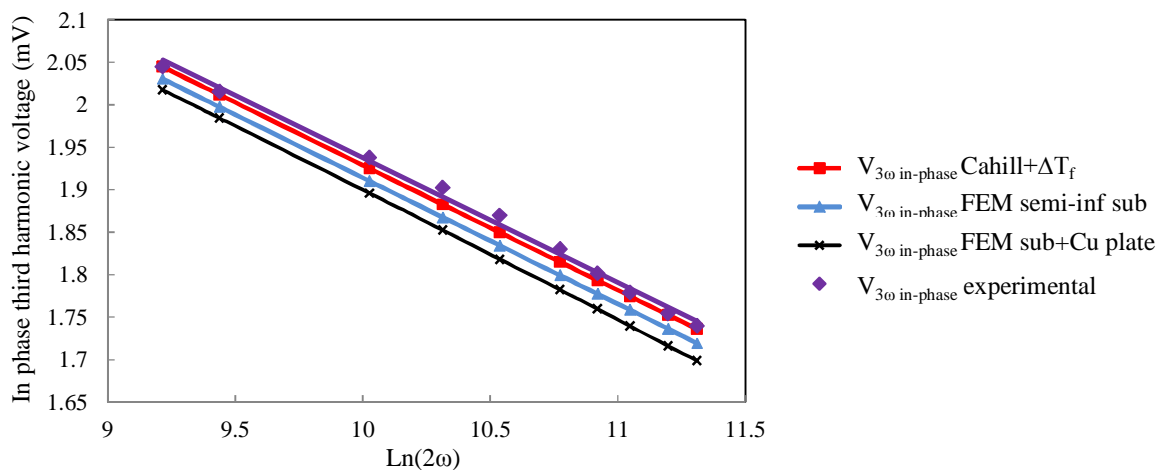


Figure 3.45: Theoretical and experimental in-phase third harmonic voltages for line 13.

In figure 3.45, the theoretical (Cahill + ΔT_f , FEM semi-inf sub, and FEM sub + Cu plate) in-phase third harmonic voltages are plotted with respect to $\text{Ln}(2\omega)$ in the linear zone for metallic line 13. Also, the measurement data are reported on the figure for comparison reasons. We can observe that the four plots are approximately similar.

The same numerical simulation study is done for the second case investigated, epitaxially grown GaAs layer on GaAs substrate at low temperature (figure 3.46). The thermal conductivities of LT GaAs film and GaAs substrate measured using the three omega method were found to be 11.62 W/m.K and 44.39 W/m.K respectively. Metallic line 16 is used for this simulation study.

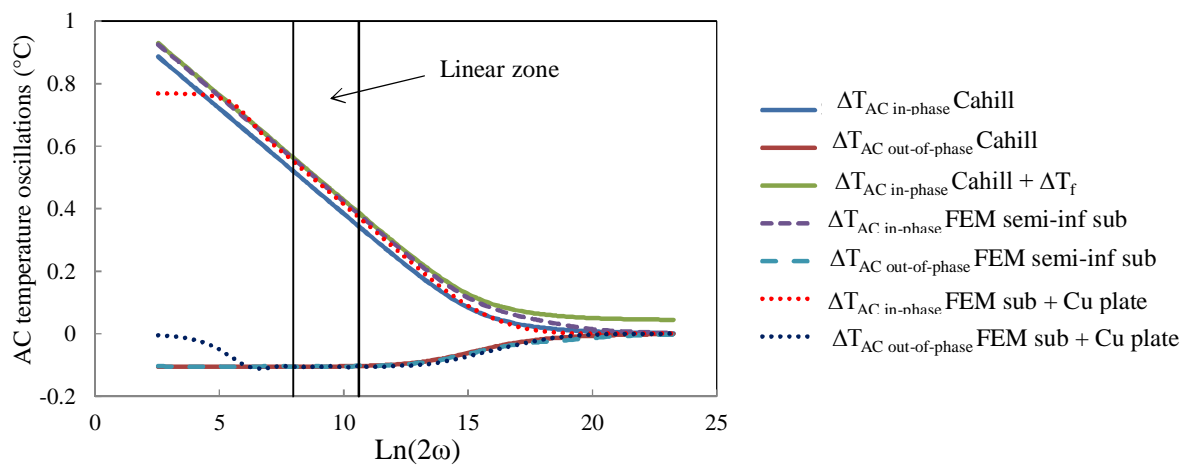


Figure 3.46: Comparison of AC temperature oscillations with respect to Cahill and FEM for metallic line 16 deposited on LT GaAs/GaAs.

The temperature rise ΔT_f due to the thin layer is smaller in this case than for $\text{SiO}_2/\text{Si } p^{++}$ sample, since the thermal conductivity of LT GaAs is higher than that of SiO_2 thin film. Similar results as for $\text{SiO}_2/\text{Si } p^{++}$ are obtained when comparison is done in the linear zone. However, we can notice better agreement than the former sample at frequencies higher than the linear zone upper frequency limit. This might be due to the fact that SiO_2 has a thermal conductivity far smaller than that of $\text{Si } p^{++}$, whereas the difference between the thin layer and substrate thermal conductivities in the case of LT GaAs/GaAs is quite smaller than for $\text{SiO}_2/\text{Si } p^{++}$. The following figure presents the theoretical and experimental in-phase third harmonic voltages obtained in the linear regime for metallic line 16 on LT GaAs/GaAs sample.

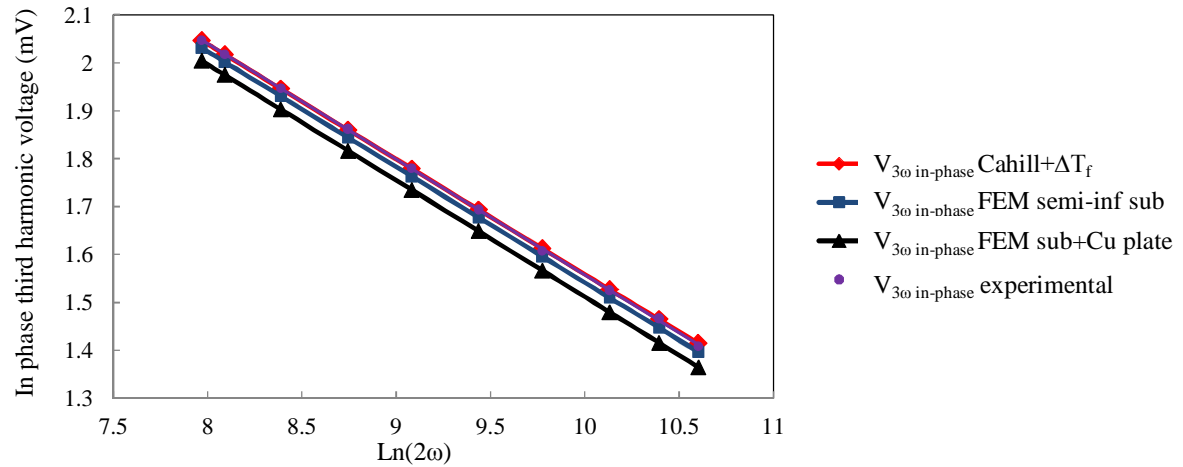


Figure 3.47: Theoretical and experimental in-phase third harmonic voltages for line 16.

We can observe similar results for theoretical (Cahill+ ΔT_f , FEM semi-inf sub, and FEM + Cu plate) and experimental data.

II.6. Conclusion

In this section, the three omega differential technique has been described. It gives the possibility to measure the thermal conductivities of thin films deposited on substrate. This can be done on condition that the thickness of the deposited film is far smaller than the width of the metallic line on the surface of sample. Consequently a 1D heat flow is produced in the direction perpendicular to the metallic line-film interface. Moreover, the thermal conductivity of the thin film must be smaller than that of the substrate. The three omega differential technique has been tested successfully on two samples, SiO_2 placed over boron doped Si substrate of resistivity $0.0014 \text{ } \Omega \cdot \text{cm}$ and epitaxial grown layer on GaAs substrate at low temperature. The average thermal conductivities of Si and GaAs substrates are found to be 85.81 W/m.K and 44.39 W/m.K respectively. On the other hand thermal conductivities of 1.38 W/m.K and 11.62 W/m.K are obtained for a thin film of SiO_2 and LT GaAs layer respectively. Consequently the ratio k_s/k_f is 61 and 4 for $\text{SiO}_2/\text{Si } p^{++}$ and LT GaAs/GaAs samples respectively. We have successfully applied the three omega differential technique given by Cahill on LT GaAs/GaAs sample of k_s/k_f ratio much smaller than that of $\text{SiO}_2/\text{Si } p^{++}$.

Numerical simulations have also been performed for both samples. In case of FEM simulations two configurations are investigated, one considering a semi-infinite substrate and another close to the real structure. These simulations are compared to Cahill's solution with and without taking the thin film into account. Cahill's solution temperature oscillations for a thin film-on-substrate system are always higher by ΔT_f than those of a substrate-only system.

In the linear zones a good agreement between the numerical simulations and Cahill's solution for both samples has been found. Whereas, for frequencies above the linear zone upper frequency limit, the results do not agree well in the case of $\text{SiO}_2/\text{Si p}^{++}$ sample. This is due to the fact that the thermal resistance R_f of the SiO_2 thin film is more important than that of LT GaAs layer.

Conclusion

A theoretical study using finite element method has been done for the three omega method. Cahill's constraints have been added to metallic-line-on substrate system and the structure has been simulated by applying FEM. Temperature oscillations obtained by FEM have been plotted with respect to the natural logarithm of the thermal excitation frequency 2ω and compared to Cahill's analytical solution. The results have showed very good agreement for both theoretical studies. A structure consisting of a finite thickness substrate is simulated using FEM. The effect of a finite substrate appears at low frequencies when compared to Cahill's solution. The FEM in-phase temperature oscillations stay constant while the out-of-phase ones tend to zero at these frequencies. The variation of the thickness of the substrate has shown no influence when compared to Cahill's solution in the linear zone. However, an increase in the thickness of the metallic line conductor decreases the value of the temperature oscillations obtained by Cahill. A variation in the value of the thermal conductivity of the heating element has no influence on the temperature oscillations. In addition a heat convection condition on the surface of substrate is of insignificant effect.

The three omega differential technique has been also theoretically tested using the finite element method. The thermal conductivity of SiO_2 thin film deposited on boron doped Si substrate was measured to be 1.38 W/m.K. Also, a thermal conductivity of 11.62 W/m.K was obtained for an epitaxial grown GaAs layer on GaAs substrate at low temperatures. These thermal conductivity values correspond to the values found in literature. Two models have been numerically simulated for a thin film-on-substrate system: the first for a thin film deposited over an infinite substrate and the second for a system placed on a copper plate. Temperature oscillations plotted for the first and the second model and with respect to Cahill's solution have shown good agreement in the linear regime frequency zones for both two layer samples. For frequencies higher than the linear zone upper frequency, the temperature oscillations no more correspond in the case of $\text{SiO}_2/\text{Si p}^{++}$ sample, while for LT GaAs/GaAs sample, we have found better agreement. This is due to the fact that the difference between the thermal conductivities of the thin film and the substrate underneath is lower in the case of LT GaAs/GaAs than for $\text{SiO}_2/\text{Si p}^{++}$.

We can conclude from this chapter that Cahill's analytical solution is an approach method whereas, FEM is considered to be a more precise way to simulate the real structure. Experimental measurements and numerical simulations have been performed for a metallic line deposited on one layer and two layer materials. In the next chapter, the three omega

method is tested on soft materials. Theoretical studies based on Cahill's analytical formalism and numerical simulations by FEM are implemented. The materials tested in this study are in the micro or sub-micro scales. But the three omega method is also efficient for nano-scale samples [XIN 2014].

REFERENCE

- [ASH 2002] M. ASHEGHI, K. KURABAYASHI, R. KASNAVI, and K.E. GOODSON
“Thermal conduction in doped single-crystal silicon films”,
Journal of Applied Physics, Vol. 91, pp 5079-5088, 2002.
- [BOR 2001] T.BORCA-TASCIUC, A.R. KUMAR, and G. CHEN
“Data reduction in 3ω method for thin film thermal conductivity determination,”
Review of scientific instruments, Vol. 72, pp. 2139-2147, 2001.
- [CAH 1990] D.G. CAHILL
“Thermal conductivity measurement from 30 to 750K: the 3ω method,”
Review of scientific instruments, Vol. 61, pp 802-808, 1990.
- [CAH 1994] D. G. CAHILL, M. KATIYAR, and J. R. ABELSON
“Thermal conductivity of a-Si:H thin film”,
Physical Review B, Vol. 50, pp 6077-6081, 1994.
- [CAH 2003] D.G. CAHILL, W.K. FORD, K.E. GOODSON, G.D. MAHAN, A. MAJUMDAR, H.J. MARIS, R. MERLIN, and S.R. PHILLPOT
“Nanoscale thermal transport,”
Journal of applied physics, Vol. 93, pp 793-817, 2003.
- [CLA 2011] S.P.R. CLARK, P. AHIRWAR, F.T. JAECKEL, C.P. HAINS, A.R. ALBRECHT, T.J. ROTTER, L.R. DAWSON, G. BALAKTISHNAN, P.E. HOPKINS, L.M. PHINNEY, J. HADER, and J.V. MOLONEY
“Growth and thermal conductivity analysis of of polycrystalline GaAs on CVD diamond,”
Journal of vacuum science and technology B, Vol. 29, 03C130, 2011.
- [COM 2009] COMSOLAB <http://www.comsol.com> April, 2009.
- [COM 2012] Heat transfer module user’s guide
Version 4.3, May 2012.
- [CUI 2011] J. CUILIERE
“Introduction à la méthode des éléments finis,” Editor : DUNOD
ISBN 978-2-10-056438-5, 2011
- [DHA 2005] G. DHATT, G. TOUZOT, and E. LEFRANCOIS
“Méthode des éléments finis,”
Paris : Lavoisier, ISBN 2-7462-0979-9, 2005.
- [FAN 2006] X. A. FAN, J. Y. YANG, W. ZHU, H. S. YUN, R. G. CHEN, S. Q. BAO, and X. K. DAUN
“Microstructure and thermoelectric properties of n-type $\text{Bi}_2\text{Te}_{2.85}\text{Se}_{0.15}$ prepared by mechanical alloying and plasma activated sintering,”
Journal of alloys and compounds, Vol. 420, pp 256-259, 2006.

- [HOR 2010] M. HOERTEIS, T. GUTBERLET, A. RELLER, and S.W. GLUNZ
“High temperature contact formation on n-type silicon: basic reaction and contact model for seed-layer contacts,”
Advanced functional material, Vol. 20, pp 476, 2010.
- [INY 2003] A.V. INYUSHKIN, A. N. TALDENKOV, A. Y. YAKUBOVSKY, A.V. MARKOV, L. MORENO-GARSIA, and B.N. SHARONOV
“Thermal conductivity of isotopically enriched $^{71}\text{GaAs}$ crystal,”
Semiconductor Science and Technology, Vol. 18, pp 685-688, 2003.
- [JAC 1999] A.W. JACKSON, J.P. IBETTSON, A.C. GOSSARD, and U.K. MISHRA
“Reduced thermal conductivity in low temperature grown GaAs,”
Applied physics letters, Vol. 74, pp 2325-2327, 1999.
- [JAC 2002] A. JACQUOT, B. LENOIR, A. DAUSCHER, M. STOLZER, and J. MEUSEL
“Numerical simulation of the 3ω method for measuring the thermal conductivity,”
Journal of applied physics, Vol.91, pp 4733-4738, 2002.
- [LEE 1996] D.G. CAHILL
“Heat transport in thin dielectric films”,
Journal of Applied Physics, Vol. 81, pp 2590-2592, 1996.
- [LEW 1996] R.W. LEWIS
“The finite element method in heat transfer analysis,”
Chichester: Wiley, ISBN 0-471-94362-2, 1996.
- [MAI 2009] F. MAILLY, N. DUMAS, N. POUS, L. LATORRE, O. GAREL, E. MARTINCIC, F. VERJUS, C. PELLET, E. DUFOUR-GERGAM, and P. NOUET
“Pirani pressure sensor for smart wafer level packaging,”
Sensors and actuators A: Physical, Vol.156, pp 201-207, 2009.
- [MATLAB] Optimization toolbox user’s guide
R2014b, copyright 1990-2014 Mathworks, Inc.
- [SLA 1964] G. SLACK
“Thermal conductivity of pure and impure silicon, silicon carbide, and diamond”,
Journal of Applied Physics, Vol. 35, pp 3460-3466, 1964.
- [SZE 1985] S.M. SZE
“Semi-conductor devices physics and technology,”
2nd edition John Wiley & sons, Inc. Appendix G, pp 538, 1985.
- [TON 2006] T. TONG and A. MAJUMDAR
“Reexamining the 3ω technique for thin film thermal characterization,”
Review of scientific instruments, Vol. 77, pp 104902, 2006.

- [XIN 2014] C. XING, C. JENSEN, T. MUNRO, B. WHITE, H. BAN, and M. CHIRTOC
“Thermal property characterization of fine fibers by the 3-omega technique,”
Applied thermal engineering, Vol. 71, pp 589-595, 2014.

Chapter IV

Inkjet printing technology for polymer testing by the 3ω method

Introduction

The three omega method has proven the ability to measure accurately the thermal conductivity of solid and soft materials. Nevertheless, in case of soft materials the application of the three omega method is still challenging because up to now it generally requires techniques that are time consuming and costly such as photolithography and shadow mask. In this chapter we present an alternative for this kind of materials based on inkjet printing technology. To evaluate the performance of the technique proposed, polyimide (PI) samples have been prepared by using two methods, photolithography and inkjet printing. We show that the thermal conductivities retrieved in both cases by means of the three omega method are very close; demonstrating that inkjet printing technology is a good candidate for characterization of flexible materials in terms of thermal conductivity.

In a first section, physical properties such as glass transition temperature and thermal conductivity of polymers are defined. In section II, the application of photolithography on PI is described. The thermal conductivity of PI is then measured at different temperatures using the three omega method. On the other hand, a special procedure is used to prepare metallic line on the surface of polydimethyl siloxane (PDMS) for the three omega measurements. Afterwards, its thermal conductivity is determined at different temperatures. Numerical simulations are performed for both samples and then theoretical to experimental comparisons are done.

Section III introduces inkjet printing technology as an alternative to photolithography process. This technology is applied on two kind of polymers, PI and polyetherether ketone (PEEK). The compatibility of the three omega method with inkjet printing technology is tested. Next, both samples with printed metallic lines are numerically simulated using FEM.

I. Polymers

I.1. Introduction

Polymers exist naturally in living plants and animals under the form of DNA, proteins, polysaccharides... They are extracted to fabricate clothing, shelter, weapons, and other human necessities. However it was in 1920 that the scientists started to understand the different properties of polymers. Hermann Staudinger has discovered that polymers are of a macromolecular structure [RIN 2004]. They are made of very large molecules containing a large number of small molecules connected together by covalent bonds. During the last 20 years, it is the synthetic polymers that emerge highly into commercial industries such as nylons, polyethylene, polystyrene, silicones, and so on. Synthetic polymers are produced through a process called polymerization. Polymerization is linking together a set of small identical molecules, usually called monomers, by applying different chemical reactions, to form macromolecules or polymers. Most of the synthetic polymers are organic made up of covalent compounds of carbon. However certain synthetic polymers are made up of inorganic atoms such as silicon [YOU 1991]. Nowadays, polymers attract a strong attention due to the large number of applications offered extending from foams and coatings to electronic and biomedical devices.

I.2. Structure of Polymers

As previously mentioned, polymers are made of repeated units of molecules to form large or macromolecules. Normally, macromolecules have a linear structure. However, they can also possess a non-linear structure depending on the method of polymerization. Therefore, the structure of polymers can also be branched or cross-linked as shown in figure 4.1.

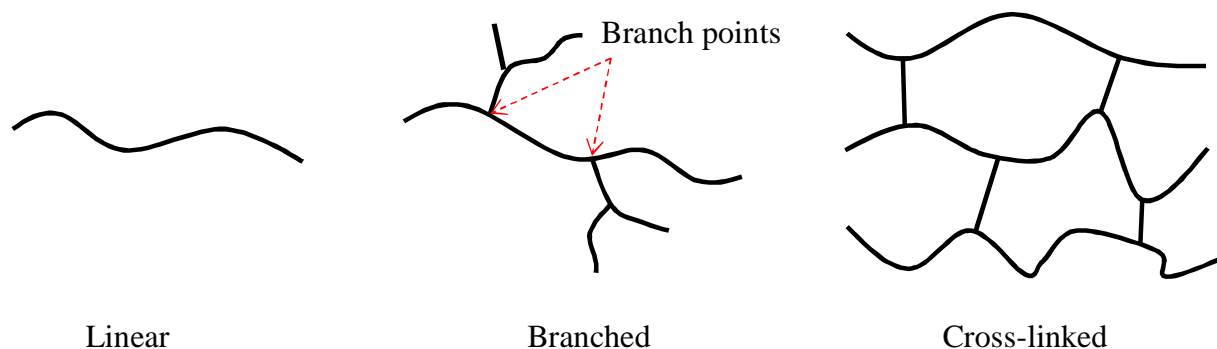


Figure 4.1: Linear and non-linear structures of polymers

A polymer's structure is said to be branched when a number of side chain molecules is connected to the main chain molecule at branch points. While, the cross-linked polymers are

formed of a set of several polymer chains which are connected or held together through covalent bonds.

Polymers exhibit two types of morphologies: amorphous and crystalline. In their amorphous state, polymers have disordered chain structure where molecules are oriented randomly. On the contrary in case of crystalline polymers, molecules are arranged closely in a discernible order. Semi-crystalline polymers form crystalline regions in some area within an amorphous structure [GOO 2004].

The knowledge of the polymers structure can help in determining the group to which the polymer belongs as will be explained in the following section.

I.3. Classification of polymers

Polymers are divided into three different groups: thermoplastics, elastomers and thermosets. Moreover, thermoplastics can be semi-crystalline or amorphous (Figure 4.2).

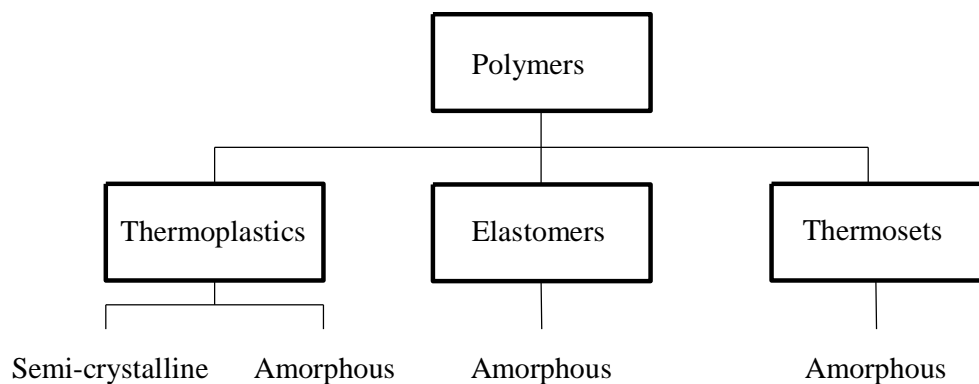


Figure 4.2: Polymers classification

I.3.a. Thermoplastics

Thermoplastics are polymers that have a linear or branched structure. This kind of polymers can be easily processed. At first they are softened by heating to the melting temperature. Then, they can be given any shape by applying high pressure through different processing techniques such as extrusion or moulding. Finally they are cooled down to room temperature to keep the desired shape [YOU 1991]. High intermolecular forces exist between chains in case of thermoplastics. Consequently, molecules are strongly sustained together and the polymer will be solid at room temperature. Some examples of thermoplastics are polyimide (PI) and poly(ether ether ketone) (PEEK). They are classified as high performance polymers as they are able to resist high temperatures, have low flammability and low smoke emission, and possess high rigidity and hardness. PEEK is known to have high wearing

properties and is mostly used in aerospace industry [STU 2002]. When a thermoplastic polymer is subjected to extremely high temperatures, it will undergo plastic flow and the chain molecules start to slip over one another. This causes the polymer to lose its strength. Thermoplastics can be amorphous or semi-crystalline.

I.3.b. Elastomers

Elastomers are rubbery polymers with cross-linked structure. They are amorphous. These polymers can be highly stretched when stressed. When removing this stress, the polymer can recover its original dimensions. This phenomenon is explained by the low cross link density structure of the polymer. Upon stretching, the polymer chains are extended but are kept held together through crosslinks. When the stress is released, they will move back and maintain their original position. An example of elastomers is silicone which is thermally stable and has a high resistivity to water. They are mostly used as electrical insulators and in medical implants.

I.3.c. Thermosets

Thermosets are amorphous polymers with cross-linked structure. This type of polymers irreversibly cures. It can be cured by heating at high temperatures or by applying chemical reactions. Once cooled thermosets harden permanently. They cannot be reshaped again. If reheated, such kind of polymers will degrade instead of melting. They possess an excellent rigidity since the molecular chains are well connected through a high degree of crosslinking. Examples of thermosets are: phenolic resins, amino resins, polyester resins, and polyurethanes. Thermosets are not studied in this chapter.

I.4. Chemical properties of polymers

The resistance of polymers to chemicals highly depends on their molecular structure. Polymers of carbon-carbon backbones with hydrophobic groups attached to the main chain are known to have good oxidation resistance and low moisture absorption. Hydrophobic groups are chemical groups that do not interact with water molecules since they are non-polar and do not form hydrogen bonds. As a result, this kind of polymers can highly resist aggressive aqueous solutions. On the other hand, polymers of carbon-carbon backbones with ester or amide groups attached to the main chain have high moisture absorption. This causes strong acids and alkalis to be soaked by the polymer and consequently destroying it. All in all, moisture and aqueous solution sensitivities increase with the existence of hydrophilic groups

(polar groups that dissolve in water or other solvents) in the polymer's main chain [GOO 2000].

Surface adhesion is another chemical property which greatly occurs in the presence of polar groups in the main chain or side groups of a polymer. Being hydrophilic, polar groups cause absorption of moisture. This results in building hydrogen bonds and consequently leading to good adhesion properties [GOO 2000].

I.5. Physical properties

In this section we present several physical properties of polymers. It is important to understand such properties to be able to explain the results obtained after applying the three omega method. Thermal conductivity and glass transition temperature are two important physical properties that must be taken into consideration when choosing a polymer for a particular electronic or biomedical application.

I.5.a. Volume resistivity and electrical conductivity

Electrical resistivity of a given material can be defined by the following equation:

$$R = \rho \frac{L}{A}$$

where R is the electrical resistance in Ω , L is the length in m, A is the area in m^2 and ρ is the electrical resistivity in $\Omega \text{ m}$. Consequently, the volume resistivity is the electrical resistance through one centimeter or meter cube of material. It is expressed in $\Omega \text{ cm}$ or $\Omega \text{ m}$.

Polymers are known to be excellent insulators therefore possessing a high volume resistivity in the order of $10^{12} \Omega \text{ cm}$ [GOO 2000].

Electrical conductivity is a measure of the material's ability to conduct an electrical current. Basically, it is the reciprocal of the electrical resistivity:

$$\sigma = \frac{1}{\rho}$$

where σ is the electrical conductivity in Siemens per meter (S/m). Since polymers are classified to have the very high electrical resistivity characteristics of insulators, they possess very low electrical conductivities.

I.5.b. Specific heat capacity

The specific heat capacity is a fundamental property that defines the amount of heat needed to change the temperature of a one unit mass of a given material by one degree. It is given in the following equation:

$$C = \frac{\Delta Q}{m\Delta T}$$

where C is the specific heat capacity in $\text{J}/(\text{Kg}\cdot\text{K})$, ΔQ is the amount of heat required in Joules (J), m is the mass of material in Kg and ΔT is the temperature gradient in kelvin (K).

Specific heat capacity can be given at constant external pressure (C_p) or when maintaining constant material volume (C_v). Basically, at room temperature, C_p and C_v are slightly different for most solid materials.

The heat capacity has a weak temperature dependence at high temperatures (above the Debye temperature Θ_D) while it decreases down to zero as the temperature approaches the zero kelvin. This is illustrated in figure 4.3. For most polymers, the Debye temperature is below room temperature [GUN 1994].

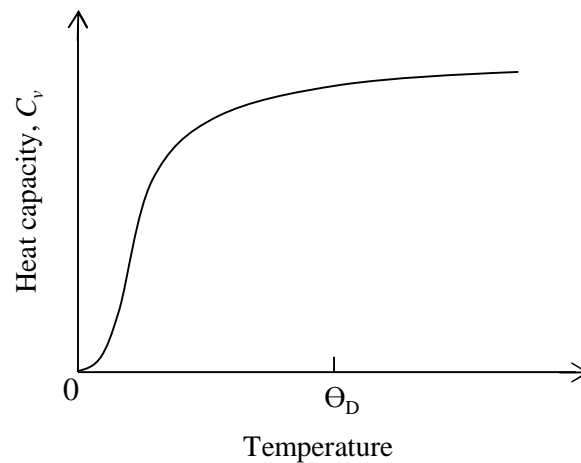


Figure 4.3: The temperature dependence of heat capacity.

Moreover, the heat capacity depends on the state of the polymer if it is crystalline, amorphous or semi-crystalline and if it is melt or glassy [MAR 2007].

I.5.c. Glass transition temperature

The glass transition temperature T_g is one of the most important properties that defines a polymer. The glass transition temperature is the temperature range where a polymer changes from a brittle glassy state to a more pliable or rubbery state. Consequently a polymer having a glass transition temperature above room temperature will act in a brittle manner. However if T_g is below room temperature then the polymer is known to be an elastomer.

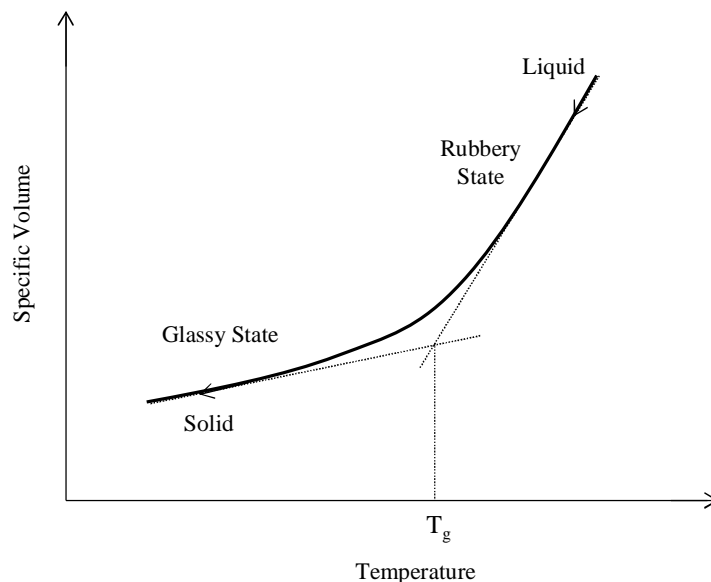


Figure 4.4: Specific volume of various states of polymers as affected by temperature.

Figure 4.4 represents the different states of a polymer with respect to its transition temperature T_g . The specific volume of a polymer is the ratio of volume to its mass and is expressed in m^3/Kg . Upon cooling, an amorphous polymer passes from a liquid/rubbery like to a solid/ glassy like state. We can notice that in the rubbery state, the slope of the curve of the specific volume versus temperature is higher than that in the glassy state. T_g is the temperature defined by the intersection of the two slopes of the rubbery and glassy states.

I.5.d. Thermal conductivity

Thermal conductivity of polymers is an important property for polymers processing and application design. Typically, the polymer's thermal conductivity is lower than that of metals and ceramics and thus explaining the behavior of polymers as insulators. In polymers, only phonons are responsible for transfer of heat because of the absence of the free movement of electrons. The thermal conductivity of polymers is given by Debye equation [POH 1963]:

$$k = \frac{C_p v l}{3}$$

where k is the thermal conductivity in W/(m.K), C_p is the specific heat capacity per unit volume in J/Kg.K, v is the average phonon velocity in m/s and l is the phonon mean free path in meters. Generally, polymers have low thermal conductivities ranging from 0.1 W/(m.K) to 0.6 W/(m.K) [MAR 2007].

The thermal conductivity of polymers has been studied for temperatures below and above the glass transition temperature T_g [DAS 1996, HAN 2011].

- **Thermal conductivity in the region below the glass transition temperature:**

In this region, the thermal conductivity of polymers depends on phonons mean free path; the higher the mean free path the lower is the thermal resistance of polymer and the higher is the thermal conductivity.

In the region below T_g and upon rising the temperature, the polymer's chains will straighten causing the phonon mean free path to increase and the phonons are less scattered. Consequently the thermal resistance of polymer decreases linearly as temperature increases. So, in the region below T_g , the thermal conductivity of polymer increases linearly with the rise in temperature.

- **Thermal conductivity in the region above the glass transition temperature:**

In this region, the thermal conductivity is controlled by the vibrational motion of the polymer chains. As temperature rises, the polymer passes to its rubbery state. The chain segments start to experience thermal motion and large torsional rotation and slide past each other. This phenomenon has two consequences:

- a. The movement of the chains might cause the appearance of microvoids. This results in scattering of phonons. As temperature rises, the number of microvoids increases and the thermal resistance of polymer increases too.
- b. During vibration, the chain segments might become closer therefore increasing their mobility. This causes a linear decrease of thermal resistance.

Polymers which have strong bonding and heavy chain segments and where the probability of chain entanglement is high, undergo consequence type (a). In this case, the thermal conductivity decreases as temperature rises. Examples of such polymers are a number of

synthetic rubbers and PVC (polyvinyl chloride). However, polymers of weak bonding and light chain segments, undergo consequence type (b). In that case, the thermal conductivity increases with increasing temperature. All in all, polymers react differently at temperatures above T_g .

I.6. Polymers in flexible electronics

Flexible electronics technology is rapidly growing and finds applications in different fields such as lightning, radio frequency identification circuitry, displays and photovoltaic [ZAR 2011, YUA 2011, PIER 2008, JAN 2011]. Polymers exhibit different mechanical, optical and chemical properties which render them competitors in such flexible electronic applications. Among these properties are optical clarity, high exploitation temperatures, high flexibility, and robustness that are essential in fabricating flexible electronic devices. Some of the polymers which have mostly emerged in the field of flexible electronics are polycarbonate (PC) [KO 2012], polyethylene terephthalate (PET) [ZAR 2011, MAC 2007], polyethylene naphthalate (PEN) [ZAR 2011, MAC 2007], polyetheretherketone (PEEK) [SUN 2007], polydimethylsiloxane (PDMS) [HAG 2009] and polyimide (PI) [XU 2011]. Thermal management is necessary in many applications. The material used must either prevent heat transfer or be a good thermal conductor. For example, low thermal conductivity materials are required in thermoelectric fields [SHE 2013]. However, materials of high thermal conductivity are desired to achieve heat dissipation in different electronic applications [CHU 2001]. So, there is a need to know the material thermal conductivity of polymers. The three omega method is a good way to carry out this task.

I.7. Conclusion

Polymers structure and classification were briefly described in this section. Polymers can have linear, branched or cross-linked structures. Moreover, they are classified as thermoplastics, elastomers, or thermosets according to their structure. Also, the chemical and physical properties of polymers were recalled. Polymers possess low electrical and thermal conductivities. The glass transition temperature (T_g) identifies the polymer's state. At temperatures higher than T_g , the polymer is in its rubbery state, while for temperatures lower than T_g , the polymer is in its glassy state. As temperature rises the thermal conductivity of polymers possessing strong bonding and heavy segment chains increases in the glassy region and then decreases slowly in the rubbery region. The thermal conductivity of polymers having weak bonding and light structure continues to increase in the rubbery region.

In order to identify the polymer suitable for a particular electronic application, it is necessary to determine the polymer's thermal conductivity. Thermal conductivity of different polymers such as polyimide [KUR 1999], polyaniline [KAU 2007], and polymethyl methacrylate [PUT 2003] has been successfully measured by the three omega method.

In the coming section, the three omega method is used to measure the thermal conductivities of PI at temperatures below its T_g and PDMS at temperatures above its T_g .

II. Measurement of the thermal conductivity of polymers using the 3ω method by preparing samples using photolithography

II.1. Introduction

Polyimide (PI) and polydimethylsiloxane (PDMS) are polymers that possess different properties which render them important materials in different electronic and biomedical applications [TIE 2006, PAT 2008, GHO 1996]. The thermal conductivity of these polymers is measured using the three omega method. Preparing samples for the three omega method is done using photolithography. Metallic lines are deposited over PI using conventional photolithography. In case of PDMS, a special photolithography process is applied to fabricate metallic lines embedded close to the surface of PDMS. Finally, numerical simulation is performed using FEM method. In particular, an improved model is designed for PDMS substrate for which the metallic lines are embedded in its surface.

II.2. Thermal conductivity measurement of Polyimide

The material used here is a black opaque polyimide sheet of 1 mm thick bought from Goodfellow Company. As already said, polyimide is a polymer possessing unique thermal, chemical, and mechanical characteristics. It has high chemical resistance to alcohols, acetones, diluted acids, and halogens. Its maximum exploitation temperature reaches 320°C. Therefore, polyimide is compatible with photolithography. The polyimide sample from Goodfellow is an MTB opaque black version of MT; MT is aluminum oxide filled with increased thermal conductivity of 0.45 W/m.K. In order to measure the rugosity of the sample surface, an analysis has been made by using a scanning probe microscope. The rugosity was found to be around ± 250 nm with respect to an average value.

II.2.a. Sample preparation using photolithography

The steps described here consist of the known basic procedure of photolithography that has been applied to different kind of materials (chapter 2). Initially, the polyimide substrate is cleaned ultrasonically in acetone for 5 minutes and then in propanol-2 for 5 minutes. Then it is blown dry by compressed nitrogen. To ensure the absence of any water molecule, dehydration is performed by placing the substrate on a 110 °C hot plate for 5 minutes. Next, a liquid photoresist (AZnLOF 2020) from AZ Electronic Materials is applied on the substrate's surface and spin coated at 2500 rpm for 20 seconds. This operation results in a 1 μm uniform thick layer of photoresist. Then, after photoresist coating, the polyimide substrate is placed in a 110 °C oven for 10 minutes to remove excess photoresist solvent and to promote adhesion between the photoresist and the substrate. An oven is used to ensure more uniform heating. A negative optical mask (the same as the one used in chapter 2) is placed over the photoresist where it is exposed to ultra violet light for 5 seconds ($\lambda=365\text{ nm}$, intensity=11 mW/cm^2). Before development, the substrate is reheated in an oven at 110 °C for another 10 minutes. This step is usually called post-exposure bake (PEB). Holding the substrate vertically in AZ 326 MIF developer (AZ Electronic Materials) for about 3 minutes, the negative photoresist that was not exposed to ultraviolet light is dissolved. Afterwards, the substrate is directly placed in diluted water for 20 seconds and dried with compressed nitrogen gas. After these different steps, the polyimide substrate is ready for metallization. A 400 nm layer of gold is deposited on polyimide surface by evaporation with a 10 nm layer of chromium to ensure adhesion between the metallic lines and polyimide surface. The procedure is terminated with liftoff through which the remaining and un-needed photoresist is removed. Figure 4.5 shows a microscope image of a metallic line deposited on polyimide substrate by photolithography.



Figure 4.5: A metallic line of 20 μm width prepared by photolithography.

The measurement by means of an optical microscope demonstrates a 19.67 μm -width line instead of the 20 μm targeted.

II.2.b. Measuring the thermal conductivity at different temperatures

Measurements using the three omega method were done on different metallic lines deposited by photolithography on polyimide. Table 4.1 summarizes the properties of three of the metallic lines (19, 20, and 21). These properties include the width $2b$, length l , resistance R_0 at room temperature (25.4 $^{\circ}\text{C}$), the temperature coefficient of resistance β_h and the rms power per meter applied on each metallic line. The temperature coefficient of resistance was measured using the hot plate method as described in chapter 2.

Table 4.1: Properties of metallic lines 19, 20, and 21.

line	$2b$ (μm)	l (mm)	R_0 (Ω)	β_h ($^{\circ}\text{C}^{-1}$)	Power rms (W/m)
19	10	3	24.253	3.26E-3	3.19
20	20	10	38.806	3.55E-3	0.932
21	10	5	39.6509	3.58E-3	1.8

To start the three omega method measurements, the potentiometer R_v of the differential amplifier circuit is varied till reading a minimum fundamental voltage at frequency ω at the lock-in amplifier's output as described in chapter 2. Correspondingly, the third harmonic voltage $V_{3\omega}$ at frequency 3ω is measured. Measurements are done for the linear regime frequency range. This frequency range is calculated from the data given by Goodfellow: thermal conductivity of 0.45W/m.K, a density of 1420 Kg/m^3 and a specific heat capacity of 1090 $\text{J}/\text{Kg.K}$. The lower frequency limit is the same for the three metallic lines since it depends on the thickness of the substrate and is calculated to be 0.578 Hz. However, the higher frequency limit changes according to the width of the metallic line. Lines 19 and 21 have the same width and their higher frequency limit found to be 37 Hz. For line 20 it is calculated to be 9.25 Hz.

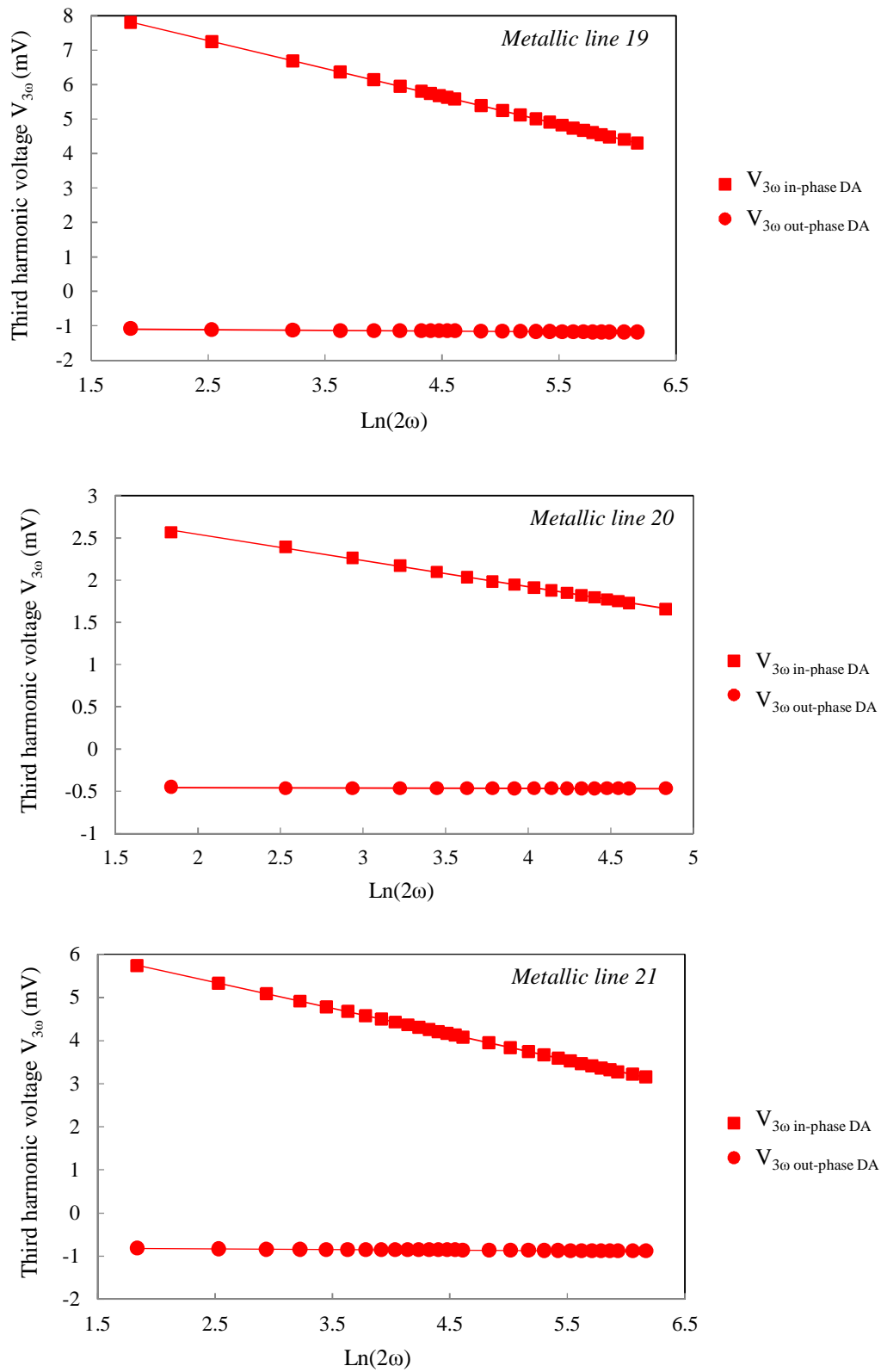


Figure 4.6: The in-phase and out-of-phase third harmonic voltages measured over polyimide for lines 19, 20, and 21.

Figure 4.6 represents the in-phase and out-of-phase third harmonic voltages measured in the linear regime for each of the lines 19, 20 and 21. The squares and circles in red represent the in-phase and out-of-phase measurements done by the differential amplifier circuit. We can notice that the in-phase third harmonic voltages measured over the linear regime are linear with respect to $\ln(2\omega)$. Correspondingly the out-of-phase voltages are constant. The slopes of linearity are determined for each metallic line and then the thermal conductivities are calculated.

In table 4.2 we can find the thermal conductivity values of polyimide over metallic lines 19, 20, and 21 at room temperature ($T_0 = 25.4$ °C).

Table 4.2: Calculated thermal conductivities of polyimide at $T_0 = 25.4$ °C.

Metallic line	Thermal conductivity k (W/m.K)
19	0.491
20	0.495
21	0.508

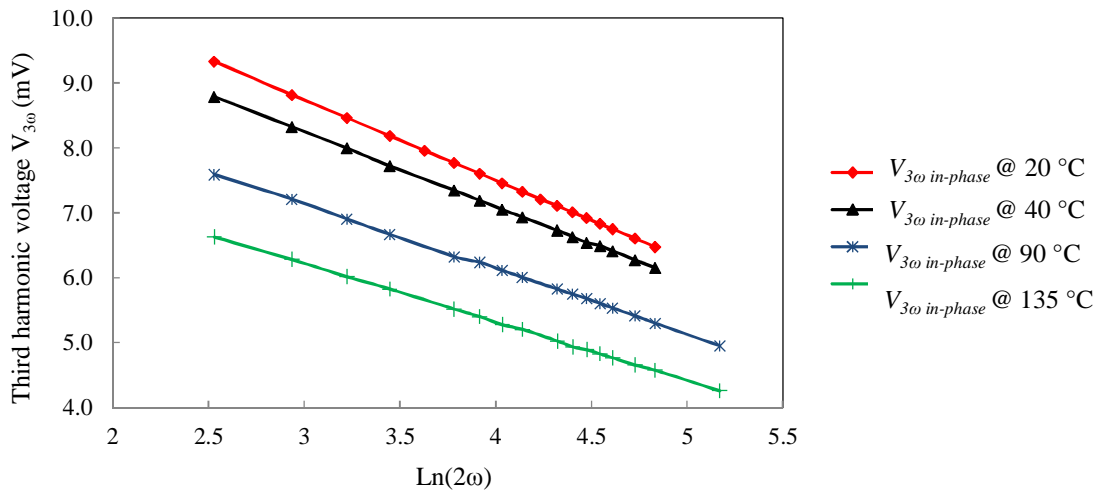
The average thermal conductivity over polyimide is found to be 0.498 W/m.K. We can see that the thermal conductivities measured using the three omega method are in good agreement with the value given by the supplier. Moreover, an error analysis was done and a measurement precision of about ± 7 % was found for the three metallic lines.

Thermal conductivity measurements of polyimide at different temperatures using the three omega method are done. The PI sheet is placed on a hot plate where several thermocouples are attached to the sample's surface to record its temperature. The objective is to measure the thermal conductivity of PI at 40 °C, 100 °C and 160 °C. Actually, we did not use the metallic lines presented in table 4.1 for the thermal conductivity measurements at different temperatures. These metallic lines were used several times for repeatability measurements. Consequently their pads were deformed and they are no longer suitable for further measurements. For this reason, thermal conductivities are calculated at 40 °C, 100 °C and 160 °C using new metallic lines of properties listed in table 4.3. For the same purpose, the measurement of the thermal conductivity of PI is redone at room temperature which is equal to $T_0 = 20$ °C in this case.

Table 4.3: Properties of metallic lines 22, 23, and 24 deposited on polyimide at $T_0 = 20\text{ }^\circ\text{C}$.

Metallic line	$2b$ (μm)	l (mm)	R_0 (Ω)	β_h ($^\circ\text{C}^{-1}$)	Power rms (W/m)	T_0 ($^\circ\text{C}$)
22	30	9.2	19.68	3.87E-3	1.03	20
23	20	9.2	30.98	3.65E-3	2.43	20
24	20	9.2	30.25	3.87E-3	1.11	20

For every metallic line, measurements are initially done at room temperature T_0 where the resistance R_0 is measured by the use of the 4-wire method. Then, power is applied on the metallic line and the third harmonic voltages are measured at different frequencies included in the linear regime. Afterwards, the hot plate's temperature is increased manually. The resistance of the metallic line is recorded when the thermocouple readings appear to be somehow stable (variation around $\pm 0.5\text{ }^\circ\text{C}$) and the third harmonic voltage measurements are repeated for the same linear regime.

**Figure 4.7: The in-phase third harmonic voltages measured over PI at different temperatures (metallic line 23).**

We have noticed that the temperatures measured at the surface of polyimide near the desired metallic line are not equal to the temperatures set by the hot plate. Therefore, at 40 °C, 100 °C and 160 °C the average temperatures recorded by the thermocouples are 40 °C, 90 °C and 135 °C respectively.

At initial temperature T_0 , the rms powers per unit length applied to the metallic lines are as listed in table 4.3. As temperature rises, the metallic line resistance increases causing the rms power to slightly change from its initial value. Consequently, at every temperature, the generator's input is adjusted in order to keep the same rms power for all measurements.

Figure 4.7 represents the in-phase third harmonic voltages measured at different temperatures by the use of the differential amplifier circuit for metallic line 23. These voltages are plotted versus $\ln(2\omega)$ for the linear regime corresponding to the thermal conductivity obtained at each temperature. We can notice that the amplitude of $V_{3\omega \text{ in-phase}}$ decreases as temperature rises. Similarly, the slope of linearity between $V_{3\omega \text{ in-phase}}$ and $\ln(2\omega)$ decreases with temperature resulting in an increase in the thermal conductivity of polyimide. The change in the value of the thermal conductivity with temperature causes a change in the linear regime frequency limits. As a result, the linear zones are not the same for the measurements done at the four different temperatures.

Table 4.4 shows the values of the resistances of each metallic line at different temperatures together with the values of the calculated thermal conductivities. The temperatures listed in this table are the average measured temperatures of the thermocouples connected on the surface of the polyimide sample near the metallic line.

Table 4.4: The resistances of the metallic lines and the thermal conductivities of Polyimide at different temperatures.

Metallic line	Temperature (°C)	Metallic line Resistance (Ω)	Thermal conductivity (W/m.K)
22	20	19.68	0.488
	40	21.08	0.522
	90	24.91	0.639
	135	28.56	0.710
23	20	30.98	0.492
	40	32.85	0.541
	90	38.58	0.640
	135	43.84	0.706
24	20	30.25	0.498
	40	32.19	0.527
	90	38.03	0.628
	135	43.61	0.727

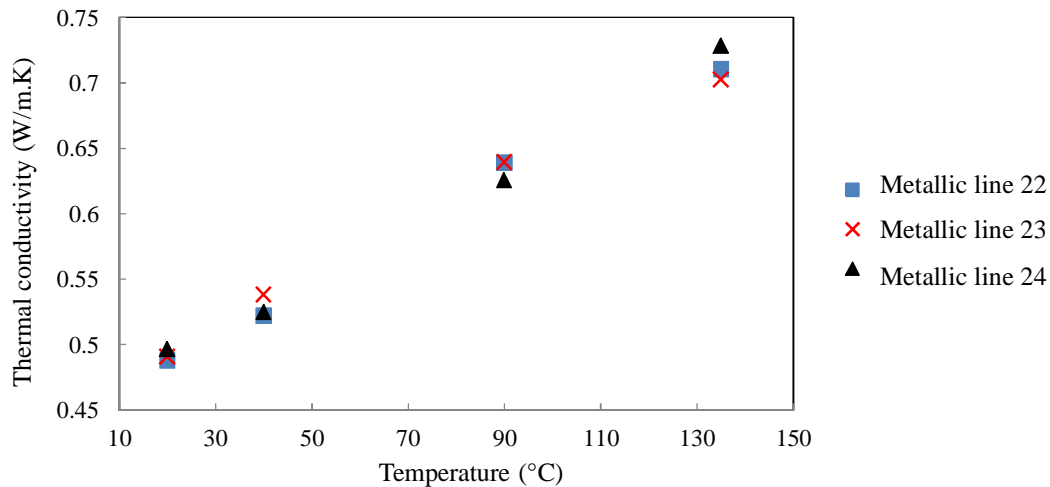


Figure 4.8: Thermal conductivities measured by lines 22, 23, and 24 at different temperatures.

Table 4.5 represents the average thermal conductivities of polyimide determined at different temperatures.

Table 4.5: Average thermal conductivity of Polyimide at different temperatures.

T (°C)	20	40	90	135
k_{avg} (W/m.K)	0.492	0.530	0.635	0.714

In figure 4.8, we can notice that the thermal conductivities measured at each temperature by metallic lines 22, 23 and 24 are in good agreement. The average thermal conductivity of polyimide measured using the three omega method is found to be 0.492 W/m.K at 20 °C. The average thermal conductivity of PI obtained at 25.4 °C is 0.498 W/m.K as presented before in table 4.2. Moreover, we can observe that the thermal conductivity of polyimide increases with temperature. This is due to the fact that the thermal conductivity is measured at temperatures below the glass transition temperature $T_g \sim 320$ °C of polyimide. As explained in section I.5.c, in the regions below T_g , the thermal conductivity of a polymer increases as temperature rises.

II.2.c. Comparison using Cahill's formula

After measuring experimentally the thermal conductivity of PI at different temperatures using the three omega method, Cahill's formula is applied for comparison. The thermal conductivities measured over line 24 at 20 °C, 40 °C, 90 °C and 135 °C are substituted in Cahill's formula (equation 4.1) and the experimental third harmonic voltages are compared to the theoretical ones (equation 4.2). The following equations have been extensively detailed in chapter 1.

$$\Delta T_{AC}(2\omega) = \frac{p_{rms}}{\pi k} \int_0^{\infty} \frac{\sin^2(\eta b)}{(\eta b)^2 \sqrt{\eta^2 + q^2}} d\eta \quad (4.1)$$

$$V_{3\omega} = \frac{1}{2} V_0 \beta_h \Delta T_{AC} \quad (4.2)$$

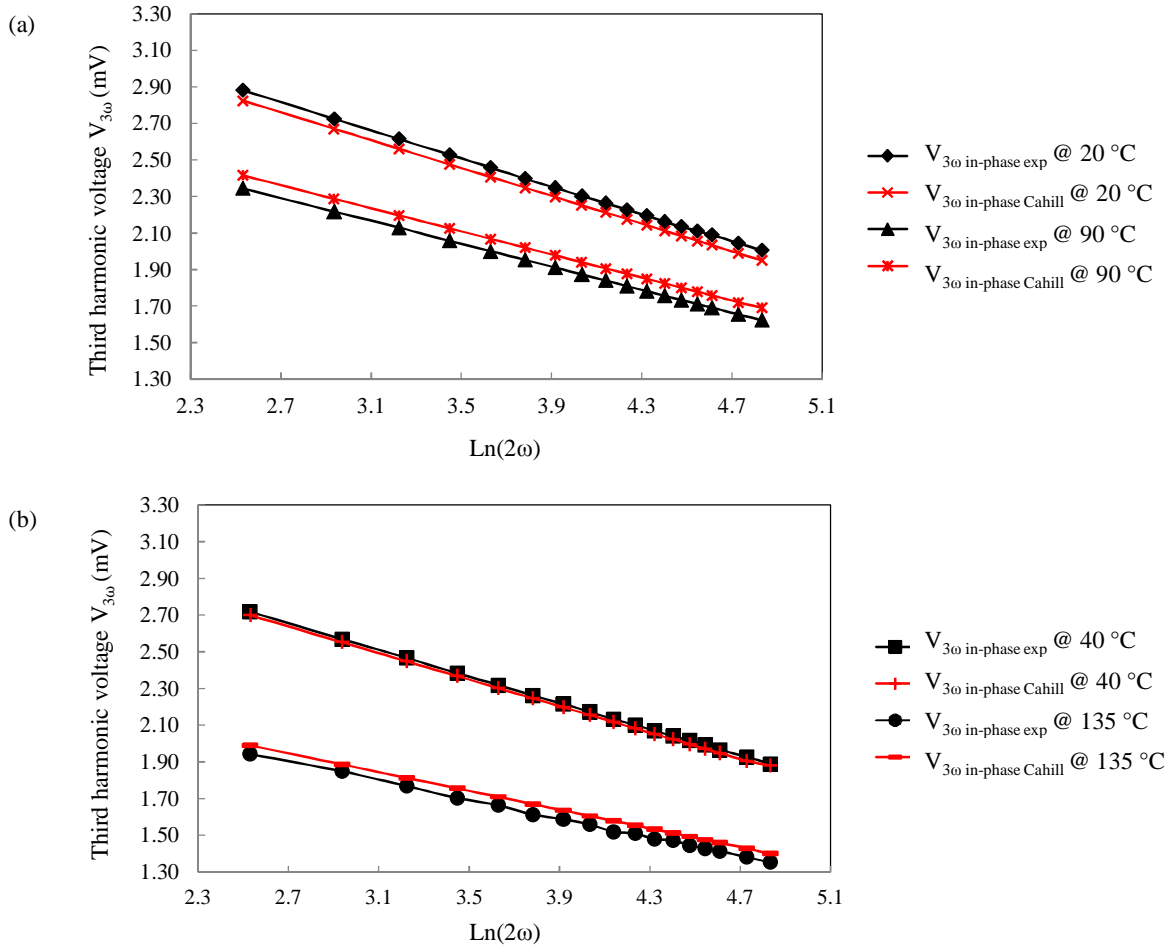


Figure 4.9: Comparison of experimental and theoretical (Cahill) third harmonic voltages at (a) 20 °C and 90 °C and at (b) 40 °C and 135 °C for line 24.

Figure 4.9 shows the experimental third harmonic voltages measured at different temperatures using the three omega method over line 24 in black. The data in red are those extracted from Cahill's formula. We have chosen a common linear zone ($f_{min}= 1$ Hz and $f_{max}= 10$ Hz) for the four measurements to make the figure clearer and easier to compare between theoretical and experimental results. We can notice that at each temperature both findings are in good agreement.

Cahill's formula (equation 4.1) depends mainly on the material's thermal conductivity and on the rms power per unit length applied on the metallic line deposited on the surface of material. However, we can see that it is independent on the temperature T_0 at which we initiate the manipulations.

II.3. Thermal conductivity measurement of Polydimethylsiloxane (PDMS)

PDMS is a popular silicon based polymer that is used in different electronic and medical applications. PDMS offers many advantages like simplicity of fabrication and high flexibility making it suitable to serve as a substrate in flexible electronics. Recently, microwave applications where PDMS is used as a dielectric substrate possessing appropriate mechanical properties have been addressed. Reconfigurable and deformable antennas have been realized using this material [TIE 2006, HAG 2009]. On the other hand, in medical fields, PDMS is valued for its optical transparency, chemical inertness, impermeability to water, and non-toxicity. This makes it a suitable material for example to fabricate microfluidic devices [KUN 2006, COO 2002] such as capillary electrophoretic separation devices [HON 2001], and to build neural implant wireless devices [HAS 2011]. In addition to the aforementioned physical and chemical properties, thermal conductivity is an important property to control for PDMS processing and for accurate application design [DAW 2006]. The polymer material used here is a Dow Corning 184 silicon elastomer.

II.3.a. Sample preparation

Metallic deposition on PDMS by conventional techniques such as sputtering and evaporation is found to be impractical [LEE 2005]. PDMS undergoes a low surface energy which results in poor adhesion of metals to its surface. Hage-Ali et al. [HAG 2009] have proposed a metal fabrication procedure which results in metallic patterns embedded close to the surface of PDMS where an adhesion mechanism is used as an intermediate between the metal layer and PDMS surface.

Initially, a 100 nm layer of molybdenum is sputtered on the surface of a 3 inch silicon substrate (fig 4.10a). This is followed by a photolithography process where a positive resist is patterned for the deposition of a 20 nm seed gold layer (fig 4.10b). This patterning is done through an optical mask with the desired line patterns of different lengths and of 10 μm and 20 μm width. Similar to the previous step, a photoresist is fabricated by photolithography. Afterwards, an electroplating process of a 500 nm layer of gold on the top of the seed layer is performed (fig 4.10c). The adhesion mechanism consists of sputtering a 50 nm layer of titanium followed by the deposition of a 50 nm layer of SiO_2 by plasma enhanced vapor deposition (PECVD). The final thickness of the metallic line conductor is equal to 0.5 μm . A 430 μm PDMS frame is bonded to a 20 μm thick PDMS membrane which was initially deposited by spin coating as shown in figures 4.10e and 4.10f. This procedure is then terminated by removing the molybdenum layer through etching and the desired PDMS sample to be characterized is

released (figure 4.10g).

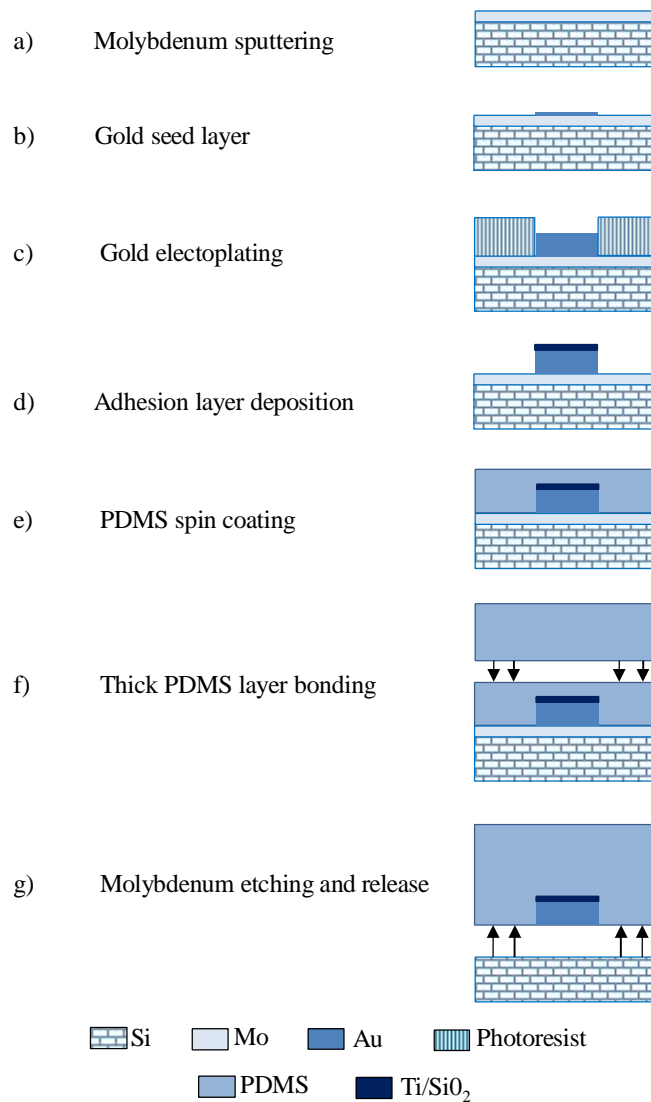


Figure 4.10: Main procedure steps for the fabrication of metallic line conductors embedded in the surface of PDMS.

The procedure followed here results in metallic lines embedded in the surface of PDMS unlike the conventional photolithography used to deposit the metallic lines on the surface of material. The PDMS sample is placed on a high resistivity silicon substrate for the ease of manipulation. A metallic line conductor is presented by means of an optical microscopy image in figure 4.11.

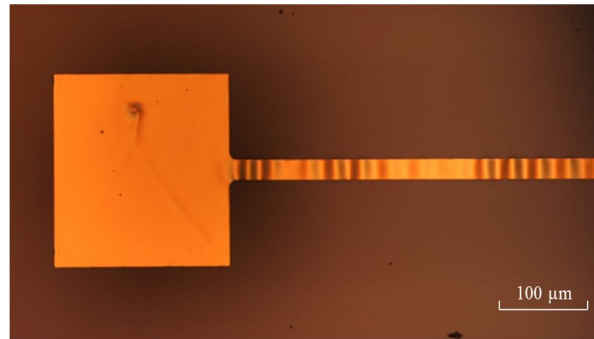


Figure 4.11: A microscopy image of a metallic line conductor embedded in PDMS surface.

II.3.b. Measuring the thermal conductivity at different temperatures

Different powers are applied to three different metallic lines (25, 26, and 27) embedded in PDMS to measure the thermal conductivity using the three omega method. In table 4.6 are given the dimensions ($2b$ and l) of these lines, the resistance R_0 at $T_0 = 22\text{ }^\circ\text{C}$, β_h , and p_{rms} applied on each metallic line.

Table 4.6: Different properties of lines 25, 26, and 27.

line	$2b$ (μm)	l (mm)	R_0 (Ω)	β_h ($^\circ\text{C}^{-1}$)	Power rms (W/m)
25	20	5	13.585	2.93E-3	0.95
26	20	12	34.582	2.85E-3	0.783
27	10	5	24.646	2.87E-3	1.78

The third harmonic voltage is measured at T_0 for frequencies between 1.4 Hz and 4.5 Hz for lines 25 and 26, and between 1.4 Hz and 18 Hz for line 27. These frequencies are determined for thermal conductivity value extracted from literature $k = 0.2\text{ W/m.K}$ [HON 2010], density of 965 Kg/m^3 , specific heat capacity of 1460 J/Kg.K , and PDMS sample thickness of $450\text{ }\mu\text{m}$.

Figure 4.12 represents the third harmonic voltages measured in the linear regime for metallic lines 25, 26, and 27.

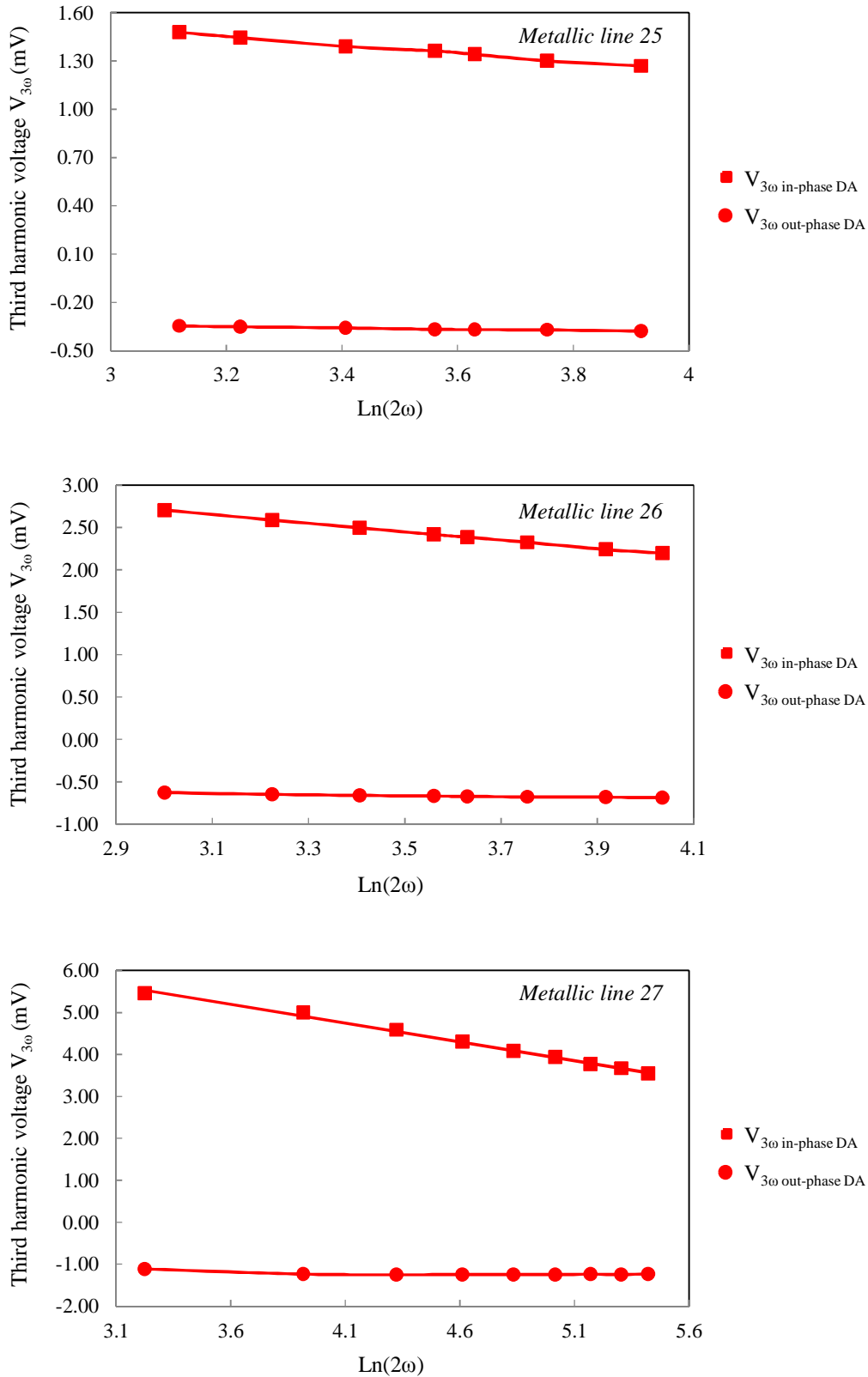


Figure 4.12: Third harmonic voltages measured in the linear regime for lines 25, 26, and 27.

For the three metallic lines, we can observe that the in-phase component is linear as a function of $\text{Ln}(2\omega)$ and the out-of-phase is constant all over the linear zone.

In table 4.7 are given the thermal conductivity values obtained at T_0 for each of the metallic lines.

Table 4.7: Thermal conductivity values measured at $T_0=22$ °C.

Metallic line	Thermal conductivity k (W/m.K)
25	0.213
26	0.204
27	0.213

The average thermal conductivity of PDMS obtained $k_{avg}= 0.21$ W/m.K corresponds to the values given in literature. Moreover, an error analysis was performed and resulted in a measurement precision of $\sim \pm 9$ %.

The thermal conductivity of PDMS is also measured at different temperatures using the three omega method. It was determined at 60 °C and 100 °C, which are temperatures higher than PDMS glass transition temperature $T_g= -125$ °C. Measurements are done on three or more metallic lines at each temperature. The following table summarizes the thermal conductivity values (minimal, maximum, and average) obtained at 60 °C and 100 °C.

Table 4.8: Thermal conductivity values at 60 °C and 100 °C.

Temperature (°C)	k_{min}	k_{avg}	k_{max}
60	0.22	0.225	0.229
100	0.244	0.257	0.267

Table 4.8 shows that the thermal conductivity of PDMS increases with temperature. But, PDMS is known to have a long and strong bonding between silicon and oxygen atoms in its molecular chain. Therefore, PDMS must follow consequence type (a) as stated in section I.5.d. That is to say, the thermal conductivity of PDMS decreases with increasing temperatures at the region above the glass transition temperature.

Systematic errors are aroused while measuring the thermal conductivity of PDMS at different temperatures using the three omega method:

- Measurements were done over PDMS in its rubbery state. A problem occurred between the micromanipulator needles and PDMS surface. As mentioned in chapter 2, the needles have

a radius of 7 μm at one of its extremities. Such needles are not compatible with a polymer material in its rubbery state. When their extremity is placed on a metallic line pad, it might cause deformation of the pad and the surface of PDMS underneath equally. One of the possible solutions was to use the other extremity of the needle which is larger and less needle-like. But, this solution produces unstable measurements and consequently uncertainties in the value of the thermal conductivity.

- The hot plate used to heat the PDMS sample is the one used when performing the temperature coefficient of resistance measurements. As explained in chapter 2, vibrations and variations in metallic line resistance value are produced when setting the hot plate's temperature. This variation in the metallic line resistance changes the value of the initial voltage V_0 and consequently the value of the power across the metallic line.

The increase in the thermal conductivity of PDMS produced with increasing temperature might be due to the systematic errors produced by the micromanipulator needles and the hot plate.

The variations of the thermal conductivity of PDMS as a function of temperature are very slight when compared to the changes obtained in the value of the thermal conductivity of polyimide. Till now, such variations cannot be measured by the three omega method experimental setup built in the laboratory which precision measurement is $\sim \pm 10\%$.

These errors can be reduced by:

- Using micromanipulator needles with circular extremity (larger extremity) therefore eliminating the possibility of sample's deformation and unstable measurements.
- Using an oven instead of a hot plate. Consequently, no vibrations are generated when changing the temperature.
- Generally, improving the three omega method experimental setup measurement precision.

II.3.c. Comparison with Cahill's formula

In this section, the experimental results of the three omega method measurements done on PDMS at room temperature are compared to Cahill's solution. The density, specific heat capacity and average thermal conductivity of PDMS are taken to be 965 Kg/m^3 , 1460 J/Kg.K , and 0.21 W/m.K respectively.

Figure 4.13 shows a comparison between the real third harmonic voltages obtained in the linear regime experimentally and according to Cahill for line 27 (see table 4.6).

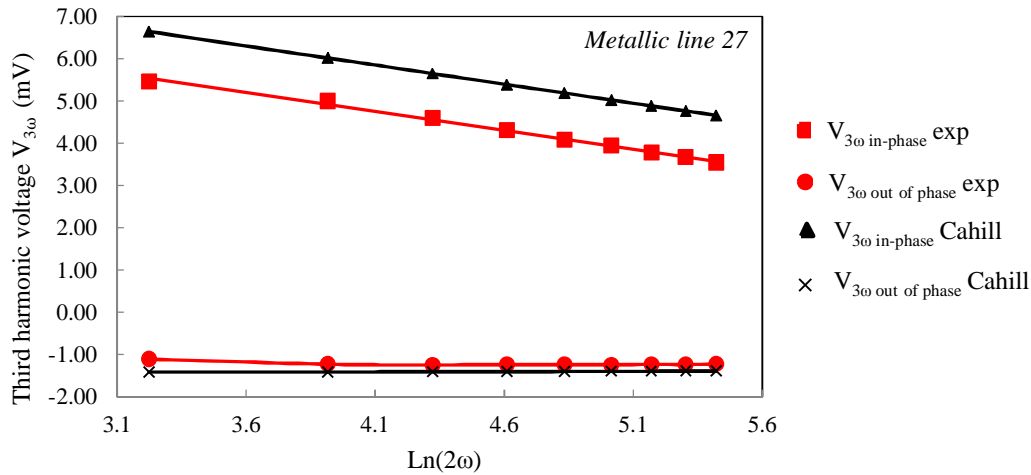


Figure 4.13: Experimental and theoretical in-phase and out-of-phase third harmonic voltages for metallic line 27.

We can notice that $V_{3\omega \text{ in-phase}}$ determined by Cahill are higher in magnitude. An explanation for this difference can be partially found in the fact that Cahill's solution is defined for a metallic line deposited on the surface of material while our sample consists of metallic lines integrated in the PDMS membrane where a SiO_2 layer is introduced for adhesion purposes.

II.4. Modeling improvement using FEM method

II.4.a. Applying numerical simulation to Polyimide sample

As described in chapter 3, numerical simulations of the 3ω method based on the FEM take into account the exact geometry of the heater, the materials underneath the heater and the physical properties of these different materials. Furthermore, FEM requires the knowledge of the structure's initial temperature before starting any simulation. The choice of this parameter allows us to simulate the behavior of a metallic line fed by a power $p(t)$ and placed over a polymer substrate heated to a temperature of 135°C as in the case, for example, of the experimental study.

Numerical simulation using COMSOL[®] has been discussed in details in chapter 3. We just recall that due to symmetry along normal line to the metallic strip, we only need to consider a half structure as presented in figure 4.14. Thus the boundary conditions for the temperature

are taken to be the following: isothermal on the bottom and on lateral faces and natural convective cooling on the top of the structure.

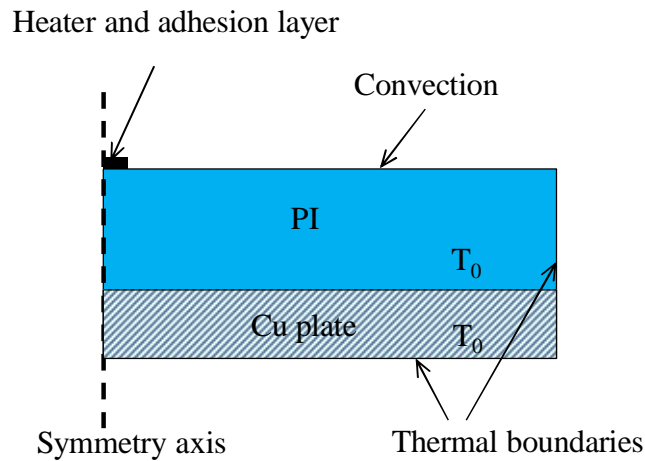


Figure 4.14: Simulated structure (not to scale). $T_0 = 20\text{ }^\circ\text{C}$, $40\text{ }^\circ\text{C}$, $90\text{ }^\circ\text{C}$, or $135\text{ }^\circ\text{C}$.

To perform the numerical simulations, we proceed as follows. Initially, we begin with a preliminary static study on the structure where the initial temperature is considered to be uniform only in the copper plate. This study is done in steady state since no power is supplied to the metallic line $p(t)=0$. In order to perform the needed calculations, we use the average thermal conductivity values of PI measured for the four temperatures ($20\text{ }^\circ\text{C}$, $40\text{ }^\circ\text{C}$, $90\text{ }^\circ\text{C}$ and $135\text{ }^\circ\text{C}$) corresponding to four possible temperature values of the copper plate. This first calculation allows us to determine the initial temperature distribution in the structure. The temperature distribution obtained is very close to uniform distribution. Afterwards, simulation in time domain is done to determine the temperature evolution with respect to time in the metallic line conductor and consequently to deduce the amplitude of the third harmonic voltage.

Figure 4.15 shows the experimental third harmonic voltages, in black, measured at different temperatures using the three omega method over line 24. The data in red are those obtained from FEM simulation.

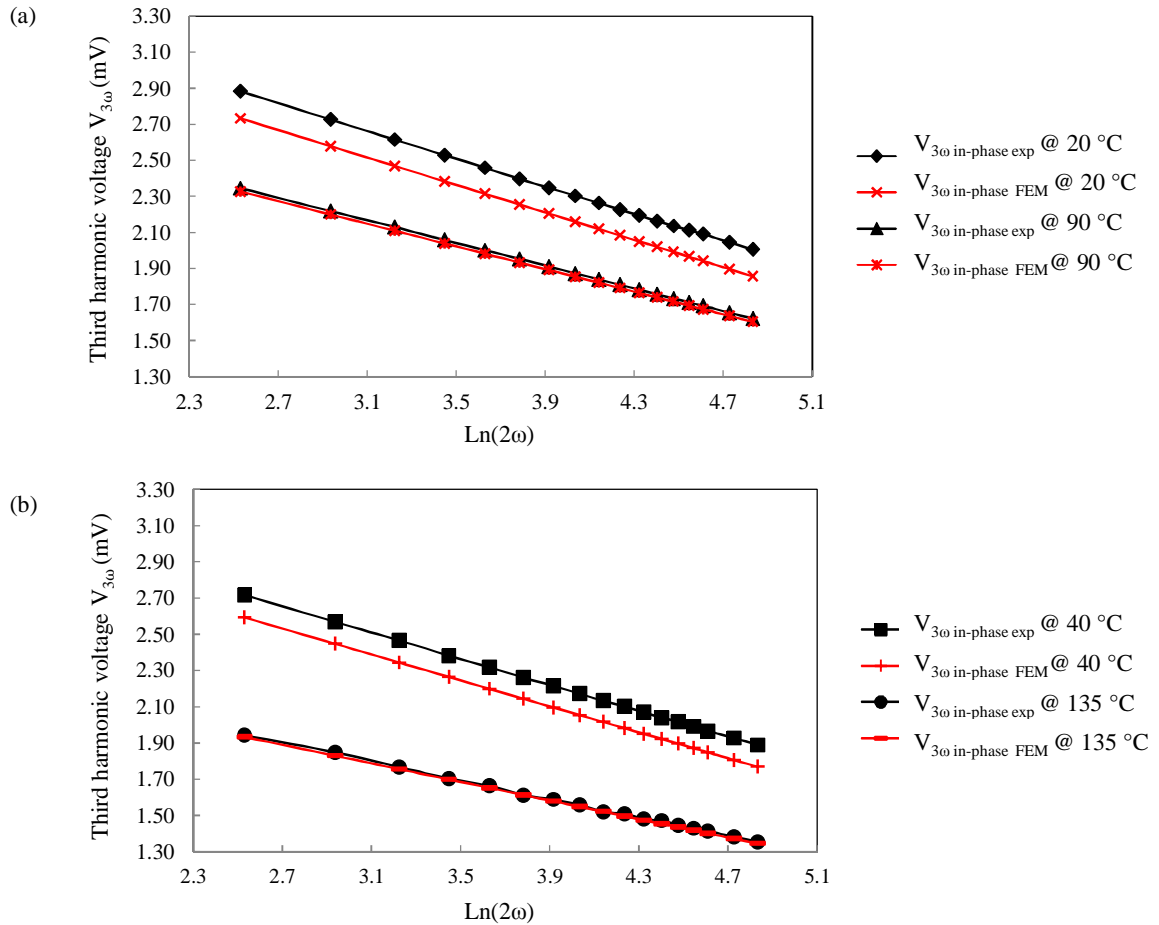


Figure 4.15: Comparison of experimental data and FEM solution at (a) 20 °C and 90 °C and at (b) 40 °C and 135 °C for line 24.

In the four cases, we can observe that the experimental results and theoretical data obtained by numerical simulation are very close. Also, as we have seen in figure 4.9, Cahill's solution agrees with the obtained experimental data. As Cahill assumes, the magnitude of the temperature variations at the level of the metallic line are independent of the substrate's initial temperature. It is only the value of the thermal conductivity of the material under test that varies with temperature.

II.4.b New FEM model designed for PDMS sample

In this section we are interested in the resolution of the problem dealing with diffusion of heat into a medium from an oscillating heater located near the surface but embedded in the medium under test.

As explained in section II.3.a, the sample for the three omega measurements was prepared through a procedure which differs from conventional ways applied to solid materials. At the end of the fabrication process, the heating element which consists of two conductors (gold and

titanium) is inserted in the medium under test. Let us also recall that under the heater there is a very thin layer (50 nm) of SiO_2 (Figure 4.16).

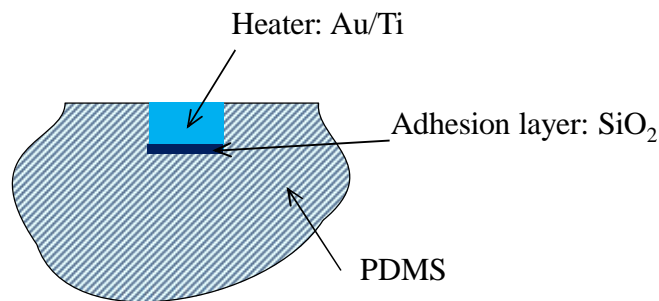


Figure 4.16: Heater embedded in PDMS.

As explained in chapter 3, in Cahill's formalism, it is supposed that an infinitely long heater with a width equal to $2b$, is placed on the surface of a semi-infinite medium. In addition, to obtain Cahill's integral formula, an infinitely thin layer is assumed. For our model, it is obvious that assumptions made by Cahill are not all taken into consideration. These approximations can justify the difference observed between the experimental and theoretical data (Figure 2.13), so simulations using the finite element method (FEM) are performed.

Due to symmetry along normal line to the metallic strip, we only need to consider a half structure as presented in figure 4.17.

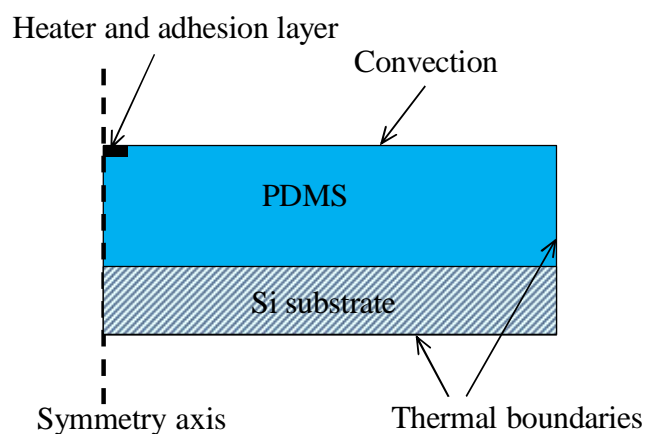


Figure 4.17: The simulated structure (not to scale).

The boundary conditions for the temperature are taken to be the following: isothermal on the bottom and on lateral faces and natural convective cooling on the top of the structure. The silicon substrate ($350\ \mu\text{m}$ thick) used for manipulation purposes, has a high thermal conductivity compared to that of PDMS. Therefore, this substrate can be considered as a heat

sink at ambient temperature similar to the copper plate used in the preceding section (figure 4.14) to perform experimental measurements.

The finite element method requires the creation of a mesh for the studied structure. One can mention that fine meshing is applied on thin layers (heater and SiO₂ adhesion layer) to achieve a more reliable heat transfer modeling (Figure 4.18).

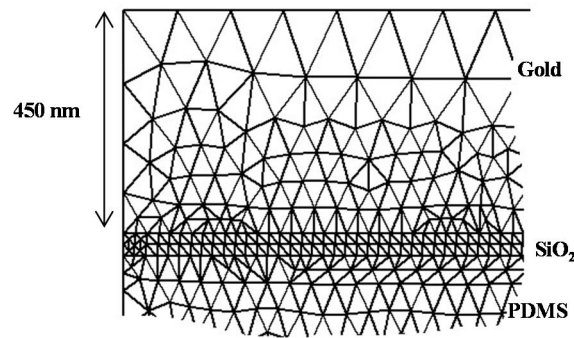


Figure 4.18: Cross-sectional view of the grid near the heater.

In order to compare temperature oscillations obtained by the two simulation studies (Cahill's formula and FEM), we use for the calculations the measured average value of the thermal conductivity of PDMS $k_{avg} = 0.21$ W/m.K (density of 965 Kg/m³, specific heat capacity of 1460 J/Kg.K). For FEM modeling, the knowledge of the thermal properties of gold (thermal conductivity: 317 W/m.K, density: 19300 Kg/m³, specific heat capacity: 129 J/Kg.K) and high resistivity silicon (thermal conductivity: 148 W/m.K, density: 2330 Kg/m³, specific heat capacity: 700 J/Kg.K, thickness: 350 μ m) is required. The effect of the titanium layer is not taken into account in this study. For simplicity, the 50 nm layer of titanium is united with the 400 nm layer of gold and a conducting element made of gold possessing a thickness of 450 nm is considered. The density, specific heat capacity, and thermal conductivity values used in simulation for the SiO₂ layer are 2500 Kg/m³, 775 J/Kg.K, and 1.4 W/m.K respectively. Other parameters needed while performing simulations by FEM such as power are found in table 4.6 (lines 25, 26, and 27).

Initially, we have set a frequency variation of 0.01 Hz to 10 MHz. Figure 4.19 shows a plot of temperature oscillations obtained for line 27 as a function of the natural logarithm of the thermal excitation frequency 2ω .

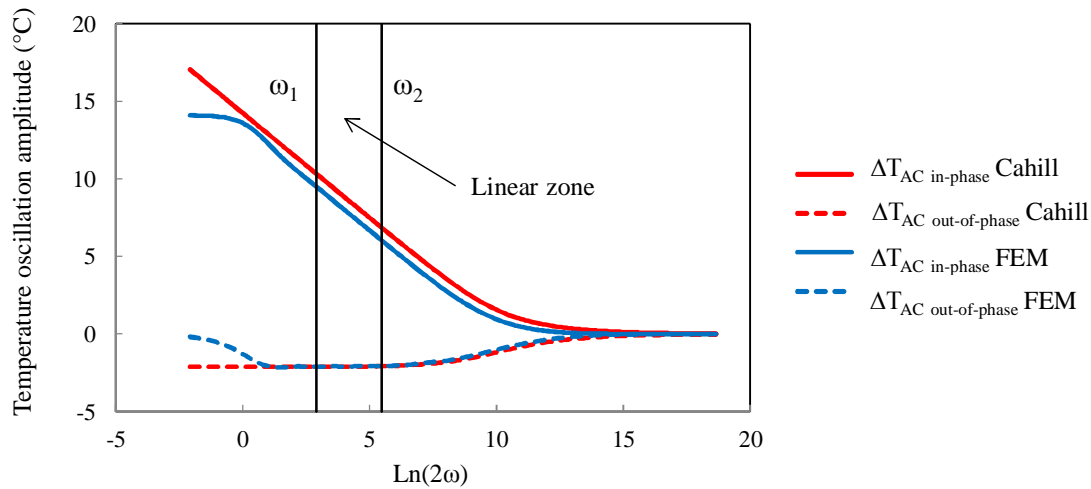


Figure 4.19: A plot of the real and imaginary parts of temperature oscillations with respect to 2ω for line 27 at room temperature.

As described in chapter 3, for the lower frequencies we can see the influence of the high resistivity silicon substrate [RAU 2003, JAC 2002, WAN 2009]. In the linear regime, the slope of the curve calculated by Cahill's formula and the one given by numerical simulation are identical. So, the determination of the thermal conductivity when the metallic line is embedded in the surface of material is possible with 3ω method. Moreover, the presence of the SiO_2 thin layer seems to have no impact on the slope of the curve. We can notice in the linear zone that the in-phase temperature oscillations found by FEM are lower in magnitude than those calculated by Cahill's method. This is a good indication when observing figure 4.13 where the experimental measurements are also lower in magnitude than Cahill's solution.

To be more precise, we uniquely focus on the in-phase third harmonic voltages as a function of $\text{Ln}(2\omega)$. In figure 4.20 the in-phase third harmonic voltages are plotted in the linear regime with respect to experimental results, Cahill, and COMSOL[®] simulation for line 27. In order to study the influence of the fact that the metallic line is embedded near the surface of PDMS and that a thin layer of SiO_2 exists between the metallic line and PDMS, different numerical simulations using FEM have been performed. In a first simulation, called "model 1", the metallic line is deposited on the surface of substrate as if conventional photolithography has been used for fabrication. For a second simulation called "model 2", the metallic line is embedded near the surface of the substrate. "Model 3" is simply "model 2" on which the thin layer of SiO_2 is added between the metallic line and the substrate surface.

“Model 3” is equivalent to the real structure. For all the above models, we have simulated the PDMS substrate placed on the silicon substrate of high thermal conductivity.

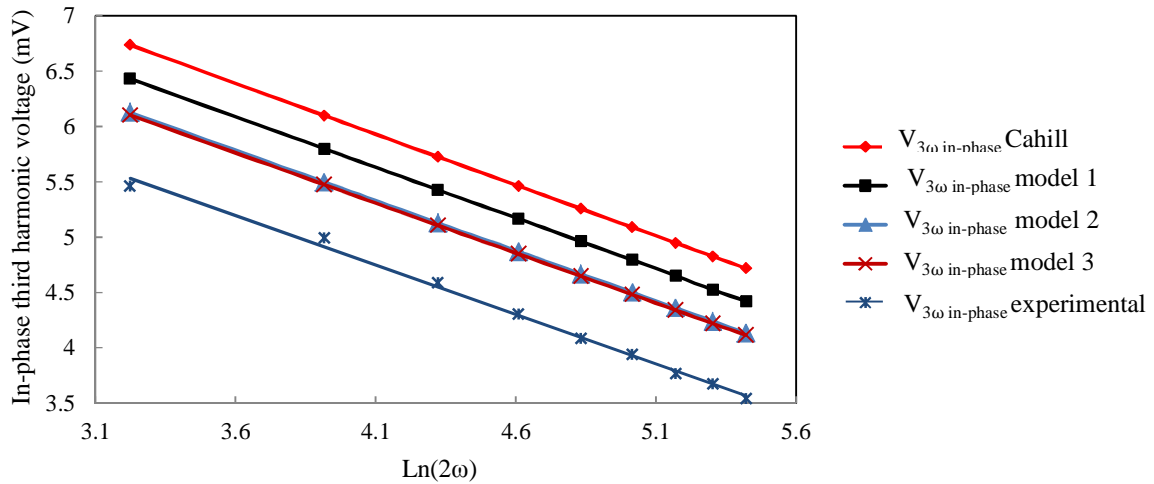


Figure 4.20 Amplitude of the in-phase third harmonic voltages for line 27 plotted with respect to Cahill formula, models 1, 2, 3 and experimental measurements.

As noted in section II.3.c, Cahill method always overestimates the experimental measurements. We can observe that the more the simulated structure approaches the real structure under-test, the more the theoretical curve becomes close to the experimental one. The fact that the metallic line has a certain thickness (model 2) has decreased the in-phase third harmonic voltage $V_{3\omega}$. This decrease will be enhanced if the metallic line is embedded near the surface of substrate. However, the presence of the SiO_2 layer of 50 nm thickness has no influence. But, at the end, the theoretical values are always higher by 10 % to 15 % than the experimental values.

II.5. Conclusion

Metallic lines were successfully deposited over polyimide polymer using photolithography. Measurements were performed at different temperatures to measure the thermal conductivity of polyimide using the three omega method. The average thermal conductivities of polyimide were found to be 0.492 W/m.K, 0.498 W/m.K, 0.530 W/m.K, 0.635 W/m.K, and 0.714 W/m.K at 20 °C, 25.4 °C, 40 °C, 90 °C and 135 °C respectively. For temperatures below its glass transition temperature, polyimide’s thermal conductivity increases with increasing temperature. On the other hand, a special procedure was applied for PDMS sample preparation. Instead of depositing the metallic lines on the surface of PDMS, they were embedded in its surface. The average thermal conductivity of PDMS was found to be 0.21 W/m.K at room temperature when using the three omega method. The average thermal

conductivities at 60 °C and 100 °C were measured to be 0.225 W/m.K and 0.257 W/m.K respectively. We have found that the thermal conductivity of PDMS increases with increasing temperature in the regions above its glass transition temperature. Cahill's solution was compared to experimental results over PDMS. Also, numerical simulations using FEM method were performed for metallic lines embedded near the surface of PDMS. Cahill's solution overestimated the experimental measurements, while the data found by FEM method showed a better agreement with the experimental results. However, Cahill's analytical solution remains a reliable method to examine the experimental results in a short period of time.

For PI, the sample was prepared using conventional photolithography while a special procedure was applied for PDMS sample preparation. In the following section, inkjet printing technology will be used for sample preparation instead of photolithography. This technology competes photolithography process in terms of time and cost.

III. Characterization of polymers using the 3 ω method by preparing samples using inkjet printing technology

III.1. Introduction

During the last decade, inkjet printing technology has emerged in the field of electronics and especially in the fabrication of plastic electronic devices. It has appeared as a competitor to photolithography because of its simplicity of use. Lithography employs a basic procedure of multiple and expensive steps. Moreover, it includes the use of different kind of chemical products that might be harsh on some kind of polymers. In this section, we present the feasibility of the three omega method when metallic line conductors are prepared by means of an inkjet printing technology. When applying such technology, the metal-based ink is directly printed on the substrate where no chemical and solvent application is required and no mask patterning is needed. In this way, the number of processing steps and the amount of material used is reduced which implies reduction of time, cost and waste [PER 2010]. It is the first time, to the best of our knowledge, that the three omega method is associated to the inkjet printing technology for the measurement of thermal conductivity.

The compatibility of inkjet printing technology with the three omega method is tested on PI and PEEK. Experimental measurements are then compared to Cahill's solution. Finally, an improved model is designed using FEM method.

III.2. Applying inkjet printing technology on PI and PEEK

III.2.a. Sample preparation by inkjet printing technology

In this study, the inkjet printer used is a DMP-2800 from FUJIFILM Dimatix. It has a platinum plate of 210x315 mm printing surface area that can be controlled in X, Y and θ directions. This plate is equipped with a vacuum system to tightly hold the substrate. Furthermore, the printer has an alignment camera that permits to choose the starting point of printing and to observe preceding printed patterns. DMP-2800 inkjet printer employs the piezoelectric drop on demand method that provides small drops and high placement accuracy. A printing head of 16 piezoelectric nozzles which operates in a bend mode is used. One of the walls of the ink chamber is made of a piezoelectric ceramic material. When a firing voltage is applied, this wall is bended causing droplet ejection as presented in figure 4.21 [PER 2010].

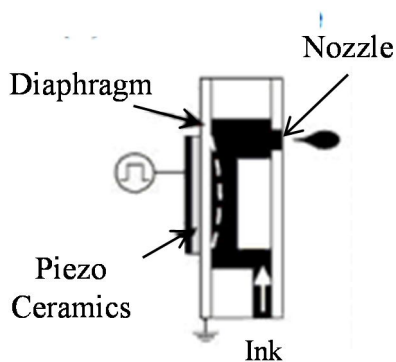


Figure 4.21: Piezoelectric bending mode [PER 2010].

The printing ink used to prepare the metallic lines is solvent based silver nanoparticles from SunTronic. Before starting the printing process, the substrate was cleaned in isopropanol under ultrasound waves for 5 minutes. Then, the substrate was loaded in the printing machine and aligned correctly on the platinum plate. The desired metallic lines pattern for the three omega measurements were designed on DMP's pattern editor program. The firing voltage of the piezoelectric nozzles was set to 30 volts. At the end of the printing process, the substrate was unloaded and sintering process was performed at 200°C for 30 minutes.

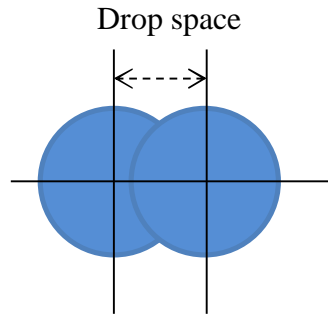


Figure 4.22: Space between two ink droplets.

The available printing head used in the study has nozzles of $40\ \mu\text{m}$ diameter. The first trials were done on polyimide substrate. On the pattern editor program, the metallic lines were designed to have a width equivalent to two droplets with a drop space set to $25\ \mu\text{m}$ (figure 4.22). Actually, the average droplet diameter produced when printed on the polyimide substrate is equal to $35\ \mu\text{m}$. Figure 4.23(a) shows a metallic line printed by the DMP-2800 inkjet printer on PI substrate. The average metallic line width measured under an optical microscope is found to be approximately $58\ \mu\text{m}$.

On the other hand, on PEEK substrate, one drop was set for the metallic line width. This resulted in an average width of $37\ \mu\text{m}$. Figure 4.23(b) show a metallic line printed on PEEK substrate.

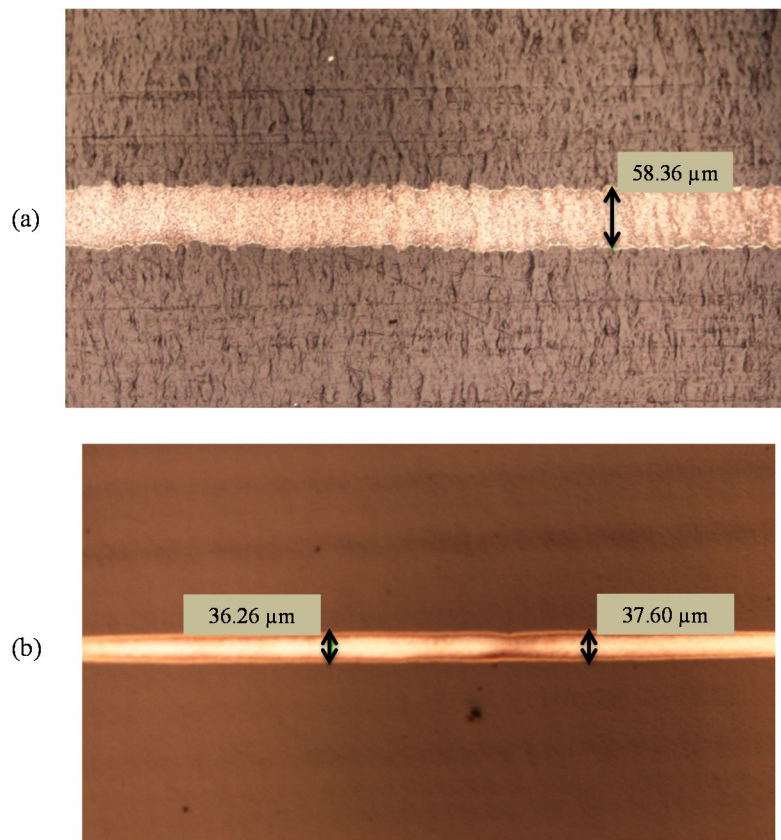


Figure 4.23: Metallic lines printed by inkjet technology on PI (a) and PEEK (b).

Once the design of metallic lines on the samples by inkjet printing technology is well controlled, we have investigated the measurement of the thermal conductivity of this kind of samples.

III.2.b. Thermal conductivity measurement of PI

The thermal conductivity measurements were done on several metallic lines printed on the surface of Polyimide at room temperature $T_0 = 23.2$ °C by the use of the three omega method. Among them are lines A, B, and C listed with their properties in table 4.9. The parameter $2b_{\text{avg}}$ is the average width measured over a metallic line.

Table 4.9: Properties of metallic lines deposited by inkjet technology on Polyimide substrate.

line	$2b_{\text{avg}}$ (μm)	l (mm)	R_0 (Ω)	Power rms (W/m)
A	51	1	36.675	2.36
B	58	2	39.825	4.57
C	64	2	32.838	1.18

The temperature coefficients of resistance β_h of the printed metallic lines are determined by the use of the hot plate method. Figure 4.24, shows an increasing linear graph of temperature versus resistance of the printed metallic line B.

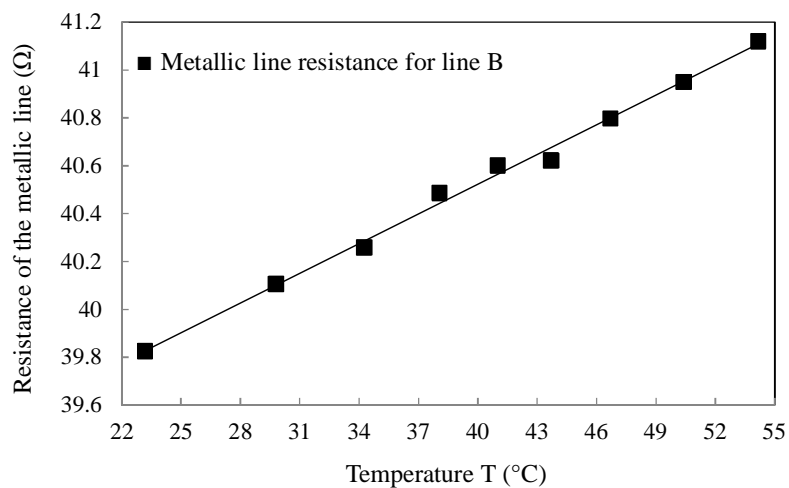


Figure 4.24: Metallic line resistance measured at different temperatures for line B.

The temperature coefficients of resistance β_h of metallic lines A, B and C are listed in table 4.10. We can notice that the temperature coefficient of resistance for the silver printed metallic lines is around three times lower than that of the gold metallic lines.

Table 4.10: Temperature coefficient of resistance of lines A, B, and C measured by the hot plate method.

Metallic line	A	B	C
β_h ($^{\circ}\text{C}$)	9.05E-4	1.04E-3	1.28E-3

The linear regime frequency upper and lower limits are determined in order to measure the third harmonic voltages. We recall the thickness of the polyimide substrate $t_s = 1$ mm. The lower frequency limit is calculated to be 0.578 Hz for the three printed metallic lines. The higher frequency limits are found to be 1.14 Hz, 1.1 Hz, and 0.904 Hz for metallic lines A, B, and C respectively.

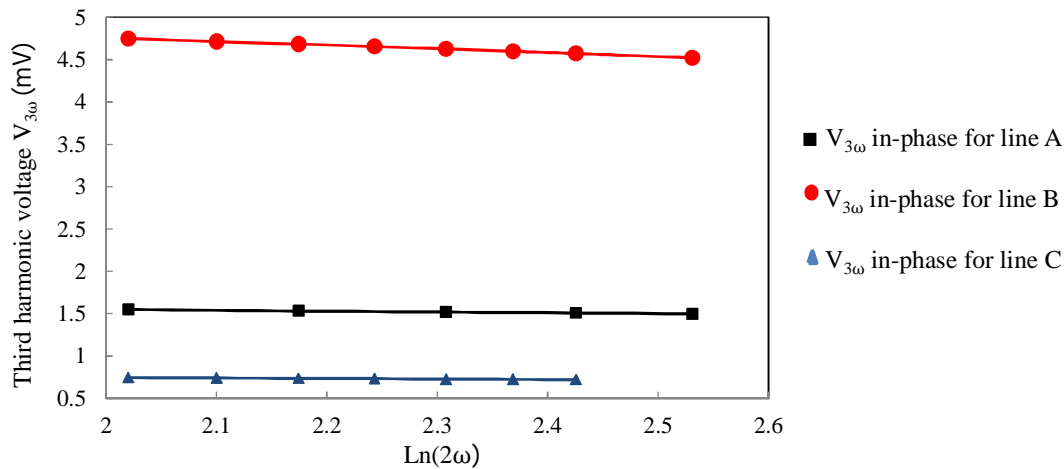
**Figure 4.25: Measured in-phase third harmonic voltages for lines A, B, and C plotted over the linear regime frequency range of each line.**

Figure 4.25 represents the in-phase third harmonic voltages for the printed metallic lines A, B, and C plotted over the linear regime frequency range corresponding to the calculated thermal conductivity. We can notice that for the three lines, the third harmonic voltages follow a linear path. We can find in table 4.11 the thermal conductivity values measured for polyimide through lines A, B, and C.

Table 4.11: Thermal conductivities measured for polyimide through inkjet printed lines.

Metallic line	A	B	C
k (W/m.K)	0.518	0.500	0.529

We can notice that the thermal conductivity values measured here are in good agreement with those measured by metallic lines deposited by photolithography over polyimide (table 4.2).

As we can notice in figure 4.23, the metallic line printed on polyimide substrate is of non-uniform width. However, this non-uniformity has no effect on the value of the calculated thermal conductivity. This can be explained by observing equation 1.53 where the parameter $2b$ is not considered when calculating the thermal conductivity of material.

II.2.c. Thermal conductivity measurement of Polyether ether ketone (PEEK)

The previous section has showed that the thermal conductivity of Polyimide can be measured using the three omega method over metallic lines prepared by inkjet printing technology. In this section another material is used to confirm the compatibility of the three omega method with inkjet printing technology. The material used here is Polyether ether ketone (PEEK). PEEK is a thermoplastic polymer with good wear resistance, good insulating properties and high heat distortion temperature. These properties render it an important material in electronics, automotive, aircraft and health care industries [FRA 1991]. The PEEK polymer used here is bought from Goodfellow. It has a thickness of 1mm, density of 1260 Kg/m³, specific heat capacity of 1340 J/Kg.K, and a thermal conductivity of 0.25 W/m.K.

Table 4.12 represents the different properties of three printed metallic lines used to measure the thermal conductivity of PEEK.

Table 4.12: Different properties of metallic line D, E, and F printed on PEEK.

line	Average $2b$ (μm)	l (mm)	R_0 (Ω)	β_h ($^{\circ}\text{C}^{-1}$)	Power rms (W/m)
D	35	2	127.95	5.61E-04	0.677
E	37	2	160.96	5.35E-04	1.293
F	40	2	154.31	5.40E-04	1.334

The temperature coefficient of resistance β_h of the metallic lines is measured using the hot plate method. We can notice that in this case the values of β_h are smaller than those measured for PI. The printing head used in printing the metallic lines over PEEK is different than the one used when preparing PI sample.

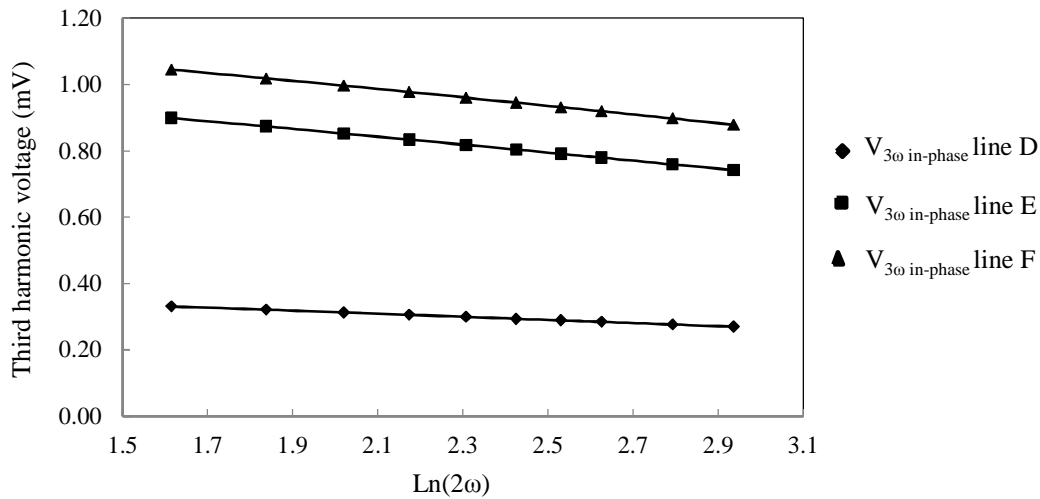


Figure 4.26: The in-phase third harmonic voltages measured over lines D, E, and F.

Figure 4.26 represents the in-phase third harmonic voltages measured over metallic lines D, E, and F printed on PEEK substrate. The in-phase third harmonic voltages are close in value for metallic lines E and F since approximately the same power is applied on these lines. Moreover lines E and F have somehow the same dimensions. The power applied on line D is half of that applied on E and F. We can find the values of the thermal conductivities measured by each line over PEEK substrate in table 4.13.

Table 4.13: PEEK thermal conductivity measured by lines D, E, and F.

Metallic line	D	E	F
k (W/m.K)	0.272	0.298	0.294

The average thermal conductivity measured for PEEK substrate is found to be $k_{avg} = 0.288$ W/m.K. This value is in good agreement with the thermal conductivity of PEEK given by the supplier (Goodfellow).

III.3. Experimental-theoretical comparison for PI and PEEK

III.3.a. Polyimide

Experimental measurements performed over PI are compared to Cahill's solution. The experimental and theoretical in-phase and out-of-phase third harmonic voltages are plotted for metallic lines B for an average width $2b = 58 \mu\text{m}$.

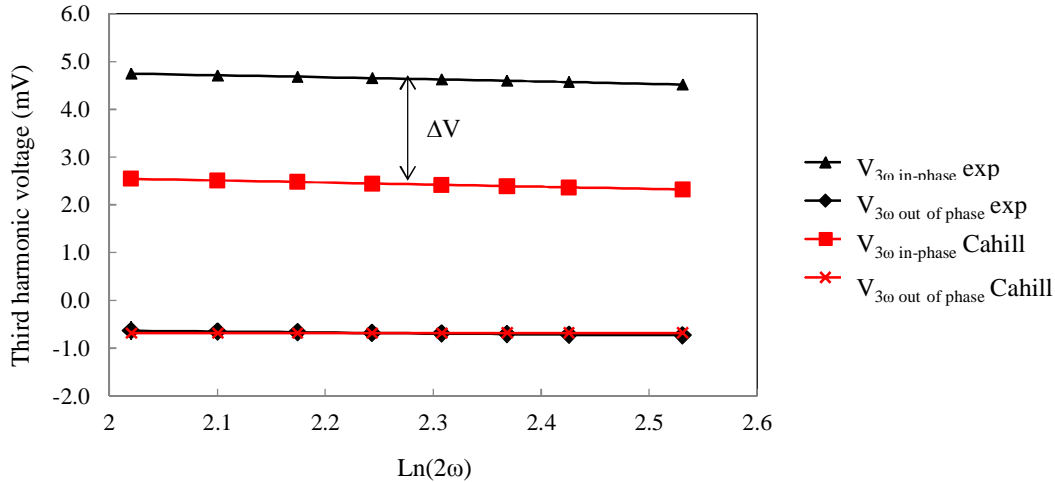


Figure 4.27: Theoretical and experimental in-phase and out-of-phase third harmonic voltages measured on line B over PI substrate.

In figure 4.27, we can observe that experimental in-phase measurements overestimate Cahill's solution.

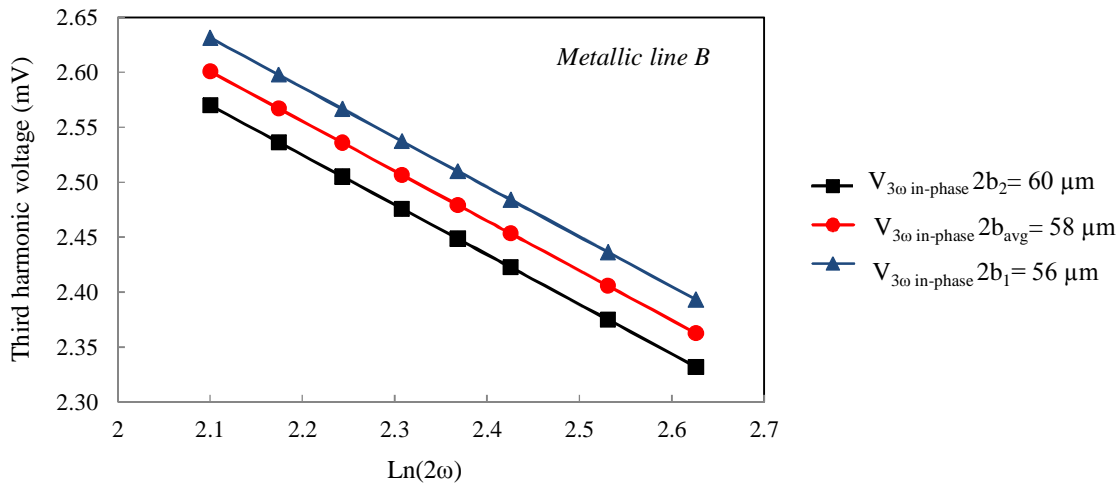


Figure 4.28: The in-phase third harmonic voltages plotted with respect to Cahill for $2b_1 = 56 \mu\text{m}$, $2b_{\text{avg}} = 58 \mu\text{m}$ and $2b_2 = 60 \mu\text{m}$.

Now, the effect of the variation of the width of the metallic line printed using inkjet printing technology on PI is studied using Cahill's formula (equation 4.1). The average width measured on metallic line B is $2b_{\text{avg}} = 58 \mu\text{m}$. We consider three different width $2b_1 = 56 \mu\text{m}$, $2b_{\text{avg}} = 58 \mu\text{m}$, and $2b_2 = 60 \mu\text{m}$. Cahill's solution is plotted for the three different widths (figure 4.28). We can notice that the magnitude of the in-phase third harmonic voltage increases as the width decreases. However, the slope is the same for the three different linear graphs. Consequently, the variation of the metallic line width on polyimide substrate has no influence on the calculated thermal conductivity.

III.3.b. PEEK

As for polyimide substrate, experimental measurements and theoretical data obtained by Cahill's method are plotted for comparison reasons for metallic line F on PEEK as shown in figure 4.29. We can always notice an offset ΔV in the in-phase third harmonic voltages.

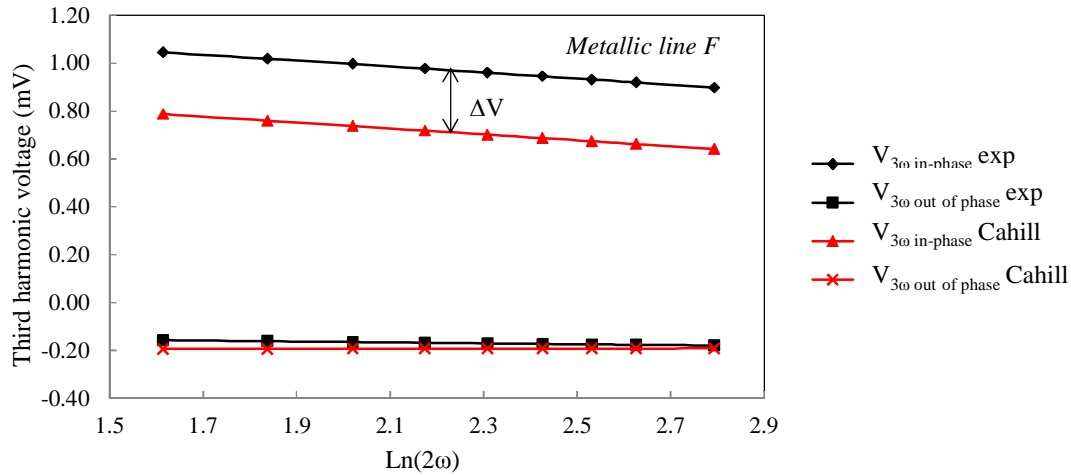


Figure 4.29: Theoretical and experimental in-phase and out-of-phase third harmonic voltages measured on line F over PEEK substrate.

The difference between the experimental and Cahill's in-phase third harmonic voltages ΔV for both PI and PEEK reminds us of the frequency independent temperature oscillation ΔT_f produced due to a film-on-substrate system as explained in chapter 3. The offset ΔV is calculated for both PI and PEEK and found to be 2.1 mV and 0.254 mV respectively. However this difference (ΔV) has no influence on the calculated thermal conductivity.

III.4. Modeling improvement using FEM method

III.4.a. Applying numerical simulation to polyimide with printed metallic lines

As presented in figure 4.23, the inkjet printing process produces non-uniform metallic lines on the surface of the two polymers. Moreover, these metallic lines are of variable thickness. In this section we study among others things, the influence of width and thickness variation observed when using inkjet printing on the in-phase third harmonic voltages. This width effect has already been investigated in section III.3.a. However, numerical simulation using COMSOL[®] is also performed to examine this effect together with the influence of the metallic line thickness.

The heating element of width $2b$ made of solvent based silver nanoparticles is placed on the surface of the medium under-test (polyimide). Only half of the structure is simulated and the temperature boundary conditions are set as in section II.4.a.

Different parameters such as the width ($2b$) and the thickness (t) of the metallic line and the solvent based silver nanoparticles thermal conductivity (k) are investigated to verify their influence on the precision of the thermal conductivity retrieved by the method proposed.

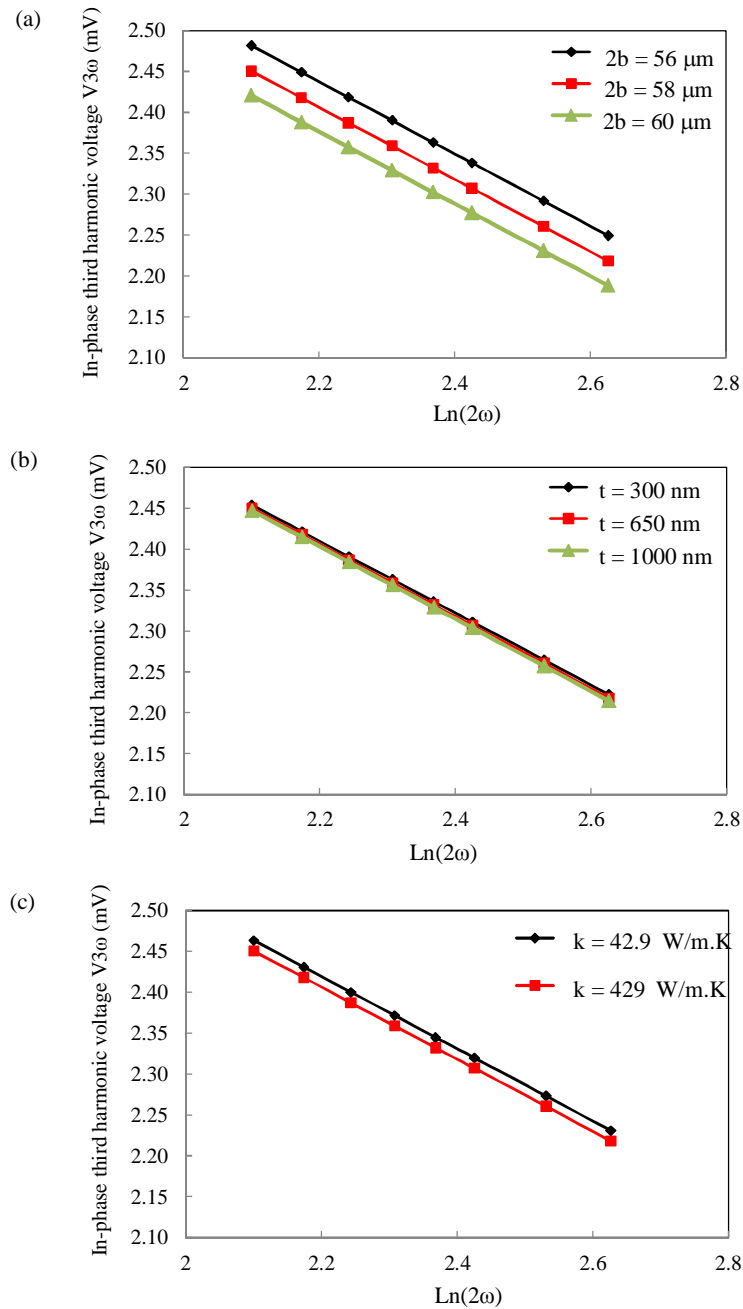


Figure 4.30: The theoretical in-phase third harmonic voltages calculated by FEM for different metallic line width $2b$ (a) different metallic line thickness t (b) and different thermal conductivities of printed ink (c).

In figures 4.30(a), 4.30(b) and 4.30(c), the in-phase third harmonic voltages are plotted for different metallic line widths $2b$, thickness t and thermal conductivities k . These studies are done for metallic line B. We can notice that the slope keeps its value in each study. We conclude that the variation of the parameters $2b$, t and k has no influence on the calculated thermal conductivity. This conclusion is coherent with the one drawn in chapter III.

- Effects of the thermal contact resistance

As discussed in section III.3, the experimental in-phase third harmonic voltages plotted for line B overestimate Cahill's solution. This is due to the existence of a thermal contact resistance between the printed metallic line and the surface of substrate. This resistance is given by:

$$R_f = \frac{\Delta T_f * 2b}{P_{rms}} \quad (4.3)$$

where R_f is the thermal contact resistance in $W/m^2.K$, ΔT_f is the frequency independent temperature oscillations in K, $2b$ is the metallic line width in meters, and p_{rms} is the rms power applied to the metallic line in W/m.

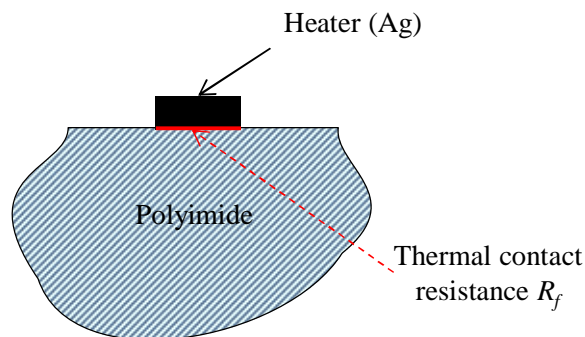


Figure 4.31: Thermal contact resistance R_f between the printed metallic line and the surface of PI.

The frequency independent temperature oscillations are calculated for metallic line B and are found to be $\Delta T_f \sim 7.15$ °C. Consequently, according to equation 4.3, the thermal contact resistance R_f is equal to $90.5E-6$ $m^2.K/W$. Thus, in order to improve modeling, a thin thermally resistive layer is added to the structure between the printed metallic line and the surface of substrate to simulate resistance R_f (figure 4.31). Figure 4.32 shows the experimental and theoretical simulation (FEM and Cahill) data. On one hand, we note that FEM modeling and Cahill's method lead to comparable results when the contact thermal resistance is not taken into account. On the other hand, thanks to the new FEM modeling approach that

introduces the contact thermal resistance, the simulation findings agree now very well with the measured data.

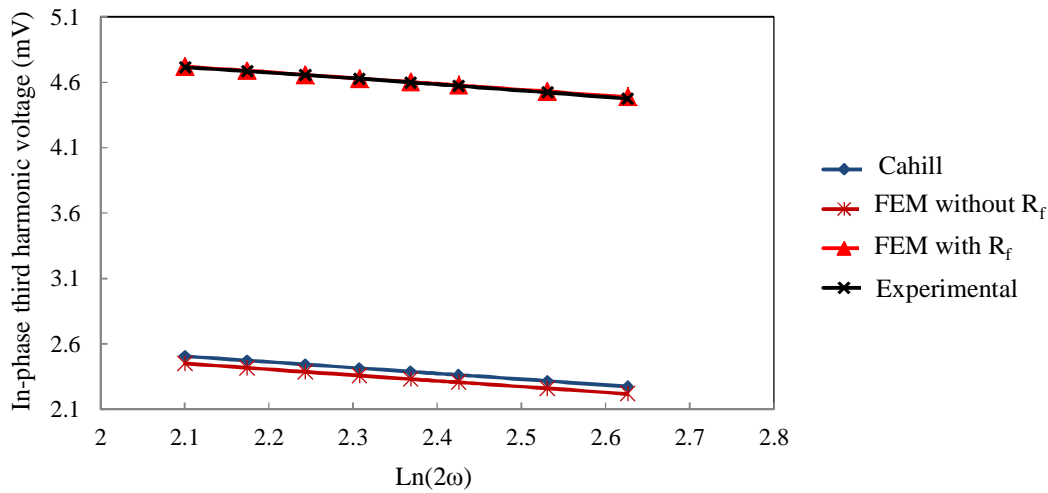


Figure 4.32: In-Phase third harmonic voltage obtained by different methods for PI substrate (Cahill's formula, FEM and experimental measurements).

The study of all these effects have shown that the method proposed using inkjet technology allows the thermal conductivity measurement with a good level of confidence.

The effect of the thermal contact resistance is also studied for AC temperature oscillations measured over a wide frequency range. Figure 4.33 presents the AC temperature oscillations plotted with respect to Cahill's solution and FEM modelling for frequencies between 0.01 Hz and 10 MHz. For Cahill's solution (in red), the thermal contact resistance is not taken into consideration.

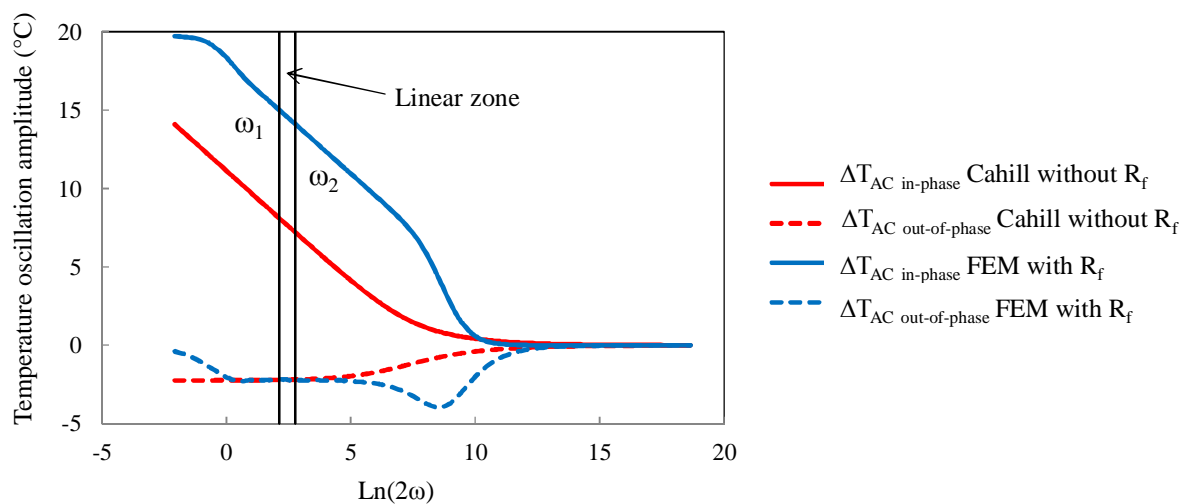


Figure 4.33: In-phase and out-of-phase temperature oscillations plotted over a wide frequency range.

In the linear zone, we can observe similar slopes for the data obtained by Cahill's solution and FEM modeling in the linear regime. However, at higher frequencies starting at around 90 Hz, the FEM in-phase AC temperature oscillations plotted with respect to the natural logarithm of the thermal excitation frequency 2ω are no more parallel to Cahill's based solution. Also, the FEM out-of phase temperature oscillations deviate from Cahill's solution.

III.4.b. Applying numerical simulation to PEEK with printed metallic lines

In figure 4.23(b), a metallic line printed on PEEK substrate using inkjet printing technology is presented. We can see that less variations are produced at the level of the width of the printed metallic line on PEEK than on PI substrate (figure 4.23 (a)). This is due to the fact that the surface of PEEK is not as rough as that of PI.

On the other hand, as for PI substrate, Cahill's solution overestimates the experimental measurements performed on PEEK substrate due to a thermal contact resistance R_f . This resistance is calculated according to equation 4.3 for metallic line F and found to be $R_f = 48.97E-6 \text{ m}^2 \cdot \text{K/W}$. The contact resistance is introduced in FEM modeling and comparison between experimental and theoretical (Cahill and FEM) data is performed (Figure 4.34).

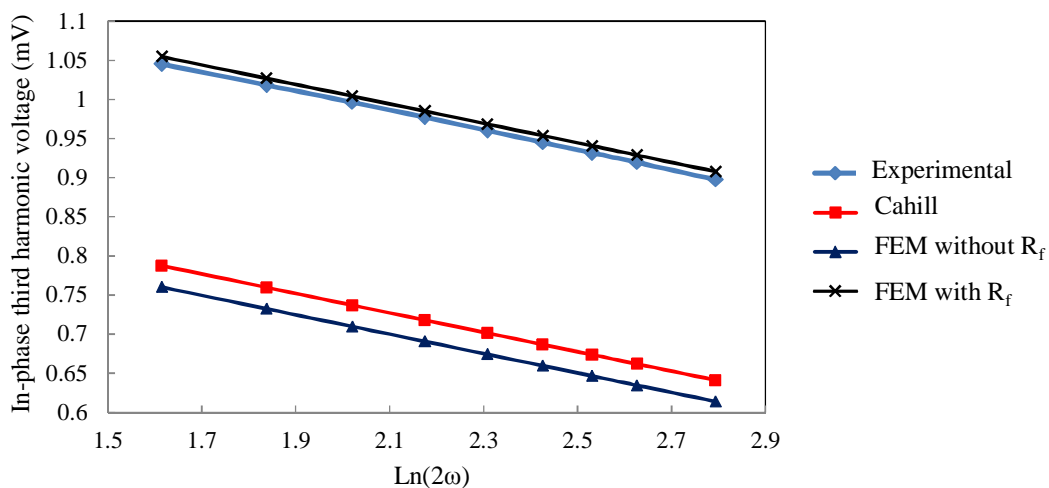


Figure 4.34: In-Phase third harmonic voltage obtained by different methods for PEEK substrate (Cahill's formula, FEM and experimental measurements).

The conclusions drawn after comparison are similar to those found for PI substrate in figure 4.32. FEM modeling when considering the thermal contact resistance agrees well with the experimental data.

III.5. Conclusion

In this section, we have proposed the measurement of the thermal conductivity of PI and PEEK using the three omega method together with inkjet printing technology for sample preparation. Different polymer materials possess low chemical resistance to different solutions and solvents used in photolithography process. This renders the measurement of their thermal conductivity using the three omega method somehow difficult. Consequently, a new technology, inkjet printing technology, was introduced to deposit the metallic lines on the surface of polymers without the use of any chemical product. Inkjet printing technology is now considered to be a competitor to photolithography due to its simplicity and cost. Initially, metallic lines were printed using this technology on PI substrate. We were able to produce metallic lines of 60 μm average width. Linear regime frequency range was calculated and the third harmonic voltages were measured using the three omega method. An average thermal conductivity of 0.515 W/m.K was calculated at 23 °C. We have observed that this value is in good agreement with the value determined when using metallic line deposited by photolithography over PI. This proves that the three omega method is compatible with inkjet printing technology. PEEK is one of the polymers that are not compatible with photolithography. In our study metallic lines of around 40 μm width were printed on PEEK by inkjet printing technology. The three omega method was applied and an average thermal conductivity of 0.288 W/m.K was calculated. This value showed a good agreement with the thermal conductivity value given by the supplier. This confirms again the compatibility of the three omega method with inkjet printing technology. When comparing the experimental in-phase third harmonic voltages measured using the three omega method with Cahill's theoretical data for PI and PEEK, it was found that experimental $V_{3\omega \text{ in-phase}}$ overestimates the theoretical $V_{3\omega \text{ in-phase}}$. This is due to the existence of a thermal resistance between the printed metallic lines and the surface of substrate. This thermal resistance is calculated. Then a thin thermal resistive layer is inserted between the printed metallic line and surface of substrate in order to investigate the effect of this resistance by means of FEM. The numerical simulation results showed a good agreement with the experimental data.

Conclusion

Polymers are classified into three groups: thermoplastics, elastomers, and thermosets. Different chemical and physical properties of polymers were recalled in this chapter. The thermal conductivity of polymers was measured at different temperatures using the three omega method. Samples for the three omega method measurements are usually prepared by photolithography. However, not all polymers are compatible with this process due to their low chemical resistance to chemical solutions.

The thermal conductivity of polyimide was measured using the three omega method. The metallic lines were successfully deposited on the surface of PI by photolithography. The thermal conductivities of polyimide at 20 °C, 25.4 °C, 40 °C, 90 °C, and 135 °C were found to be 0.492 W/m.K, 0.498 W/m.K, 0.53 W/m.K, 0.635 W/m.K, and 0.714 W/m.K respectively. One can see that the thermal conductivity of PI increases with increasing temperature.

Also, the thermal conductivity of PDMS was measured. A special procedure was used to prepare PDMS sample for the three omega measurements. Actually, the metallic lines are embedded in the surface of PDMS. The thermal conductivity was successfully measured and an average value of 0.21 W/m.K at 22 °C was obtained. The thermal conductivity was also measured at different temperatures and it has been found that PDMS thermal conductivity increases with increasing temperature. The error produced by the experimental setup when using soft flexible materials as PDMS is due to the micromanipulator tips on one hand and the manual hot plate used to heat the sample on the other hand.

Inkjet printing technology was also used with the three omega method. In particular, we have demonstrated that the thermal conductivity of polyimide can be measured by using metallic lines printed by inkjet technology. The thermal conductivity obtained by this technique agrees very well with that measured through metallic lines prepared by photolithography. These metallic lines were printed easily in a short period of time without the use of different chemicals and solvents as required in photolithography. We succeeded in performing measurements on metallic lines printed on a relatively rough surface of polyimide sheet. In addition, although the printed metallic lines are not perfectly homogeneous in terms of width, it seems that no perturbations were induced to measurements done in the linear zone. In order to confirm the compatibility of the three omega method with inkjet printing technology, metallic lines were printed on PEEK. Its thermal conductivity was measured and found to be close to the value given by the supplier. This investigation demonstrates that this

technique will permit the characterization of many polymers that have a low chemical resistivity.

The printing head used in this study introduces some limits concerning the width of the fabricated metallic lines; a minimum width of 40 μm can be achieved. Using this printer permits only measurements on relatively thick substrates. The limits that we faced concerning the metallic lines width can be overcome by replacing the printing head by another having smaller nozzle diameter that can produce narrower metallic lines. This yields to the ability of characterizing thin polymer films over substrates of known thermal conductivities. Finally, this technology can be applied on polymers with a maximum operational temperature higher than 200 $^{\circ}\text{C}$.

In this chapter, an innovative method for measuring the thermal conductivity of polyimide and polyether ether ketone has been presented. The method is based on the use of inkjet printing technology that offers important benefits regarding cost and timeliness. In the current context of the booming of the applications based on flexible materials this method is very promising.

REFERENCES

- [CHU 2001] D.D. L. CHUNG
“Materials for thermal conduction,”
Applied Thermal Engineering Vol. 21, pp1593-1605, 2001.
- [COO 2002] J. COOPER and M.G. WHITESIDES.
“Polydimethylsiloxane as a material for fabricating microfluidic devices,”
Accounts of Chemical Research, Vol. 35, No.7, pp 491-499, 2002.
- [DAS 1996] P. DASHORA and G. GUPTA
“On the temperature dependence of the thermal conductivity of linear
amorphous polymers,”
Polymer, Vol. 37, pp 231-234, 1996.
- [DAW 2006] A. DAWSON, M. RIDES, and J. NOTTAY
“The effect of pressure on the thermal conductivity of polymer melts,”
Polymer Testing, Vol. 25, pp. 268-275, 2006.
- [FRA 1991] N. L. FEANCHINA and T. J. McCARTHY
“Surface modifications of Poly(ether ether ketone)”,
Macromolecules Vol. 24, pp 3045-3049, 1991.
- [GHO 1996] M. K. GHOSH and K. L. MITTAL
“Polyimide: Fundamentals and Applications,”
Copyright by M. Dekker Inc, 1996.
- [GOO 2000] M.T. GOOSEY
“Electronics Applications of Polymers II,”
Rapra technology limited, 2000.
- [GOO 2004] V. GOODSHIP
“Practical guide to injection moulding,”
Rapra technology limited and AGBURG limited, 2004.
- [GUN 1994] H. GUNTHER
“Polymer Properties at Room and Cryogenic Temperatures,”
The international cryogenics monograph series, 1994.
- [HAG 2009] S. HAGE-ALI, N. TIERCELIN, P. COQUET, R. SAULEAU, H. FUJITA,
V. PREOBRAZHENSKY, and P. PERNOD.
“A Millimeter-wave microstrip antenna array on ultra-flexible micromachined
Polydimethylsiloxane (PDMS) polymer,”
IEEE Antenna and Wireless Propagation Letters, Vol. 8, pp 1306-1309,
2009.
- [HAN 2011] Z. HAN, A. FINA
“Thermal conductivity of carbon nano tubes and their polymer nano
composites,”

Progress in Polymer Science, Vol. 36, pp 914-944, 2011.

- [HAS 2011] C. HASSLER, T. BORETIUS, and T. STIEGLITZ
“Polymers for Neural Implants,”
Journal of Polymer Science: Part B: Polymer Physics, Vol. 49, pp. 18-33,
2011.
- [HON 2001] J. W. HONG, T. FUJI, M. SEKI, T. YAMAMOTO, and I. ENDO
“Integration of gene amplification and capillary gel electrophoresis on a
polydimethylsiloxane-glass hybrid microchip,”
Electrophoresis, Vol. 22, pp. 328-333, 2001.
- [HON 2010] J. HONG, J. LEE, C. K. HONG and S. E. SHIM
“Effect of dispersion state of carbon nanotube on the thermal conductivity
of poly(dimethylsiloxane) composites,”
Current Applied Physics, Vol. 10, pp. 359-363, 2010.
- [JAC 2002] A. JACQUOT, B. LENOIR, A. DAUSCHER, M. STOLZER and
J. MEUSEL
“Numerical simulation of the 3ω method for measuring the thermal
conductivity,”
Journal of Applied Physics, Vol. 91, pp.4733-4738, 2002.
- [JAN 2011] S. JANFAOUI, C. SIMON, N. COULON, and T. MOHAMMED- BRAHIM
“Behavior of the parameters of microcrystalline silicon TFTs under
mechanical strain,”
Solid state electronic, Vol. 93, pp 1-7, 2011.
- [KAU 2007] P. B. KAUL, K. A. DAY, and A.R. ABRAMSON
“Application of the three omega method for the thermal conductivity
measurement of polyaniline,”
Journal of Applied Physics Vol. 101, pp 083507, 2007.
- [KO 2012] H. KO, R. KAPADIA, K. TAKEI, T. TAKAHASHI, X. ZHANG, and A.
JAVEY
“Multifunctional, flexible electronic systems based on engineered
nanostructured material,”
IOP Science, Nanotechnology, Vol.23, 344001 (pp 1-11), 2012.
- [KUN 2006] J. KUNCOVA-KALLIO and J. KALLIO PASI.
“PDMS and its suitability for analytical microfluidic devices,”
Proceedings of the 28th IEEE, pp. 2486-2489, 2006.
- [KUR 1999] K. KURBAYASHI, M. ASHEGHI, M. TOUZELBAEV, and K. E.
GOODSON, “Measurement of the thermal conductivity anisotropy in
polyimide films,”
IEEE Journal of Microelectromechanical Systems Vol.8, pp 180-191,
1999.
- [LEE 2005] K. J. LEE, K.A. FOSSER, and R. G. NUZZO

- “Fabrication of stable metallic embedded in Poly(dimethylsiloxane) and model applications in non-planar electronic and lab-on-a-chip device patterning, ”
Advanced Functional Materials, Vol. 15, pp.557-566, 2005.
- [MAC 2007] W. A. MACDONALD, M. K. LOONEY, D. MACKERRON, R. EVESON, R. ADAM, K. HASHIMOTO, and K. RASKOS,
“Latest advances in substrates for flexible electronics,”
Journal of the SID, Vol. 15, pp 1075-1083, 2007.
- [MAR 2007] J. E. MARK
“Physical Properties of Polymers Handbook,”
Springer science +Business media , LLC, 2007.
- [PAT 2008] J. N. PATEL, B. KAMINSKA, B. L. GRAY, and B. D. GATES
“PDMS as a sacrificial substrate for SU-8-based biomedical and microfluidic applications,”
Journal of Micromechanics and Microengineering, Vol. 18, 095028 (pp 1-11), 2008.
- [PER 2010] J. PERELAER and U.S. SCHUBERT
“Inkjet printing and alternative sintering of narrow conductive tracks on flexible substrates for plastic electronic applications, Radio frequency identification fundamentals and applications, design methods, and solutions,”
Cristina Turcu (Ed.), ISBN: 978-953-7619-72-5, In Tech. 2010.
- [PIER 2008] T. PIER, K. KANDOUSSI, C. SIMON, N. COULON, T. MOHAMMED-BRAHIM, and H. LHERMITE
“Excimer laser annealing of microcrystalline silicon,”
Physica status solidi, Vol. 5, pp 3234-3238, 2008.
- [POH 1963] R. O. POHL
“The Applicability of the Debye Model to Thermal Conductivity,”
Zeitschrift ffor Physik, Vol. 176, pp 358-369, 1963.
- [PUT 2003] S. A. PUTNAM, D. G. CAHILL, B. J. ASH, and L. S. SCHDLER
“High precision thermal conductivity measurements as a probe of polymer/nanoparticle interface,”
Journal of Applied Physics, Vol. 94, pp 6785-6788, 2003.
- [RAU 2003] C.E. RAUDZIS and F. SCHATZ
“Extending the 3ω method for thin-film analysis to high frequencies,”
Journal of Applied Physics, Vol. 93, pp.6050-6055, 2003.
- [RIN 2004] H. RINGSDORF
“Hermann Staudinger and the future of polymer research, Jubilees-Beloved Occasions for Cultural Piety,”
Angewandte Chemie International Edition., Vol. 43, pp 1064 –1076
Wiley-VCH Verlag GmbH & Co. KGaA, Weinheim, 2004.

- [SHE 2013] B. SHEN, Z. ZENG, C. LIN, and Z. HU
“Thermal conductivity measurement of amorphous Si/SiGe multilayer films by 3 omega method,”
International Journal of Thermal Sciences, Vol. 66, pp 19-23, 2013.
- [STU 2002] B. H. STUART
“Polymer Analysis,”
John Wiley & Sons, LTD, 2002.
- [SUN 2007] Y. SUN and J. A. ROGERS
“Inorganic semiconductors for flexible electronics,”
Advanced Materials, Vol.19, pp 1897-1916, 2007.
- [TIE 2006] N. TIERCELIN, P. COQUET, R. SAULEAU, V. SENEZ and H. FUJITA.
“Polydimethylsiloxane membranes for millimeter-wave planar ultra-flexible antennas, ”
Journal of Micromechanical Microengineering, Vol.16, pp 2389-2395, 2006.
- [WAN 2009] H. WANG and M. SEN
“Analysis of the 3-omega method for thermal conductivity measurement,”
International Journal of Heat and Mass Transfer, Vol.52, pp.2102-2109, 2009.
- [XU 2011] X. XU, H. SUBARRAMAN, D. PHAM, A. HOSSEINI, X. LIN, and R. T. CHEN
“Transfer and characterization of silicon nanomembrane based photonic devices on flexible polyimide substrate,”
Optoelectronic interconnects and component integration X, edited by Alexei L. Glebov, Ray T.Chen, Proc. of SPIE 7944, 79440F, 2011.
- [YOU 1991] R. J. YOUNG and P. A. LOVELL
“Introduction to Polymers,”
Taylor & Francis, Second edition 1991.
- [YUA 2011] L. YUAN, Y. TAO, J. CHEN, J. DAI, T. SONG, M. RUAN, Z. MA, L. GONG, K. LIU, X. ZHANG, X. HU, J. ZHOU, and Z. L. WANG
“Carbon nanoparticles on carbon fabric for flexible and high-performance field emitters”,
Advanced Functional Materials XX, pp 1-7, 2011.
- [ZAR 2011] V. ZARDETTO, T. M. BROWN, A. REALE, and A. D. CARLO
“Substrates for flexible electronics: A practical investigation on the electrical, film flexibility, optical, temperature, and solvent resistance properties”,
Journal of Polymer Science Part B: Polymer Physics, Vol. 49, pp 638-648, 2011.

General conclusion

General conclusion

In the past few years, the field of flexible or organic electronics has rapidly grown due to the manufacturing technology improvements, high quality processed organic or polymeric materials, and low cost potential. Nevertheless, despite these developments, challenges are still to take up in terms of fabrication and performance of polymeric materials. Such materials offer multiple advantages which permit their exploitation extensively in a large number of flexible electronic applications. The low thermal conductivity of polymers allows their use as dielectrics in many electronic applications such as insulators, intermetallic dielectric layers, encapsulants and dielectric substrates. One of the important issues when fabricating flexible electronics is thermal management. The thermal property which translates the ability to conduct or prevent heat transfer is the thermal conductivity. Therefore, the knowledge of this data is of great importance when selecting a polymer material. Among the different techniques available for the determination of the thermal conductivity of material, we have chosen the three omega method. This method requires heating a metallic line conductor just in contact with the surface of the material under test by an alternating current source. For most solid materials, photolithography process is applied for metallic line deposition on the surface of material. However, in case of soft materials, such a process might cause damage. Consequently, an alternative process based on inkjet printing technology is proposed to print metallic lines on surface of polymer materials to measure their thermal conductivities by means of the three omega method.

In the first chapter we have presented the most commonly used steady state and transient methods to measure the thermal conductivity of materials. Comparison done between these methods has led to the choice of the three omega method, a transient one, which requires few minutes to initiate the measurements. It is considered simple to be implemented. Starting with the heat conduction equation given by Carslaw and Jaeger together with the application of Cahill's assumptions, we have derived Cahill's AC temperature oscillation integral formula. The measured third harmonic voltages are plotted with respect to the natural logarithm of the thermal excitation frequency 2ω . The linear zone of this plot is defined by determining its lower and upper frequency limits. Knowing these frequency limits, the third harmonic voltage measurements can be performed and then the thermal conductivity of the material under test can be extracted.

In order to measure accurately the third harmonic voltages across the metallic line conductor, a three omega method-based experimental setup has been constructed as presented

in chapter II. Two systems, the Wheatstone bridge and the differential amplifier circuits have been designed and realized to extract the third harmonic voltage across the metallic line conductor and to eliminate any spurious third harmonic voltage that might add to the three omega measurements. We have presented the photolithography process used for the deposition of metallic lines on surface of material. Then, we have successfully validated the three omega method-based experimental setup by measuring the thermal conductivities of four materials ranging from insulators to semiconductors. Measurements done using the differential amplifier circuit have shown better results than those obtained when using the Wheatstone bridge circuit. Finally, an error analysis has been achieved and the measurement precision of the three omega method-based experimental setup built in the laboratory was found to be around $\pm 10\%$.

In chapter III, numerical simulations using FEM have been performed to study Cahill's approximations on a metallic line-on-substrate system. These approximations have been applied on the structure and then it was numerically simulated to obtain the temperature oscillations for a large range of frequencies. We have found that Cahill's analytical solution agrees well with FEM results. Moreover, the finite thickness substrate has no influence on the temperature oscillations in the linear regime. Similarly, the variation of the thickness and width of a metallic line does not affect the calculated value of the thermal conductivity. The differential three omega method has also been implemented. The thermal conductivities of 1.38 W/m.K and 11.62 W/m.K of a SiO₂ thin film and an epitaxial grown GaAs layer on GaAs substrate at low temperatures have been measured respectively. Finite element simulations have been performed for a thin film deposited over an infinite substrate and for a thin film-on-substrate system placed on a copper plate. The results of both models together with Cahill's analytical solution have shown a good agreement when compared in the linear zone.

In the last chapter, the three omega method is tested on polymer materials. The concern is the ability to deposit metallic conductors on the surface of polymers without causing any damage to the material. At first, metallic lines have been successfully deposited on PI sample using photolithography process. It was found that the thermal conductivity of PI, measured by the three omega method, increases with increasing temperature. Metallic lines were also fabricated by applying a special procedure to measure the thermal conductivity of PDMS. In this case, the metallic lines were embedded into its surface. The thermal conductivity of 0.21 W/m.K was obtained at 22 °C. A new FEM model for PDMS sample has been designed. We

have found that the results obtained by FEM modelling are in better agreement than Cahill's solution with the experimental measurements. This is due to the fact that the simulated PDMS structure with the embedded metallic line near the surface is closer to reality than Cahill's solution assuming an infinite thin heating element on the surface of material. In a second part of the chapter, metallic lines were printed on the surface of PI sample using inkjet printing technology. The results demonstrated that the three omega method is compatible with inkjet printing technology. Another polymer sample, PEEK, was prepared by this technology for the three omega measurements. A thermal conductivity of 0.288 W/m.K at 22 °C was obtained. All in all, we have shown that the three omega method is feasible when metallic line conductors are prepared by means of inkjet printing technology.

In order to bring some improvements to the system proposed, we envisage the use of an anti-vibratory probe station that might permit the reduction of the three omega method-based experimental setup measurement error. Also, the hot plate used to determine the temperature coefficient of resistance can be replaced by an oven. In this way, the sample is heated uniformly and no vibrations are generated when adjusting temperature.

Most of the previous works related to the three omega method are based on one of the common mode cancellation techniques, either the Wheatstone bridge or the differential amplifier circuit. In this study, the three omega method experimental setup has been validated by applying both cancellation techniques. Then thin films and polymer materials have been characterized using only the differential amplifier electronic circuit. However, the Wheatstone bridge circuit stays an operational technique to measure the thermal conductivity of different materials.

Enhancements can be performed at the level of the inkjet printer employed throughout the study. We have shown that metallic lines of minimum width of 37 μm were achieved when printed on PEEK substrate. Using the DMP-2800 printer allows performing the three omega measurements on relatively thick substrates. Narrower metallic line width might be achieved if using printing heads of smaller nozzle diameter. We note that the droplet diameter depends on the type of the surface of polymer to be tested.

Recently, super-fine inkjet (SIJ) printing technology has appeared as a powerful tool for nanotechnology research. Such technology is capable of printing pattern widths less than 1/10 of those produced by conventional inkjet printing technologies. Such a process is done by controlling the volume of the droplet ejected through the nozzle from the printing head. Metallic lines of few microns in width can be printed if applying this technology. This will

permit the characterization of polymer substrates of lower thicknesses using the three omega method.

Appendix A

Theoretical approach of the three omega method

Table of contents

A.1. Line heater study inside an infinite cylinder.....	A3
A.2. Line heater study at the surface of substrate.....	A7
A.3. The effect of the substrate's thickness.....	A8
REFERENCE APPENDIX A.....	A11

A.1. Line heater study inside an infinite cylinder

Cahill has first assumed a one dimensional line heater encased inside an infinite cylinder (figure A.1). According to Carslaw and Jaeger [CAR 1959] the equation of conduction of heat in cylindrical coordinates is given by:

$$\frac{1}{\alpha} \frac{\partial T}{\partial t} = \frac{\partial^2 T}{\partial r^2} + \frac{1}{r} \frac{\partial T}{\partial r} + \frac{1}{r^2} \frac{\partial^2 T}{\partial \theta^2} + \frac{\partial^2 T}{\partial z^2} \quad (\text{A.1})$$

where T is the instantaneous temperature and α is the thermal diffusivity in m^2/s defined as:

$$\alpha = \frac{k}{\rho c_p} \quad (\text{A.2})$$

where k is the thermal conductivity in $\text{W}/\text{m}\cdot\text{K}$, ρ is the density Kg/m^3 and c_p is the specific heat capacity in $\text{J}/\text{Kg}\cdot\text{K}$.

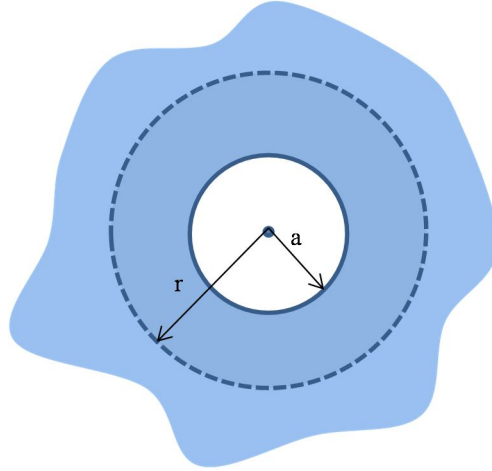


Figure A.1: Cross section of the infinite cylindrical sample.

Assuming that the cylinder is of axis z and that the boundary conditions are independent of θ and z (no circumferential or axial temperature gradient), equation (A.2) is reduced to:

$$\frac{\partial^2 T(r,t)}{\partial r^2} + \frac{1}{r} \frac{\partial T(r,t)}{\partial r} - \frac{1}{\alpha} \frac{\partial T(r,t)}{\partial t} = 0 \quad (\text{A.3})$$

As presented in figure A.2, the instantaneous temperature $T(r,t)$ is equal to the ambient temperature T_0 plus the DC temperature rise $\Delta T_{DC}(r)$ and the steady state temperature oscillations $\Delta T_{AC}(r,t)$.

$$T(r,t) = T_0 + \Delta T_{DC}(r) + \Delta T_{AC}(r,t) \quad (\text{A.4})$$

$$\Delta T_{DC}(r) = T_{DC}(r) - T_0 \quad (\text{A.5})$$

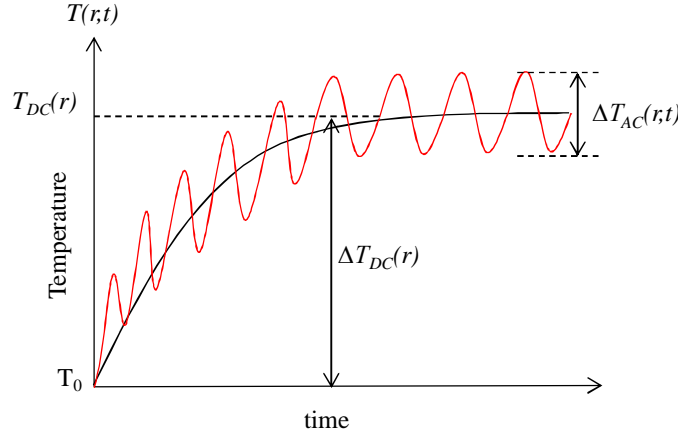


Figure A.2: Behavior of temperature oscillations in the heater.

Substituting equations (A.4) and (A.5) in (A.3) gives:

$$\frac{\partial^2 \Delta T_{AC}(r,t)}{\partial r^2} + \frac{1}{r} \frac{\partial \Delta T_{AC}(r,t)}{\partial r} - \frac{1}{\alpha} \frac{\partial \Delta T_{AC}(r,t)}{\partial t} = \frac{\partial}{\partial r} \left(r \frac{\partial \Delta T_{DC}(r)}{\partial r} \right) = 0 \quad (\text{A.6})$$

The DC temperature rise will not be taken into account in the solution since the thermal conductivity is extracted from steady state temperature oscillations.

$$\frac{\partial^2 \Delta T_{AC}(r,t)}{\partial r^2} + \frac{1}{r} \frac{\partial \Delta T_{AC}(r,t)}{\partial r} - \frac{1}{\alpha} \frac{\partial \Delta T_{AC}(r,t)}{\partial t} = 0 \quad (\text{A.7})$$

To solve equation A.7 separation of variables is used where

$$\Delta T_{AC}(r,t) = \Delta T_{AC}(r)\Theta(t) \quad (\text{A.8})$$

Temperature oscillations are produced at an angular frequency twice the excitation angular frequency. So the temporal evolution $\Theta(t)$ is a function of 2ω :

$$\Theta(t) = \cos(2\omega t) = \Re(\exp(i2\omega t)) \quad (\text{A.9})$$

Substituting (A.9) and (A.8) in (A.7) gives:

$$\begin{aligned} \cos(2\omega t) \frac{\partial^2 \Delta T_{AC}(r)}{\partial r^2} + \cos(2\omega t) \frac{1}{r} \frac{\partial \Delta T_{AC}(r)}{\partial r} - \frac{1}{\alpha} \Delta T_{AC}(r) \frac{\partial}{\partial t} \cos(2\omega t) &= 0 \\ \cos(2\omega t) \frac{\partial^2 \Delta T_{AC}(r)}{\partial r^2} + \cos(2\omega t) \frac{1}{r} \frac{\partial \Delta T_{AC}(r)}{\partial r} - \frac{2\omega i^2}{\alpha} \Delta T_{AC}(r) \cdot \sin(2\omega t) &= 0 \\ \Re \left\{ \left[\frac{\partial^2 \Delta T_{AC}(r)}{\partial r^2} + \frac{1}{r} \frac{\partial \Delta T_{AC}(r)}{\partial r} - q^2 \Delta T_{AC}(r) \right] \exp(i2\omega t) \right\} &= 0 \end{aligned} \quad (\text{A.10})$$

where q is the wavenumber of the thermal wave in radian per meter and is defined by [PAR 2010]:

$$q = \sqrt{\frac{i2\omega}{\alpha}} \quad (\text{rad/m}) \quad (\text{A.11})$$

We can notice that a part of equation A.10, $\frac{\partial^2 \Delta T_{AC}(r)}{\partial r^2} + \frac{1}{r} \frac{\partial \Delta T_{AC}(r)}{\partial r} - q^2 \Delta T_{AC}(r) = 0$ is a modified Bessel equation of order zero and argument qr . The general equation of the modified Bessel equation is given by [BEL 1968]:

$$x^2 \frac{d^2 y}{dx^2} + x \frac{dy}{dx} - (x^2 + \nu^2)y = 0 \quad (\text{A.12})$$

The solution of this equation is:

$$y = c_1 I_\nu(x) + c_2 K_\nu(x)$$

where $I_\nu(x)$ and $K_\nu(x)$ are the modified Bessel functions of the first and second kind of order ν and having an argument x .

If we substitute for $x=qr$ and $\nu=0$ in equation A.12, we can notice that equation 1.44 is the real part of a modified Bessel function of order zero and argument qr . Therefore, the solution of equation A.10 is given by:

$$\Delta T_{AC}(r,t) = \Re\{[c_1 I_0(qr) + c_2 K_0(qr)] \exp(i2\omega t)\} \quad (\text{A.13})$$

Figure A.3 shows a plot of the zero order modified Bessel functions $I_0(x)$ and $K_0(x)$ of the first and second kind respectively. We can notice that $I_0(x)$ tends to infinity for large values of x . On the contrary, $K_0(x)$ tends to zero as x tends to infinity.

To find the unknown constants c_1 and c_2 in equation A.13 the boundary conditions are applied.

As the radial distance r from the heater tends to infinity, the steady state temperature oscillations starts to decay. Moreover, $K_0(qr)$ approaches zero, while $I_0(qr)$ tends to infinity. Therefore:

$$\text{For } r \rightarrow \infty: \quad \Delta T_{AC}(\infty, t) = 0 \quad (\text{A.14})$$

$$I_0(qr) \rightarrow \infty \quad (\text{A.15})$$

$$K_0(qr) = 0 \quad (\text{A.16})$$

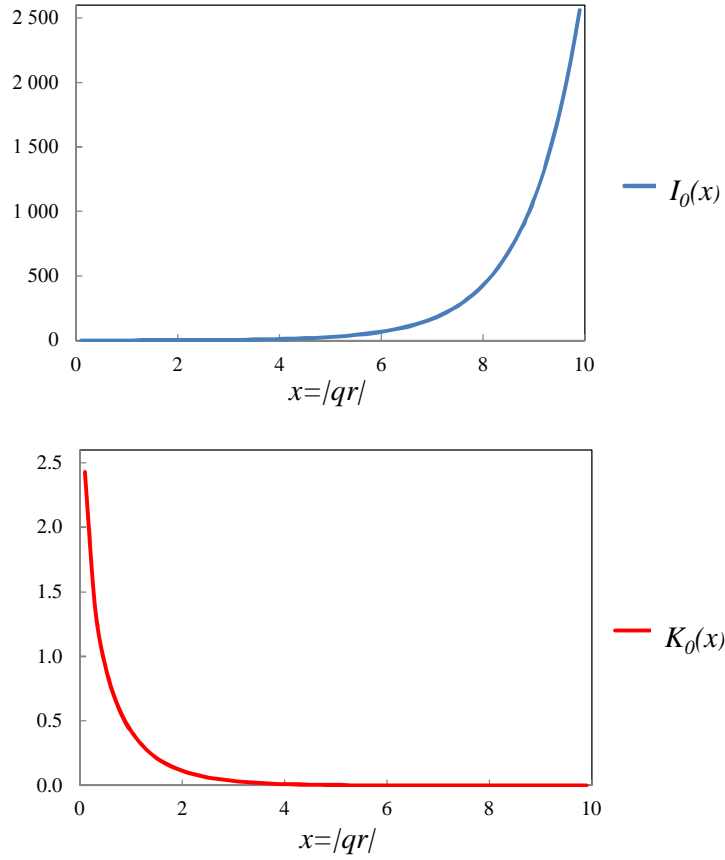


Figure A.3: Zero order modified Bessel functions $I_0(x)$ and $K_0(x)$ of the first and the second kind respectively.

Substituting equations A.14, A.15 and A.16 in equation A.13, the unknown c_1 is found to be zero.

$$c_1=0 \tag{A.17}$$

The rate of heat conduction through a medium in a certain direction is expressed by Fourier’s law of heat conduction (1D heat conduction) in cylindrical coordinates:

$$q_w = \frac{dQ}{dt} = -kA \frac{dT}{dr} \tag{A.18}$$

where q is the heat rate in W and A is the cross-sectional surface area in m^2 .

According to equation A.18, the dissipated heat by the heater at a radial distance $r=a$ from the center of the infinite cylinder is defined by:

$$q_w = \Re(P_{rms} \exp(i2\omega t)) = \lim_{a \rightarrow 0} \left[-kA_s \frac{\partial \Delta T_{AC}(r,t)}{\partial r} \right]_{r=a} \tag{A.19}$$

where k is the thermal conductivity of specimen, P_{rms} is the power dissipated due to direct current in the metal line, and $A_s = 2\pi rl$ is the surface area of the cylinder at a distance $r=a$ from its center.

Substitute $A_s = 2\pi rl$ in equation A.19 and solve for c_2 :

$$q_w = \Re(P_{rms} \exp(i2\omega t)) = \lim_{a \rightarrow 0} \left[-k2\pi rl \frac{\partial}{\partial r} (\Re\{[c_2 K_0(qr)] \exp(i2\omega t)\}) \right]_{r=a}$$

For small values of x , $K_0(x) = -\ln(x)$ [ABR 1972].

$$\rightarrow c_2 = \frac{P_{rms}}{2\pi kl} = \frac{p_{rms}}{2\pi k}, \text{ where } p_{rms} \text{ is the rms power per unit length.}$$

Substituting the calculated values of c_1 and c_2 in equation A.13 yields:

$$\Delta T_{AC}(r, t) = \Re \left\{ \left[\frac{P_{rms}}{2\pi k} K_0(qr) \right] \exp(i2\omega t) \right\} = |\Delta T_{AC}(r)| \cos(2\omega t + \phi) \quad (\text{A.20})$$

$$\Delta T_{AC}(r) = \frac{P_{rms}}{2\pi k} K_0(qr) = \Delta T_{ACin-phase}(r) + i\Delta T_{ACout-phase}(r) \quad (\text{A.21})$$

where

$$\begin{aligned} \Delta T_{ACin-phase}(r) &= \frac{P_{rms}}{2\pi k} \Re(K_0(qr)) \\ \Delta T_{ACout-phase}(r) &= \frac{P_{rms}}{2\pi k} \Im \left(\frac{P_{rms}}{2\pi k} K_0(qr) \right) \end{aligned} \quad (\text{A.22})$$

Therefore, equation A.22 shows that the AC temperature oscillations produced due to a line heater embedded inside an infinite cylinder are found to have the form of a zero order modified Bessel function of the second kind.

A.2. Line heater study at the surface

Equation A.22 is derived for a one-dimensional line heater enclosed inside an infinite cylinder. However, the 3-omega method is carried out for metal lines deposited on the surface of a semi-infinite specimen. In order to acquire a similar model to that of the 3-omega method, the surface area of the infinite cylinder in the previous section is cut into half orthogonally to the radial axis as described in figure A.4.

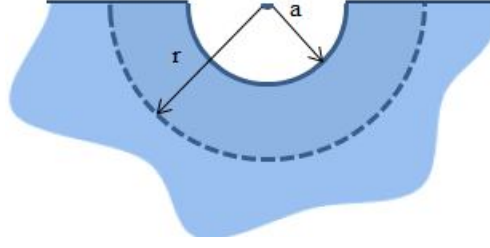


Figure A.4: Cross section of a semi- infinite half cylindrical sample.

Cutting the surface area of the infinite cylinder into half yields $A_s = \pi r l$.

Substituting $A_s = \pi r l$ in A.19 and solving for $c_1 = 0$ gives:

$$q_w = \Re(P_{rms} \exp(i2\omega t)) = \lim_{a \rightarrow 0} \left[-k\pi r l \frac{\partial}{\partial r} (\Re\{[c_2 K_0(qr)] \exp(i2\omega t)\}) \right]_{r=a}$$

$$\rightarrow c_2 = \frac{P_{rms}}{\pi k l} = \frac{P_{rms}}{\pi k}$$

Re-substituting for c_1 and c_2 in equation A.13 we can notice that the steady state temperature oscillations are divided by two when comparing it with equation A.22:

$$\Delta T_{AC}(r, t) = \Re \left\{ \left[\frac{P_{rms}}{\pi k} K_0(qr) \right] \exp(i2\omega t) \right\} = |\Delta T_{AC}(r)| \cos(2\omega t + \phi) \quad (\text{A.23})$$

$$\Delta T_{AC}(r) = \frac{P_{rms}}{\pi k} K_0(qr) = \Delta T_{ACin-phase}(r) + i\Delta T_{ACout-phase}(r) \quad (\text{A.24})$$

where,

$$\begin{aligned} \Delta T_{ACin-phase}(r) &= \frac{P_{rms}}{\pi k} \Re(K_0(qr)) \\ \Delta T_{ACout-phase}(r) &= \frac{P_{rms}}{\pi k} \Im(K_0(qr)) \end{aligned} \quad (\text{A.25})$$

In reality, the specimen is not semi-finite; however it has finite thickness t_s . The thermal penetration depth must not exceed the specimen thickness otherwise we will be measuring the thermal properties of what is underneath the specimen.

A.3. The effect of the substrate's thickness

As shown in the figure below, the exponential function decays to 1% of its initial magnitude after five length constants. However, a Bessel function decays faster than an exponential one rendering the thermal waves to decrease to less than 1% of their initial amplitudes after five length constants. Thus, for a semi-finite specimen, the thickness t_s must be five times greater than the thermal penetration depth.

$$t_s > 5\lambda \quad (\text{A.26})$$

Where the thermal penetration depth is given by:

$$\lambda = \frac{1}{|q|} = \sqrt{\frac{\alpha}{2\omega}} \quad (\text{A.27})$$

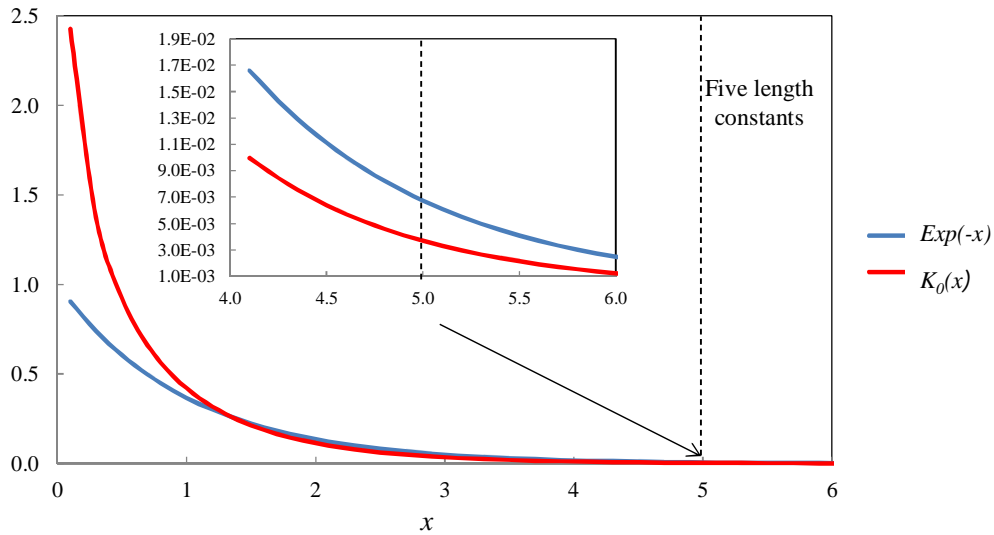


Figure A.5: Comparison between a decaying exponential function $Exp(x)$ in (blue) and a zero order modified Bessel function of the second kind $K_0(x)$ in (red) for a unit length constant.

REFERENCE APPENDIX A

- [ABR 1972] M. ABRAMOWITZ and I. A. STEGUN
“Handbook of mathematical functions with formulas, graphs and mathematical tables,”
Dover Publications, INC., New York, 1972.
- [BEL 1968] W. W. BELL
“Special functions of scientists and engineers,”
Copyright 1968, D. Van Nostrand Company, Ltd.
- [CAR 1959] H. S. CARSLAW and J.C. JAEGER
“Conduction of Heat in Solids,”
2nd ed. Oxford :Oxford University Press, 1959.
- [PAR 2010] B. Y. PARK, J. PARK, and D. KIM
“Note: Three omega method to measure the thermal properties of subnanoliter liquid samples,”
Review of Scientific Instruments, Vol.81, pp 066104, 2010.

Appendix B

Linear regression analysis

Table of contents

B.1. Least square estimate coefficients.....	B3
B.2. Standard error.....	B4
B.3. Linear least square fitting for $V_{3\omega \text{ in-phase}}$ versus $\text{Ln}(2\omega)$	B4
REFERENCE APPENDIX B.....	B7

B.1. Least square estimate coefficients

In order to find the best linear fit for the set of measured points $(x_i, y_i) = (\ln(2\omega)_i, V_{3\omega\text{in-phase}_i})$ the least square method is applied. This method attempts to minimize the sum of squares of deviations or the residual. The deviation is defined as the vertical distance between a data point and the best fit line. The smaller the deviations are the better is the fit.

$$\text{Residual} = \chi^2 = \sum_{i=1}^N (y_i - \hat{y}_i)^2 \quad (\text{B.1})$$

where N is the total number of data measured, y_i are the data points, and \hat{y}_i are the values from the best fit.

$$\text{The data follows a linear relation, so} \quad \hat{y}_i = \hat{A} + \hat{B}x_i \quad (\text{B.2})$$

where \hat{A} and \hat{B} are the least square estimates of the unknown coefficients A and B respectively.

χ^2 is minimum when its derivative with respect to \hat{A} and \hat{B} tends to zero. Differentiating equation B.1 with respect to \hat{A} and \hat{B} and setting them to zero we can find the least square estimates of A and B .

$$\frac{d\chi^2}{d\hat{A}} = 2N\hat{A} + 2\hat{B}\sum_{i=1}^N x_i - 2\sum_{i=1}^N y_i = 0 \quad (\text{B.3})$$

$$\frac{d\chi^2}{d\hat{B}} = 2\hat{B}\sum_{i=1}^N x_i^2 + 2\hat{A}\sum_{i=1}^N x_i - 2\sum_{i=1}^N x_i y_i = 0 \quad (\text{B.4})$$

Solving for equation B.3 and B.4 the coefficients \hat{A} and \hat{B} are as given below:

$$\hat{B} = \frac{\sum_{i=1}^N (x_i - \bar{x})(y_i - \bar{y})}{\sum_{i=1}^N (x_i - \bar{x})^2} \quad (\text{B.5})$$

$$\hat{A} = \bar{y} - \hat{B}\bar{x} \quad (\text{B.6})$$

where \bar{x} and \bar{y} are the mean values [STE 2002] of x_i and y_i respectively.

$$\bar{x} = \frac{1}{N} \sum_{i=1}^N x_i \quad (\text{B.7})$$

$$\bar{y} = \frac{1}{N} \sum_{i=1}^N y_i \quad (\text{B.8})$$

B.2. Standard error

To gain some idea about the accuracy of our predictions, the estimated standard error of regression must be determined. It is a measure of the scatter of data about the regression line. It gives a first impression of how well the fitted equation fits the measured data. This standard error is given by:

$$s_{\varepsilon} = \sqrt{\frac{\sum_{i=1}^N (y_i - \hat{y}_i)^2}{N - 2}} \quad (\text{B.9})$$

The above statistic allows us to calculate the standard error of the regression slope coefficient \hat{B} :

$$s_B = \frac{s_{\varepsilon}}{\sqrt{\sum_{i=1}^N (x_i - \bar{x})^2}} \quad (\text{B.10})$$

A more standardized statistic which determines the goodness of the fit is the coefficient of determination R^2 .

$$R^2 = 1 - \frac{SSR}{SST} = 1 - \frac{\sum_{i=1}^N (y_i - \hat{y}_i)^2}{\sum_{i=1}^N (y_i - \bar{y})^2} \quad (\text{B.11})$$

Where $SSR = \chi^2$ and SST are the residual sum of squares and the total sum of squares respectively. R^2 is bounded between 0 and 1. If R^2 is close to 1, this indicates that x_i and y_i are in a strong linear relation [YAN 2009].

B.3. Linear least square fitting for $V_{3\omega}$ in-phase versus $\text{Ln}(2\omega)$

A linear regression analysis is performed for the in-phase third harmonic voltages measured versus the natural logarithm of the thermal excitation frequency 2ω (equation 2.18). In tables B.1, B.2, B.3 and B.4 we present the linear least square fitting results for the four materials, borosilicate, gallium arsenide, indium phosphide and high resistivity silicon substrate respectively.

Table B.1 Linear least square fitting for third harmonic measurements done on BrSiO₂.

	Line	N	R ²	\hat{A} (mV)	\hat{B} mV/ln(rad/s)	s_{ϵ} (mV)	s_B mV/ln(rad/s)
WB	1	14	0.9997	2.5198	-0.2172	3.014E-3	1.008E-3
	2	13	0.9991	0.1928	-0.0205	2.056E-4	1.86E-4
	3	15	0.9996	0.6469	-0.0559	8.927E-4	2.957E-4
AD	1	14	0.9999	2.2694	-0.1925	2.804E-4	9.386E-5
	2	13	0.9994	0.1907	-0.0198	1.598E-4	1.445E-4
	3	15	0.9995	0.6709	-0.0582	1.086E-3	3.596E-4

Table B.2 Linear least square fitting for third harmonic measurements done on GaAs.

	Line	N	R ²	\hat{A} (mV)	\hat{B} mV/ln(rad/s)	s_{ϵ} (mV)	s_B mV/ln(rad/s)
WB	4	8	0.9886	0.0595	-0.00405	8.578E-5	1.772E-4
	5	9	0.9851	0.00631	-0.000443	1.075E-5	2.221E-5
	6	12	0.9946	0.03035	-0.001854	8.015E-5	4.288E-5
AD	4	8	0.9830	0.05897	-0.004183	1.087E-4	2.246E-4
	5	9	0.9410	0.00603	-0.0004376	2.165E-5	4.473E-5
	6	12	0.9992	0.0292	-0.001825	2.899E-5	1.551E-5

Table B.3 Linear least square fitting for third harmonic measurements done on InP.

	Line	N	R ²	\hat{A} (mV)	\hat{B} mV/ln(rad/s)	s_{ϵ} (mV)	s_B mV/ln(rad/s)
WB	7	13	0.9996	0.5112	-0.03125	4.388E-4	1.789E-4
	8	11	0.9798	0.1564	-0.0105	3.561E-4	5.013E-4
	9	10	0.9882	0.1407	-0.00969	2.334E-4	3.743E-4
AD	7	14	0.9999	0.5377	-0.03273	2.803E-4	1.032E-4
	8	11	0.9964	0.1581	-0.0105	1.539E-4	2.136E-4
	9	11	0.9984	0.1539	-0.01035	9.858E-5	1.387E-4

Table B.4 Linear least square fitting for third harmonic measurements done on Si.

	Line	N	R^2	\hat{A} (mV)	\hat{B} mV/ln(rad/s)	s_ϵ (mV)	s_B mV/ln(rad/s)
WB	10	14	0.9983	0.1437	-0.00924	1.506E-4	1.089E-4
	11	24	0.9978	0.3956	-0.02398	8.701E-4	2.367E-4
	12	11	0.9926	0.2776	-0.01906	2.778E-4	5.475E-4
AD	10	14	0.9990	0.1408	-0.00918	1.153E-4	8.337E-5
	11	24	0.9974	0.4169	-0.02509	9.861E-4	2.683E-4
	12	11	0.9838	0.2736	-0.01875	4.071E-4	8.022E-4

The coefficient of determination R^2 for all measurements is around 1. This indicates a good linear relation between the in-phase third harmonic voltages and the thermal excitation frequency 2ω in the linear regime. Moreover, we can notice that the uncertainties in the slope s_B are unimportant. This means that the scatter of data around the regression line is small.

REFERENCE APPENDIX B

- [STE 2002] A. STEWART
“Basic statistics and epidemiology, a practical guide,”
Radcliffe Medical Press Ltd, 2002.
- [YAN 2009] X. YAN and X. G. SU
“Linear regression analysis : Theory and Computing,”
World Scientific Publishing Co. Pte. Ltd., 2009.

Publications

N. AL-KHUDAR, P.Y. CRESSON, Y. ORLIC, P. COQUET, P. PERNOD, and T. LASRI
“Measurement of the thermal conductivity of polydimethylsiloxane polymer using the three omega method,”
Key engineering materials, Vol. 613, pp 259-266, 2014.

N. AL-KHUDARY, P.Y. CRESSON, W. WEI, H. G. HAPPY and T. LASRI
“Inkjet printing technology for polymer thermal conductivity measurement by the three omega method,”
Polymer testing, Vol. 40, pp187-195, 2014.

International conference

N. AL-KHUDAR, P.Y. CRESSON, Y. ORLIC, P. COQUET, P. PERNOD, and T. LASRI
“Measurement of the thermal conductivity of polydimethylsiloxane polymer using the three omega method,”
The 11th International symposium on measurement technology and intelligent instruments (ISMTII), RWTH, Aachen, Germany, 2013.

National conference

N. AL-KHUDARY, P.Y. CRESSON and T. LASRI
“Measuring the thermal conductivity of substrates using the 3 omega method,”
15^{ème} Journée national du réseau doctorale en microélectronique (JNRDM), Marseille, 2012.

Abstract

The characterization of polymers is gaining a great attention as they are one of the main constituents of future flexible or organic electronics. Given the fact that thermal management is an important issue in the frame work of flexible electronics, the knowledge of the thermal conductivity of polymer materials is needed.

In this work, we propose the measurement of polymer material thermal conductivity using the three omega method. This method requires heating a metallic line conductor placed on the surface of the material under test by an alternating current source. The first measurements were done on polydimethyl siloxane (PDMS) polymer material for which a special procedure that consists in embedding the metallic conductors near the surface has been applied.

In addition to the well-known limitations of photolithography process which are the cost and the process duration, a particular concern lies in the fabrication of the metallic conductors by such process which might be destructive in case of polymer materials. Consequently, we propose an alternative method for this kind of materials based on inkjet printing technology. The thermal conductivities of polyimide and polyetherether ketone have been successfully measured using the three omega method combined with inkjet printing technology for sample preparation.

Numerical simulations using finite element method (FEM) are also performed. Finally, the experimental measurements are compared to Cahill's analytical solution and FEM modelling.

The overall results demonstrate that the inkjet printing technology is a good candidate for the characterization of flexible substrates in terms of thermal conductivity.

KEYWORDS:

Flexible electronics, polymers, thermal conductivity, three omega method, inkjet printing technology

Résumé

Dans le domaine de l'électronique souple, les substrats flexibles à base de polymères sont de plus en plus utilisés. Si dans les prochaines années, les structures de propagation mises en œuvre sur ce type de substrat véhiculent une puissance, alors la connaissance de la conductivité thermique de ces matériaux est essentielle.

Dans ce travail, nous mesurons la conductivité thermique de matériaux de type polymère en utilisant la méthode 3 omégas. Des mesures ont été effectuées sur du polydiméthylsiloxane (PDMS). Un procédé technologique particulier est utilisé pour la fabrication des échantillons de PDMS. De ce fait, les conducteurs métalliques sont encapsulés dans le polymère et non en surface de ce dernier. Mais cela est sans conséquence sur les valeurs de conductivité thermique mesurées.

Les procédés photolithographiques utilisés traditionnellement pour réaliser les lignes métalliques sont coûteux. Par conséquent, nous proposons pour ce type de matériaux une méthode alternative pour la réalisation des lignes conductrices par la technologie d'impression jet d'encre. Les conductivités thermiques du polyimide et polyétheréthercétone ont été mesurées en utilisant la méthode 3ω combinée à la technologie d'impression par jet d'encre.

Des simulations numériques basées sur la méthode des éléments finis ont été développées au cours de la thèse. Les mesures expérimentales obtenues sont comparées aux résultats obtenus par une solution analytique et par notre modélisation numérique.

Ainsi durant cette thèse nous montrons avec succès la possibilité d'utiliser la technologie d'impression jet d'encre pour mesurer la conductivité thermique d'un substrat souple.

MOTS-CLES:

Électronique souple, polymères, conductivité thermique, méthode 3 omégas, impression par jet d'encre.